

ALMA MATER STUDIORUM – UNIVERSITÀ DI BOLOGNA

DOTTORATO DI RICERCA IN

Meccanica e Scienze Avanzate dell'Ingegneria (DIMSAI)

Ciclo XXX

Settore Concorsuale di afferenza: 09/C2

Settore Scientifico disciplinare: ING-IND/10

**Experimental Analysis of Droplet Generation in Presence of
Newtonian and non-Newtonian Flows within Microjunctions**

Presentata da: **Behnam Rostami**

Coordinatore Dottorato:

Prof. Ing. Marco Carricato

Relatore:

Prof. Ing. Gian Luca Morini

Esame finale anno 2018

DEDICATION

*This thesis is dedicated to my beloved parents and brothers who offered
unconditional love, support and encouragement*

ACKNOWLEDGEMENT

Thanks to God Almighty for the completion of the Ph.D. thesis.

I would like to express my deepest gratitude and appreciation to my supervisor, Prof. Gian Luca Morini for his continuous support, guidance, patience and invaluable advice and suggestions throughout my candidature. It would be impossible to finish this thesis without his support and inputs. He also provided me with scholarship during my studies in Bologna. The opportunity to study in the oldest university in the world and to live in an ancient city has broadened my horizon and opened new chances in my career. I should take this opportunity to especially thank Dr. Beatrice Pulvirenti for her helpful discussion and precious advices during my studies in University of Bologna. Many thanks to Prof. Paola Fabbri from Department of Civil, Chemical, Environmental, and Materials Engineering who kindly provided us the access to her laboratory to measure physical properties of the fluids.

I would like to extend my wholeheartedly thanks to anyone who directly or indirectly helped me passionately and sincerely, starting from my friends Danish Rehman and Dr. Giacomo Puccetti and also Dr. Stefania Falcioni, Maurizio Chendi, Fabrizio Casarini and Franco Ferri for their technical support in laboratory.

To my parents and brothers, I would not have been where I am today without their enduring love, support, patience and unwavering faith throughout this period. They, once again, reminded me any desire is achievable by one-heartedness. I thank them immensely.

It is hard to mention all the good things I experienced in Italy. Over these three years Italy has become my second home with one of the most unique cultures and kindest people, not forgetting wonderful peaceful nature and delicious food.

Hopefully this thesis can give quite a contribution to the engineering research in Italy.

ABSTRACT

During the last two decades, microdroplets have attracted increasing interest among researchers due to the wide spread of promising technological applications such as biological analysis, cancer diagnosis, drug discovery and chemical reactions. With respect to traditional emulsion methods which are usually able to produce droplets with a broad size variation (polydispersed emulsions), microfluidic devices have been developed to produce monodispersed microdroplets with a controllable size. The diameter and size variation of droplets are controlled by a series of parameters, including the geometries and dimensions of the microfluidic devices, properties of the liquids, flow rates and surfactant concentrations. Although a massive amount of experimental studies have been performed, the effects of controlling parameters and relevant mechanisms have not been completely understood and supplementary work is needed in this direction. In many cases, the application of monodispersed emulsions in biological and pharmaceutical areas involves the generation of non-Newtonian droplets (i.e. in blood or DNA analysis) and in this field there are a series of aspects which are, up to now, under-investigated.

In this Ph.D. thesis, droplet formation has been analyzed experimentally, thanks to a series of specific tests on simple microfluidic devices devoted to droplet generation based on the use of T-junctions or micro cross-junctions. The experimental work has been focused on the analysis of the control of droplet regime which can be activated in a microfluidic droplet generator in presence of Newtonian and non-Newtonian dispersed phases, with or without the addition of surfactants. The mechanism of the droplet formation has been studied by following the evolution of the interface between the immiscible liquids at the microjunction thanks to the post processing of images acquired by using a speed camera connected to an inverted microscope. In order to study the behavior of non-Newtonian shear thinning liquids during droplet formation, Xanthan gum aqueous solutions have been used because their rheological properties are very similar to those of blood. The effect on the droplet regimes of the main controlling parameters, such as the flow rates of the immiscible liquids introduced in the

microfluidic device, fluid viscosity and interfacial tension has been studied with the aim to individuate the range of these controlling parameters for which the microfluidic device is able to produce monodispersed droplets with an assigned volume and frequency.

SOMMARIO

In questa tesi di Dottorato viene effettuata una analisi sperimentale della generazione di gocce liquide mono-disperse mediante l'uso di micro-giunzioni a T e a croce. E' possibile generare un flusso di gocce liquide con caratteristiche geometriche predeterminate introducendo il liquido da suddividere in gocce all'interno di una micro-giunzione assieme ad un altro liquido (immiscibile) utilizzato come vettore per le gocce. Le dimensioni delle gocce possono essere variate aggiustando le portate dei due liquidi introdotti nella giunzione. L'analisi si è concentrata sull'individuazione delle principali modalità di formazione delle gocce utilizzando diverse combinazioni di liquidi immiscibili Newtoniani (acqua, olio siliconico) e non newtoniani (soluzioni di Xanthan gum in acqua) con o senza l'introduzione di surfattanti, quali il Tween 20.

Variando i principali parametri di controllo (portate in ingresso, rapporto di viscosità tra i liquidi introdotti nella giunzione, tensione all'interfaccia liquido/liquido) è possibile osservare un cambiamento nel meccanismo di formazione delle gocce all'interno della giunzione e quindi ottenere gocce con dimensioni diverse e con una diversa stabilità delle dimensioni delle gocce all'uscita della giunzione. Questo soggetto è stato estensivamente investigato da molti ricercatori negli ultimi anni in quanto la formazione di emulsioni mono-disperse è un topic di estremo interesse in molti campi industriali che vanno dall'industria alimentare, a quella dei cosmetici, all'area medica e biologica. Per questo motivo in questa Tesi ci si è dedicati all'analisi di una serie di aspetti tecnici che non hanno ricevuto la dovuta attenzione sino a questo momento in letteratura quali ad esempio:

- Il ruolo svolto dal rapporto tra le viscosità dei liquidi immiscibili introdotti nella giunzione in presenza di liquidi non –Newtoniani con caratteristiche reologiche simili a quelle del sangue umano;

- L'uso di giunzioni a T in cui i due liquidi immiscibili vengono introdotti nella giunzione attraverso i due canali contrapposti in presenza di liquidi non-Newtoniani;
- Lo studio dettagliato del meccanismo di breakup delle gocce in un ampio range di condizioni operative imposte all'ingresso della giunzione;
- Misura della frequenza delle gocce generate, del tempo di breakup, delle dimensioni delle singole gocce al variare dei liquidi utilizzati e delle condizioni operative imposte;
- Valutazione della varianza della dimensione delle gocce al variare delle condizioni operative imposte all'ingresso della giunzione al fine di individuare la combinazione di condizioni operative in corrispondenza delle quali la generazione di emulsioni mono-disperse viene garantita.

Questo tipo di informazioni sono preziose per tarare accurati modelli numerici in grado di simulare il processo di formazione delle gocce all'interno di microdispositivi a fluido e di ottimizzarne il funzionamento.

I principali risultati ottenuti in questa tesi possono essere così riassunti:

- Il meccanismo di formazione delle gocce è influenzato dal rapporto tra le portate volumetriche introdotte nella giunzione (α), dal valore del rapporto tra le viscosità associate ai due liquidi immiscibili (λ), dal numero di Capillarità (Ca) associato alle due fasi.
- Le giunzioni a T a flussi contrapposti possono essere utilizzate per generare emulsioni di liquidi Newtoniani monodisperse in soluzioni acquose solo in presenza di canali con comportamento idrofilico. In presenza di pareti idrofobiche la generazione di gocce mono-disperse risulta fortemente inibita.
- Le giunzioni a croce garantiscono la produzione di emulsioni mono-disperse per un ampio range di condizioni operative per liquidi Newtoniani immiscibili caratterizzati da un basso valore del rapporto tra le viscosità della fase dispersa e continua.
- La formazione di gocce avviene per "schiacciamento" (squeezing) a basse portate volumetriche dei liquidi introdotti nella giunzione. Quando la portata volumetrica della fase continua introdotta nella giunzione aumenta, la goccia viene formata a

seguito dell'azione prodotta dalla fase continua sull'interfaccia liquido/liquido (dripping). Aumentando ancora la portata volumetrica della fase continua si genera una instabilità dell'interfaccia liquido/liquido che finisce per produrre il distacco della goccia fuori dalla giunzione (jetting).

Quando la fase dispersa è un liquido non-Newtoniano dotato di una viscosità che diminuisce all'aumentare dello sforzo di taglio, prima del distacco della goccia si forma un lungo filamento tra la matrice dispersa in ingresso nella giunzione e la goccia in fase di formazione. Quando la goccia si stacca, il filamento si rompe generando una serie di gocce satellite che possono unirsi con la goccia principale aumentando la variazione del diametro delle gocce prodotte.

I dati raccolti hanno permesso di costruire delle mappe generali in base alle quali è possibile conoscere con quale meccanismo (squeezing, dripping e jetting) le gocce vengono prodotte al variare delle condizioni operative imposte.

CONTENTS

ACKNOWLEDGEMENT	i
ABSTRACT	iii
SOMMARIO	v
CONTENTS	ix
FIGURES.....	xv
TABLES	xxv
NOMENCLATURE	xxvii
Chapter 1 Droplet Generation in Microfluidics: State-of-the-Art	1
1.1 Introduction	1
1.2 Geometry and dimension of the junction	4
1.2.1 T-junction configurations	4
1.2.2 Flow-focusing configurations.....	5
1.3 Droplet formation and controlling mechanisms.....	6
1.3.1 Effect of flow rate.....	9
1.3.2 Effect of geometry	13
1.3.3 Effect of viscosity	18
1.3.4 Effect of interfacial tension	20
1.3.5 Effect of wettability in droplet generation.....	22
1.3.6 Effect of non-Newtonian properties	22

1.4	Droplet characteristics	25
1.4.1	Droplet formation time	25
1.4.2	Filament, thread and microthread	26
1.5	Models of droplet formation	27
1.5.1	Droplet formation models in squeezing regime	28
1.5.1.1	Correlations dependent on flow rate ratio α	28
1.5.1.2	Two-stage models	29
1.5.1.3	Models based on a force balance	30
1.5.2	Droplet formation models in dripping and jetting regimes	30
1.6	Governing forces and droplet size.....	31
1.6.1	Governing forces on a droplet	31
1.6.1.1	Pressure drop.....	32
1.6.1.2	Shear force	36
1.6.1.3	Interfacial tension	38
1.7	Scope of the thesis.....	39
1.8	Outline of the thesis.....	40
	Chapter 2 Experimental Setup and Data Reduction	43
2.1	Experimental apparatus	43
2.2	Data reduction and governing parameters.....	46
2.3	Microchannels	48
2.3.1	Cross-slot microchannels.....	48
2.3.2	T-junction	50
2.4	Working fluids.....	51
2.4.1	Density measurement	52
2.4.2	Viscosity measurement.....	54
2.4.3	Surface and interfacial tension	58

2.5	The effect of surfactant	59
2.6	Processing of the images	61
2.6.1	Analysis of the images.....	62
2.6.2	Edge detection	64
2.6.3	Post-processing of the image	65
2.6.4	Neck detection	66
2.6.5	Droplet size.....	67
2.6.5.1	Polydispersity.....	68
2.7	Uncertainty	68
Chapter 3 Experimental Investigation of Droplet Formation at Micro Cross- Junctions		71
3.1	Newtonian and non-Newtonian emulsions at low values of Ca_c	73
3.1.1	Effect of Ca_c and α	78
3.1.2	Analysis of the drop diameter for low α	80
3.1.3	Polydispersity	83
3.2	Newtonian and non-Newtonian emulsions at large Ca_c values.....	86
3.2.1	Squeezing regime	87
3.2.2	Dripping regime.....	89
3.2.3	Jetting regime	91
3.2.4	Effect of Ca_c	93
3.2.5	Effect of Q_d	95
3.2.6	The droplet regime maps	96
3.2.7	Prediction of droplet regimes	100
3.2.8	Polydispersity	103
3.2.9	Effect of Xanthan gum concentration.....	108
3.2.10	Effect of Ca_d	109

3.3	Droplet formation dynamics.....	115
3.3.1	Droplet formation time	116
3.3.1.1	Effect of Q_c	116
3.3.1.2	Effect of Q_d	119
3.3.1.3	Effect of Xanthan gum concentration	123
3.3.1.4	Length of microthread	124
3.3.2	Breakup mechanism	125
3.3.3	Geometry effects.....	130
3.3.3.1	Flow maps.....	131
3.3.3.2	Droplet size at low flow rate ratio	132
Chapter 4 Experimental Investigation of Droplet Formation at a Micro T-Junction		139
4.1	Water without surfactant	140
4.2	Water with surfactant	148
4.2.1	Flow map	149
4.2.2	Effect of Ca_c and Q_d	152
4.2.3	Breakup distance.....	158
4.2.4	Polydispersity	160
4.3	Droplets in Newtonian and non-Newtonian carrier medium by a new microchannel.....	162
4.3.1	Droplet-based flow regime	162
4.3.1.1	Effect of α and Ca_c	168
4.3.1.2	Breakup distance.....	171
4.3.1.3	Polydispersity.....	172
Chapter 5 Conclusions and Recommendations for Future Work		175
5.1	Key findings of the thesis.....	176
5.2	Recommendations for future work.....	183

References 185

FIGURES

<p>Figure 1.1. Three most common microfluidic geometries used for droplet generation; (a) T-junction, (b) flow-focusing and (c) co-flow device [5]. The dispersed phase is indicated in blue while continuous phase is in yellow.</p>	3
<p>Figure 1.2. Typical illustration of T-junction with three distributions of the continuous phase CP and dispersed phase DP along them for (a) cross-flow, (b) perpendicular cross-flow and (c) opposed-flow.</p>	4
<p>Figure 1.3. Three typical categories of microfluidic flow-focusing devices; (a) axisymmetric capillary co-flowing device, (b) flow-focusing channel and (c) cross-junction geometry from Fu <i>et al.</i> [37].</p>	5
<p>Figure 1.4. Schematic of a planar flow-focusing geometry from Lee <i>et al.</i> [28] where W_{or} and W_{out} represent orifice and outlet channel width values, respectively, $2a$ is the inner channel width and Δz is a distance downstream of the end of the inner channel.</p>	6
<p>Figure 1.5. Illustration of droplet generation in a typical flow-focusing device; (a) squeezing regime, (b) dripping regime and (c) jetting regime from Lee <i>et al.</i> [28].</p>	8
<p>Figure 1.6. The interface between two immiscible fluids and the dispersed phase neck from Garstecki <i>et al.</i> [41].</p>	10
<p>Figure 1.7. Non-dimensional length of plugs as a function of flow rate ratio (here Q) and continuous Capillary number (here Ca) from Liu and Zhang [39].</p>	11
<p>Figure 1.8. Linear dependence of the drop size on flow rate ratio when $\alpha > 1$ from Garstecki <i>et al.</i> [41] where water droplets in different oil flows with diverse viscosities.</p>	12
<p>Figure 1.9. (a) The illustration of λ-junction from Yeom and Lee [52] and (b) Y-junction from Raj <i>et al.</i> [51].</p>	13
<p>Figure 1.10. The dispersion processes in the three kinds of microchannels in the same</p>	

range of continuous phase flow rate from Wang <i>et al.</i> [55].	14
Figure 1.11. Droplet generation along a venturi-shaped micro T-junction from Wang <i>et al.</i> [56] for (a) an ordinary T-junction and (b & c) modified T-channels.	14
Figure 1.12. Droplet formation in the four rounded flow-focusing devices at two different flow rate ratios where R is the radius of the curvature from Gulati <i>et al.</i> [61].	17
Figure 1.13. The effect of viscosity ratio λ in droplet formation process at a fixed flow rate ratio $\alpha = 0.25$ and $Ca_c = 0.006$ from Liu and Zhang [45].	18
Figure 1.14. Phase diagram of flow-focusing geometry and T-junction from Nunes <i>et al.</i> [50].	20
Figure 1.15. Schematic diagram of a pendant drop from a nozzle from Zhang [75].	26
Figure 1.16. Tiny microthread before the droplet detachment from Kowalewski [76].	27
Figure 1.17. The forces acting on the emerging droplet in the filling stage from Glawdel <i>et al.</i> [85].	31
Figure 1.18. The related regimes corresponding to pressure variation upstream of a T-junction from Li <i>et al.</i> [87].	32
Figure 1.19. A schematic illustration (top view) of the shape of the tip of the immiscible thread at an intermediate stage of break-up from Garstecki <i>et al.</i> [41].	33
Figure 1.20. Schematic representation of drop creation in the presence of cross-flow shear from Husny and Cooper-White [63].	36
Figure 2.1. Microchip on the working desk of the inverted microscope with the indication of the inlets (Q_c and Q_d) and outlet.	43
Figure 2.2. The lay-out of the experimental setup.	44
Figure 2.3. An overview of the experimental apparatus.	45
Figure 2.4. Zoomed view of the inverted microscope.	45
Figure 2.5. Micro cross-junction (<i>Dolomite Microfluidics Co.</i>) with two linear 4-way connectors.	49
Figure 2.6. Cross-slot microchannels used for the experiments: (a) geometry of junctions #1; (b) geometry of junction #2; (c) channel cross-section at the junction and (d) channel cross-section far from the junction.	49

Figure 2.7. Geometry of the T-junction (a) top view and (b) side view.....	51
Figure 2.8. Automatic cabinet water stills (<i>Aquatron A4000D</i>) for production of pure distilled water.....	52
Figure 2.9. Analytical balance (<i>RADWAG AS 220.R2</i>) used for density measurements.	53
Figure 2.10. The Cannon-Fenske Viscometer.....	54
Figure 2.11. Viscometer with rotating discs (<i>Brookfield DV-II +Pro</i>) used to measure the viscosity of non-Newtonian working fluids.....	55
Figure 2.12. Comparison between experimental values of apparent viscosity of Xanthan gum aqueous solutions with 0.2 wt% and 0.5 wt% (0.2 XG and 0.5 XG) and the literature values reported in [91] for a liquid temperature of 23°C.....	57
Figure 2.13. Tensiometer (<i>KSV Sigma 700</i>) used for the determination of surface and interfacial tensions.	58
Figure 2.14. Molecular structure of the surfactant from Shui <i>et al.</i> [32].	60
Figure 2.15. The interfacial tension of silicone oil and water with different percentages of Tween 20.	61
Figure 2.16. Sequence of raw images showing the squeezing and the breakup of water in oil (W/O) droplets obtained by imposing water (0.8 ml/h) and silicone oil (1.6 ml/h) volumetric flow rates.....	62
Figure 2.17. (a) Raw image of a droplet in a cross-junction ($Q_c = 1.6$ and $Q_d = 0.16$ ml/h) and (b) complement of the image of the junction without droplet.	63
Figure 2.18. (a) Gray levels image and (b) binary image of the droplet.	64
Figure 2.19. (a) Edges extracted by Canny method and (b) reconstruction of the domain by filling it (dark zone).	65
Figure 2.20. Determination of the droplet center for three consecutive snapshots.	65
Figure 2.21. (a) Raw image and (b) edge of the droplet for the micro T-junction.....	66
Figure 2.22. The detection of minimum width when $Ca_c = 0.0081$, $\alpha = 0.5$ and $t = -0.4$; (a) raw image with window borders in red, (b) cropped image, (c) saturated image, (d) binary image and (e) the edge of the thread by Canny method.	67

Figure 3.1. Droplet formation mechanisms for 0.5 XG+T as dispersed phase and silicone oil as continuous phase by fixing $Q_c = 1.5$ ml/h and by increasing $Q_d = 0.015, 0.2$ and 1.5 ml/h, respectively.	74
Figure 3.2. Comparison between the droplet regimes obtained by using a Newtonian (W) and a non-Newtonian (0.5 XG+T) dispersed phase in combination with silicone oil as continuous phase by increasing α at similar Capillary number Ca_c	75
Figure 3.3. Droplet flow maps as a function of flow rate ratio α ; (a) W, (b) W+T, (c) 0.3 XG+T and (d) 0.5 XG+T.	77
Figure 3.4. Non-dimensional diameter D^* of the droplets for; (a) W and W+T and (b) 0.3 XG+T and 0.5 XG+T in a continuous flow of silicone oil as a function of the flow rate ratio.	79
Figure 3.5. Dimensionless droplet diameter as a function of flow rate ratio α	80
Figure 3.6. Non-dimensional droplet diameter as a function of $q Ca_c^x$	82
Figure 3.7. Non-dimensional droplet diameter as a function of $(\varepsilon + \omega\alpha) Ca_c^x$	82
Figure 3.8. Polydispersity Pl of droplet as a function of Ca_c and flow rate ratio α for different dispersed phases: (a) W, (b) 0.3 XG+T and (c) 0.5 XG+T in silicone oil.	84
Figure 3.9. Droplet regimes obtained by fixing the volumetric flow rate of the Xanthan gum aqueous solution (0.2 XG+T) equal to $Q_d = 0.1$ ml/h and $Q_c =$ (a) 0.3 ml/h (squeezing regime), (b) 3 ml/h (dripping regime) and (c) 10 ml/h (jetting regime).	86
Figure 3.10. Squeezing regime when $Q_c = 0.8$ ml/h and $Q_d = 0.08$ ml/h for pure water (W) emulsions.	88
Figure 3.11. Dripping regime when $Q_c = 4$ ml/h and $Q_d = 0.2$ ml/h for 0.3 XG+T emulsions.	90
Figure 3.12. Jetting regime when $Q_c = 10$ ml/h and $Q_d = 0.1$ ml/h for 0.4 XG+T emulsions.	91
Figure 3.13. Thread instability during jetting: (a) pure water W ($Q_c = 4$ ml/h and $Q_d = 20$ ml/h); (b) 0.3 XG+T ($Q_c = 8$ ml/h and $Q_d = 0.1$ ml/h).	92
Figure 3.14. Effect of continuous Capillary number where $0.3 \leq Q_c \leq 20$ and $Q_d = 0.1$ ml/h for W, W+T and three concentrations of Xanthan gum solution, 0.2 XG+T, 0.3 XG+T and 0.5 XG+T.	93

Figure 3.15. Droplet dimensionless diameter of the (a) Newtonian and (b) non-Newtonian emulsions as a function of the continuous Capillary number obtained when $Ca_c \geq 0.01$ and $Q_d = 0.1$ ml/h.	94
Figure 3.16. Non-dimensional diameter of the droplet as a function of the flow rate ratio α when $Ca_c > 0.01$: (a) Newtonian dispersed phases (W and W+T) and (b) non-Newtonian dispersed phases (0.3 XG+T and 0.5 XG+T).	95
Figure 3.17. Droplet regimes as a function of the continuous Capillary number (Ca_c) and the flow rate ratio (α) by considering as dispersed phase: (a) W, (b) W+T, (c) 0.3 XG+T and (d) 0.5 XG+T.	97
Figure 3.18. Droplet regimes, DJ, DC and PF, of the emulsions by considering in silicone oil: (a) W, (b) W+T, (c) 0.3 XG+T and (d) 0.5 XG+T as dispersed phase.	99
Figure 3.19. (a) Trend of the droplet diameter D^* as a function of Ca_c ; (b) derivative of D^* with respect to Ca_c as a function of Ca_c	102
Figure 3.20. Polydispersity Pl of droplet as a function of Ca_c and α for different dispersed phases in silicone oil; (a) W, (b) W+T, (c) 0.3 XG+T and (d) 0.5 XG+T.	104
Figure 3.21. Droplets of water and Tween 20 (W+T) in silicone oil (SO) obtained by fixing the value of the flow rate ratio (α) and the Capillary number linked to the continuous phase (Ca_c).	105
Figure 3.22. Droplets of Xanthan gum aqueous solution (0.3 XG+T) in silicone oil obtained by fixing the value of the flow rate ratio (α) and the continuous Capillary number (Ca_c).	106
Figure 3.23. Main droplet and satellite droplet observed for three consecutive droplets obtained for $Ca_c = 0.160$ and $\alpha = 0.1$ using 0.5 XG+T as dispersed phase.	107
Figure 3.24. Effect of Xanthan gum concentration on droplet non-dimensional diameter for various flow rates while open symbols stand for 0.3 XG+T and close symbol represent 0.5 XG+T.	108
Figure 3.25. Effect of Xanthan gum concentration on droplet non-dimensional diameter as a function of Xanthan gum concentration (wt%) when $Q_c =$ (a) 1 and (b) 4 ml/h.	109
Figure 3.26. Images of the droplet formation process for different controlling regimes.	113

Figure 3.27. Droplet regime map at different Ca_c and Ca_d ; (a) W, (b) W+T, (c) 0.3 XG+T and (d) 0.5 XG+T.....	115
Figure 3.28. Droplet formation time against Q_c	117
Figure 3.29. Droplet formation time t_f (ms) as a function of Q_c (ml/h) for 0.2 XG+T.	119
Figure 3.30. Droplet formation time against Q_d for (a) Newtonian and (b) non-Newtonian emulsions.	120
Figure 3.31. Droplet formation time t_f (ms) as a function of Q_d (ml/h) for 0.3 XG+T.	121
Figure 3.32. Frequency of the droplet f for various values of Q_c and Q_d for pure water (W) emulsions.....	122
Figure 3.33. Frequency of the droplet f for various values of Q_d when $Q_c = 1, 2$ and 4 ml/h; closed symbols represent 0.3 XG+T while open symbols stand for 0.5 XG+T.....	122
Figure 3.34. Frequency of the droplet f as a function of Q_c for 0.2 XG+T and 0.5 XG+T when $Q_d = 0.1$ ml/h.	123
Figure 3.35. Non-dimensional microthread length \bar{L} for three different concentrations of Xanthan gum solution as a function of the flow rate ratio α when $Q_d = 0.1$ ml/h.	124
Figure 3.36. The necking in different moments when $Ca_c = 0.0032$ and $\alpha = 0.3$	126
Figure 3.37. (a) Evolution of minimum width w_{min} and the radius of curvature κ of water-oil interface and (b) – (g) necking to rupturing of a water droplet in oil flow when $Ca_c = 0.0032$ and $\alpha = 0.5$	127
Figure 3.38. The characteristics of the channel and water-oil interface.....	128
Figure 3.39. The trend of the variation in minimum width w_{min} and radius of curvature κ versus t when $\alpha = 0.5$; open symbols correspond to w_{min} while closed symbols denote κ	129
Figure 3.40. The trend of the variation in minimum width w_{min} and radius of curvature κ versus τ when $\alpha = 0.5$; open symbols correspond to w_{min} while closed symbols denote κ	129
Figure 3.41. Junction geometry and channel dimensions.....	130
Figure 3.42. Droplet flow regimes as a function of α ; (a) channel #1 and (b) channel #2.	131
Figure 3.43. Typical droplets generated by using: (a) junction #1 and (b) junction #2.	132

Figure 3.44. D^* as a function of the flow rate ratio (α) for different values of the Capillary numbers Ca_c ; (a) junction #1 and (b) junction #2.....	133
Figure 3.45. The dimensionless minimum width as a function of α ; open symbols correspond to the data for channel #1 while closed symbols denote of channel #2.	134
Figure 3.46. D^* as a function of α for different Ca_c values; (a) junction #1 and (b) junction #2.....	135
Figure 3.47. Comparison between the power-law correlation ($q Ca_c^x$) and experimental data obtained for (a) junction #1 and (b) junction #2.	135
Figure 3.48. Comparison between the new correlation ($\varepsilon + \omega\alpha$) Ca_c^x and experimental data obtained for (a) junction #1 and (b) junction #2.	136
Figure 3.49. Δz and a for (a) the junction used in this thesis and (b) a planar flow-focusing device [28].	137
Figure 3.50. Comparison between the new correlation ($\varepsilon + \omega\alpha$) Ca_m^x and experimental data obtained for (a) junction #1 and (b) junction #2.	138
Figure 4.1. Parallel flow obtained by introducing pure water and silicone oil in the micro T-junction when (a) $Q_c = 3$ ml/h and $Q_d = 0.9$ ml/h and (b) $Q_c = 126.2$ ml/h, $Q_d = 15$ ml/h.	141
Figure 4.2. A sketch with the indication of the height of the continuous (h_c) and dispersed (h_d) phase in a parallel flow. The interface thickness is highlighted.	141
Figure 4.3. Comparison between the prediction of Equation (4-10) and the experimental results in terms of depth ratio β^{-1} as a function of α^{-1}	145
Figure 4.4. (a) Depth of the continuous phase h_c and (b) of the dispersed phase h_d compared with the theoretical predictions of Equation (4-10).	145
Figure 4.5. Droplet regimes as a function of flow rate ratio α and of Ca_c for silicone oil droplets in pure water.....	146
Figure 4.6. The generation of a silicone oil droplet at large values of Q_c obtained by squeezing by using pure water as continuous phase.	147
Figure 4.7. Effect of Tween 20 on the flow pattern (a) at the junction and (b) downstream of the junction in the absence as well as two different concentrations of Tween 20.....	148
Figure 4.8. Images sequence obtained by fixing $Q_c = 3$ ml/h and by varying Q_d from 0.3	

ml/h (a) to 3 ml/h (b) to 5.1 ml/h (c).....	150
Figure 4.9. Droplet regimes as a function of flow rate ratio α and of Ca_c for silicone oil droplets in water with the addition of Tween 20 (2 wt%).	152
Figure 4.10. Non-dimensional length of the droplets as a function of flow rate ratio α for different continuous Capillary numbers Ca_c	153
Figure 4.11. Effect of Q_d (ml/h) on the transition between DJ and DC regime.	155
Figure 4.12. Non-dimensional droplet length as a function of α for both DJ and DC regimes.....	155
Figure 4.13. Dimensionless plug length as a function of α for DJ regime.	156
Figure 4.14. Non-dimensional length of the droplets as a function of Ca_c for different values of α for DJ regime.....	157
Figure 4.15. Comparison between the power-law correlation of Equation (4-11) and the experimental data obtained.	157
Figure 4.16. Typical shape assumed by the interface in DC regime before the droplet breakup and definition of $x_{breakup}$	158
Figure 4.17. Breakup distance $x_{breakup}$ as a function of the flow rate ratio α for fixed values of the Capillary number Ca_c	159
Figure 4.18. Polydispersity Pl of silicone oil droplets in water with 2 wt% of Tween 20 as a function of α and Ca_c	161
Figure 4.19. Droplet flow maps for silicone oil (SO) droplets as a function of flow rate ratio α and Capillary number Ca_c in hydrophilic T-junction with (a) W, (b) W+T, (c) 0.2 XG and (d) 0.2 XG+T as the continuous phase.....	163
Figure 4.20. Squeezing regime for silicone oil (SO) droplet in 0.2 wt% Xanthan gum solution with 2 wt% Tween 20 (0.2 XG+T) when $Q_c = 0.5$ and $Q_d = 0.05$ ml/h.....	164
Figure 4.21. Dripping regime for silicone oil (SO) droplet in 0.2 wt% Xanthan gum solution with 2 wt% Tween 20 (0.2 XG+T) when (a) $Q_c = 5$ and $Q_d = 0.05$ ml/h and (b) $Q_c = 2$ and $Q_d = 2$ ml/h.....	165
Figure 4.22. Jetting regime for silicone oil (SO) droplet in water with 2 wt% Tween 20 (W+T) when $Q_c = 2$ and $Q_d = 4$ ml/h; (a) at the junction and (b) downstream of it.....	165

- Figure 4.23. Droplet breakup mechanism for silicone oil (SO) droplets as a function of flow rate ratio α and Capillary number Ca_c in hydrophilic T-junction with (a) W, (b) W+T, (c) 0.2 XG and (d) 0.2 XG+T as the continuous phase. 166
- Figure 4.24. Droplet breakup mechanism for silicone oil (SO) droplets as a function of dispersed Ca_d and continuous Capillary number Ca_c in hydrophilic T-junction with (a) 0.2 XG and (b) 0.2 XG+T as the continuous phase. 167
- Figure 4.25. Non-dimensional length \bar{L} of the silicone oil (SO) droplets as a function of flow rate ratio α in hydrophilic T-junction with (a) W, (b) W+T, (c) 0.2 XG and (d) 0.2 XG+T as continuous phase. 168
- Figure 4.26. The power-law correlation fitted to the experimental data for different values of α as a function of Ca_c in hydrophilic T-junction with (a) W, (b) W+T, (c) 0.2 XG and (d) 0.2 XG+T as the continuous phase. 170
- Figure 4.27. The non-dimensional length of the silicone oil microdroplets in water with Tween 20 (W+T) as carrier medium; closed symbols represent the first T-junction (hydrophobic) while open symbols stand for the second T-junction (hydrophilic). 171
- Figure 4.28. The breakup distance from the junction for different values of α as a function of Ca_c in hydrophilic T-junction with (a) W, (b) W+T, (c) 0.2 XG and (d) 0.2 XG+T as the continuous phase. 172
- Figure 4.29. The polydispersity Pl values for different values of α as a function of Ca_c in hydrophilic T-junction with (a) W, (b) W+T, (c) 0.2 XG and (d) 0.2 XG+T as the continuous phase. 173
- Figure 5.1. Typical droplet-based flow map obtained for a micro cross-junction. 177
- Figure 5.2. Typical flow map obtained for the first micro T-junction in opposed flow configuration (hydrophobic walls). 180
- Figure 5.3. Typical flow map obtained for the micro T-junction in opposed flow configuration with hydrophilic walls. 182

TABLES

Table 1.1. A comparison of the previous works in T-junction and flow-focusing devices.	24
Table 1.2. The range of volumetric flow rates Q and Capillary number Ca employed in Chapter 3.	41
Table 1.3. The range of volumetric flow rates Q and Capillary number Ca employed in Chapter 4.	42
Table 2.1. Measured density of the working fluids.	53
Table 2.2. The viscosity of Newtonian and non-Newtonian fluids.	55
Table 2.3. Range of shear rate tested with the viscometer.	57
Table 2.4. Surface tension (fluid/air) and Interfacial tension (fluid/silicone oil) of the working fluids.	59
Table 3.1. Range of volumetric flow rates α and Ca_c tested during the experimental runs.	72
Table 3.2. Geometrical characteristics of the junction #1.	72
Table 3.3. Polydispersity of D^* as a function of the imposed values of α and Q_c for 0.3 XG+T droplets in silicone oil.	85
Table 3.4. Polydispersity of D^* as a function of the imposed values of α and Q_c for 0.5 XG+T droplets in silicone oil.	85
Table 3.5. Characteristic values of viscosity ratio λ for the working fluids considered in this work.	110
Table 3.6. Typical viscosity ratio range for each observed droplet regime.	111
Table 3.7. Length of microthread L_{micro} (μm) as a function of flow rates of 0.3 XG+T and	

0.5 XG+T.....	125
Table 3.8. Characteristic values of the cross-junctions.....	131
Table 4.1. Range of volumetric flow rates α and Ca_c tested in T-junction.....	140
Table 4.2. Range of volumetric continuous flow rate Q_c with the corresponding Ca_c	162

NOMENCLATURE

<i>a</i>	half of inner channel width (μm)
<i>A</i>	aspect ratio ($= H/W$)
<i>b, c</i>	function of geometry
<i>C</i>	dimensionless constant
<i>Ca</i>	Capillary number ($= \mu u / \sigma_i$)
<i>d</i>	thickness of the neck (μm)
<i>D</i>	droplet diameter (μm)
<i>f</i>	frequency (Hz)
<i>F</i>	force (N)
<i>G</i>	shear rate ($= \Delta u / \Delta z$)
<i>h</i>	depth of flow (μm)
<i>H</i>	height of the channel (μm)
<i>k</i>	consistency index ($\text{Pa}\cdot\text{s}^{n-1}$)
<i>l</i>	thread length (μm)
<i>L</i>	length of plug (μm)
<i>m, n</i>	fitting parameter
<i>N</i>	number of the droplets
<i>p</i>	pressure (Pa)
<i>Pl</i>	polydispersity
<i>Pr</i>	perimeter (μm)

q	constant value
Q	volumetric flow rate (ml/h)
r	radius of curvature (μm)
R	restriction ratio ($= W_j/W_w$)
R^2	correlation coefficient
Re	Reynolds number ($= \rho u D_{hl}/\mu$)
S	surface cross-section (μm^2)
t	time (ms)
u	velocity (m/s)
V	volume (m^3)
w	width of the interface (μm)
W	width of the channel (μm)
x, y	mass center
z	downstream distance of the channel (μm)

Greek Letters

α	flow rate ratio ($= Q_d/Q_c$)
β	depth ratio ($= h_d/h_c$)
ε	fitting constant
δ	blocking coefficient
ρ	density (kg/m^3)
μ	viscosity (cP)
κ	radius of curvature
ν	kinematic viscosity (cSt)
λ	viscosity ratio ($= \mu_d/\mu_c$)
Λ	width ratio ($= W_d/W_c$)
ω	fitting constant ($= d/W_c$)

σ	tension (Nm^{-1})
θ	contact angle ($^\circ$)
τ	dimensionless time
ξ	onset of shear thinning
χ	dD^*/dCa_c
$\dot{\gamma}$	shear rate (s^{-1})

Subscripts

<i>a</i>	axial
<i>b</i>	breakup
<i>B</i>	buoyancy
<i>block</i>	blocking
<i>c</i>	continuous
<i>com</i>	complete
<i>cr</i>	critical
<i>d</i>	dispersed
<i>Def</i>	modified drag
<i>det</i>	detachment
<i>DL</i>	dynamic lift
<i>f</i>	formation
<i>fl</i>	filament
<i>g</i>	growth
<i>G</i>	gravity
<i>growth</i>	elongating rate
<i>h</i>	horizontal
<i>hl</i>	hydraulic
<i>i</i>	interfacial

<i>I</i>	inertial
<i>in</i>	induction
<i>j</i>	at the junction
<i>ll</i>	liquid-liquid
<i>m</i>	modified
<i>M</i>	gas momentum
<i>max</i>	maximum
<i>micro</i>	microthread
<i>min</i>	minimum
<i>neck</i>	necking
<i>or</i>	orifice
<i>outlet</i>	outlet
<i>r</i>	radial
<i>ref</i>	reference
<i>s</i>	surface
<i>S</i>	shear
<i>sl</i>	solid-liquid
<i>squeeze</i>	decreasing rate of the neck
<i>SP</i>	static pressure
<i>w</i>	far from the junction
<i>0</i>	shear-rate
<i>Superscripts</i>	
<i>n</i>	power-law index
<i>x</i>	power-law coefficient
*	dimensionless

Chapter 1

Droplet Generation in Microfluidics: State-of-the-Art

1.1 Introduction

In recent years, microdroplets have attracted broad interest all over the world due to their vast range of applications. They have been extensively applied in a variety of fields. Two distinct but complementary motivations gave rise to the interest in droplet manipulating within microjunctions [1]. First, the desire to generate well-calibrated droplets in material science applications such as food industries or pharmaceutical areas. In this context, microfluidic devices have been devised to produce droplets with low size variations and reproducible diameters, also to allow complex combinations to be designed and investigated [2, 3]. A second aim emerges from lab on a chip applications where the droplets are treated as microreactors in which small (femto – to nanoliter) liquid volumes are manipulated [4]. The miniaturization of the system is an important advance in search for drugs which demand robust methods to find, refine and test a probable drug candidate, drug discovery [4]. Consuming just a few microliters of sample, requiring small cell numbers, less than a single human patient biopsy and a high degree of automation are the advantages of droplet microfluidics in biomedical and single-cell studies [5]. The introduction of microfluidics facilitated the production and manipulation of chemical or biochemical reactions in emulsions [1] which were initiated before the birth of microfluidics via reactions in many small volumes [6, 7]. Intermolecular reactions of various reagents and reactants may take place in merging channel geometries including T shapes. A very prominent benefit of miniaturized reactions highlighted by the researchers is the reaction time which is of the order of milliseconds.

Emulsion droplets are small containers that can be used to contain biological material

including DNA, cells, molecules and bacteria [5]. Cellular compartmentalization is crucial for evolution of living organisms. High throughput structure-based systems with the ability to control the supply of reactants and to produce droplets with low size variation has attracted broad interest in molecular evolution [7] and protein crystallization [8-10]. Multiple parallel reactions are needed in a number of applications (from drug discovery to gene-expression analysis) and the capabilities of microfluidics to reduce the use of expensive reagents makes microscale reaction an unrivaled option [11]. The droplets form small reaction three dimensional containers that can be filled by the compounds at the moment of formation, mixed rapidly by the reactants and transported along channel. Nowadays, microfluidic devices can be fabricated easily thanks to soft lithography with PDMS or 3D printing, as examples of rapid fabrication method. Unlike conventional methods, combining droplet-based valve microfluidics and luminescence-based colorimetry makes a novel platform in blood and DNA analysis in which the determination of biomolecules is achieved by means of visualization with a small consumption of reagents, low cost detection system and a short time. With the development of microvalve-based droplet techniques, this method may be applied in identifying anticancer drug by color assays and it can be employed for drug discovery and biological screening [12]. Single-cell study is made possible by encapsulation of single cells into microdroplets in which the cell is later analyzed. To analyze the intracellular components such as DNA and RNA, the cells can be lysed. Moreover, mammalian cells can be cultivated inside microdroplets for several days [5]. Aqueous droplets as the cell-sized compartments can be efficiently used in order to keep together genes, RNAs and proteins.

The generation of the droplets with homogeneous diameter can be obtained thanks to the microfluidics devices in a very efficient way with respect to traditional methods such as agitated dispersion [13], solvent evaporation method [14] and emulsification/gelation method [15] in which droplets with broad size variations were usually produced. Hitherto, a number of different microdroplet generators were proposed to generate droplets, like micro T-junctions [16], flow-focusing [17, 18] and co-flow devices [19] as shown in Figure 1.1.

Thorsen *et al.* [16] firstly used a micro T-junction for the generation of monodispersed droplets [16, 20] as well as bubbles [21]. In a T-junction configuration the dispersed phase (or droplet forming phase) and the continuous phase (or carrier fluid) are introduced by using two different inlets of the junction. The dispersed and the continuous phase can be introduced perpendicularly each to other or face-to-face. The dispersed phase stream starts to penetrate

into the main channel and forms a droplet which leaves the junction along the outlet of microchannel [22]. In this way the dispersed phase breaks into monodispersed droplets regularly spaced along the outlet of the junction.

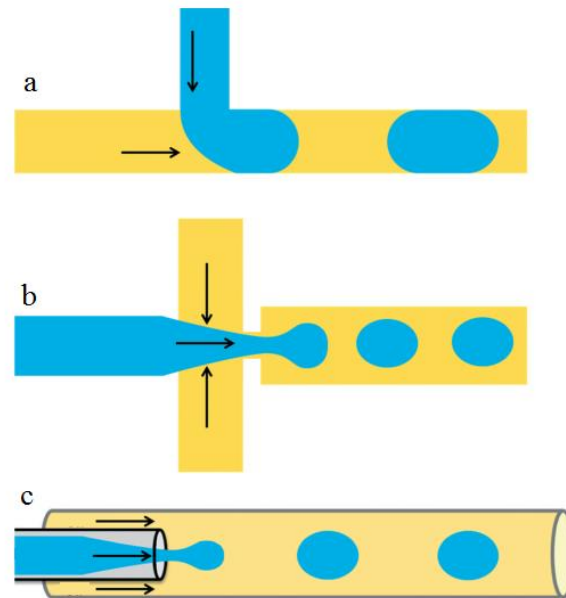


Figure 1.1. Three most common microfluidic geometries used for droplet generation; (a) T-junction, (b) flow-focusing and (c) co-flow device [5]. The dispersed phase is indicated in blue while continuous phase is in yellow.

Flow-focusing configuration has been also proposed as droplet generator during last years. The dispersed phase is usually sheared-off symmetrically by a continuous phase which is introduced into the junction from two opposite directions (Figure 1.1b). Axisymmetric flow-focusing microdevices confine droplets in central axis of the outlet microchannel by protecting droplets from shear or damage due to adhesion or wetting at the walls.

Rayleigh-Plateau instability of the dispersed phase which is injected by a Capillary tube or orifice into another immiscible co-flowing fluid is the reason of drop forming in co-flow devices. A sample of co-flow microdevice is depicted in Figure 1.1c.

The three above-explained devices for the generation of monodispersed droplets are the most common ones but other types of microdroplet generators have also been devised such as microchannel terraces [23], to enhance the productivity of the emulsions. Thanks to 5000 to 30000 assembled microchannels per chip which increase drastically the throughput. This solution can be an attractive option for the applications in which high productivity is needed.

Although the low productivity of T-junctions and flow-focusing devices as compared to microchannel terraces can be a big drawback, they are the most preferred configurations because of their relative ease in fabrication and simplicity in drop controlling. The main characteristics of an emulsion generator is its ability to generate reproducible droplets with low size variation. The controlling parameters in drop diameter and size variation are geometry and dimension of the microchip [24-26], properties of liquids [27, 28], flow rates of working fluids introduced into the junction [29-31] and surfactant concentration [32-34]. In this thesis different geometries of the microjunctions will be studied in order to optimize the generation of both Newtonian and non-Newtonian monodispersed emulsions.

1.2 Geometry and dimension of the junction

The effect of junction geometry is an important aspect to be investigated for the correct design of microdroplet generators.

1.2.1 T-junction configurations

A typical micro T-junction can be used as droplet generator by adopting configurations depicted in Figure 1.2. The configurations differ in terms of introduction of the dispersed phase (DP) and of the continuous phase (CP) as shown in Figure 1.2.

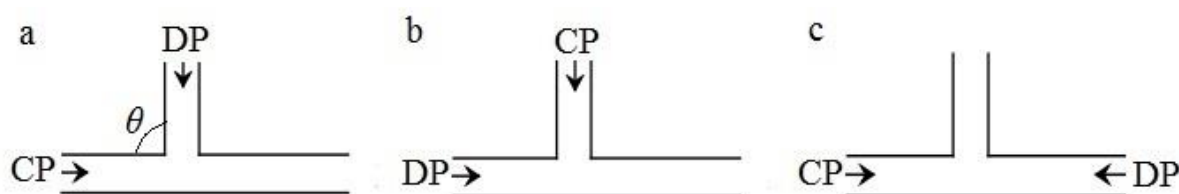


Figure 1.2. Typical illustration of T-junction with three distributions of the continuous phase CP and dispersed phase DP along them for (a) cross-flow, (b) perpendicular cross-flow and (c) opposed-flow.

More in detail

- (i) Figure 1.2a shows a T-junction used in a “cross-flow” configuration. In this case the droplet is generated thanks to the introduction of a dispersed phase along the vertical arm which shear-off the continuous phase flowing along the main channel.

- (ii) Figure 1.2b shows a T-junction under a cross-flow configuration in which the introduction of the continuous and dispersed phase is reversed with respect to the first case. In this case the main channel is filled with the dispersed phase and the continuous phase penetrates the main channel through the vertical branch. Interruption of the dispersed phase by the continuous phase which creates an obstruct causes the droplets generation. This configuration is used to generate large droplets [35].
- (iii) Figure 1.2c shows a T-junction under an opposed-flow configuration; dispersed and continuous phase are introduced face-to-face and the generated droplets pass through the main channel to the outlet. The configuration is mainly used for bubble generation [36]. Recently Shui *et al.* [32] tested the opposed-flow configuration also for liquid droplet generation.
- (iv) By varying θ ($< 90^\circ$) (Figure 1.2a) a Y-junction or λ -junction can be obtained. The effect of introduction of a liquid with different angle with respect to the main channel can be beneficial or not to the droplet generation.

1.2.2 Flow-focusing configurations

The typical flow-focusing microdevices can be subdivided into three types, according to the geometry of the junction as depicted in Figure 1.3.

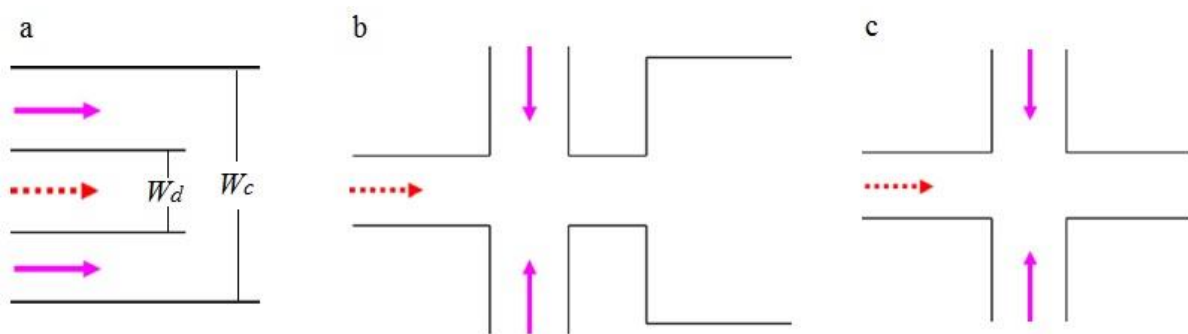


Figure 1.3. Three typical categories of microfluidic flow-focusing devices; (a) axisymmetric capillary co-flowing device, (b) flow-focusing channel and (c) cross-junction geometry from Fu *et al.* [37].

Figure 1.3a and Figure 1.4 show a typical configuration of the droplet generation. Pressure driven flow drives a liquid into parallel microchannels surrounding a central parallel stream containing a second immiscible liquid. The central channel ends within the microdevice and the liquids are forced to flow along a downstream contraction. Viscous stresses and

squeezing pressure are responsible of the generation of droplets at the outlet [28]. The other configurations shown in Figure 1.3b and c work in a similar way, but in the case of Figure 1.3c, no contraction is present after the merging of the immiscible liquids.

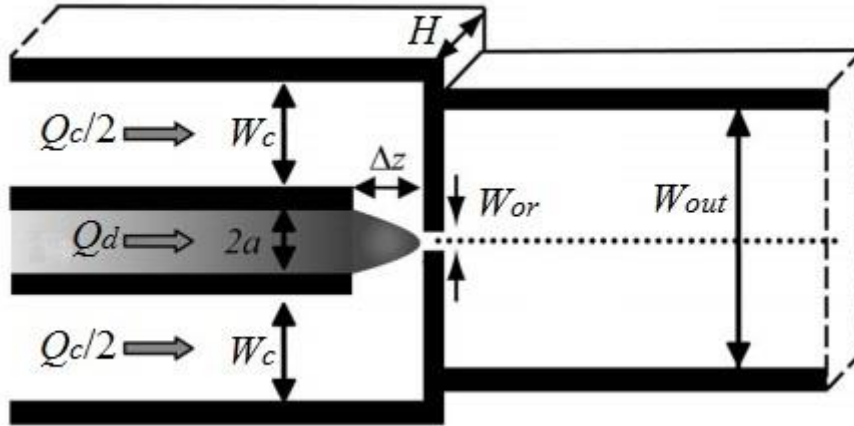


Figure 1.4. Schematic of a planar flow-focusing geometry from Lee *et al.* [28] where W_{or} and W_{out} represent orifice and outlet channel width values, respectively, $2a$ is the inner channel width and Δz is a distance downstream of the end of the inner channel.

1.3 Droplet formation and controlling mechanisms

Droplets can be generated in the junctions in different ways thanks to the different predominant forces acting on the immiscible liquids. Based upon both experimental and numerical investigations, it is now possible to distinguish different droplet regimes which can be activated under different operative conditions. In order to obtain the generation of the droplets, the dispersed phase must penetrate the main channel, this is possible only if its pressure overcomes the Laplace pressure (Equation (1-1)) where r_a and r_r are the radius of axial and radial curvature of the interface between the immiscible liquids.

$$\Delta p_L = \sigma \left(\frac{1}{r_a} + \frac{1}{r_r} \right) \quad (1-1)$$

The classification of the droplet regimes can be done in two distinct ways:

- (i) By observing the position in which the droplet breakup occurs (i.e. at the junction or downstream)

- (ii) By considering the physical mechanism which is the responsible of the breakup

Following the first criterion at low values of continuous flow rates Q_c , the shear force is usually negligible and the droplet generation is observed when the pressure drop force is able to overcome the interfacial force opposes to the interface. At low values of Q_c , droplets are generally formed at the junction (**DJ**) thanks to the dominance of the pressure which is responsible of the squeezing of the neck connecting the droplet to the source of the dispersed phase, squeezing mechanism [38]. Since the droplet partially blocks the channel, a pressure build-up is produced [39]. If Q_d increases, the droplet breakup moves downstream of the junction (**DC**). In fact, an increase of Q_d means that more material is injected into the junction. In this case, the interface is not easy to pinch-off and the breakup position is shifted far from the center of the junction [39]. When the droplet breakup occurs downstream of the junction, an elongated filament is observed before the breakup. The filament is broken during the droplet generation in an abrupt way and it can generate satellite droplets. Parallel flow (**PF**) takes place at high values of Q_d because the continuous flow is not able to oppose the dispersed flow. In this case no droplets are generated and only two parallel flows can be observed at the outlet of the junction [39, 40].

If the second criterion is used in order to distinguish the droplet regimes in which a different physical mechanism is the responsible of the droplet generation: squeezing regime (**SR**), dripping regime (**DR**) and jetting regime (**JR**). In squeezing regime (which usually corresponds to DJ regime) the droplet blocks the main channel and the pressure exerted by the continuous phase increases. Then the dispersed phase is squeezed by the continuous phase at the center of the junction and a droplet is formed at the junction.

Dripping regime is generated if Q_d or Q_c are increased. In this case, the growing droplet still fills the channel but only partially. The detachment point moves downstream of the junction thanks to the action of the continuous phase which produces a shear stress on the interface by creating a filament before the breakup. As the shear force exerted on the filament increases by increasing the continuous phase flow rate, the breakup tends to take place downstream of the junction. In spite of the squeezing regime in which the pressure drop is the dominant, in dripping regime shear force plays a more important role.

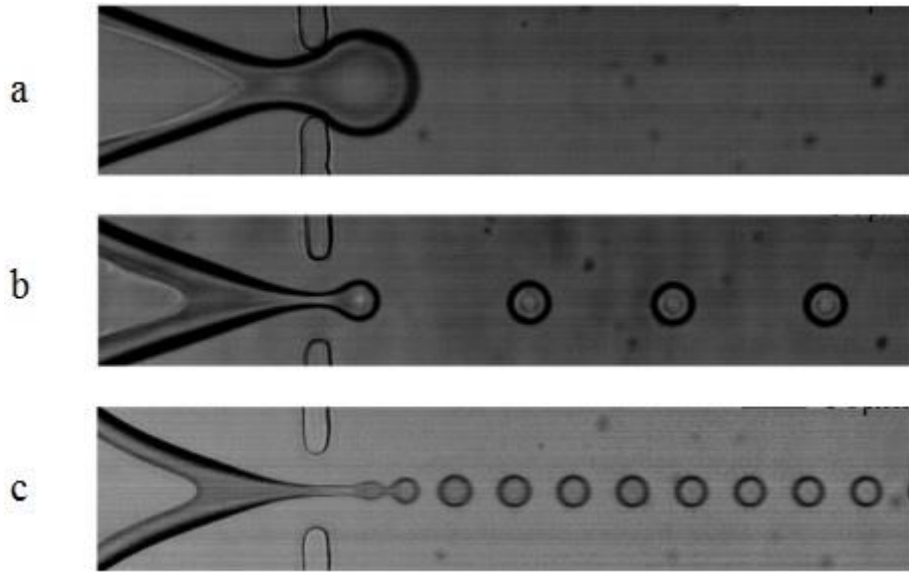


Figure 1.5. Illustration of droplet generation in a typical flow-focusing device; (a) squeezing regime, (b) dripping regime and (c) jetting regime from Lee *et al.* [28].

Jetting regime can be activated at high values of Q_c , shear force is still predominant but the droplets are generated downstream of the junction while a long and unstable thread is sustained. It is possible to consider dripping and jetting regimes to coincide with DC regime.

In Figure 1.5 a representation of squeezing, dripping and jetting regimes obtained in a flow-focusing droplet generator similar to the scheme of Figure 1.3a is given.

The works appeared in literature demonstrate that the control of the droplet characteristics in terms of volume and frequency can be obtained if one is able to control the droplet regimes at the junction. The droplet regimes can be varied by the changing the values governed by two dimensionless parameters, the Capillary number Ca (see Equation (1-2)) and the flow rate ratio (Equation (1-3)) defined as follows.

$$Ca_c = \frac{\mu_c u_c}{\sigma}, \quad Ca_d = \frac{\mu_d u_d}{\sigma} \quad (1-2)$$

$$\alpha = \frac{Q_d}{Q_c} \quad (1-3)$$

However, although a huge number of studies has been performed on the control of the

droplet generation, not all the physical aspects of the phenomenon have been clarified. Many contradictory findings have been reported in the papers published in the past and some aspects are still open questions.

In this section a critical review of the main conditions reported in the published works has been made with the aim to highlight the main aspects which are still under-investigated.

1.3.1 Effect of flow rate

As a rule of thumb, an increase of dispersed flow rate Q_d or a decrease of continuous flow rate Q_c , thanks to the reduction of the viscous force is responsible of larger droplets.

In squeezing regime (SR) (low Q_c and Q_d) Garstecki *et al.* [41] claimed that the droplet production is mainly controlled by the flow rates. They argued that the length of drop or bubble, at low values of Ca_c , is determined by two steps; the first step is linked to the growth of the dispersed phase neck which continues till it blocks the carrier fluid; the length of plug is approximately equal to the width of the main channel $L_{block} = W_c$. Then the upstream pressure increases and squeezes the neck by reducing the neck characteristic width (d) (see Figure 1.6). Assuming the decreasing speed of the neck width approximately equal to the mean velocity of the continuous phase ($u_{squeeze} \approx u_c$) and elongating of the drop at rate u_{growth} , they proposed a simple expression for the prediction of the final length of the droplet in the form of

$$L \approx W_c + \frac{d}{u_{squeeze}} u_{growth} \quad (1-4)$$

which can be rewritten as (Equation (1-5)) if the cross-section does not vary through the junction.

$$L = W_c + \frac{d}{Q_c} Q_d \quad (1-5)$$

Equation (1-5) can be rewritten in the dimensionless form as follows:

$$\frac{L}{W_c} = 1 + \omega\alpha \quad (1-6)$$

where L is the length of the plug generated (see Figure 1.6) scaled with W_c which is the width of the main channel, $\omega (= d/W_c)$ is a fitting constant of order one related to typical neck width and α is the flow rate ratio defined by Equation (1-3).



Figure 1.6. The interface between two immiscible fluids and the dispersed phase neck from Garstecki *et al.* [41].

The simple correlation between the dimension of the droplet and the flow rate ratio α proposed by Garstecki *et al.* [41] for squeezing regime (Equation (1-6)) was verified by numerical and experimental studies for T-junctions by Chiarello *et al.* [42], Piccin *et al.* [43] and Xu *et al.* [44] and also for flow-focusing devices by Liu and Zhang [39]. Since L_{block} is not always equal to W_c but depends on channel geometry, the Equation (1-6) can be written in a more general form by considering $L_{block} = \varepsilon W_c$. In this way the correlation proposed by Garstecki *et al.* [41] becomes:

$$\bar{L} = \frac{L}{W_c} = \varepsilon + \omega\alpha \quad (1-7)$$

where ε is a fitting constant which depends on junction geometry. The values of ε and ω change from one publication to another one because of junctions having different geometries are generally studied. As a logical outcome of Equation (1-7) it becomes evident that larger flow rate ratio α mean longer microdroplets as confirmed by many studies. Gupta and Kumar [24, 26], Liu and Zhang [39, 45] (see Figure 1.7) and De Menech *et al.* [46] analyzed theoretically the dependence of the size of the droplet on the flow rate ratio α while Xu *et al.* [47] Garstecki *et al.* [41] and Xu *et al.* [44] confirmed Equation (1-7) experimentally.

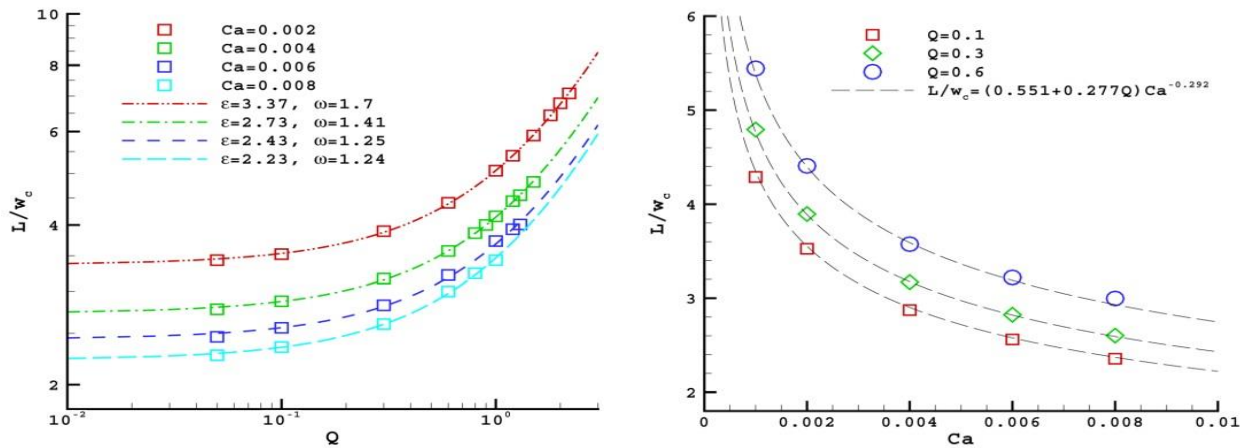


Figure 1.7. Non-dimensional length of plugs as a function of flow rate ratio (here Q) and continuous Capillary number (here Ca) from Liu and Zhang [39].

Another common experimental observation is that the size of the droplet decreases with increasing Q_c (Ca_c) while α is kept constant. The observation highlights that continuous Capillary number Ca_c plays a role on the size of the droplet even in the squeezing regime but the parameter is not as significant as it is in dripping and jetting regimes. It can be concluded that α is not the only parameter effective on the size of the droplet but it seems that both flow rates are controlling the droplet size.

Garstecki *et al.* [41] studied experimentally a water flow as the dispersed phase in a silicone oil flow at a T-junction. As demonstrated in Figure 1.8 dimensionless length of the drop shows a linear dependence on flow rate ratio α (for $\alpha > 1$) while in the cases of $\alpha \leq 1$ the droplet size is not a strong function of flow rate ratio. This behavior was explained by the ‘shearing’ model: at low values of Q_d (Q_{water} in Figure 1.8) the flow of the dispersed fluid would be much slower than that of host fluid and therefore it would not affect the balance between the shear stress and the interfacial tension. On the contrary by increasing Q_d , the shear stress exerted by the continuous liquid on the droplet decreases thanks to the reduced difference of the velocity of the two fluids [41]. In Figure 1.8 the x -axis is the flow rate ratio α defined in Equation (1-3).

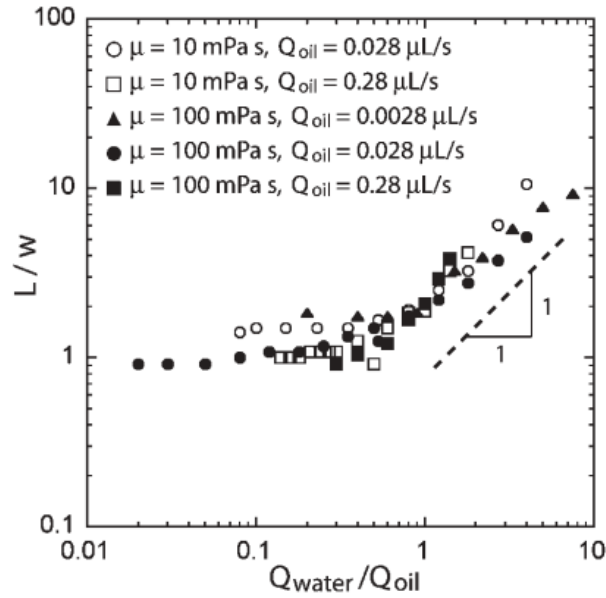


Figure 1.8. Linear dependence of the drop size on flow rate ratio when $\alpha > 1$ from Garstecki *et al.* [41] where water droplets in different oil flows with diverse viscosities.

In spite of squeezing regime in which flow rate ratio is important, in dripping regime (DR), due to the enhancement of Q_c (Ca_c), the size of the droplet depends strongly on Capillary number [46]. A very sharp decrease of the size of the droplet is predicted by De Menech *et al.* [46] and Liu and Zhang [45, 48]. Going from squeezing to dripping regime, in dripping regime the balance between the shear force and interfacial force determines the drop size [38]. An increase of Q_c pinches-off the droplet earlier and the droplet size is reduced.

The few available models proposed to study the transition from dripping to jetting regime were summarized in a review paper by Christopher and Anna [49]. They studied the methods for synthesizing uniform streams of droplets and bubbles, focusing on those systems utilizing pressure-driven flows. The droplet diameter was found to decrease monotonically with increase of continuous flow rate Q_c . It is possible to increase the droplet diameter by reducing the interfacial tension between the immiscible liquids by introducing surfactants.

With a constant increase of continuous flow rate Q_c flow pattern shifts from dripping to jetting regime (JR). As the Capillary number is further increased, the breakup point moves progressively downstream and a jet is formed [46]. There exists a scarcity of studies focused on jetting regime due to the unsteady essence of the jet formed along the outlet channel and the production of multiple satellite droplets after breakup of the main droplet. In the jetting regime,

the dispersed fluid can flow out of the source as a single thread or jet, the length of which may be several times the dimensions of the nozzle before the jet destabilizes and droplets pinch-off from the tip [50].

1.3.2 Effect of geometry

Qian and Lawal [36] simulated the Taylor flow in the three configurations of T-junctions (shown in Figure 1.2). They found theoretically that the bubbles produced by using the cross-flow (Figure 1.2a) and opposed-flow (Figure 1.2c) configurations are of comparable lengths, but shorter than those generated by the configuration of Figure 1.2b. However, the conclusion was reversed by the experimental data obtained by Xu *et al.* [47] who tested the two configurations of Figure 1.2a and b by observing longer droplets with the configuration of Figure 1.2a. Raj *et al.* [51] simulated the bubble formation process for different T-junction modes (including cross-flow (Figure 1.2a) and opposed-flow (Figure 1.2c)) and a Y-junction. The bubble length was found to be totally independent of the geometry of the device used.

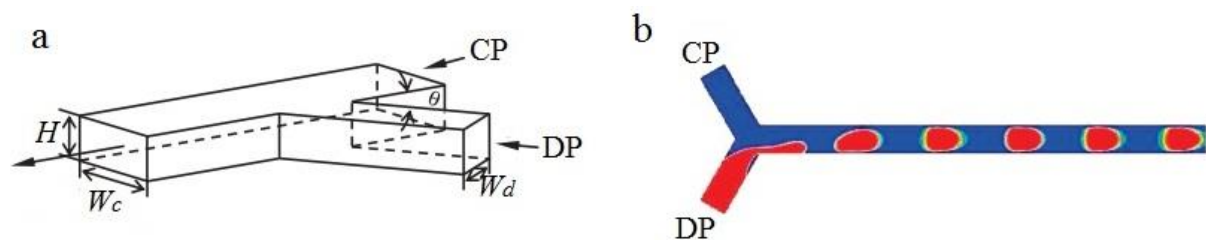


Figure 1.9. (a) The illustration of λ -junction from Yeom and Lee [52] and (b) Y-junction from Raj *et al.* [51].

Other studies focused on the effect of geometry of the junction were made by Yeom and Lee [52] who studied the λ -junction of Figure 1.9a, Raj *et al.* [51] and Steegmans *et al.* [53] who studied the Y-junction of Figure 1.9b by changing the angle between the inlet and main channel. Das and Das [54] simulated the drop movement over an inclined surface.

Wang *et al.* [55] studied T-junction microfluidic device with an embedded capillary. The introduction of a capillary tip into the main channel of a T-channel (see Figure 1.10) is able to greatly reduce the dimension of the droplets with low consumption of continuous phase. This kind of droplet generator can be applied into many fields, as monodispersed droplets smaller than the channel scale can be easily prepared in this way and it can be used for many applications such as the preparation of microbead and microspheres (Figure 1.10).

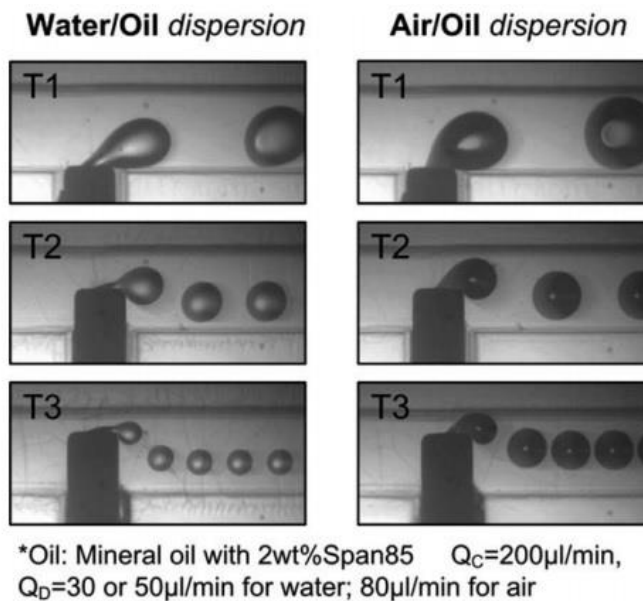


Figure 1.10. The dispersion processes in the three kinds of microchannels in the same range of continuous phase flow rate from Wang *et al.* [55].

Simple modifications on the ordinary T-junction by introducing a Venturi-shaped microchannel (Figure 1.11) has been studied by Lattice-Boltzmann method verified by experimental investigations [56] in order to observe the effects on the size of droplet and on the frequency of droplet. The results proved clearly that the smaller droplets may be generated under the operation of high flow rate ratios high-efficiently in contrast to the much bigger droplets in ordinary T-junction geometry under the same conditions. This work verified that multiphase flows can be very sensitive to tiny difference in terms of channel geometry.

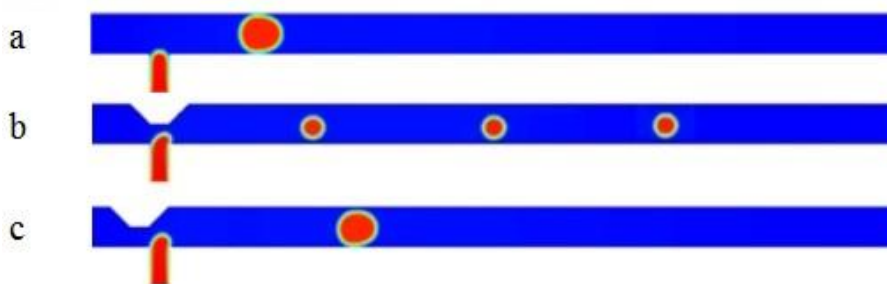


Figure 1.11. Droplet generation along a venturi-shaped micro T-junction from Wang *et al.* [56] for (a) an ordinary T-junction and (b & c) modified T-channels.

A series of works have been focused on the analysis of the effects of the width ratio (Equation (1-8)) and the aspect ratio (Equation (1-9)) of the junction.

$$\Lambda = \frac{W_d}{W_c} \quad (1-8)$$

$$A = \frac{H}{W} \quad (1-9)$$

It has been demonstrated that a change of these two key parameters in the design of a droplet generator can influence the characteristics of droplets in terms of size, spacing and rate of production. Garstecki *et al.* [41] discussed the role of Λ and A for five different T-junctions and concluded that when $\Lambda \geq 0.5$, the size of the droplet could be correctly predicted by Equation (1-7) for squeezing regime but not for $\Lambda < 0.5$ in which shear force distorts the droplet. In order to stay in squeezing regime, $A_c (= H/W_c)$ should be kept less than unity while $\Lambda \geq 0.5$. The critical Capillary number for transition from the squeezing to dripping regime was on the order of 10^{-2} in the case of square cross-section (A and $\Lambda = 1$). Raj *et al.* [51] performed an analysis on the effect of the channel size on the drop/slug lengths. The drop/slug size was found to be independent of the channel size in the transitional region between squeezing and dripping regimes ($Ca_c > 0.01$) when the flow rate ratio between the dispersed and continuous phase (α) is less than 0.5. For $\alpha > 1$ a parallel flow was observed against the experimental results when A_c & $A_d < 1$ and $0.5 \leq \Lambda \leq 1$ but a slug flow with an over-predicted length occurred for $\Lambda = 0.5$, $A_c < 1$ & $A_d > 1$. Christopher *et al.* [57] indicated Λ as a crucial factor for the droplet size by fixing $A_c = 1/3$ and varying Λ from 0.4 to 2.5. They studied the droplet volume against ratio of channel widths Λ within a T-junction. The volume of droplet diminished by increasing Ca_c . At low values of Λ (< 1) the measured volume was approximately constant but as the width ratio exceeds unity ($\Lambda > 1$), the droplet size increases approximately linearly with width ratio. The lower values of Capillary number Ca_c , the more sensitivity of the droplet volume on the width ratio Λ could be seen. Varying the width ratio ($0.3 < \Lambda < 1$), Glawdel *et al.* [38] carried out the experiments in transitional regime and observed larger droplet were produced with larger width ratio Λ values. They tested the effect of variation of Λ from 0.3 to 1, while A_c was in the range of 0.3 to 0.6, in the transitional region between squeezing and dripping regimes. They observed that larger values of Λ determines larger droplets at lower frequencies, even if $\Lambda < 1$. In the aforementioned paper the pinch-off is controlled solely by A_c . Gupta and Kumar [24] employed Lattice Boltzmann method to investigate the effect of A_c on the plug size. The plug size increased with the increase of the channel depth for a fixed

Capillary number Ca_c and flow rate ratio α .

In order to take into account all the geometrical factors which play role on the droplet generation, Lee *et al.* [28] defined a modified Capillary number for planar flow-focusing geometry containing all of the geometrical dimensions of the junction as follows:

$$Ca_c \equiv \frac{\mu_c a \Delta u}{\sigma \Delta z} = \frac{\mu_c Q_c a}{\sigma H \Delta z} \left[\frac{1}{W_{or}} - \frac{1}{2W_c} \right] \quad (1-10)$$

where W_{or} and W_{out} represent orifice and outlet channel width values, respectively, $2a$ is the inner channel width and Δz is a distance downstream of the end of the inner channel.

The restriction ratio of the channel width R (Equation (1-11)) is another important parameter especially in flow-focusing devices. This parameter is defined when the width of the junction varies along the microchannel.

$$R = \frac{W_j}{W_w} \quad (1-11)$$

where W_j and W_w represent the width values at the junction and far from it, respectively.

The critical shape of the neck before the breakup stage was controlled by H_c varying from 0.3 to 0.6. Lee *et al.* [28] confirmed that the upstream geometry in a planar flow-focusing device plays little role in the transient growth of the thread. They adopted four restriction ratios R ($= 0.05, 0.0625, 0.1$ & 0.25) in their study and obtained longer threads if the restriction ratio is increased.

Dang *et al.* [58] considered three different flow-focusing micordroplet generators to study the effect of the input, orifice and output width values on the particle size. By investigating of various experimental geometrical conditions, continuous and dispersed flow rates and concentration of poly (ethylene glycol) (PEG) hydrogel solution, PEG hydrogel microparticles were optimized. Li *et al.* [59] performed an analysis for the geometry optimization of a flow-focusing device and revealed that despite the squeezing volume which can be tuned by manipulating the continuous phase flow rate, the blockage volume in the

squeezing regime depends solely on the focusing region geometry. Abate *et al.* [60] summarized the stability of microdroplet generators with different inlet channel geometries. In flow-focusing devices with three different junction geometries, due to the symmetric injection of fluids, they evidenced unstable polydispersed droplet at low Capillary numbers while monodispersed droplets were generated at high Capillary numbers.

Gulati *et al.* [61] reported the effect of variation in degrees of rounding in flow-focusing geometries. The ratios of the radius of curvature to channel width was the parameter taken into account in this study and it was found that the largest rounding caused largest droplets to be generated (Figure 1.12). Castro-Hernández *et al.* [62] identified three geometrical parameters including the distance between the inner inlet channel and the outlet channel in a flow-focusing geometry, the width of the outlet channel and its length for a finite element simulation on a non-planar three-dimensional flow-focusing device. It terminated in fabrication of four optimum designs by the use of soft lithography techniques and testing the built channels experimentally.

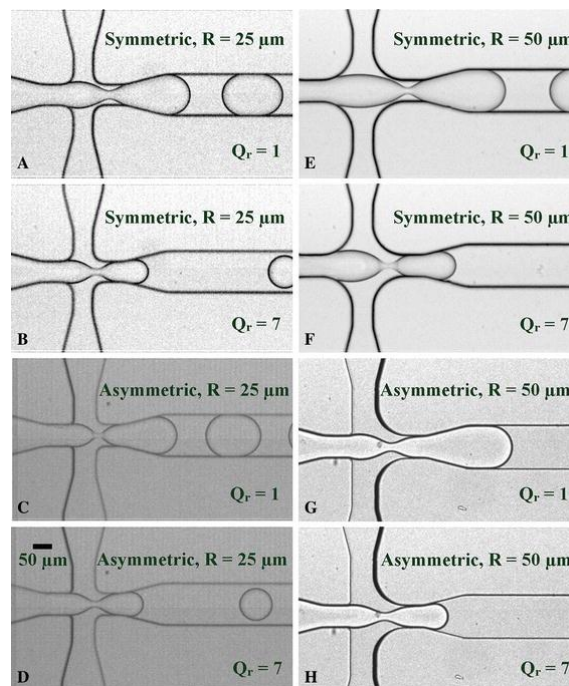


Figure 1.12. Droplet formation in the four rounded flow-focusing devices at two different flow rate ratios where R is the radius of the curvature from Gulati *et al.* [61].

1.3.3 Effect of viscosity

Viscosity is another important parameter governing the droplet size. Based upon the study performed by Garstecki *et al.* [41], later supported by numerical investigations by De Menech *et al.* [46] and Liu and Zhang [45], the droplet size was found to be approximately independent of viscosity ratio λ (Figure 1.13) in squeezing regime, as confirmed by Equation (1-6) proposed by Garstecki *et al.* [41]. The main contribution in the droplet final size comes from the growth stage in which λ plays a negligible role. The effect of continuous phase viscosity on pressure drop force is limited because of the short breakup stage resulting from high magnitude of pressure drop force [22].

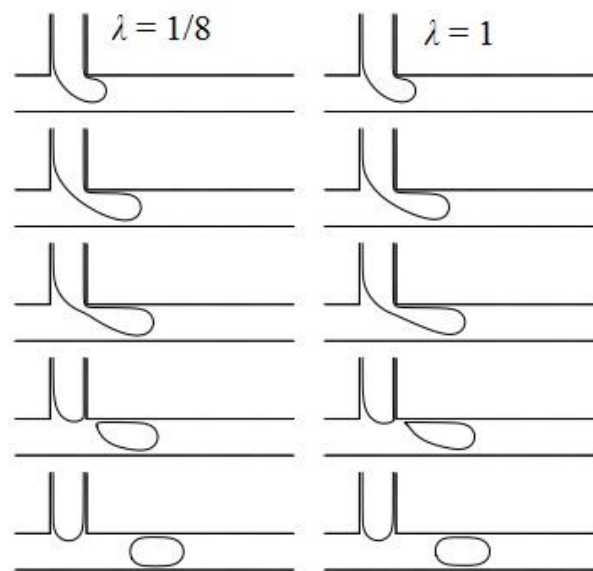


Figure 1.13. The effect of viscosity ratio λ in droplet formation process at a fixed flow rate ratio $\alpha = 0.25$ and $Ca_c = 0.006$ from Liu and Zhang [45].

Viscosity plays a complex role in droplet generation and contradictory findings have been reported in literature. Due to the contribution of μ_c to pressure drop force, the interface is sheared-off earlier and smaller droplets are expected by increasing μ_c . As expected, the more viscous continuous phase (higher values of μ_c), the smaller droplets should be generated, as confirmed by Garstecki *et al.* [41], Husny and Cooper-White [63], Raj *et al.* [51] and Yeom and Lee [64]. On the contrary Christopher *et al.* [57] observed that droplet diameter increases if the continuous phase viscosity is higher. The same inconsistency may be observed in investigations in which viscosity ratio was considered as an operative parameter. Unlike De

Menech *et al.* [46] and Liu and Zhang [45], Bashir *et al.* [65] obtained larger droplets for higher values of viscosity ratio λ defined as the ratio between the viscosity of the dispersed and the viscosity of the continuous phase (Equation (1-12)).

$$\lambda = \frac{\mu_d}{\mu_c} \quad (1-12)$$

More studies with clear information on adopted parameters are needed in order to fully understand the role of viscosity on the droplet volume. There is a scarcity of works dealing with the effect of the viscosity of the dispersed phase on the droplet characteristics. When the viscosity of the dispersed phase increases, the neck becomes longer and the detaching time enhances, so the smaller droplets are produced by increasing dispersed phase viscosity.

In dripping regime, shear force increases proportional to the continuous phase viscosity μ_c , so the size of droplets is inversely proportional to μ_c . As expected, the larger viscosity ratio λ is, the larger droplet should be generated which was confirmed by the earlier works [57, 63, 64]. Nevertheless different results are reported for the dependence of drop size on viscosity ratio λ [26, 45, 46]. An increase of μ_d determines an increase of viscous pressure in thread which opposes the Capillary pressure; it leads to less material being transferred within longer threads and smaller droplets generated as supported by [64]. They found a decreasing behavior for drop size as a function of both viscosities. In their study, an increase of μ_c and/or μ_d determines smaller droplets [64].

In jetting regime shear force is the predominant force and the droplets are sensitive to μ_c but μ_d plays a marginal role. Increase of continuous viscosity μ_c leads to generation of smaller droplets [63]. The drag force within the shear-driven regime exerted on the droplet depends very weakly on the viscosity of the droplet, so the viscosity of the dispersed phase μ_d does not influence the size of droplets appreciably [46]. Liu and Zhang [48] studied the droplet formation in a micro cross-junction by using the Lattice-Boltzmann method in dripping regime. They observed a very weak dependence of the droplet size on viscosity ratio λ ; they proposed a correlation in which the viscosity ratio λ is absent and the drop size is found to be linked to the Capillary number Ca_c and flow rate ratio α only.

Droplet formation and breakup dynamics in flow-focusing devices from dripping to

jetting regime were investigated experimentally by Fu *et al.* [37]. They found out that in dripping regime for low viscosity ratios the minimum width of the thread varied with a power-law dependence on the remaining time and the droplet size changes with flow rate ratio α and Capillary number Ca_c . On the other hand with an increase of the viscosity ratio λ , the dispersed thread showed a linear thinning procedure. They concluded that in jetting regime viscosity ratio λ and flow rate ratio α influence the stable jet width.

Cubaud and Mason [66] measured the droplet size and linked it to fluid properties, flow parameters and channel geometry in dripping and jetting regimes. In their study the regimes of thread instabilities were classified and the critical thread length before jetting droplets and the critical length of a viscous tail before breakup in dripping were also examined. Seo *et al.* [29] declared the surface energy of the device which influences the emulsification of the liquids as an important parameter amongst various controlling factors. Combining two consecutive flow-focusing microdroplet generators, they made a double droplet generator useful for the production of double emulsions. Nunes *et al.* [50] reviewed the investigations linked to both dripping and jetting regimes in flow-focusing and co-flow devices as well as T-junctions (see Figure 1.14).

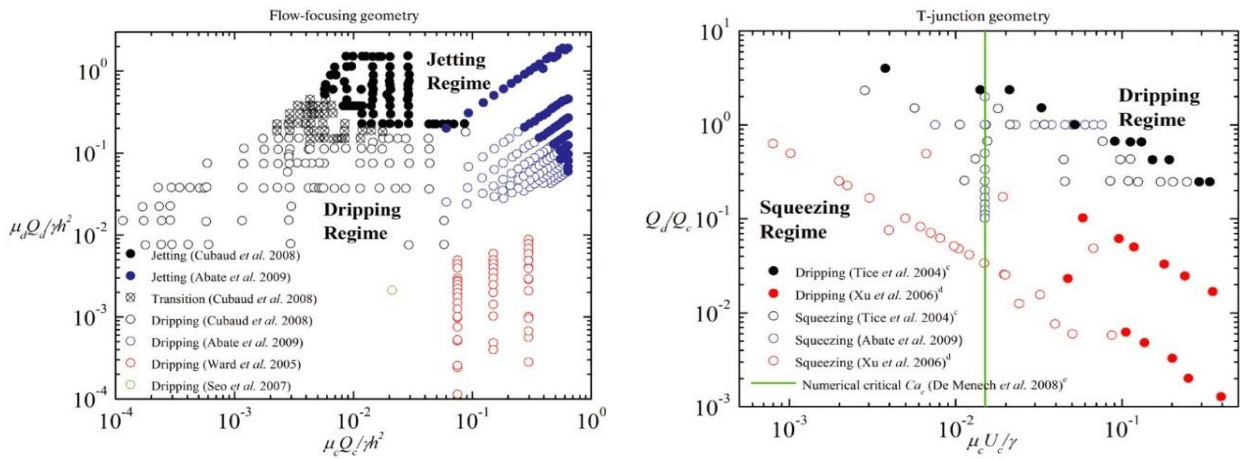


Figure 1.14. Phase diagram of flow-focusing geometry and T-junction from Nunes *et al.* [50].

1.3.4 Effect of interfacial tension

Due to the dominance of surface forces in microscale (high surface to volume ratio), interfacial tension σ_i is one of the most important terms playing role in droplet formation. The addition of surfactant to the fluids simplifies the generation of the droplets and lessens the

chance of the coalescence of the droplets. Since the droplet size depend on Ca_c , the value of droplet size can be seen as a function of interfacial tension and shearing force. With the variation of the surfactant concentration, the interfacial tension is reduced, which causes the variation of the droplet size at the same shearing force. The surfactant adsorption in liquid-liquid system acts dynamically in the droplet formation and influences the interfacial tension at the detaching moment. In order to make the adsorption process shorter and weaker and consequently to keep the interfacial tension at minimum and constant value, large concentration of surfactant, over the critical micelle concentration (CMC), defined as the concentration of detergents above which micelles are spontaneously formed, are usually employed. Reducing σ_i decreases the mixing energy and helps the formation of the stable interface between liquids [32]. Lower concentration of surfactant can be responsible of a variation in droplet sizes caused by the unsaturated adsorption.

A typical surfactant molecule consists of a hydrophilic head and a hydrophobic tail and in the solution these molecules go spontaneously to the interfaces where hydrophilic part stays in the water and hydrophobic tail can stick out in the air. A liquid tends to have a surface as small as possible, so it is easier to make spherical shape by a soap as compared to water. Soaps are called surfactants because of acting on surface, they reduce surface tension. Hydrophilic-Lipophilic Balance (HLB) value could be used to determine if a surfactant is hydrophobic or hydrophilic. Emulsifiers with high HLB values (more hydrophilic) make O/W droplets; on the contrary, surfactants with low HLB values (more hydrophobic) give W/O emulsions [32].

According to the previous studies, the adsorption of surfactant on the interface can be divided into three steps. The first step is diffusive and/or convective transport of the surfactant molecules from the volume phase to the so-called “subsurface”, a boundary layer located directly adjacent to the interface with a thickness approximately equal to the diameter of a single surfactant molecule. In the second step, surfactant molecules are self-assembled from the “subsurface” into the interface. With the proceeding of the adsorption, the surfactant molecules become less in the volume phase, which causes an imbalance in the equilibrium between the micelles and molecules. The concentration gradient between the micelles and molecules leads in a third step to disaggregation of the micelles and dissolution of the surfactant molecules into the volume phase. High concentration can accelerate the dissolution of the surfactant molecules, so the dynamic interfacial tension decreases with the increase of the surfactant concentration [67].

1.3.5 Effect of wettability in droplet generation

Wettability of the channel walls is an important factor in droplet generation. It can be achieved by either the use of coating on the inner walls or addition of surfactant to the continuous phase flow. The interaction of a droplet with the channel wall is characterized by the contact angle. Liu and Zhang [45] simulated the droplet generation with different contact angles of the walls, i.e., $\theta = 110^\circ, 130^\circ, 150^\circ$ and 180° . They observed that the contact angle influenced droplet shape, frequency, the distance between two neighboring droplets and the detachment point. The droplet diameter decreased as the contact angle increased but the squeezing-to-dripping transition occurred at the same critical Ca_c for different wetting conditions. The wetting property had more significant effect on droplet size at small Ca_c and its effect diminished gradually when Ca_c increased.

1.3.6 Effect of non-Newtonian properties

Despite the importance and application of non-Newtonian fluids in industrial and pharmaceutical fields, the analysis of dispersed non-Newtonian fluids was disregarded till now.

Among non-Newtonian properties of the fluids, the elasticity and molecular weight has received more attention. The elasticity of the fluid as well as channel dimension on polymeric drop formation was studied by Steinhaus *et al.* [68] while a Newtonian fluid was the carrier medium using poly(ethylene oxide) (PEO) solutions with different molecular weight (MW) and varying microchannel dimensions with constant orifice width to depth ratio. Higher MW Boger fluids possessing longer relaxation times and larger extensional viscosities exhibited longer thread lengths and longer pinch-off times.

Hong and Cooper-White [69] utilized Carbopol dispersions to study the drop formation and breakup mechanism in silicone oil in a flow-focusing channel. By the use of Carbopol which shows shear thinning and elastic properties as the dispersed phase, they observed that the drop size of these non-Newtonian fluids showed bimodal behaviour varying the viscosity ratio λ .

Based upon a work carried out by Husny and Cooper-White [63] on the effects of viscosity ratio and fluid elasticity on the mechanism of drop formation, two distinct regions of filament thinning dynamics, a “pre-stretch” region and an exponential self-thinning region,

were observed for the highest molecular weight of polyethylene oxide (PEO) studied. The presence of elasticity within these low viscosity fluids resulted in the production of secondary drops of varying sizes upon final breakup.

Lee *et al.* [70] studied the effect of viscoelasticity of Boger fluids used as dispersed phase on the breakup dynamics to quantify the impact of viscoelasticity on the tipstreaming phenomenon, caused by surfactant transport to, from, and along, deforming interfaces that leads to the generation of long filaments.

Arratia *et al.* [71, 72] used polyacrylamide solutions with different molecular weights and elasticity as the dispersed phase to study the filament thinning and droplet breakup. The polymeric filaments showed much slower evolution and their morphology featured multiple connected drops. Measurements of filament thickness as a function of time exhibited different thinning behavior for the different aqueous fluids. For Newtonian fluids, the thinning process showed a single exponential decay of the filament thickness but for low MW fluids decay rate was slower than for the Newtonian fluid and the decay time increased with polymer having a large MW. For high MW fluids, the initial exponential decay crossed over to a second exponential decay in which elastic stresses were important.

Effect of molecular weight and concentration on drop formation and breakup of low viscous elastic fluids was studied by Tirtaatmadja *et al.* [73]. Measurements of the relaxation times of polyethylene oxide solutions having different molecular weights were significantly higher than the relaxation times estimated from Rouse-Zimm theory, even though the solutions were within the dilute concentration region. The effective relaxation times exhibited expected scaling with molecular weight but with an additional dependence on the polymer concentration.

Table 1.1 summarizes some of the above-mentioned studies in a compact way to highlight the different studies carried out in microdroplet generation.

Table 1.1. A comparison of the previous works in T-junction and flow-focusing devices.

Regime	Ca_c	Aim of the study (The effect of)	Method	Ref.
<i>T-junction</i>				
SR	0.001 – 0.01	Geometry	LBM	24
DR	0.01 – 0.08	Viscosity and geometry	LBM	26
SR & DR	–	Unsteadiness of flow rate	Experimental	31
SR, DR & JR	0.001 – 0.01	Interfacial tension	Experimental	32
SR & DR	0.07 – 1.18	Flow rates	Experimental	35
SR	0.002 – 0.005	Geometry and Capillary number, flow ratio, viscosity	Experimental	38
JR & PF	2 E-4 – 0.8	Flow rates	Experimental	40
SR	≤ 0.01	Flow rates, viscosity and geometry	Experimental	41
SR	7 E-4 – 0.02	Flow rate ratio, Capillary number	Experimental	42
SR	–	Surface treatment	Experimental	43
<i>Flow-Focusing</i>				
DR & JR	6 E-4 – 0.1	Viscosity	Experimental	27
SR, DR & JR	0.08 – 8	Geometry and fluid properties	Experimental	28
DR & JR	–	Flow rates	Experimental	29
DR & JR	0.00004– 0.05	Viscosity ratio	Experimental	37
DJ, DC & PF	0.001 – 0.008	Flow rate ratio and Capillary number	LBM	39
SR & DR	0.002 – 0.035	Flow rate ratio, viscosity ratio and Capillary number	LBM	48
SR	–	Flow rate and geometry	Experimental	58
JR	0.33 – 2.6	Viscosity ratio	Experimental	69
DR & JR	0.03 – 0.8	Viscoelasticity & surfactant	Experimental	70
SR	≤ 0.01	Flow rates	Experimental	105
SR	–	Variation in rounding degree	Experimental & computational	61

1.4 Droplet characteristics

The dynamics of the generation of microdroplet within confined geometries shows marked differences with pendant drops. Droplet formation from a nozzle is mainly under the influence of gravity. On the contrary in confined geometries, blockage of the microchannel creates the pressure difference along the microdroplet which accelerates the breakup. Although the process of the droplet generation in microchannels is much faster than that of nozzle due to the existence of a continuous phase, it is more complex because of both confinement of the microchannel and interaction of two fluids. Studying droplet formation dynamics could be a real challenge and trouble because of short time needed for droplet generation.

1.4.1 Droplet formation time

The droplet formation time t_f is generally a sum of two parts: (i) the time required for growing t_g mainly governed by the mean velocity of dispersed phase and (ii) the time taken for necking and breakup t_b mainly determined by the mean velocity of continuous phase [45]. An extra stage named induction stage t_{in} , when the dispersed phase pressure overcomes the Laplace pressure should also be considered [69]. The droplet formation time t_f is influenced by the same parameters controlling droplet size including flow rate and viscosity of the working fluids. The effect of the continuous flow rate Q_c on the drop periodicity was studied as a function of viscosity ratio λ and the dispersed phase fluid type by Husny and Cooper-White [63] while Q_d was kept fixed. An increase of the cross-flow shear resulted in an exponential decrease of the period between subsequent drops, as seen previously [74]. An increase of λ caused a substantial reduction in the period between drops. Increasing λ provides a very effective way of decreasing drop size and increasing drop number per unit time f at a chosen cross-flow rate. Zhang *et al.* [45] plotted dependence of drop formation time as a function of both Q_c and Q_d . They observed a descending trend of t_f with increasing Q_c and/or Q_d . They showed that the droplet formation time decreased as Capillary number, coupled effect of continuous phase viscosity and interfacial tension together with the mean velocity of continuous phase, increased. Arrarita *et al.* [72] presented an experimental investigation of the effects of elastic stresses on the drop breakup processes in a cross-flow microchannel. The breakup time increased as the MW increased and for all fluids, the breakup time decreased exponentially with flow rate ratio. Hong and Cooper-White [69] showed that the elasticity of dispersed phase tends to shorten the drop generation time and to prevent the generation of secondary drops.

1.4.2 Filament, thread and microthread

A filament from the inlet of the dispersed phase to the tip of the droplet is found in dripping and jetting regimes. The studies about filament length and diameter in pendant drops has received much attention. On the contrary the characteristics of the filament in microjunctions are under-investigated. For instance; Zhang [75] studied dynamics of growth and breakup of viscous pendant drop (Figure 1.15). The effects of physical and geometric parameters on the nonlinear dynamics of drop growth and breakup were investigated with the focus on drop breakup and subsequent formation of satellite droplets. The maximum or limiting length that a drop attains prior to its breakup and the volume of a drop increased significantly with increasing Reynolds and Capillary numbers.

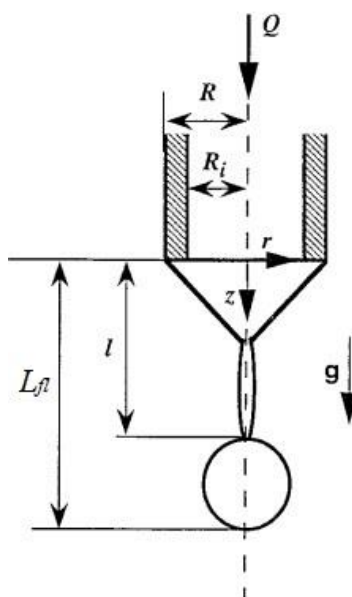


Figure 1.15. Schematic diagram of a pendant drop from a nozzle from Zhang [75].

The breakup of a low viscous fluid is initially governed by a potential flow scaling law controlled by a balance between inertial and capillary forces while in high viscosity fluids the dynamics may initially follow viscous scaling law where only viscous and capillary forces are important.

Unlike the extensive researches on filament dynamics of pendant drop, filament study in confined geometries like microchannels is scarce. Analysis of the filament dynamics during the drop detachment stage revealed that there are two distinct regions; a pre-stretch region and an exponential self-thinning region [63]. Dimensionless filament length and diameter and

Hencky strain were studied as a function of time-to-breakup of the filament t_{fb} . Both length and diameter of filaments produced at the T-junction exhibited a linear dependence on t_{fb} .

Steinhaus *et al.* [68] showed that higher MW Boger fluids exhibit longer thread lengths and longer pinch-off times. Based upon the works performed by Arratia *et al.* [71, 72] polymeric filaments exhibited much slower evolution and their morphology featured multiple connected drops. Measurements of filament thickness showed two main temporal regimes: flow- and capillary-driven. At early times both polymeric and Newtonian fluids were flow-driven, and filament thinning was exponential. At later times, Newtonian filament thinning crossed over to a capillary-driven regime, in which the decay was algebraic.

Hong and Cooper-White [69] confirmed that shear thinning Carbopol fluids produce large secondary drops, when compared to Newtonian-like Carbopol fluids as a result of this thicker filament between the primary and subsequent drop undergoing breakup.

Experimental visualization of tiny microthread forming the neck between thread and droplet has been obtained by Kowalewski [76] as shown in Figure 1.16.

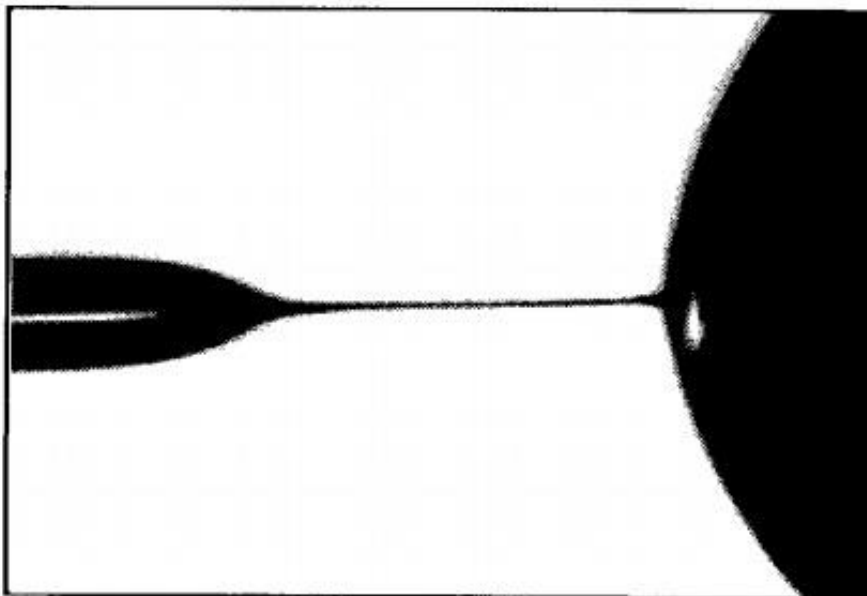


Figure 1.16. Tiny microthread before the droplet detachment from Kowalewski [76].

1.5 Models of droplet formation

Many studies over the last years have been dedicated to microfluidic droplet formation.

Flow parameters including continuous and dispersed phase flow rates and viscosities, interfacial tension and wettability, as well as junction geometry influence the droplet characteristics. The above-mentioned controlling factors as well as confinement exerted by the microchannel make the droplet generation of complex prediction.

The governing forces of a droplet formation are interfacial tension force F_σ , liquid inertial force F_I , shear force F_S , dynamic lift force F_{DL} , static pressure difference force F_{SP} , gravity F_G , liquid momentum F_M and buoyancy F_B [77-79] whilst gravity, gas momentum and buoyancy effects are negligible. Detailed calculations of the forces are illustrated in literature [77, 80].

Droplet formation at a permeable membrane is a two-stage process and the force equilibrium is applied at the end of growth stage while the detachment time is normally correlated to continuous flow rate or dispersed phase pressure. Some of these models [79] have led to satisfactory predictions but no comparison with other researchers' data has been made. The continuous phase at a permeable membrane is regarded as infinite in extent and a similar assumption can be made for droplet formation in microchannels controlled by jetting regime. Therefore, the force balance models for droplet formation at a permeable membrane provide the basis for the theoretical study of droplet formation in the dripping and jetting regimes.

1.5.1 Droplet formation models in squeezing regime

As mentioned before, in squeezing regime droplet size is mainly controlled by the pressure drop force and interfacial tension whereas the shear force is negligible. Some studies have been presented the models for predicting the droplet diameters under squeezing and transitional regimes. These models can be divided in these categories:

1.5.1.1 Correlations dependent on flow rate ratio a

As shown in Section (1.3.1), Garstecki *et al.* [41] provided a scaling law to predict the length of the plug in squeezing regime. Garstecki *et al.* [41] considered droplet formation time t_f as the filling and breakup times. The filling time t_g is controlled by channel size and dispersed phase flow rate as $t_g \propto 1/Q_d$ while the breakup time t_b depends on continuous flow rate $t_b \propto 1/Q_c$. Therefore the droplet size can be estimated as $t_f \times Q_d$ while $t_f = t_g + t_b$ agrees with the correlation given by (Equation (1-6)).

1.5.1.2 Two-stage models

Two-stage models in squeezing and dripping regimes are suggested to fit better experimental and numerical data by consisting both growth and detachment stages [81]. The final droplet volume is obtained as a sum of two values including an initial volume (growth stage) V_{cr} and a volume generated during the detachment stage ($V_{det} (= t_b Q_d)$).

$$V_D = V_{cr} + t_b Q_d \quad (1-13)$$

where V_{cr} is the critical volume that represents the volume at which drag force exerted on the droplet is just as large as the interfacial tension-based force that attaches the droplet to the pore mouth, determined by a force or torque balance; t_b is the time needed for necking; and Q_d is the dispersed phase flow rate. V_{cr} is in fact the droplet volume that would be obtained when the droplet detachment process was very fast ($t_b \rightarrow 0$) and only a force or torque balance is relevant. The value of V_{cr} depends on, among other parameters, the interfacial tension and the shear stress caused by the continuous-phase flow rate. The droplet volumes were made dimensionless by relating them to the volume of a droplet having a diameter equal to the hydraulic diameter of the cross-flow channel. These dimensionless droplet volumes were plotted as a function of the capillary number. The droplet volume decreases as a function of Capillary number, and the droplet size increases somewhat with an increasing dispersed phase flow rate.

Van der Graaf *et al.* [82] correlated V_{cr} and V_{det} to Ca_c and they proposed a model able to work in a good way for both squeezing and jetting regimes. The volume of the droplet (V_D) is calculated as a function of Capillary number and of the flow rate of the dispersed phase.

$$V_D = V_{cr,ref} Ca_c^m + t_{neck,ref} Ca_c^n Q_d \quad (1-14)$$

where $V_{cr,ref}$ is the critical volume at $Ca = 1$ and $t_{neck,ref}$ is the necking time at $Ca = 1$ was used to fit all of the data and m and n are fitting parameters which depend on the junction geometry. It was found that the equation could be simplified to $m = n$ and for this a value of - 0.75 was found, together with $V_{cr,ref} = 2.5 \times 10^{-5}$ μL and $t_{neck,ref} = 0.135$ ms. This means that V_{cr} scales with $Ca^{-0.75}$ and the diameter of the droplet scales with $Ca^{-0.25}$. This scaling behavior is a result of the specific force or torque balance in this specific geometry. For other geometries, such as

that for droplet formation from a pore in a system in which the droplet is not distorted by channel walls, V_{cr} will scale with Ca^{-1} , assuming a torque balance model, or with $Ca^{-3/2}$, assuming a force-balance model.

Zhang *et al.* [83] suggested a similar model by expressing the droplet volume as:

$$V_D = C_g W_c S_d Ca_c^m + C_n W_d S_c Ca_c^n \alpha \quad (1-15)$$

where C_g and C_n are dimensionless constants depending on junction geometry, S_c and S_d are the cross-sectional area of the channel used in order to introduce the continuous and the dispersed phase into the junction, W_c and W_d are the width values of the channel.

1.5.1.3 Models based on a force balance

None of the correlations presented until now are able to predict droplet formation in an accurate way as evidenced by Steegmans *et al.* [81] because of their dependence on fitting parameters. Models based on force balance are able to predict the droplet characteristics in a more precise way.

Few force balance models have been proposed for droplet generation in microchannels with the drop size smaller than size of microchannel (i.e. for dripping and jetting regimes) [63, 84]. Garstecki *et al.* [41] calculated controlling forces including pressure drop force, interfacial tension and shear force in squeezing regime. Christopher *et al.* [57] provided a force balance model in transitional regime. Glawdel *et al.* [85] decomposed the droplet formation into three stages as the lag, filling and necking stages and modeled it in squeezing to transitional regime based upon the work performed previously [41, 57]. Failing to estimate the forces especially pressure drop force led to an unsuccessful model. However a force balance model was not built successfully, they emphasized on the importance of the pressure drop force and interfacial tension. In dripping regime with a filament through the channel Steegmans *et al.* [86] considered wall effect corrections in force balance model for a microfluidic Y-junctions.

1.5.2 Droplet formation models in dripping and jetting regimes

No correlations have been proposed until now for the droplet generation in jetting regimes. The two-stage models may not be used in the jetting regime due to the long unstable

jet which modify the droplet breakup with respect to dripping regime. An analytical force balance model has been proposed by Husny and Cooper-White [63] and Liu and Zhang [45] but this model is unable to predict data from other publications.

1.6 Governing forces and droplet size

The droplet generation is controlled by different governing forces. In this chapter the main governing forces involved in droplet generation in squeezing regime in T-junction and flow-focusing devices are summarized with the aim to see the droplet generation as the result of a force balance between pressure drops, interfacial tensions and the shear forces.

1.6.1 Governing forces on a droplet

The forces acting on a growing droplet are pressure drop force, interfacial tension and shear force. The forces acting on the emerging immiscible thread in the filling stage are indicated in Figure 1.17.

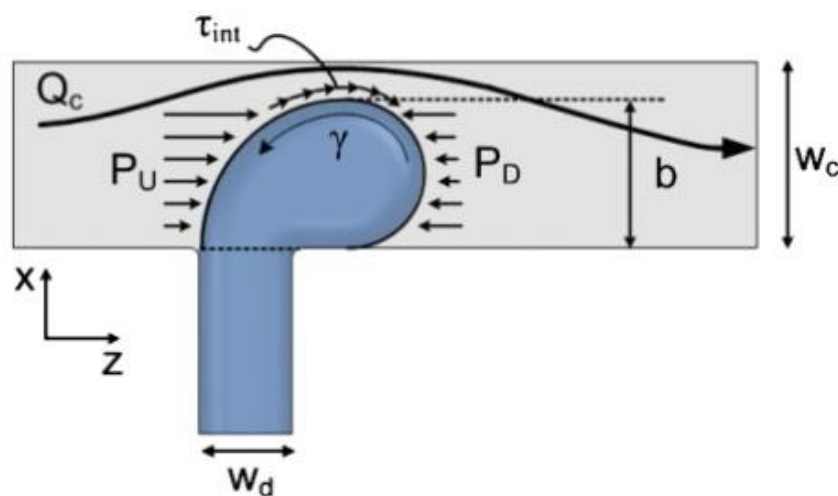


Figure 1.17. The forces acting on the emerging droplet in the filling stage from Glawdel *et al.* [85].

As the droplet grows, a pressure difference across the droplet and a shear stress on the interface due to the obstruction of the continuous phase are two forces which are countered by the interfacial tension force.

1.6.1.1 Pressure drop

As the droplet grows, a pressure difference across the droplet and a shear stress on the interface due to the obstruction of the continuous phase are two forces which are countered by the interfacial tension force (Figure 1.18).

Since the tip of dispersed phase fluid intrudes the main channel, the upstream pressure increases gradually until the convex interface approaches the opposite wall of the junction. Then it begins to decrease nearly to the initial level before the introduction of the dispersed phase. In the stage between the end of the droplet formation and the initiation of a new droplet, the dispersed phase is retracted to the inlet channel [41].

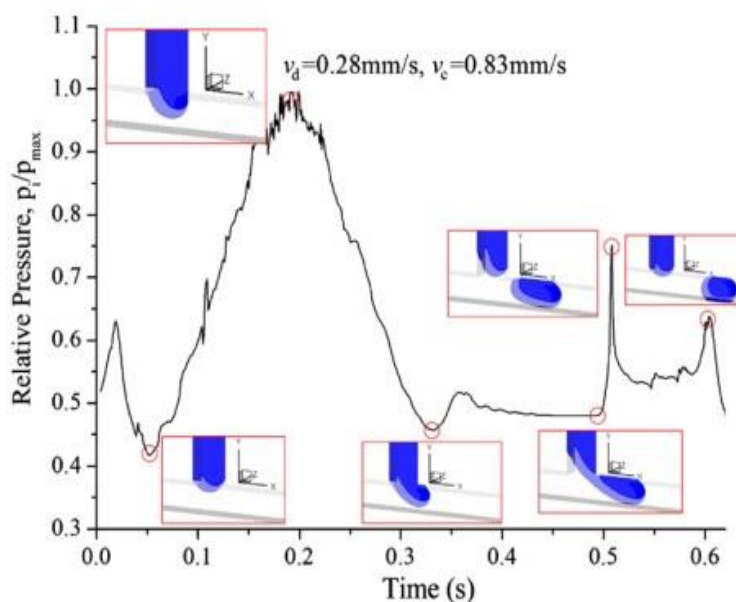


Figure 1.18. The related regimes corresponding to pressure variation upstream of a T-junction from Li *et al.* [87].

When the upstream pressure reaches the maximum value, due to the existence of the gap between the droplet and the opposite channel wall, the pressure drop does not. In fact, the pressure drop is not large enough to either break or push the droplet downstream. Increasing pressure drop moves the interface along the channel and it shows a decrease in upstream pressure because the droplet moves and the blockage decreases. After that, a constant pressure is observed because of the continuous downstream flow of the droplet. Then the interface turns into a concave neck and the droplet is close to the detachment. The pressure increases since the emerging droplet will clog the main channel. A surge in pressure before the detachment may

be observed and in this case the channel is almost blocked by the interface.

A theoretical evaluation of the pressure around the droplet can be obtained by applying to the junction the Hagen-Poiseuille equation or lubrication analysis. Garstecki *et al.* [41] proposed to estimate the pressure drop over the length of the tip which is on the order of the width ($\sim w$) of the main channel by using the Hagen-Poiseuille equation:

$$\Delta p = \frac{\mu_c Q_c w}{H w_{gap}^3} \quad (1-16)$$

where the meaning of the symbols is explained by Figure 1.19; usually, the gap between the droplet and the channel walls $w_{gap} \ll w$. The force acting on the droplet due to the pressure drop can be estimated by multiplying the pressure drop for the surface ($= H.w$):

$$F_p = \Delta p H w = O\left(\frac{\mu_c Q_c w^2}{w_{gap}^3}\right) \quad (1-17)$$

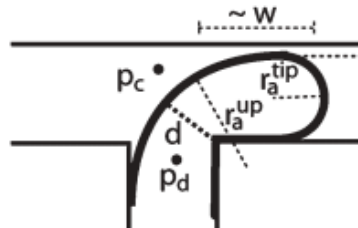


Figure 1.19. A schematic illustration (top view) of the shape of the tip of the immiscible thread at an intermediate stage of break-up from Garstecki *et al.* [41].

Christopher *et al.* [57] estimated the squeezing pressure arising from the obstruction of the channel by the emerging droplet in a similar way to Garstecki *et al.* [41], using the lubrication theory for a pressure-driven flow in a thin gap with aspect ratio w_{gap}/b where b is the length of the emerged droplet. They obtain an expression of the force linked to the pressure drop similar to the expression derived by Garstecki *et al.* [41]:

$$F_p = \Delta p H w = \frac{\mu_c u_{gap}}{w_{gap}} \frac{b}{w_{gap}} b H = \frac{\mu_c Q_c b^2}{w_{gap}^3} \quad (1-18)$$

where u_{gap} is the velocity through the gap and $Q_c = u_{gap} (w_{gap} \cdot H)$. Similarly, Glawdel *et al.* [85] obtained the pressure drop force by the use of lubrication analysis between two parallel plates:

$$F_p = \Delta p H w = \frac{12 \mu_c Q_c b}{(w_{gap} H)^2} b H = \frac{12 \mu_c Q_c b^2}{w_{gap}^2 H} \quad (1-19)$$

In this thesis the cross-junction employed during the experimental tests has a constant height ($H = 190 \mu\text{m}$) with width at the junction ($W_j = 195 \mu\text{m}$) and far from the junction ($W_w = 390 \mu\text{m}$). The cross-section is elliptical. The fully developed velocity profile of the continuous phase (i.e. silicone oil) through elliptical microchannel is following in polar coordinates (ρ, φ):

$$u(\rho, \varphi) = \frac{\Delta p}{8 \mu L} \frac{W^2 H^2}{W^2 + H^2} (1 - \rho^2) \quad (1-20)$$

From the velocity profile integrated on the channel cross-section the volumetric flow rate can be calculated ($Q = \frac{W \cdot H}{4} \int_0^{2\pi} d\varphi \int_0^1 \rho u(\rho, \varphi) d\rho$):

$$Q = \frac{\pi}{64 \mu L} \frac{H^3 W^3}{H^2 + W^2} \Delta p \quad (1-21)$$

From Equation (1-21) it is possible to obtain the pressure drop across the droplet by considering W equal to the width of the gap (W_{gap}).

$$\Delta p = \frac{64 \mu_c L}{\pi} Q_c \frac{H^2 + W_{gap}^2}{H^3 W_{gap}^3} \quad (1-22)$$

The expression of the pressure drop force can be generalized by considering non-Newtonian fluids. The fully developed velocity profile of a power-law flow through two

parallel plates with a width W can be written as follows:

$$u(x) = \frac{n}{n+1} \left(\frac{\Delta p}{kL} \right)^{1/n} \left(\frac{W}{2} \right)^{1+1/n} \left[1 - \left(\frac{2x}{W} \right)^{1+1/n} \right] \quad (1-23)$$

where k is the flow consistency index of the Ostwald–de Waele relationship, Δp is the pressure drop and n is the flow behavior index. If $n = 1$ (Newtonian fluid), Equation (1-23) takes the well-known expression:

$$u(x) = \frac{\Delta p}{8\mu L} W^2 \left[1 - \left(\frac{2x}{W} \right)^2 \right] \quad (1-24)$$

From the velocity profile the volumetric flow rate can be obtained by integrating on the channel cross-section ($Q = \int_0^H dy \int_0^W u(x) dx$):

$$Q = \frac{n}{2n+1} \left(\frac{\Delta p}{kL} \right)^{1/n} \left(\frac{W}{2} \right)^{1+1/n} WH \quad (1-25)$$

From Equation (1-25) the pressure drop across the growing droplet in presence of a non-Newtonian fluid can be written as follows:

$$\Delta p = 2^{n+1} Lk \left[\frac{2n+1}{n} \frac{Q_c}{H \cdot W_{gap}^{\frac{2n+1}{n}}} \right]^n \quad (1-26)$$

where W_{gap} is width of the gap between droplet and the channel wall and H is channel height.

However, as observed by van Steijn *et al.* [88], in rectangular microchannels a portion of the continuous phase passes through the gap and corners between the growing droplet and microchannel walls. The corners increases the cross-section available for the continuous phase and reduces the value of the pressure drop. For this reason, a leakage factor, defined as the percentage of the continuous phase flow through the gap and corners, has to be introduced in

the evaluation of the pressure drop. The leakage factor f_{leak} can be estimated as the ratio of the area linked to the gap and corners to the area of the main channel, therefore by assuming an elliptical cross-section of the droplet, f_{leak} can be written as follows:

$$f_{leak} = 1 - \frac{S_{elliptical}}{S_{channel}} = 1 - \frac{\frac{\pi}{4}WH}{WH} = 0.21 \quad (1-27)$$

From Equation (1-27) the area of the corners can be estimated as $S_{gap} = 0.21 WH$.

By introducing the leakage factor, the pressure drop force can be calculated as $F_p = \Delta p \cdot S_{elliptical}$ where $S_{elliptical} = \frac{\pi}{4}WH$:

$$F_p = 2^{n+1} Lk \left[\frac{2n+1}{n} \frac{Q_c}{H \cdot W_{gap}^{\frac{2n+1}{n}}} \right]^n \frac{\pi}{4} WH \quad (1-28)$$

1.6.1.2 Shear force

As pointed by Husny and Cooper-White [63], a droplet formed at a T-junction is subjected to hydrodynamic drag imposed by the continuous phase.

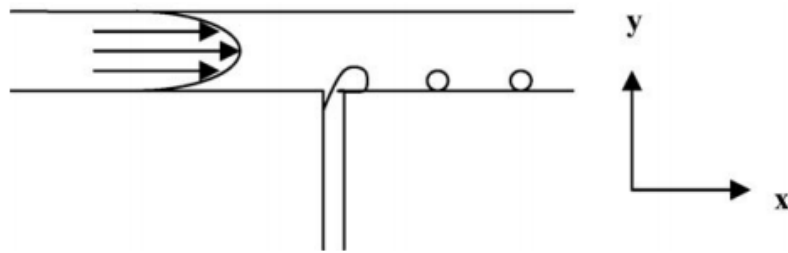


Figure 1.20. Schematic representation of drop creation in the presence of cross-flow shear from Husny and Cooper-White [63].

Assuming a fully developed laminar flow in the continuous phase channel, the expression for local liquid velocity for a power-law flow within two parallel plates can be written as:

$$u = \frac{2n+1}{n+1} u_c \left[1 - \left(\frac{D_{hl} - D_D}{D_{hl}} \right)^{\frac{n+1}{n}} \right] \quad (1-29)$$

where the hydraulic diameter of the channel D_{hl} is equal to width of the channel W . D_D is the droplet diameter. The drag force F_τ acts in the positive x -direction and serves to detach the droplet from the dispersed phase channel. It can be obtained as:

$$F_\tau = \frac{1}{2} C_{dr} \rho_c (u - u_d)^2 S_{effective} \quad (1-30)$$

where C_{dr} is the drag coefficient, $(u - u_d)$ is the relative local velocity of the fluid u with respect to the droplet velocity u_d . The effect of viscosity ratio λ (between the dispersed phase viscosity and the continuous phase viscosity) is taken into account if a modified drag coefficient (C_{dr}), for creeping flow outside a fluid sphere, as defined by Hadamard [89] and Rybczinski [90], is introduced in Equation (1-30):

$$C_{Def} = \frac{8}{Re_D} \frac{2\lambda + 3}{\lambda + 1} \quad (1-31)$$

where the Reynolds number (Re_D) for the liquid flowing around the drop is given by:

$$Re_D = \frac{\rho_c (u - u_d) D_D}{\mu_c} \quad (1-32)$$

Combining and summing up Equations (1-29) to (1-32), the drag force equation is given in Equation (1-33) for power-law fluids.

$$F_\tau = \frac{2\lambda + 3}{\lambda + 1} \mu_c \left[\frac{2n+1}{n+1} u_c \left(1 - \left(\frac{D_{hl} - D_D}{D_{hl}} \right)^{\frac{n+1}{n}} \right) - u_d \right] \pi D_D \quad (1-33)$$

1.6.1.3 Interfacial tension

The interfacial tension force F_σ is the opposing force acting in negative x -direction. It is associated with the Laplace pressure difference between upstream and downstream ends of the emerging droplet interface. The Laplace pressure jump Δp across a static interface is:

$$\Delta p_L = \sigma_i \left(\frac{1}{r_a} + \frac{1}{r_r} \right) \quad (1-34)$$

where r_a is the axial curvature and r_r is the radius of the radial curvature of the neck (Figure 1.19). The radial curvature is bounded by the height of the channel ($r_r = H/2$) whereas the axial curvature is greater at the downstream tip of the thread ($r_a = W/2$) than at the upstream side of it ($r_a = W$) [41].

The static Laplace pressure jump over the droplet interface is described as:

$$p_d - p_{back} = \sigma_i \left(\frac{1}{W} + \frac{2}{H} \right) \quad (1-35)$$

$$p_d - p_{front} = \sigma_i \left(\frac{2}{W} + \frac{2}{H} \right) \quad (1-36)$$

From Equation (1-35) and (1-36) it is possible to observe that the pressure difference $\Delta p = p_{back} - p_{front}$ between upstream and downstream of the droplet is equal to:

$$\Delta p_L = \frac{\sigma_i}{W} \quad (1-37)$$

The interfacial tension force F_σ is obtained by the multiplying the cross-section of the channel with the pressure difference:

$$F_\sigma = \Delta p_L \cdot S \quad (1-38)$$

where Δp_L is the Young-Laplace pressure and the surface area S is ($S = W.H$ for a rectangular cross-section and $S = \frac{\pi}{4}W.H$ for an elliptical cross-junction).

F_σ for a rectangular and an elliptical cross-section can be written as follows:

$$F_\sigma = \sigma_i H \quad (1-39)$$

$$F_\sigma = \frac{\pi}{4} \sigma_i H \quad (1-40)$$

The droplet size at the detachment can be obtained by means of a force balance of the above-mentioned forces, by imposing that the following equation is verified:

$$F_p + F_\tau - F_\sigma = 0 \quad (1-41)$$

1.7 Scope of the thesis

Previous investigations have shown that microfluidic droplet generators enable the production of droplets with a low size variation and reproducible diameters. It has been reported that droplet size is controlled by a number of parameters including the geometry of the junctions, properties of liquids (viscosity, interfacial tension, etc.), flow rates of two immiscible phases and surfactant concentrations. The droplet production can be classified into three controlling regimes, namely, squeezing, dripping and jetting which can be obtained by varying operatively α and Ca_c . Since droplet formation is controlled by different forces, the effect of controlling parameters varies. Although controlling parameters have been investigated by a large number of researchers, their effects have not been completely elucidated.

Although most solutions in biological and pharmaceutical applications are non-Newtonian in nature, the studies of non-Newtonian droplets are limited if compared with those focused on generation of Newtonian droplets. There is a dearth of experimental data on non-Newtonian droplet production. Studies of droplet formation dynamics have been performed extensively for pendant drops, but there is a paucity of published works on droplet formation dynamics at a microchannel. Publications on pendant drop formation show that varying the

controlling parameters (flow rate and viscosity) changes the drop formation dynamics significantly including the drop formation time, thread length and diameter, and changes the final drop size. Limited available investigations report that non-Newtonian properties also affect the droplet formation dynamics, but the exact effects have not been clarified.

Hitherto, theoretical understanding of droplet production has been limited and there is a need to develop models to predict the droplet size. Although a series of correlations and two-stage models have been proposed, they are not able to predict all the experimental data. The force balance model appears to be a good option to predict droplet diameter and obtain an insight into the controlling mechanism. Since the governing forces are different in various controlling regimes, different force balance models have to be built for each regime.

Based on the review of literature, following objectives were established for this research:

- To experimentally investigate and understand the effect of the main droplet controlling parameters (i.e. flow rate, viscosity and device geometry) on droplet production by considering a T-junction and two micro cross-junctions operating in different regimes, by considering the generation of both Newtonian and non-Newtonian (Xanthan gum) dispersed fluids.
- To study the effects of the use of surfactant on the variation of the two-phase flow from parallel flow to the droplet-based flow by the modification of the interfacial tension.
- To study the dynamic behavior of droplet production investigating the droplet formation time, elongation of the filament and thread length, droplet growth, and the breakup mechanism of the droplets at low values of Q_c and Q_d (squeezing regime). A comparison of the influence of the non-Newtonian properties on the change in the dynamics of droplet formation will be made related to the Newtonian fluids used.
- To obtain a theoretical model based on the experimental observations through force balances with the aim to predict the droplets produced in squeezing regime.

1.8 Outline of the thesis

This thesis is structured into seven chapters:

Chapter 1 reviewed the existing literature and established the objectives of this thesis.

Chapter 2 details the experimental setup and data reduction, procedure followed during the investigation. An accurate description of the preparation of non-Newtonian solutions and of the measurement of relevant fluid properties is given. A description of the post-processing for image analysis developed in MATLAB is done.

Table 1.2. The range of volumetric flow rates Q and Capillary number Ca employed in Chapter 3.

CP	DP			
	W		W+T	
	Flow rate (ml/h)	Capillary number	Flow rate (ml/h)	Capillary number
SO	$0.8 < Q_c < 49.9$	$16E-4 < Ca_c < 1E-1$	$0.3 < Q_c < 15$	$3E-3 < Ca_c < 16E-2$
	$0.016 < Q_d < 59$	$1E-6 < Ca_d < 4E-3$	$0.01 < Q_d < 8$	$6E-6 < Ca_d < 5E-3$
	0.3 XG+T		0.5 XG+T	
	Flow rate (ml/h)	Capillary number	Flow rate (ml/h)	Capillary number
	$0.3 < Q_c < 20$	$34E-4 < Ca_c < 23E-2$	$0.3 < Q_c < 15$	$4E-3 < Ca_c < 2E-1$
SO	$0.01 < Q_d < 3$	$98E-4 < Ca_d < 45E-3$	$0.01 < Q_d < 3$	$3E-2 < Ca_d < 1E-1$

Chapter 3 is focused on the experimental investigation of droplet production within a micro cross-junction. Different combination of dispersed and continuous phases are considered. The effects of controlling parameters (flow rates) and fluid properties (viscosity) are studied and their impact on the droplet size, flow regime transitions, droplet formation time and filament length is analyzed. The breakup mechanism of the generation of the droplet is discussed and the effect of the junction geometry on the size of the droplets is investigated. A large range of volumetric flow rates has been investigated as indicated in Table 1.2.

Chapter 4 presents a detailed analysis of the droplet generation at a micro T-junction. The role of the surfactant on the flow regime is discussed to put in evidence its role on the transition from parallel flow to the droplet-based flow for Newtonian fluids. The range of the flow rates investigated is indicated in Table 1.3.

Table 1.3. The range of volumetric flow rates Q and Capillary number Ca employed in Chapter 4.

DP	CP			
	W+T		W	
	Flow rate (ml/h)	Capillary number	Flow rate (ml/h)	Capillary number
SO	$1 < Q_c < 25$	$4E-4 < Ca_c < 1E-2$	$2 < Q_c < 120$	$1E-4 < Ca_c < 7E-3$
	$0.1 < Q_d < 13$	$75E-5 < Ca_d < 97E-3$	$0.05 < Q_d < 100$	$6E-5 < Ca_d < 1E-1$
SO	0.2 XG+T		0.2 XG	
	Flow rate (ml/h)	Capillary number	Flow rate (ml/h)	Capillary number
	$0.5 < Q_c < 20$	$37E-3 < Ca_c < 13E-2$	$1 < Q_c < 30$	$9E-3 < Ca_c < 34E-3$
	$0.01 < Q_d < 8$	$6E-5 < Ca_d < 5E-2$	$0.01 < Q_d < 16$	$1E-5 < Ca_d < 2E-2$

The effects of the microfabrication technique and its quality on the flow regime have been studied by considering another microchannel with the same characteristics for the rest of the chapter. The possibility of the generation of silicone oil droplets within Newtonian (water with and without surfactant) and non-Newtonian (0.2 wt% Xanthan gum aqueous solution in the absence and presence of the surfactant) carrier medium has been studied. In spite of the first T-channel employed, by the second microchannel it is possible to generate monodispersed droplets in case of pure Newtonian and non-Newtonian continuous phase without surfactant. The variation of non-dimensional length of the microdroplet has been studied as a function flow rate ratio α , continuous Ca_c and dispersed Capillary number Ca_d . The results of the second microchannel in terms of Polydispersity and flow maps has been compared with the first microchannel.

Chapter 5 presents the main conclusions of the thesis and recommendations for future work.

Chapter 2

Experimental Setup and Data Reduction

In this chapter the microchannels employed in this dissertation, experimental setup, preparation and measurements of the working fluid properties and the post-processing method are presented

2.1 Experimental apparatus

The injection of the flow into the microchannel has been depicted in Figure 2.1. After the generation of the droplet the continuous and dispersed phase flows pass through the channel to the outlet reservoir.

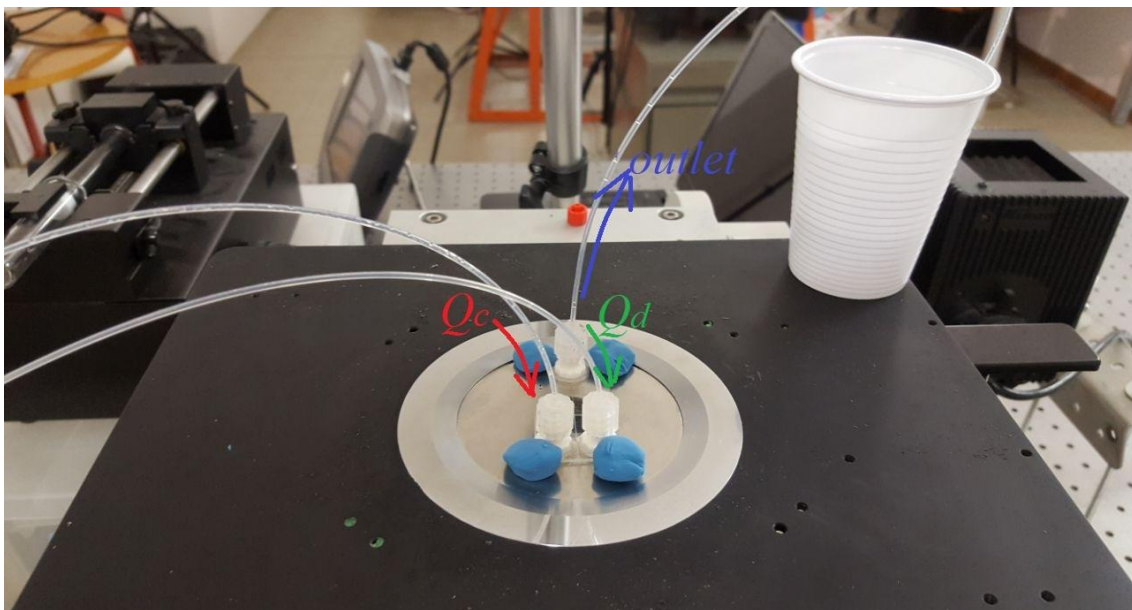


Figure 2.1. Microchip on the working desk of the inverted microscope with the indication of the inlets (Q_c and Q_d) and outlet.

The lay-out of the experimental setup for the analysis of the droplet generation is illustrated in Figure 2.2. An inverted microscope (1 in Figure 2.2, *Nikon Eclipse TE2000-U*) with an air immersion lens (3 in Figure 2.2, *Nikon CFI DS 10X*, $NA = 0.25$) is the heart of the apparatus used to visualize the droplets across the microchannel during the experimental runs. The junction is illuminated by the use of a double illumination system obtained by coupling the light of a 100 W halogen lamp (2a in Figure 2.2, *Nikon HMX Lamphouse*) from the bottom of the channel and the light made by a COB LED lamp (2b in Figure 2.2, *100 W, 9000 Lumens*) from the top of the microchannel. A high-speed camera (4 in Figure 2.2, *Olympus I-speed II*) connected to the inverted microscope allows to acquire a series of images by means of which it becomes possible to follow the dynamic evolution of the interface between the immiscible liquids during the droplet formation; a LCD monitor (5 in Figure 2.2) connected to a PC equipped with Olympus I-speed II software (6 in Figure 2.2) allows a run-time visualization of the flow within the microdevice during the experiments.

The volumetric flow rates of the continuous phase and of the dispersed phase are imposed by two independent low-noise syringe pumps (7, *Cole-Parmer Version Hills* and 8, *Harvard Apparatus PHD 4400 Programmable* in Figure 2.2) and introduced at the inlets of the junction (11 in Figure 2.2) by two gastight Hamilton syringes (9 and 10 in Figure 2.2).

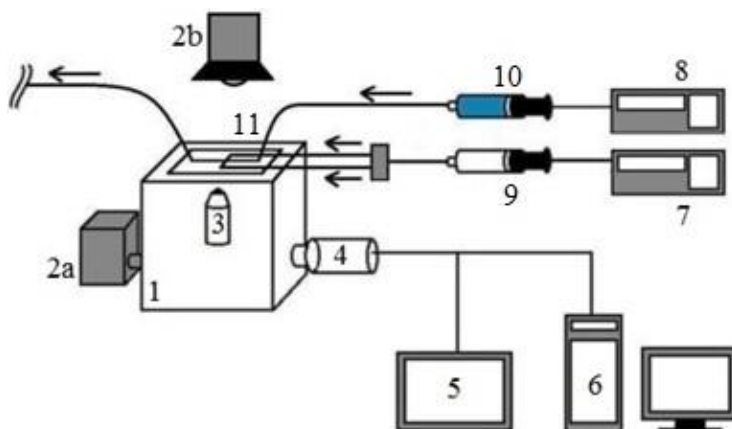


Figure 2.2. The lay-out of the experimental setup.

The experimental setup has been depicted in Figure 2.3 and Figure 2.4.

from the production of the first droplet. Once steady-state conditions are achieved, high-speed camera is activated and the video files of the droplets are recorded.

2.2 Data reduction and governing parameters

As explained in Chapter 1 by using the main results published in the open literature about droplet generation in microjunctions, the main physical parameters useful to control the droplet generation in a confined junction are:

1. The flow rates associated to the continuous (Q_c) and dispersed phase (Q_d);
2. The main physical properties of the fluids involved (i.e. density ρ and dynamic viscosity μ) for both continuous and dispersed phase fluids;
3. The interfacial tension σ_i between the immiscible liquids;
4. The parameters which define the geometry of the junction. The number of these parameters depends on the complexity of the junction (i.e. planar co-flow junction, cross-junction, T-junction, Y-junction, λ -junction). In the case of the junctions considered in this thesis the main geometrical parameters are: (i) channel height (H), (ii) channel width of the junction arm used for the introduction of the dispersed phase (W_d), (iii) channel width of the junction arm used for the introduction of the continuous phase (W_c) and (iv) minimum channel width at the junction (W_j).

The Buckingham-Pi theorem allows to determine the minimum number of independent parameters that one has to consider for the analysis of droplet generation.

It is easy to demonstrate that the following dimensionless quantities define the set of the independent governing parameters of a droplet generator:

1. Aspect ratio at the junction A_j , defined as the ratio between the channel height and width at the junction: $A_j = H/W_j$;
2. Aspect ratio of the inlets $A_{w,c}$ and $A_{w,d}$, defined as the ratio between the inlet channel height and width for both the inlets of the junction: $A_{w,c} = H/W_c$ and $A_{w,d} = H/W_d$;
3. Restriction ratio R_c and R_d , defined as the ratio between the channel width at the junction and the channel width of the inlets $R_c = W_j/W_c$ and $R_d = W_j/W_d$;

4. Width ratio Λ , defined as the ratio between the channel width linked to the inlets of the junction: $\Lambda = W_d/W_c$;
5. Volumetric flow rate ratio α , defined as the ratio between the volumetric flow rate of the dispersed phase and the volumetric flow rate of the continuous phase: $\alpha = Q_d/Q_c$;
6. Viscosity ratio λ , defined as the ratio between the viscosity of the dispersed phase and of the continuous phase: $\lambda = \mu_d/\mu_c$;
7. Reynolds number linked to the continuous and dispersed phase: $Re_c = \rho_c u_c D_{hl}/\mu_c$ and $Re_d = \rho_d u_d D_{hl}/\mu_d$ where u ($= Q/S$) is the phase velocity, S is the microchannel cross-section area and D_{hl} is the hydraulic diameter.
8. Capillary number linked to the continuous and dispersed phase: $Ca_c = \mu_c u_c / \sigma_i$ and $Ca_d = \mu_d u_d / \sigma_i$;

It is possible to observe that, from a theoretical point of view, each droplet characteristic D (i.e. volume, length and diameter) can be considered as a function of the above mentioned dimensionless parameter:

$$D = f(A_j, A_{w,c}, A_{w,d}, R_c, R_d, \Lambda, \alpha, \lambda, Re_c, Re_d, Ca_c, Ca_d) \quad (2-1)$$

However, it is possible to decrease the number of the independent parameters by considering the specific operative conditions investigated in this dissertation.

1. For the flow regimes under consideration, Reynolds numbers (Re_c, Re_d) are very small ($Re < 10$) and does not influence significantly the droplet production.
2. The junctions considered here are characterized by the same channel width of the inlets ($W_c = W_d$) then $\Lambda = 1$, $A_{w,c} = A_{w,d} = A_w$ and $R_c = R_d = R = A_w/A_j$.

Under these hypotheses a drastic reduction of the governing parameter can be obtained:

$$D = f(A_w, R, \alpha, \lambda, Ca_c, Ca_d) \quad (2-2)$$

When Newtonian fluids are considered as dispersed phase, if the liquid properties can be considered as constant, the four parameters α, λ, Ca_c and Ca_d are not independent at all because it is easy to demonstrate for micro cross-junction and T-junction, respectively that:

$$Ca_c = \frac{Q_c}{2S\sigma_i} \mu_c, \quad Ca_d = \frac{Q_d}{S\sigma_i} \mu_d = 2\alpha\lambda Ca_c \quad (2-3)$$

$$Ca_c = \frac{Q_c}{S\sigma_i} \mu_c, \quad Ca_d = \frac{Q_d}{S\sigma_i} \mu_d = \alpha\lambda Ca_c \quad (2-4)$$

In this case Equation (2-2) can be written as:

$$D = f(A_w, R, \alpha, \lambda, Ca_c) \quad (2-5)$$

On the contrary, when a non-Newtonian dispersed phase is considered, Ca_d is not constant during an experimental runs due to the variation of the fluid viscosity with the shear rate and this fact has to be considered for interpretation of the experimental results because the droplet characteristics can become a function of Ca_d too.

2.3 Microchannels

In the current dissertation three different microchannels including two cross-slot microchannels with different geometries and one T-junction have been studied.

2.3.1 Cross-slot microchannels

Two micro cross-junctions have been employed in the current thesis to consider the effects of both flow parameters and geometry variation on the droplet size (Figure 2.5).

In Figure 2.5 the sketch of the micro cross-junctions and how the working fluids are injected into the microchannel through tubes along with connectors has been shown.

The cross-slot microchannels employed in this work to create liquid droplets by focusing a liquid stream (dispersed phase) into another immiscible fluid (continuous phase) are two commercial glass micro cross-junctions #1 and #2 shown in Figure 2.6a and b (*Dolomite Microfluidics Co.*). The continuous phase is introduced into the junction by means of the lateral arms of the cross-junction; on the contrary, the dispersed phase flows in the central microchannel (see Figure 2.6a and b) where Q_c and Q_d represent the inlet volumetric flow rates

of the continuous and dispersed phase, respectively. The generated droplet produced by pinching-off the dispersed phase by two continuous flows from the lateral branches passes through the outlet.

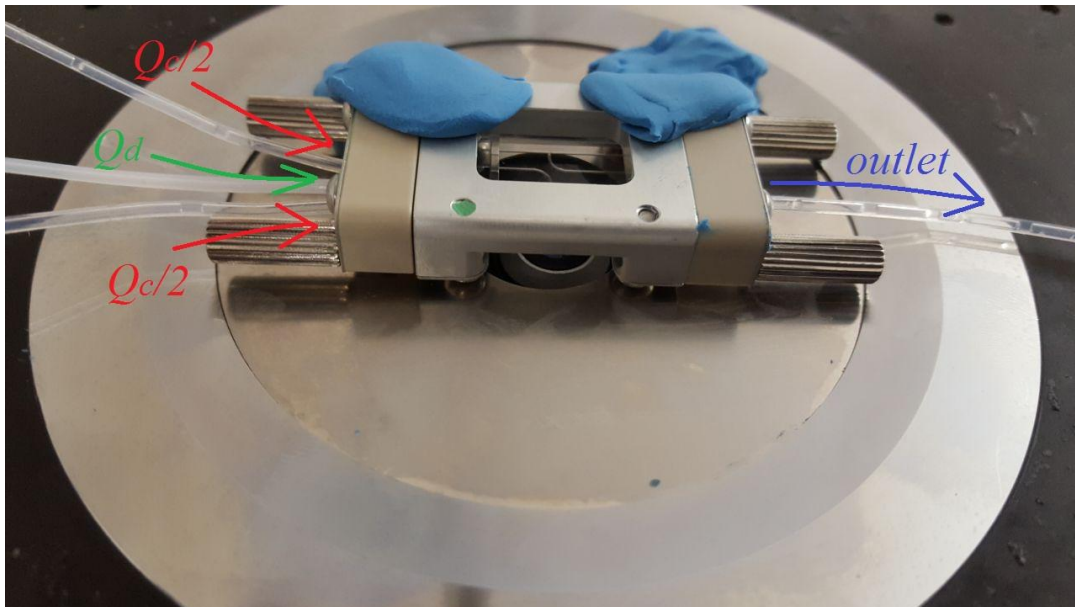


Figure 2.5. Micro cross-junction (*Dolomite Microfluidics Co.*) with two linear 4-way connectors.

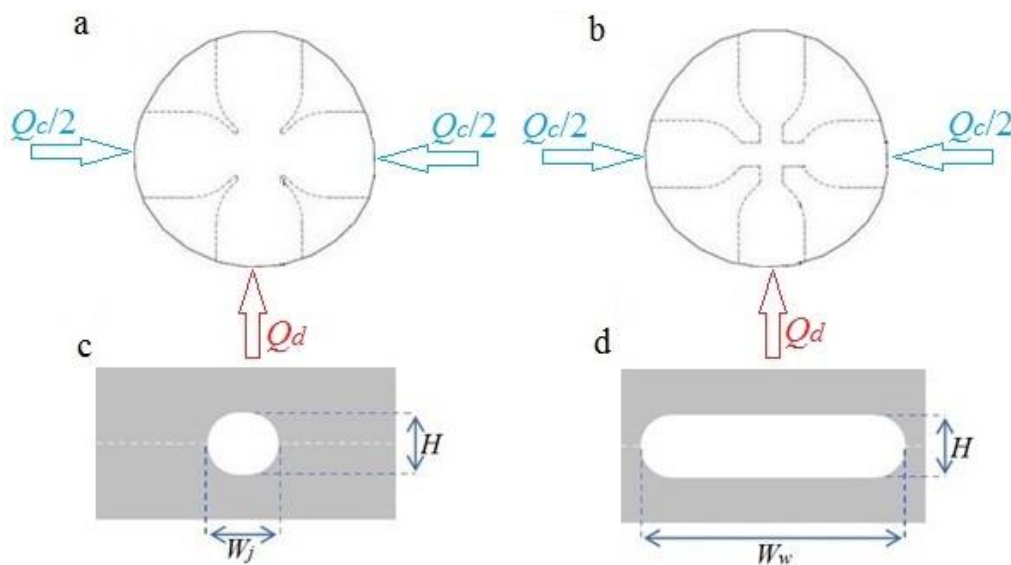


Figure 2.6. Cross-slot microchannels used for the experiments: (a) geometry of junctions #1; (b) geometry of junction #2; (c) channel cross-section at the junction and (d) channel cross-section far from the junction.

The experimental study of the generation of droplets in two microchannels different in

size has been studied with the aim of verifying the influence of the channel cross-section size on the generation of the emulsion. Two commercial micro cross-junctions (*Dolomite Microfluidics Co.*) with the hydrophobic walls enable the generation of aqueous emulsions. The microchannels fabricated in glass have a stadium shape cross-section (Figure 2.6c and d). The cross-junction is characterized by a cross-section restriction at the junction in which the width of the channel varies along the junction. The width of the channel far from the junction W_w is equal to 390 μm for channel #1 while it is 300 μm for channel #2. For channel #1 W_j which stands for the width at the junction is 195 μm while in channel #2 $W_j = 105 \mu\text{m}$. The restriction ratio $R = W_j/W_w$ changes from 0.5 for channel #1 to 0.35 in channel #2. The uniform height of the junction through the channel #1 and #2 is equal to $H = 190$ and $100 \mu\text{m}$, respectively. The aspect ratio $A_w = H/W$ is equal to $A_j = 0.97$ at the junction and $A_w = 0.49$ out of it for channel #1 while in second channel these values are $A_j = 0.95$ and $A_w = 0.33$. The glass channel surface is naturally hydrophilic and generally a surface coating is needed to make it hydrophobic and appropriate for the generation of aqueous droplets in silicone oil carrier fluid.

2.3.2 T-junction

A commercial T-junction microfluidic chip having the square cross-section area with the dimension of 300 μm has been chosen to produce silicone oil droplets in aqueous solutions (Figure 2.7). The geometrical ratios derived from the Buckingham-Pi analysis, width ratio Λ ($= W_d/W_c$) and the aspect ratio A ($= H/W$), for this configuration are equal to 1 due to the square cross-section of the T-junction. Since there is not any restriction at the junction, the restriction ratio R is 1.

Based upon the information provided by the manufacturer, the glass surfaces of the chip produced by *Translume Co.* are pure fused silica glass and have not been coated. However, the surface "wettability" is a strong function of not only the channel material but also the manufacturing method. The top surface of the microfluidic channel is polished (optical polishing), as such it is hydrophilic. In contrast the sidewalls and the bottom (translucent floor) of the microfluidic channel have been machined and have a certain roughness (surface RMS roughness is typically one micron or less). As such, they are not as hydrophilic as polished glass and in some area that have been more heavily machined they may even be considered hydrophobic.

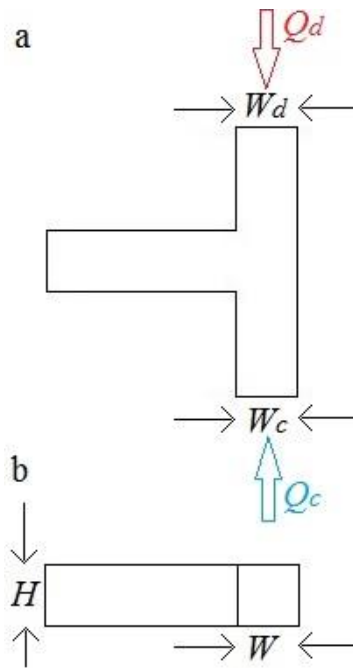


Figure 2.7. Geometry of the T-junction (a) top view and (b) side view.

The geometry of the opposed-flow T-junction used in this study is shown in Figure 2.7. Two inlet microchannels are arranged against each other head-to-head and the generated droplets at the junction pass through the main channel to the outlet; where W_c and W_d , the width of the continuous and dispersed channels, are equal to W ; H is the channel depth.

2.4 Working fluids

Different fluids have been used during the tests

- Pure distilled water (W)
- Water with surfactant (W+T)
- Silicone oil (SO)
- Xanthan gum aqueous solutions (XG)
- Xanthan gum aqueous solutions in which surfactant is added (XG+T)

The aqueous solutions containing either Tween 20 or Xanthan gum have been prepared for the maximum use of five days. Then the old samples were discarded and new solutions with similar concentrations were prepared.

Pure distilled water is obtained by using a fully-automatic cabinet water stills of all-glass construction with Pyrex borosilicate glass boiler and condenser and silica sheathed heating element (*Aquatron A4000D*) depicted in Figure 2.8.



Figure 2.8. Automatic cabinet water stills (*Aquatron A4000D*) for production of pure distilled water.

Xanthan gum (*Sigma Aldrich*) is an exocellular heteropolysaccharide produced by an aerobic submerged fermentation. Xanthan gum solutions are highly pseudoplastic due to the high-molecular weight molecule, which forms complex molecular aggregates through hydrogen bonds and polymer entanglement. Shear thinning pseudoplasticity results from disaggregation of this network and alignment of individual polymer molecules in the direction of shear force.

The physical properties of the working fluids play important roles on the droplet formation mechanism. An accurate measurement of fluid density, viscosity, surface and interfacial tension has been made for a complete characterization of the immiscible liquids.

2.4.1 Density measurement

The density of working fluids is measured by using an analytical balance (*RADWAG AS 220.R2*) and its specific kit (Figure 2.9) for liquid density measurement based on a double measurement of weight of a suspended sinker immersed in two different fluids, air and water.

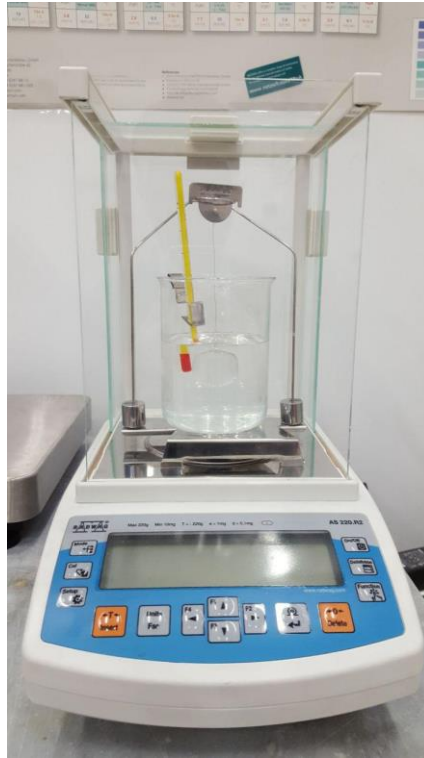


Figure 2.9. Analytical balance (RADWAG AS 220.R2) used for density measurements.

Table 2.1. Measured density of the working fluids.

Fluid		Density (kg/m ³)
Acronym	Fluid/Solution	
SO	Silicone Oil	950 ± 5.2
W	Pure Distilled Water	998 ± 0.9
W+T	Water + Tween 20	1001 ± 0.6
0.2 XG	0.2 wt% Xanthan gum solution	1000.5 ± 0.47
0.2 XG+T	0.2 wt% Xanthan gum solution + Tween 20	1003 ± 0.1
0.3 XG+T	0.3 wt% Xanthan gum solution + Tween 20	1004 ± 0.1
0.4 XG+T	0.4 wt% Xanthan gum solution + Tween 20	1004 ± 0.04
0.5 XG	0.5 wt% Xanthan gum solution	1001.9 ± 0.4
0.5 XG+T	0.5 wt% Xanthan gum solution + Tween 20	999 ± 3.3

For each liquid, the density is obtained as average of three measurements. In Table 2.1 the density values of the working fluids used in this work are shown; it is evident that the

density of the Xanthan gum solutions is very similar to the density of the pure distilled water due to the small concentrations of Xanthan gum considered. The same occurs for water with the addition of Tween 20. The measured density of silicone oil is in a good agreement with the value declared by the manufacturer.

2.4.2 Viscosity measurement

Silicone oil and water (with and without surfactant) can be considered as Newtonian fluids under the operative conditions of the experimental tests described in this work and their viscosity is independent of the shear rate. Viscosity of pure water, water with Tween 20 and silicone oil is measured at room temperature (23°C) by using appropriate Cannon-Fenske Viscometers (Figure 2.10).

The viscosity of each fluid, reported in Table 2.2 is obtained by averaging ten repeated measurements (at fixed room conditions). The measured values for pure fluids (water and silicone oil) confirm that the selected silicone oil is characterized by a viscosity twenty times larger than pure water viscosity.



Figure 2.10. The Cannon-Fenske Viscometer.

On the contrary, when Xanthan gum is added to pure water, the solution shows a typical pseudo-plastic behavior, i.e., viscosity tends to decrease with the increase of the shear rate. For these solutions, the dependence of the viscosity on the shear rate has been tested by using a viscometer with rotating discs able to measure fluid viscosity at given shear rates (*Brookfield DV-II +Pro*) (Figure 2.11).



Figure 2.11. Viscometer with rotating discs (*Brookfield DV-II +Pro*) used to measure the viscosity of non-Newtonian working fluids.

Table 2.2. The viscosity of Newtonian and non-Newtonian fluids.

Fluid	Viscosity (cP)		
	k	n	R^2
SO	18.07 ± 0.078	1.00	-
W	0.877 ± 0.002	1.00	-
W+T	1.009 ± 0.009	1.00	-
0.2 XG	861.15	0.38	0.999
0.2 XG+T	1152.6	0.337	0.999
0.3 XG+T	2562.4	0.269	0.999
0.4 XG+T	5186.8	0.21	0.999
0.5 XG	8493.5	0.18	0.999
0.5 XG+T	10530.2	0.162	1.000

When the Brookfield spindle-type viscometer is used for measuring the viscosity of Xanthan gum solutions, a different viscosity can be obtained if spindles are changed [91]. In order to eliminate these differences, by overlapping correctly the measures obtained with different spindles, a comparison with literature values of viscosity for aqueous solutions of 0.2 wt% and 0.5 wt% Xanthan gum concentrations, 0.2 XG and 0.5 XG, has been implemented [91]. The apparent viscosity of Xanthan gum solutions can be correlated to the shear rate by using the Carreau equation [92]:

$$\mu(\dot{\gamma}) = \mu_0 \left[1 + (\xi |\dot{\gamma}|)^2 \right]^{\frac{n-1}{2}} \quad (2-6)$$

where μ_0 is the zero (shear-rate) viscosity. The index n represents the degree of shear-thinning, while the time constant ξ indicates the onset of the shear-thinning behavior (higher time constant means a shear-thinning behavior shifted to lower shear rates and vice versa). In Equation (2-6) $\dot{\gamma}$ is the shear rate for a unidirectional flow and $|\dot{\gamma}|$ is the norm of the strain-rate tensor.

The result of the calibration is shown in Figure 2.12; a good agreement between the experimental results and the literature values can be observed for solutions in the range of shear rate ($\dot{\gamma}$) between 1 s^{-1} and 100 s^{-1} ; it is evident that in this range the viscosity of Xanthan gum solutions follows a power-law relationship, typical of shear thinning fluids.

The data reported in Table 2.2 highlight that the presence of 2 wt% of Tween 20 in pure water is able to increase the viscosity of 15% with respect to pure water but the behavior of the fluid is still Newtonian.

By using the Brookfield spindle-type viscometer, the apparent viscosity of Xanthan gum aqueous solutions with and without Tween 20 (2 wt%) is measured as a function of the imposed shear rate $\dot{\gamma}$ in the range 0.8 s^{-1} – 102 s^{-1} (Table 2.3). As confirmed by Figure 2.12, in the range of shear rate $\dot{\gamma}$ between 1 s^{-1} and 10^4 s^{-1} , the apparent viscosity of the Xanthan gum aqueous solutions can be correlated to the shear stress by means of the classical Ostwald-de Waele relationship:

$$\mu(\dot{\gamma}) = k|\dot{\gamma}|^{n-1} \quad (2-7)$$

The values of k and n obtained by applying Equation (2-7) to the experimental data are reported in Table 2.2; R^2 in Table 2.2 is the correlation coefficient.

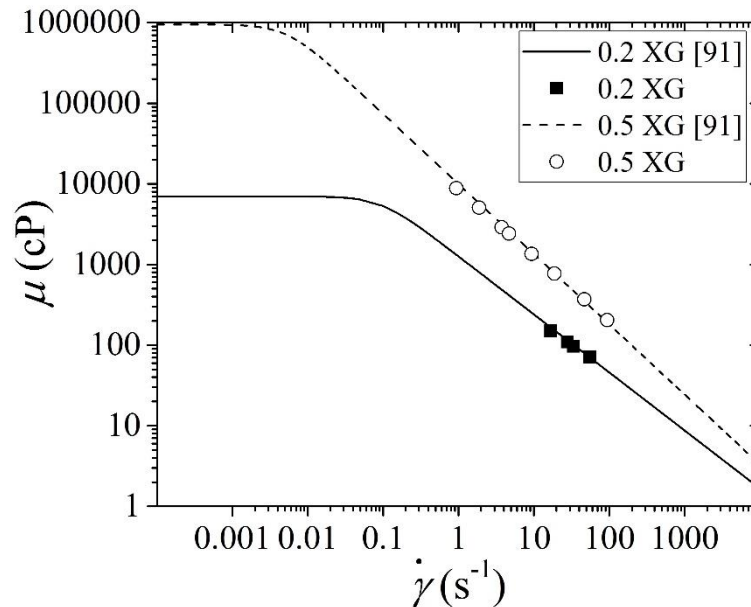


Figure 2.12. Comparison between experimental values of apparent viscosity of Xanthan gum aqueous solutions with 0.2 wt% and 0.5 wt% (0.2 XG and 0.5 XG) and the literature values reported in [91] for a liquid temperature of 23°C.

Table 2.3. Range of shear rate tested with the viscometer.

Fluid	$\dot{\gamma}$ range (s^{-1})
0.2 XG	16-56
0.2 XG+T	12-61
0.3 XG+T	1.8-71
0.4 XG+T	0.8-85
0.5 XG	0.9-94
0.5 XG+T	1-102

The viscosity of solutions in which Tween 20 is added to Xanthan gum (XG+T) exhibits

an increase with respect to the same solutions without surfactant (XG) variable from + 30% at low shear rates ($\cong 1\text{ s}^{-1}$) to + 10% at large shear rates ($\cong 100\text{ s}^{-1}$). This result confirms that the impact of the presence of a concentration equal to 2 wt% of Tween 20 on the viscosity is significant for both pure water (W+T) and Xanthan gum solutions (XG+T).

2.4.3 Surface and interfacial tension

The surface (σ_s) and interfacial (σ_i) tension of the working fluids used in this paper is measured by means of a force tensiometer (*KSV Sigma 700*) able to measure static surface and interfacial tension of liquids as shown in Figure 2.13 by pushing and pulling a platinum Du Noüy ring or a Wilhelmy plate. Corrective calculations for rings are automatically made on the experimental values via software using the model proposed by Huh and Mason [93].

The measured values are reported in Table 2.4. The interfacial tension is measured at the interface between the selected fluid and silicone oil. Each value is the average value of a ten-time repeated measurement.



Figure 2.13. Tensiometer (*KSV Sigma 700*) used for the determination of surface and interfacial tensions.

From the values in Table 2.4 it is clear the role played by Tween 20 in terms of reduction of the interfacial tension between water and Silicone oil; a concentration of 2 wt% of Tween 20 in water is able to reduce the interfacial tension of around six times. On the contrary, the

presence of Xanthan gum in water is not able to modify significantly either the interfacial or surface tension of the solutions.

Table 2.4. Surface tension (fluid/air) and Interfacial tension (fluid/silicone oil) of the working fluids.

Fluid	Surface tension fluid/air (mN/m)	Interfacial tension fluid/silicone oil (mN/m)
SO	19.30 ± 0.005	-
W	59.81 ± 0.19	42.44 ± 0.06
W+T	27.69 ± 0.38	7.697 ± 0.07
0.2 XG	59.79 ± 0.44	37.63 ± 1.49
0.2 XG+T	26.84 ± 0.29	8.767 ± 0.29
0.3 XG+T	26.43 ± 0.31	7.425 ± 0.38
0.4 XG+T	26.47 ± 0.71	7.391 ± 0.27
0.5 XG	55.10 ± 1.96	35.52 ± 2.06
0.5 XG+T	27.95 ± 0.12	6.452 ± 0.14

2.5 The effect of surfactant

In microfluidic systems, interfacial tension is found to have a dramatic effect on the multiphase flow phenomena due to dominance of the surface effects. Nonetheless, simply mixing oil and water in the absence of surfactant will not lead to the generation of stable emulsions and will revert to the two individual phases. Therefore introduction of emulsifiers such as surfactants, which reduces the interfacial tension and mixing energy, is a useful tool for generation of stable droplets; therefore the manipulation of interfacial tension is becoming a very interesting aspect in the trend of miniaturization [32]. The dynamic surfactant adsorption in the droplet formation influences the interfacial tension at the rupturing moment. In order to make the adsorption process shorter and weaker in a liquid-liquid system and to maintain the interfacial tension at minimum value, excessive amount of surfactant should be used.

The molecular structure of the surfactants shown in Figure 2.14 constitutes a hydrophilic head and a hydrophobic (lipophilic) tail which makes the selection of the proper emulsifier so vital. Appropriate surfactant may be included into the fluids to modify liquid-liquid interfacial

properties. Hydrophilic-Lipophilic Balance (HLB) value could be used to determine if a surfactant is hydrophobic or hydrophilic by the balance of the size and strength of the hydrophilic and hydrophobic parts in a surfactant molecule, respective affinity of the surfactant molecules for the water and the oil phases. Emulsifiers with high HLB values (more hydrophilic) may be used for encapsulation of oil plugs in water; on the contrary, surfactants with low HLB values (more hydrophobic) give W/O emulsions [32].

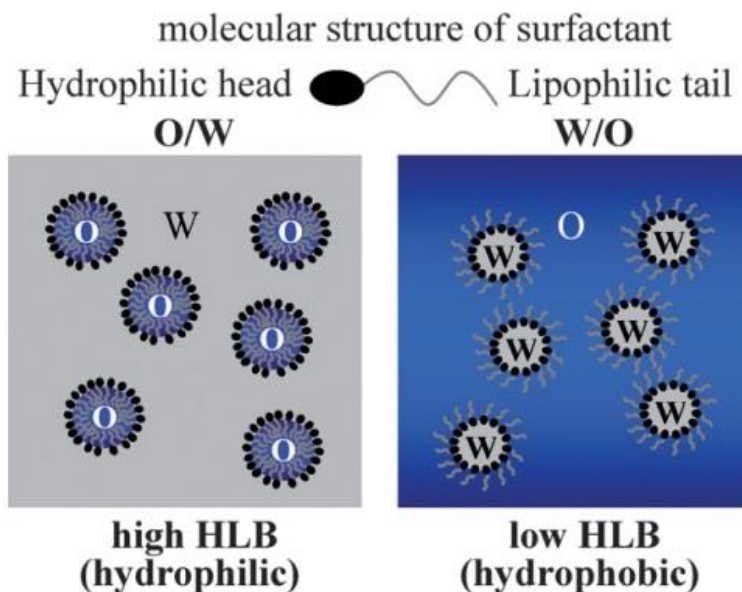


Figure 2.14. Molecular structure of the surfactant from Shui *et al.* [32].

The manipulation of surface wettability is a critical factor for droplet manipulation in microfluidic devices. The previous works have confirmed that surface wettability of fluids is crucial for two immiscible fluid flow in microfluidic devices [94-96]. The materials commonly used to fabricate microfluidic devices are oxide-covered silica and glass, natively hydrophilic, or PDMS which is normally hydrophobic. Nevertheless, only a few works have been reported on the effect of surfactants on oil-in-water microfluidics [97, 98]. The primary role in droplet formation is played by solid-liquid interfacial tension (σ_{sl}) and the modification of the liquid-liquid interfacial tension (σ_{ll}) by the use of surfactants has a secondary effect. Unlike macroscopic systems, σ_{sl} plays a dominant role, determining the emulsion type generated in microchannels, i.e. hydrophobic walls foster the water-in-oil (W/O) droplets but oil-in-water emulsions (O/W) may be generated in hydrophilic treated microchannels. The modification of solid-liquid interfacial tension is made possible by the use of either hydrophilic microchannels or hydrophobization of the same microchannels by silane molecules but fluid-fluid interfacial

tension is controlled by using different surfactants [32].

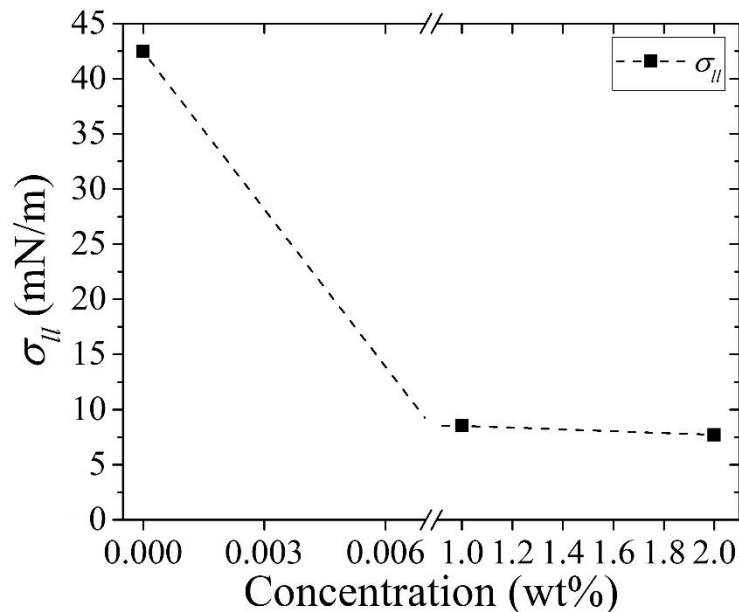


Figure 2.15. The interfacial tension of silicone oil and water with different percentages of Tween 20.

Tween 20 (miscible in water), as a hydrophilic surfactant (HLB = 16.7), is a non-ionic detergent widely used in biochemical applications. It has been used as an emulsifying agent for the preparation of stable (O/W) emulsions, so it has been solved in the carrier (water) fluid to make the generation of the oil plugs possible.

In Figure 2.15 it can be seen that the interfacial tension does not show a significant variation for the concentration of Tween 20 over CMC value (0.0074 wt%) [99]. By using concentrations of surfactants larger than CMC the interfacial tension becomes independent on the surfactant concentration. In the case of Tween 20 the interfacial tension between silicone oil and water can be considered equal to 8 mN/m (see Table 2.4) for concentrations larger than 0.0074 wt% (CMC value).

2.6 Processing of the images

A typical sequence of snapshots obtained from the high-speed camera is shown in Figure 2.16; these snapshots have been obtained by imposing a water volumetric flow rate of 0.8 ml/h and an oil volumetric flow rate equal to 1.6 ml/h.

Figure 2.16 shows the squeezing of the water liquid phase, followed by the breakup and

the formation of a water droplet in silicone oil flow, in a 15 snapshots with interval of 3 images, recorded with a frame rate 1500 fps. Each image has a resolution of 672×504 pixels and the time interval of the images is $3/1500$ s (= 2 ms). The snapshots are shown in a sequential order with the interval of three images; line by line from top to bottom, in each line from left to right. Figure 2.16 shows a high quality of the acquired images with droplet contours well defined and a level of illumination quite uniform in the whole field-of-view. The images allow recognizing with a good resolution the liquid/liquid interface as well as the solid walls of the cross-junction. The central area of the water droplet is characterized by light gray pixels but there is a dark zone around this region which puts in evidence the curved boundary of the droplet.

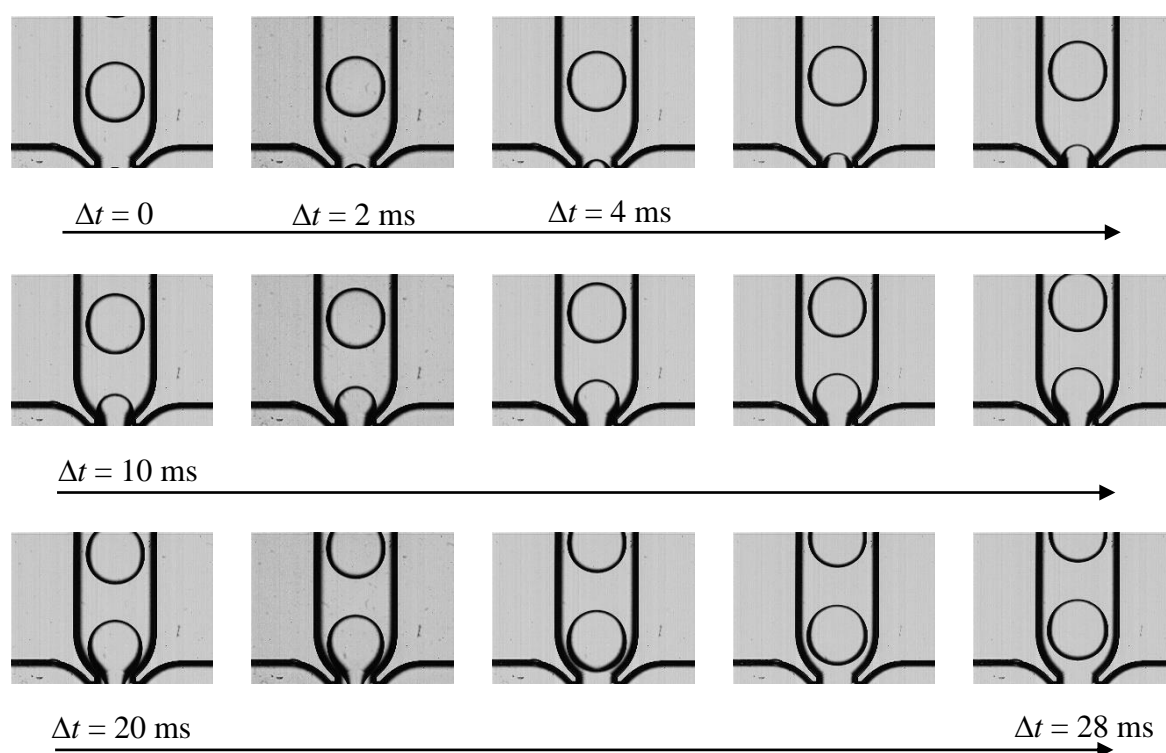


Figure 2.16. Sequence of raw images showing the squeezing and the breakup of water in oil (W/O) droplets obtained by imposing water (0.8 ml/h) and silicone oil (1.6 ml/h) volumetric flow rates.

2.6.1 Analysis of the images

The frames are analysed frame by frame by using an “in-house” MATLAB code for reconstruction of the main characteristics of the droplet interface. The weighted sum of raw image and the complement of the junction image without droplet is converted from RGB to a gray scale image. Then it is saturated to enhance the contrast between the pixels and transformed from gray to the binary format. All this process lets us employ Canny method to

detect the edge of the droplet. The process is explained in more detail as follows:

Figure 2.17a shows a raw image chosen for post-processing. The raw images are treated as numerical matrices having 672×504 elements in which each pixel is associated to a number in the range (0-256) which correspond to different gray levels of the pixel.

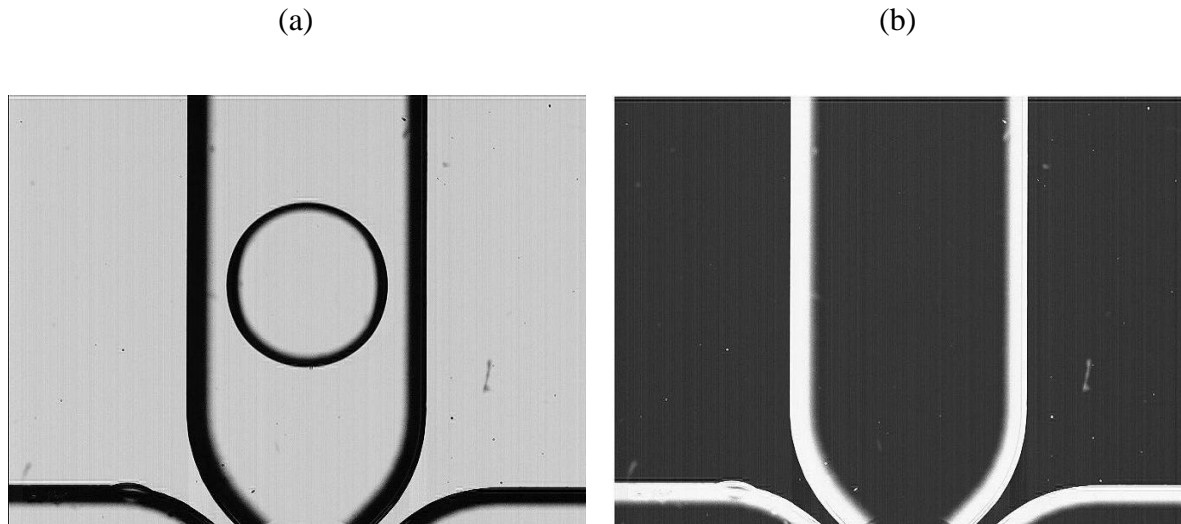


Figure 2.17. (a) Raw image of a droplet in a cross-junction ($Q_c = 1.6$ and $Q_d = 0.16$ ml/h) and (b) complement of the image of the junction without droplet.

In order to individuate the water-oil interface by avoiding any interference between the water-oil interface and the channel walls, the complement of an image of the junction (Figure 2.17b) is used with the aim to compute a characteristic threshold th for the image, which is a normalized intensity of the image, evaluated by means of the Otsu method [100]. By this method, the weighted sum of the variances of two classes of pixels in the image, the background and the foreground pixels, can be minimized.

The result is a characteristic threshold of the image that can be used for converting an intensity image to a binary image (by using *graythresh* function in MATLAB) and a threshold $th = 0.47$ has been evaluated. Then, it is possible to transform the intensity values of the gray scale into new values, in order to filter the gray levels and enhance the contrast between background and foreground pixels (by using *imadjust* function in MATLAB). The effect obtained by following this pre-processing procedure on the image shown in Figure 2.17a, is shown in Figure 2.18a. It is evident that the background contribution has been neutralized and in the processed images only the presence of the liquid/liquid interface is emphasized. Finally,

the obtained gray level maps can be converted into binary images by means of a new threshold, which for the image shown is $th = 0.7$, by using *im2bw* function in MATLAB. The binary images corresponding to the raw image is shown in Figure 2.18b.

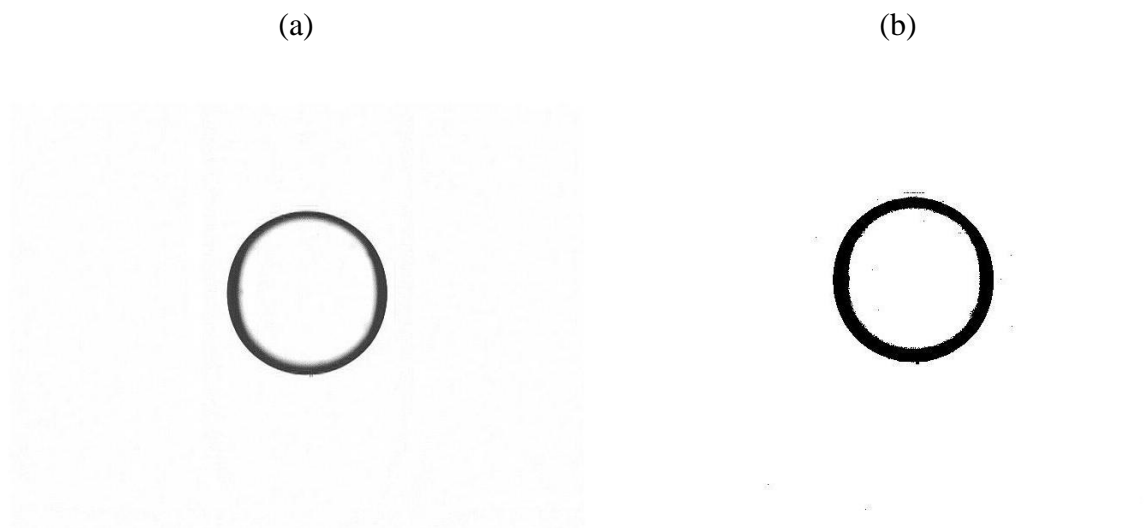


Figure 2.18. (a) Gray levels image and (b) binary image of the droplet.

2.6.2 Edge detection

It has been demonstrated that amongst different techniques available for detection of the edge of an image, Canny method [101] can offer some advantages in terms of compromise between accuracy and computational time.

By this technique, one can find edges by looking for local maximal of the gradient of the binary image. To smooth the image, a Gaussian filter is first applied to convolve with the image. Then, the method uses two thresholds, to detect strong and weak gradients and includes the weak ones in the output only if they are connected to strong gradients. This method is therefore less likely than others to be fooled by noise, and more likely to detect true weak edges.

The edges individuated by applying the Canny method to the binary image shown in Figure 2.18b are shown in Figure 2.19a. Then the domain occupied by the water phase can be reconstructed by filling the edges with the *imfill* function of MATLAB (Figure 2.19b).



Figure 2.19. (a) Edges extracted by Canny method and (b) reconstruction of the domain by filling it (dark zone).

2.6.3 Post-processing of the image

Now, it becomes possible to obtain the whole data about the droplets.

Starting from the oil/water contours, the area occupied by the aqueous phase, the perimeter of the water-oil interface and the coordinate of the center of mass of the droplet (by using the *bwboundaries* function of MATLAB). The center of mass (x_c, y_c) and also the velocity of the droplet can be calculated.

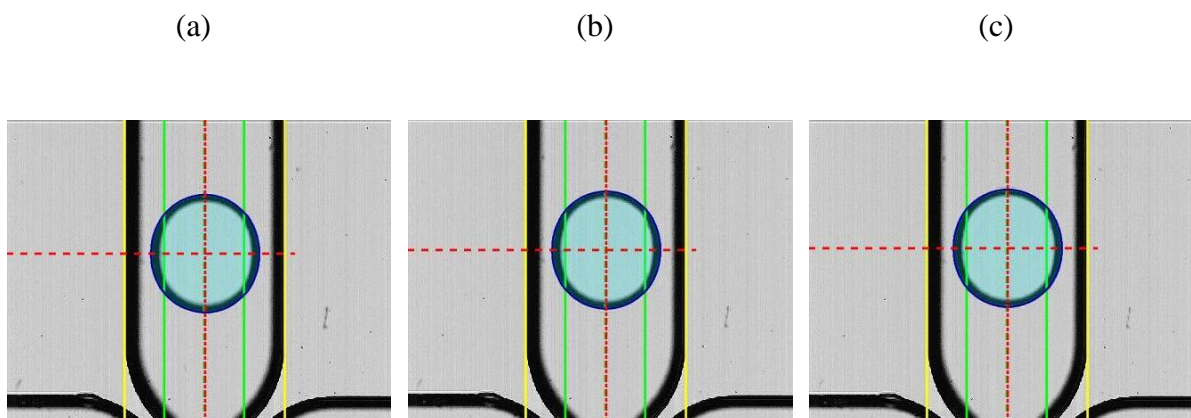


Figure 2.20. Determination of the droplet center for three consecutive snapshots.

Figure 2.20 shows the position of the coordinate for the center of the droplet (red lines)

obtained for three consecutive snapshots. The yellow lines show the position of channel walls within the junction. Considering the first two snapshots, we can obtain the velocity of the droplet by considering the displacement of the center of mass along the y -axis and the time interval between two consecutive images ($u = (y_c(2) - y_c(1))/dt$); here $dt = 1/1500$ s.

This evaluation can be repeated by considering different couple of images (i.e. in Figure 2.20, the evaluation of the droplet velocity can be obtained by considering the images 1-2, or 2-3) in order to obtain an average value of velocity for the droplet.

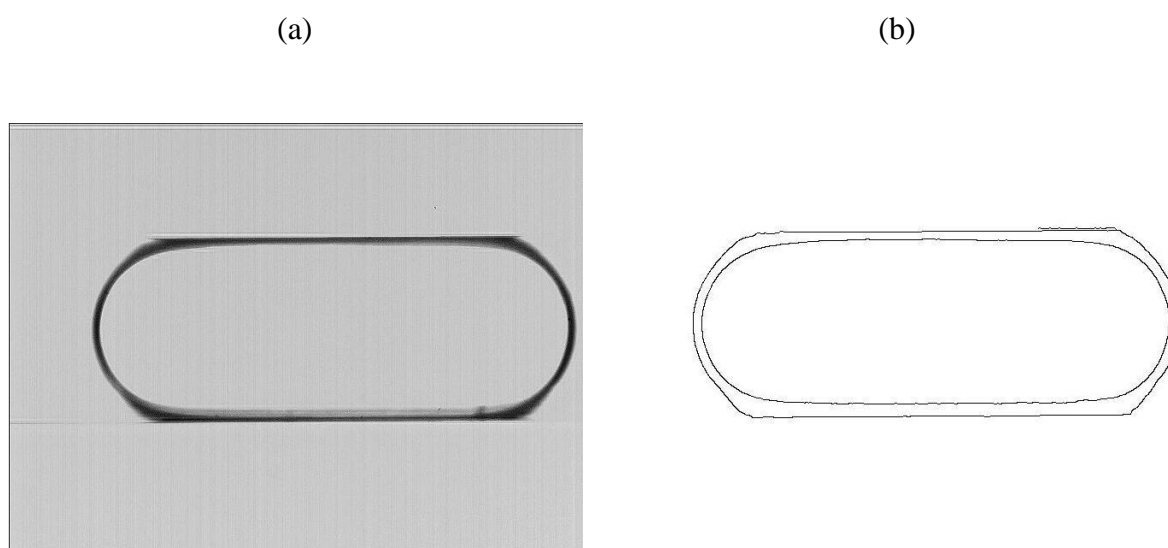


Figure 2.21. (a) Raw image and (b) edge of the droplet for the micro T-junction.

The post-processing method by MATLAB code may also be applied for plugs generated in micro T-junction. The detected edge of the microdroplets generated in T-junction is depicted in Figure 2.21b.

2.6.4 Neck detection

Despite some early work [17, 102, 103], the breakup mechanism has received little attention and flow-focusing devices have been vastly utilized to generate emulsions without scrutinizing the mechanism completed in rupturing moment of the water-oil interface. A MATLAB code has been developed to calculate the minimum width of the thread before the breakup. In Figure 2.22 the process of detecting the width has been illustrated very briefly. More detail are presented in the above Section (2.6.1) where droplet characteristics are

discussed.

Figure 2.22a shows the border in red color around the region where the minimum width happens. The cropped and focused image is presented in Figure 2.22b while the saturated grayscale of the image (Figure 2.22c) has been converted to the binary format (Figure 2.22d) and the edge of the thread could be obtained by Canny method (Figure 2.22e).

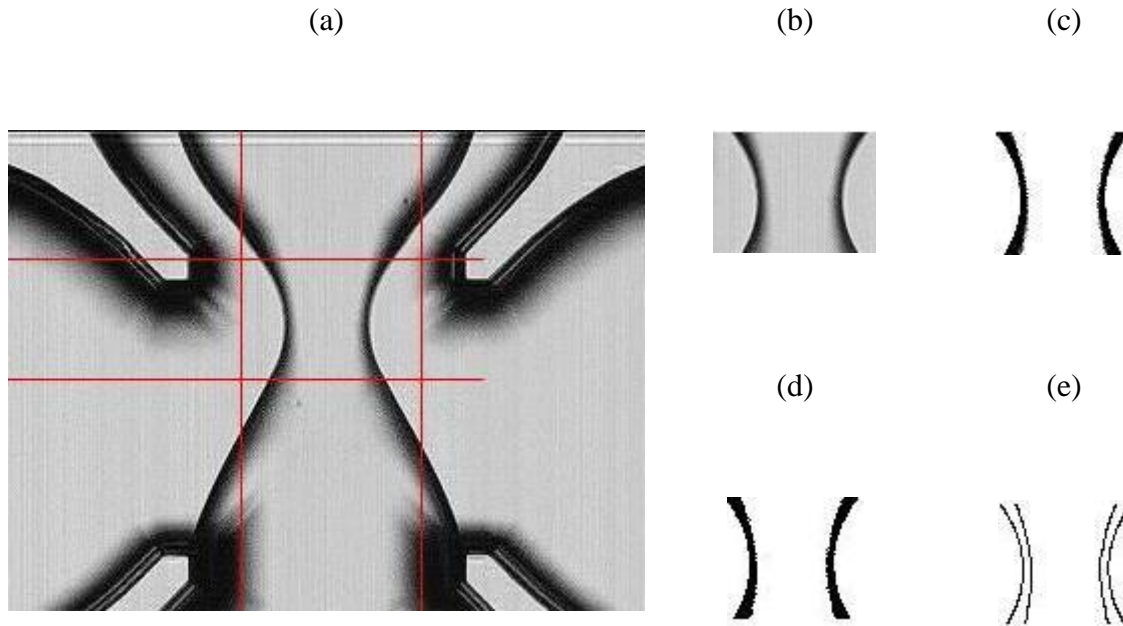


Figure 2.22. The detection of minimum width when $Ca_c = 0.0081$, $\alpha = 0.5$ and $t = -0.4$; (a) raw image with window borders in red, (b) cropped image, (c) saturated image, (d) binary image and (e) the edge of the thread by Canny method.

2.6.5 Droplet size

From the post-processing of the raw droplet images, the evolution of the liquid-liquid interface is detected. Once reconstructed the droplet contour, the average value of the non-dimensional diameter of the droplets (D^*) has been calculated, by considering the N droplets observed in a given experiment, as follows:

$$D^* = \frac{1}{N} \sum_i D_i^* = \frac{1}{N} \sum_i \frac{\sqrt{D_{h,i} D_{v,i}}}{H} \quad (2-8)$$

where $D_{h,i}$ and $D_{v,i}$ are the horizontal and vertical diameters of the i -th droplet extracted by the

images of the droplet interfaces and H is the height of the microchannel. In other words, the mean diameter of the droplet has been defined as the square root of the multiplication of horizontal and vertical diameter values and non-dimensionalized by the depth of the channel. Unlike the cases in which the mean diameter is lower than the channel depth $D^* < 1$, the droplet may not be assumed spherical anymore and the plug confined by the channel top and bottom walls take the form of either ellipse or a flattened disk when $D^* > 1$.

For the droplets generated in micro T-junction non-dimensional length of the plug (\bar{L}) has been calculated in the form of:

$$\bar{L} = \frac{1}{N} \sum_i^N \bar{L}_i = \frac{1}{N} \sum_i^N \frac{L_i}{H} \quad (2-9)$$

where L_i is the length of the i -th plug generated in micro T-junction.

2.6.5.1 Polydispersity

The standard deviation of the non-dimensional diameter associated to the N droplets is scaled on D^* in order to obtain the droplet polydispersity:

$$Pl = \frac{1}{D^*} \sqrt{\frac{\sum_i^N (D_i^* - D^*)^2}{N-1}} \quad (2-10)$$

The formulation of the polydispersity for the plugs in micro T-junction has the same format (Equation (2-10)) but the non-dimensional length \bar{L} should be replaced by D^* .

2.7 Uncertainty

One of the most important aspects in any kind of research is to have an extensive knowledge of the possibilities as well as limitations. In experimental investigations, the uncertainty linked to the experimental test rig is based upon the quality and the precision of the device available at the lab.

The uncertainty of the imposed volumetric flow rate exerted by the syringe pumps is

equal to $\pm 0.5\%$ for the *Cole-Parmer Version Hills* and $\pm 0.35\%$ for the *Harvard Apparatus PHD 4400 Programmable* based on declared accuracy of the manufacturer in the datasheet.

The ability to generate the uniform cross-section along the microchannel and right-angle sidewalls is a substantial task. In order to have the microchannels with the maximum precision and minimum surface roughness, the commercial microchannels have been purchased to study in this thesis. The channels employed in the current study have been manufactured by laser beam machining with the high quality as compared to the milling machine (*Roland MDX-40*) available at the lab. The geometrical dimensions of the junctions have been checked by means of SEM; an uncertainty of $\pm 1\%$ can be assumed. The surface roughness of the channels is less than one micron.

To estimate the typical uncertainty of non-dimensional size of the droplet, a comparison over the duration of the experiment between the mass of the dispersed-phase liquid injected by the syringe pump and the mass contained in the produced droplets is made. The difference in terms of mass obtained by this comparison can be translated in a difference in terms of droplet dimensions by obtaining that the estimated uncertainty on the droplet diameter is of the order of $\pm 1\text{-}3\ \mu\text{m}$.

To measure the physical properties of the working fluids, the accurate devices have been used and based upon the calculations, the typical uncertainty on the values of the measured fluid properties (viscosity, density and interface tension) are indicated in Table 2.1, Table 2.2 and Table 2.4.

The uncertainty in the evaluation of the Capillary number can be estimated, following Moffat [104], starting from the uncertainty associated with the measurement of the single parameters involved in the definition of Ca . The uncertainty associated with the measurement of the interfacial tension between the fluid and the silicone oil has the largest weight in the total uncertainty. In the present tests the uncertainty on Ca_c is estimated to be around $\pm 5.3\%$.

Chapter 3

Experimental Investigation of Droplet Formation at

Micro Cross-Junctions

In this chapter the experimental investigation of the droplet production by means of a micro cross-junction is described. In order to study the effect of the rheological properties of the dispersed phase, of the interface tension values between dispersed and continuous phase, of the junction geometry on the droplet formation regime, more than 400 experimental runs have been made by varying:

- The immiscible liquids used as continuous and dispersed phase by introducing surfactants and considering both Newtonian and shear thinning non-Newtonian dispersed phases;
- The geometry of the micro cross-junction.

Different ranges of volumetric flow rates have been imposed at the inlets of the cross-section as a function of the immiscible liquids considered. In Table 3.1 the range of the dispersed flow rate and the continuous flow rate is reported as a function of the liquids considered as continuous and dispersed phases. By considering the definition of the volumetric flow rate ratio (α) given in Equation (1-3) and of Capillary number (see Equation (1-2)) the experimental tests were able to cover the ranges of α and Ca_c shown in Table 3.1.

Table 3.1. Range of volumetric flow rates α and Ca_c tested during the experimental runs.

CP	DP			
	W	W+T	0.3 XG+T	0.5 XG+T
SO	$0.016 < Q_d < 59.2$	$0.01 < Q_d < 8$	$0.01 < Q_d < 3$	$0.01 < Q_d < 3$
	$0.8 < Q_c < 49.9$	$0.3 < Q_c < 15$	$0.3 < Q_c < 20$	$0.3 < Q_c < 15$
	$16E-4 < Ca_c < 1E-1$	$3E-3 < Ca_c < 16E-2$	$3E-3 < Ca_c < 23E-2$	$4E-3 < Ca_c < 2E-1$
	$0.01 < \alpha < 39$	$0.01 < \alpha < 25$	$0.01 < \alpha < 3$	$0.01 < \alpha < 1.9$

The commercial glass micro cross-junctions #1 described in Chapter 2 (see Figure 2.5) is initially considered for the experimental runs.

A hydrophobic coating has been applied on the inner walls of the junction. The cross-junction is characterized by a cross-section restriction at the junction in which the width of the channel varies along the junction (Figure 2.6). As detailed described in Chapter 2 (Section 2.3.1) the width of the channel far from the junction (W_w) is equal to 390 μm ; on the contrary, the width is gradually reduced at the junction (W_j) down to 195 μm with a *restriction ratio* $R = W_j/W_w$, equal to 0.5. The height (H) of the channels is uniform and equal to $H = 190$ μm . The *aspect ratio* of the microchannels (i.e. ratio between the channel height and width) A is equal to 0.97 at the junction and $A_w = 0.49$ far from the junction.

In Table 3.2 the main geometrical characteristics of junction #1 are summarized.

Table 3.2. Geometrical characteristics of the junction #1.

Characteristics	Junction #1
W_j (μm)	195
W_w (μm)	390
H (μm)	190
$R = W_j/W_w$	0.5
$A_j = H/W_j$	0.97
$A_w = H/W_w$	0.49

As continuous phase, silicone oil (Sigma Aldrich; $\nu = 20$ cSt, $\rho = 0.95$ g/ml @ 25 °C) is considered. On the contrary, as indicated in Table 1, deionized pure water without (W) and with the addition of Tween 20 (W+T) as well as aqueous Xanthan gum solutions with a variable concentration in weight between 0.2% and 0.5% with the addition of Tween 20 (XG+T) are considered as dispersed phase. All the properties of these liquids have been accurately measured and a detailed discussion about their characterization is reported in Chapter 2 (see Section 2.4).

3.1 Newtonian and non-Newtonian emulsions at low values of Ca_c

In the first stage of this work the attention is focused on the performance of the cross-junction as generator of monodispersed emulsions by operating at values of the Capillary number linked to the continuous phase lower than 0.02. This value of Ca_c is indicated by many authors as a natural boundary for the use of the droplet generator at low continuous flow rates [45, 46].

At $Ca_c < 0.01$ droplet formation can be obtained only by means of two mechanisms: squeezing and dripping. Typically, squeezing is obtained by using the droplet generator at low values of the volumetric flow ratio and dripping starts only when α is increased. In case of dripping, the droplet breakup generally occurs far from the center of the junction. For this reason, Liu and Zhang [39] proposed to distinguish the droplet mechanisms at low Ca_c on the basis of the position in correspondence of which the droplet breakup occurs with respect the center of the junction. Two regimes can be individuated as DJ (droplets formed at the Junction) and DC (droplet detached out of the junction). In addition to these two droplet regimes, for very large values of a parallel flow can occur; in this case no droplet formation is possible and the continuous and dispersed phases co-flow through the outlet microchannel.

In Figure 3.1 the typical droplet regimes described before, obtained by changing the volumetric flow rate of the dispersed phase (0.5 XG+T) Q_d from 0.01 to 3 ml/h for a fixed value of volumetric flow rate of the continuous phase (SO) $Q_c = 1.5$ ml/h are shown.

When low values of the volumetric flow rate of the continuous phase (silicone oil) are imposed at the entrance of the lateral arms of the cross-junction, the interfacial tension between the dispersed and the continuous phase is predominant on the viscous forces. As observed from

the numerical simulations of Liu and Zhang [39] at low values of flow rate ratio (α), droplets are usually formed at the center of the cross-junction (DJ regime) thanks to the squeezing mechanism.

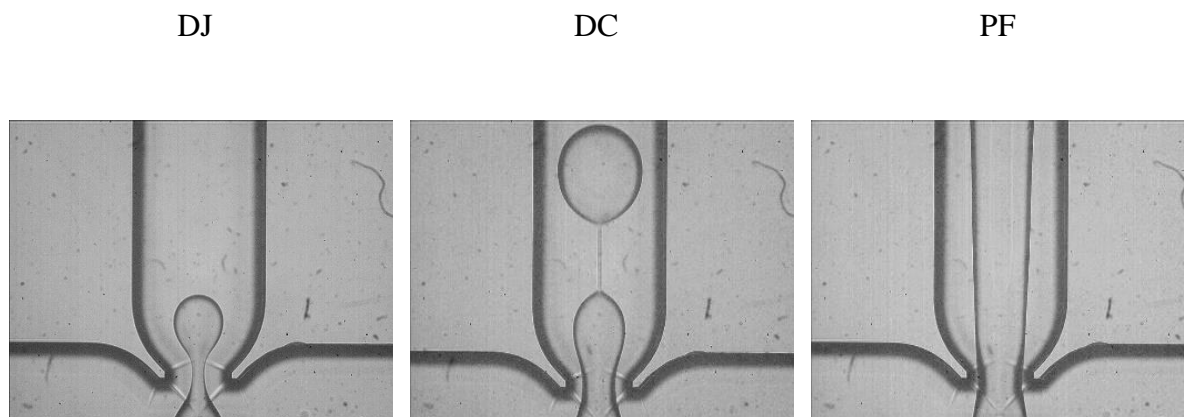


Figure 3.1. Droplet formation mechanisms for 0.5 XG+T as dispersed phase and silicone oil as continuous phase by fixing $Q_c = 1.5$ ml/h and by increasing $Q_d = 0.015, 0.2$ and 1.5 ml/h, respectively.

When α is increased, droplets are found to pinch-off downstream of the channel (DC regime) forming a thread that becomes unstable after a distance of laminar flow. This distance tends to increase with α and by moving from Newtonian to non-Newtonian dispersed flows. When α is larger than a critical value (α_{cr}), a stable parallel flow is observed where the three incoming streams co-flow in parallel to the downstream without pinching (PF regime). At low values of Capillary number the droplet detachment point is located at the center of the junction (DJ regime). In this case, the interfacial stresses dominate the drag forces. An increase of the dispersed volumetric flow rate (by fixing the continuous flow rate) causes a shift of the droplet detachment point to the downstream of the junction (DC regime) with the presence of an incoming thread which fills the full width of the central channel. If the volumetric flow rate of the dispersed phase is still increased above a critical value, the droplet formation is stopped and a stable co-flow appears downstream of the junction (PF regime). In order to better understand the role of the fluid properties of the dispersed phase on the interface evolution and on the droplet formation mechanisms, in Figure 3.2, the droplet regimes obtained by imposing a volumetric flow rate of silicone oil equal to 4 ml/h and 1 ml/h in combination with an incoming stream of pure water (W) or water with the addition of 0.5 wt% of Xanthan gum and 2 wt% Tween 20 (0.5 XG+T) are shown.

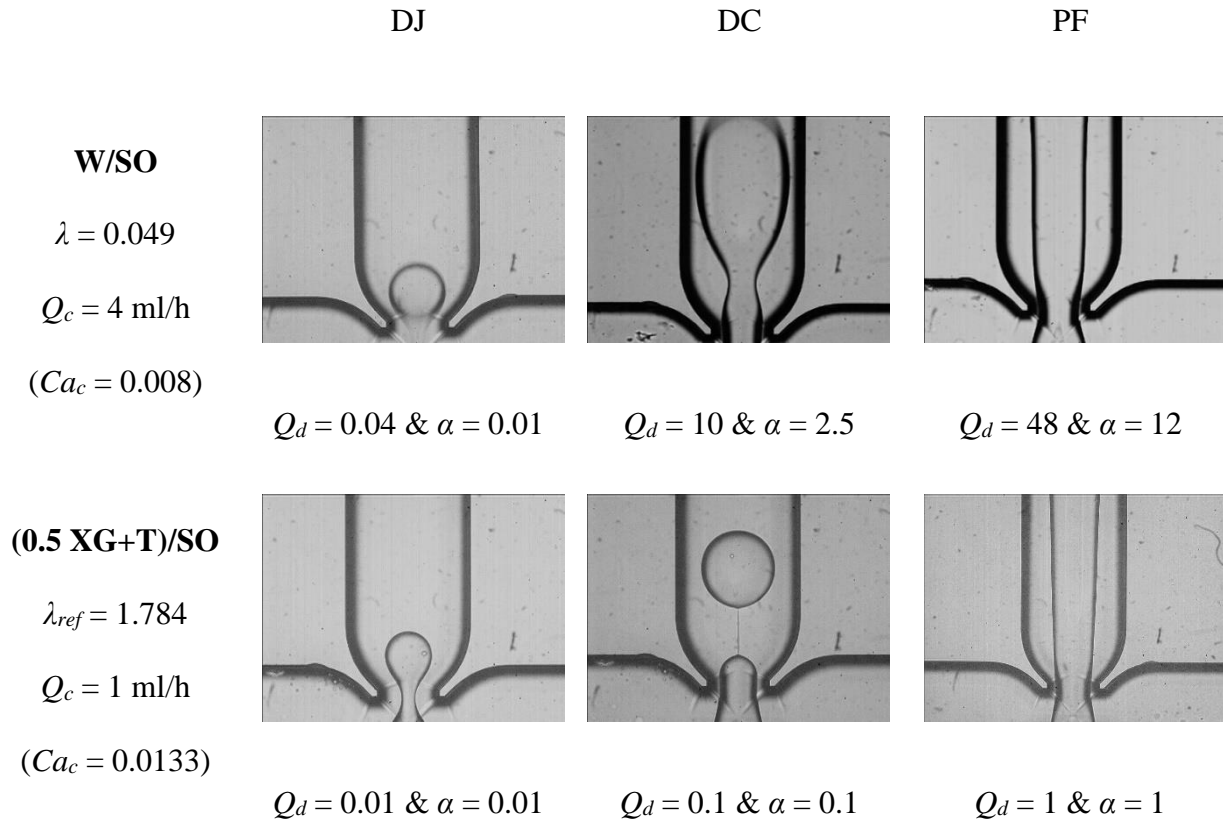


Figure 3.2. Comparison between the droplet regimes obtained by using a Newtonian (W) and a non-Newtonian (0.5 XG+T) dispersed phase in combination with silicone oil as continuous phase by increasing α at similar Capillary number Ca_c .

By comparing the images of Figure 3.2, it is possible to observe that when pure water is used as the dispersed phase, the threads formed in DJ and DC regime are typically very short and thick if compared with the typical threads formed when a Xanthan gum aqueous solution is used. In the latter case, pure observation reveals that long and thin threads are generally formed before the detachment of the droplet. This thread is generated by the force balance between the viscous drag that the continuous fluid makes on the droplet and the interfacial forces which oppose the elongation of the neck. Long threads are generally obtained by increasing the viscous drag (i.e. by increasing the volumetric flow rate of the continuous phase) and/or reducing the interfacial forces (i.e. by reducing the interfacial tensions between the immiscible liquids).

By comparing the values of Q_c and Q_d coupled to each image of Figure 3.2, it can be observed that an increase of the viscosity ratio λ determines a decrease of the value of the flow rate ratio (α) in correspondence of which the transition from a droplet regime to another one

occurs. More in detail, with Xanthan gum aqueous solution and silicone oil (high λ values, see Table 2.2), by imposing a value of $\alpha = 0.01$ droplets are formed at the cross-junction (DJ regime); for $\alpha = 0.1$ droplets are pinched-off downstream of the cross-junction (DC regime) and for $\alpha = 1$ the critical value of α is exceeded and no droplets are formed at all (PF regime). On the contrary, if water (low $\lambda = 0.049$) is used as dispersed phase with silicone oil as continuous phase, α_{cr} value increases up to 12 and the droplet breakup is moved far from the centre of the cross-junction (DC) when α is 2.5.

As rule of thumbs, a decrease of the viscosity ratio of the immiscible liquids introduced in the junction increases the values of α in correspondence of which the transition between DJ, DC and PF is observed.

In Figure 3.3 the droplet regimes as a function of the flow rate ratio α and of the Capillary number Ca_c are shown for silicone oil as the continuous phase and pure water (W) (Figure 3.3a), water with Tween 20 (W+T) (Figure 3.3b) and two Xanthan gum aqueous solutions (0.3 XG+T in Figure 3.3c and 0.5 XG+T in Figure 3.3d) as the dispersed phase. These results are obtained by varying the continuous volumetric flow rate of silicone oil from 0.5 to 4.9 ml/h ($0.0016 \leq Ca_c \leq 0.02$) and the volumetric flow rate of the dispersed phase from 0.01 to 49 ml/h.

At fixed values of Ca_c , an increase of α leads to the transition from one regime to another one. The droplet maps shown in Figure 3.3 highlight the influence of α on the transition between the regimes. Increasing Ca_c , especially at low Capillary numbers, helps the transition to occur in correspondence of lower values of α due to the higher and stronger continuous flow rate Q_c which makes the droplet to be generated earlier.

The shear force plays a more important role with the increase of the flow rates and becomes the main force responsible of the droplet breakup when dripping starts.

By observing Figure 3.3 it is evident that the critical value of α (α_{cr}) in correspondence of which the droplets production is stopped is around $\alpha_{cr} = 10$ for W (Figure 3.3a) and W+T (Figure 3.3b) and $\alpha_{cr} = 1$ for 0.3 XG+T and 0.5 XG+T (see Figure 3.3c and d).

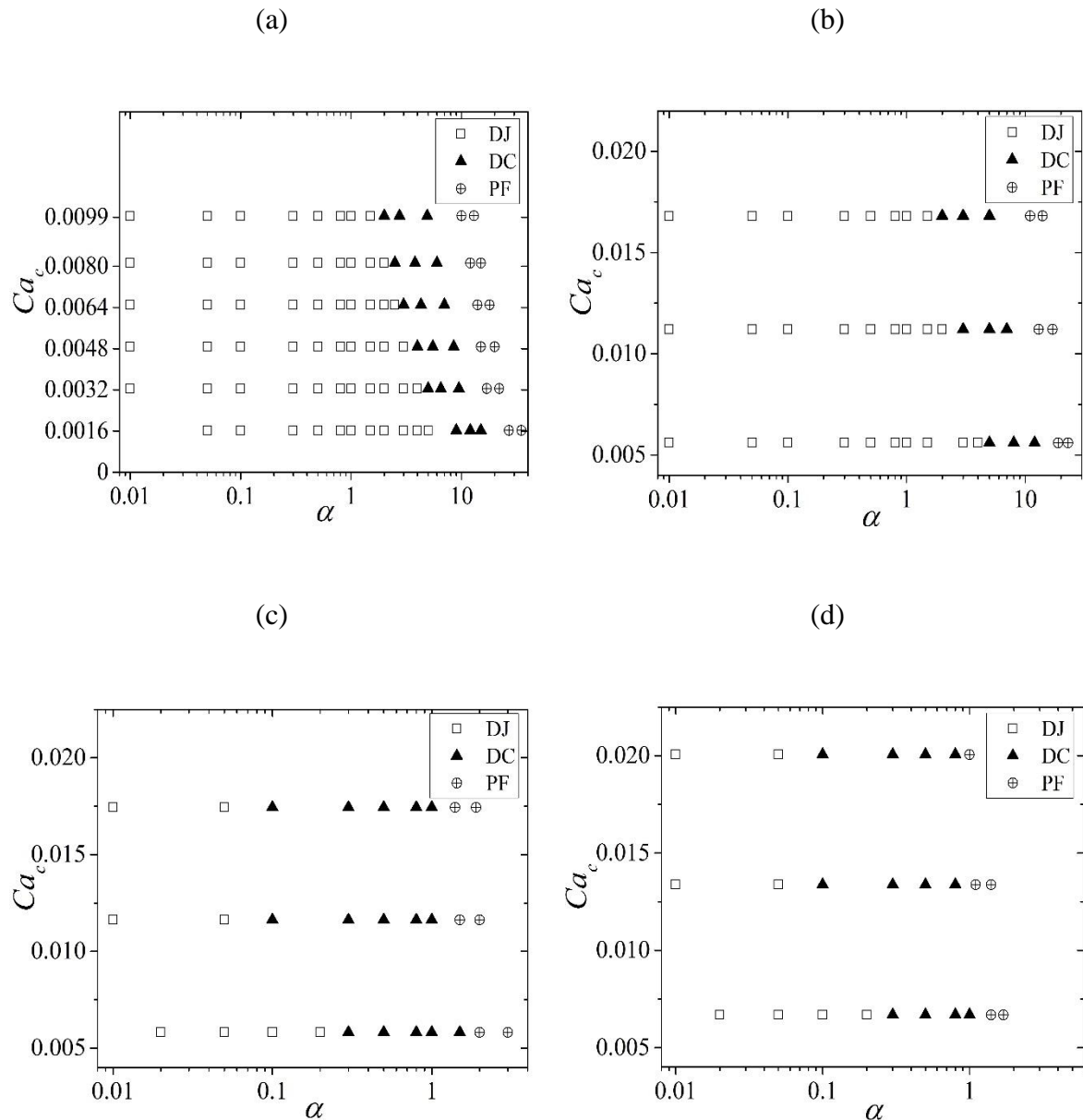


Figure 3.3. Droplet flow maps as a function of flow rate ratio α ; (a) W, (b) W+T, (c) 0.3 XG+T and (d) 0.5 XG+T.

No significant difference between the non-Newtonian flow maps may be seen although the concentrations of Xanthan gum solution varies from 0.3 to 0.5 wt%. It can be interesting to observe that the concentration of Xanthan gum changes in a significant way the viscosity of the solution (see the viscosity values reported in Table 2.2). The small difference between the droplet regimes observed by considering 0.3 XG+T and 0.5 XG+T seems to confirm that the viscosity of the dispersed phase is not able to play an important role on the droplet formation at low Capillary numbers.

By comparing Figure 3.3a and b, the role of the surfactant on the droplet regime at low Ca_c can be highlighted; Tween 20 reduces the interfacial tension between water and silicone oil without to change significantly the viscosity ratio λ . A slight decrease of the values of α linked to the transitions between DJ, DC and PF regimes can be observed because the reduction of the interfacial tension due to the presence of surfactant promotes the displacement of the droplet downstream of the junction by reducing the area linked to the DJ regime in Figure 3.3.

When Xanthan gum aqueous solutions (XG+T) are used, the immiscible liquids are characterized by higher values of the viscosity ratio λ (see Table 2.2) with respect to W and W+T; on the contrary, Xanthan gum aqueous solutions are characterized by values of interfacial tensions similar to those of W+T (see Table 2.4). Figure 3.3c and d underline that in presence of non-Newtonian solutions the transition between the droplet regimes occurs at lower values of the flow rate ratio. In the case of shear thinning non-Newtonian fluids used as dispersed phase, the droplet formation tends to occur downstream of the junction with the creation of a long thread between the nozzle and the droplet even at low Ca_c values. For this reason the area in Figure 3.3 in which DJ regime is observed is strongly reduced.

Moreover, by comparing Figure 3.3c and d it is possible to conclude that the droplet flow maps obtained for two concentrations of Xanthan gum, 0.3 XG+T and 0.5 XG+T, do not show a significant difference even if the dispersed phases are characterized by different values of the apparent viscosity. The small difference between these two non-Newtonian fluids in terms of droplet regimes confirm that the viscosity of the dispersed phase has a weak effect on the drag force. In addition, it is possible to observe that for the non-Newtonian solutions Ca_c influences the transition between the droplet regimes only for values of Ca_c lower than 0.01.

3.1.1 Effect of Ca_c and α

In Figure 3.4 the non-dimensional diameter D^* of the droplets, defined by Equation (2-8), generated by using the cross-junction has been plotted as a function of the imposed flow rate ratio α , for fixed values of Ca_c , by using pure water (W) or water with Tween 20 (W+T) (Figure 3.4a) or two Xanthan gum aqueous solutions (0.3 XG+T and 0.5 XG+T) as dispersed phase (Figure 3.4b).

For both Newtonian and non-Newtonian dispersed phase the droplet dimensions tend to increase with α , in agreement with the observations made by Garstecki *et al.* [41]. It is also

evident that, moving from DJ to DC regime, the slope of D^* as a function of α increases: this means that the dimensions of the droplets are more sensible to a variation of the flow rate ratio in DC regime than in DJ regime. The value of the dimensionless droplet diameter is around 1 in DJ regime and larger than 1 in DC regime. By increasing Ca_c , the droplet dimensions are reduced due to the increase of the continuous flow rate which causes the drop to be pinched-off earlier. This means that at low values of α (DJ regime) it is possible to obtain droplets with dimensions lower than the height of the junction ($D^* < 1$) by increasing Ca_c . On the contrary, for a fixed value of Ca_c , the larger values of α , the larger droplets can be obtained ($D^* > 1$). By comparing Figure 3.4a and b it is evident that when Xanthan gum solutions are used as dispersed phase, the droplet dimensions are usually smaller than those obtained with W and W+T.

The change of the slope of the function $D^*(\alpha)$ is linked to the transition between DJ and DC droplet regime and it occurs for W and W+T at values of α larger than 1, coherently with Figure 3.3a and b; on the contrary, for Xanthan gum solutions the transition occurs close to $\alpha = 0.1$, in agreement with Figure 3.3c and d.

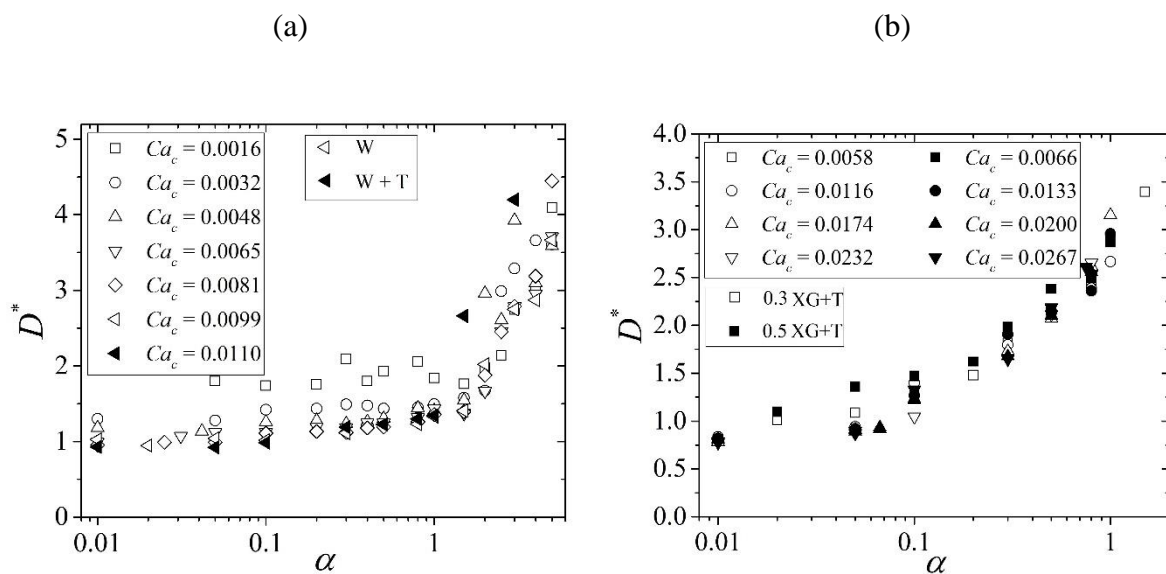


Figure 3.4. Non-dimensional diameter D^* of the droplets for; (a) W and W+T and (b) 0.3 XG+T and 0.5 XG+T in a continuous flow of silicone oil as a function of the flow rate ratio.

By comparing Figure 3.4a and b it is evident that the change of slope during the transition between the DJ and DC regime is abrupt for Newtonian dispersed phases and more gradual for non-Newtonian fluids. This fact is due to the capability of the shear thinning fluids to reduce

their viscosity when the shear rate increases; with these fluids, the action of the continuous phase on the dispersed phase changes during the droplet growing thanks to the reduction of the fluid viscosity and the variable viscous reaction of the dispersed phase is responsible of this smooth transition between droplet regimes. From Figure 3.4b it is possible to highlight that the concentration of Xanthan gum has a minor influence on the droplet dimensions.

In presence of a non-Newtonian dispersed phase and high values of the viscous ratio λ the droplet pinch-off is always associated to the presence of a thin thread between the dispersed bulk flow and the growing droplet (see Figure 3.2). At low values of Ca_c , the drag force exerted by the continuous phase on the droplet is negligible and the dynamics of the droplet generation is governed by a balance between pressure and interfacial tension. Xanthan gum solutions with surfactant (XG+T) are characterized by reduced values of the interfacial tension with respect to pure water (W) and this boosts the droplet breakup.

3.1.2 Analysis of the drop diameter for low α

In this subsection a spotlight on the dependence of D^* as a function of Ca_c and α for low values of α (< 1) is done by considering pure water as dispersed phase in a silicone oil continuous flow. Under these conditions the droplet formation is essentially due to squeezing and the droplet formation occurs at the junction (DJ regime).

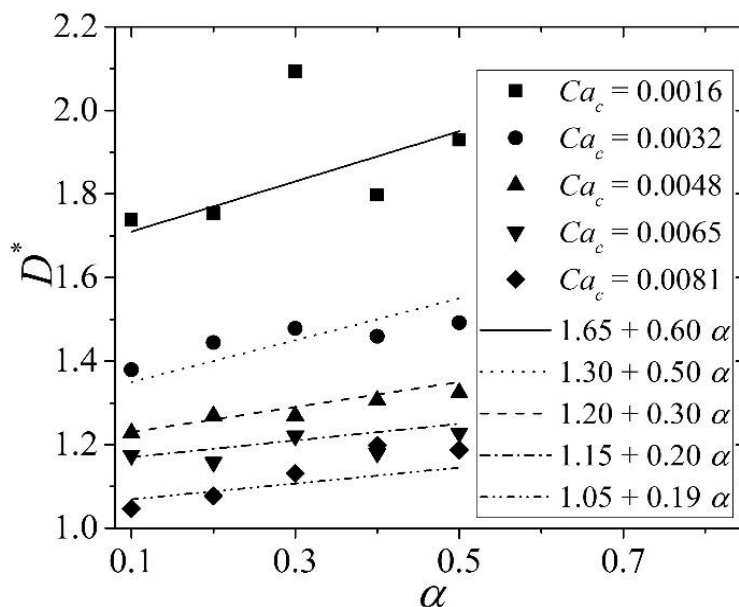


Figure 3.5. Dimensionless droplet diameter as a function of flow rate ratio α .

As observed previously, in DJ regime the droplet formation is mainly affected by the flow rate ratio [41] and longer droplets can be obtained by using larger α . However, the variation of D^* with α is limited when α is lower than 1, if compared with the variation which occurs for larger α (DC regime, dripping regime).

Figure 3.5 demonstrates that D^* depends also on Ca_c for a fixed value of α . It should be noted that in the cases of low values of Ca_c , the slope of the fitted curves on the experimental data in Figure 3.5 is higher, so the rate of the enhancement in terms of D^* is amplified when α is increased. The higher Ca_c , the less influence of Q_d may be seen; the droplet is pinched off earlier due to the high continuous flow rates. In this case the droplet formation time is reduced and the droplet is generated earlier; this result suggests that the effect of Q_d on the droplet volume through the formation time cannot be ignored at low continuous flow rates. As explained above, both Q_d and Q_c play undeniable roles in the size of the final droplet (Figure 3.5) and the data of Figure 3.5 highlight that the droplet volume is influenced by the flow rates of both fluids and not only by α as indicated in literature for squeezing regime [39, 42, 44]. Some numerical simulation seems to confirm this experimental observation.

It is evident that the dimensionless diameter of the droplets increases with α . In Figure 3.5 a linear trend ($D^* = \varepsilon + \omega\alpha$) of the experimental data can be observed; here, ε and ω are two fitting constants which depend on the channel geometry [44], as well on Ca_c . This fact is in disagreement with the simple squeezing model proposed by Garstecki *et al.* [41] which can be considered only an approximation of the real data in which the role of Ca_c is disregarded.

Since it is clear that the non-dimensional diameter of the droplet D^* is a function of both flow rates and not only of α , the dependence of D^* on Ca_c has been examined in Figure 3.6. It is possible to observe that the experimental data can be approximated by considering an exponential law on Ca_c , like $D^* = q Ca_c^x$.

This power-law behavior is in agreement with both experimental and numerical investigations proposed by many authors in cross-junctions as well as T-channels [39, 42, 57, 105, 106]. The power-law exponent which fits the present experimental data is equal to -0.31 and it is in good agreement with previous studies [39, 57]. The error bar in Figure 3.6 gives an indication of the variation of the droplet volume observed experimentally. At low flow rates error bar becomes very large, which means that the droplet dimensions become more variable.

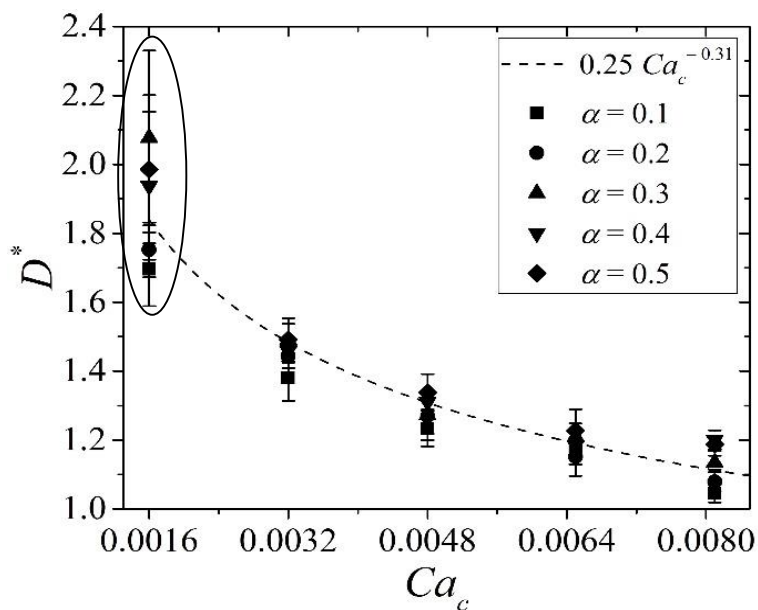


Figure 3.6. Non-dimensional droplet diameter as a function of $q Ca_c^x$.

In Figure 3.7 a modification of the power-law used in Figure 3.6 is proposed with the aim to introduce α in the correlation.

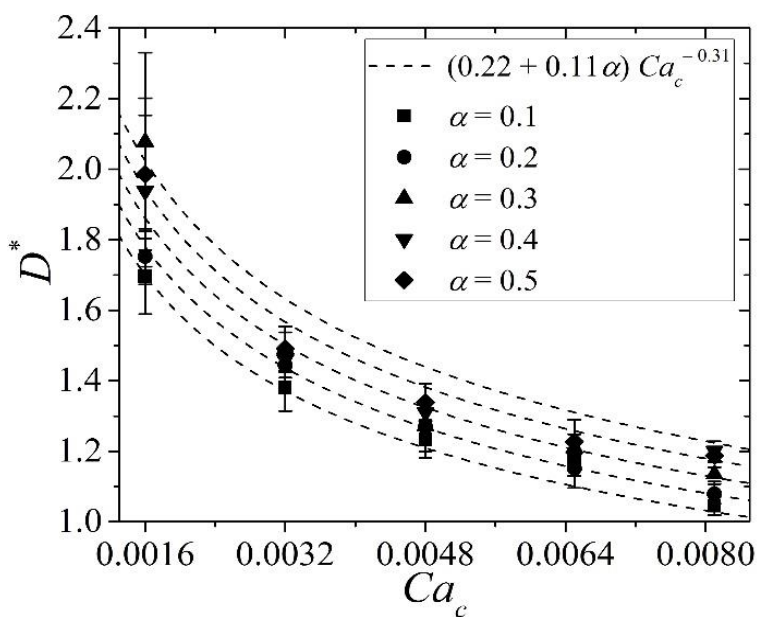


Figure 3.7. Non-dimensional droplet diameter as a function of $(\varepsilon + \omega\alpha) Ca_c^x$.

A new scaling law which combines the linear and power-law dependence on α and Ca_c , respectively, is shown in Figure 3.7; this correlation is able to predict the experimental results even at low flow rates (low Ca_c).

The experimental data seem to suggest a scaling law in the form $D^* = (\varepsilon + \omega\alpha) Ca_c^x$ where ε , ω and x are equal to 0.22, 0.11 and -0.31 respectively.

3.1.3 Polydispersity

The dimensions of the droplets generated in the cross-junction can be highly uniform (low Pl values) if the operative condition (Ca_c and α) are opportunely selected. In order to show that the level of uniformity of the droplets produced by using the cross-junction at low Ca_c values depends on both Capillary number and flow rate ratio, in Figure 3.8 the droplet polydispersity Pl , defined by Equation (2-10), is plotted as a function of Ca_c and α for W (Figure 3.8a), 0.3 XG+T (Figure 3.8b) and 0.5 XG+T (Figure 3.8c).

For pure water (W), droplets are generated at low Ca_c (< 0.01) with a low polydispersity Pl ($< 6\%$) when the volumetric flow rate ratio α ranges between 0.1 and 2. In this region the cross-junction is able to guarantee a uniform droplet generation in terms of dimensions. On the contrary, when the value of α is increased ($\alpha > 2$), the droplet dimension D^* increases and the possibility to have droplet coalescence becomes higher. The merging of two or even more sequential droplets changes the size of the droplets drastically. The onset of coalescence is responsible of the increase of polydispersity Pl ($> 10\%$) observed for $\alpha > 2$ and $Ca_c < 0.008$ (see Figure 3.8a). This fact underlines that it is difficult to obtain a regular generation of homogeneous droplet in terms of dimensions by using pure water if large values of α are imposed. The addition of surfactant to water enhances the droplet generation at lower α values and it is able to guarantee a more stable and uniform droplet production.

Figure 3.8b and c put in evidence that the tested cross-junction is able to guarantee a uniform production of droplets at low Capillary numbers ($Ca_c < 0.02$) for a large range of values of the flow rate ratio α ($0.1 < \alpha < 1$) when Xanthan gum solutions are used as dispersed phase. Also by using Xanthan gum aqueous solutions as dispersed phase, polydispersity values lower than 6% can be obtained for $0.1 < \alpha < 1.2$ when $0.006 < Ca_c < 0.02$. This confirms that a micro cross-junction operating in DJ or DC regime is able to guarantee, within a large range of operative conditions, the production of uniform droplets both in presence of Newtonian and non-Newtonian dispersed phases.

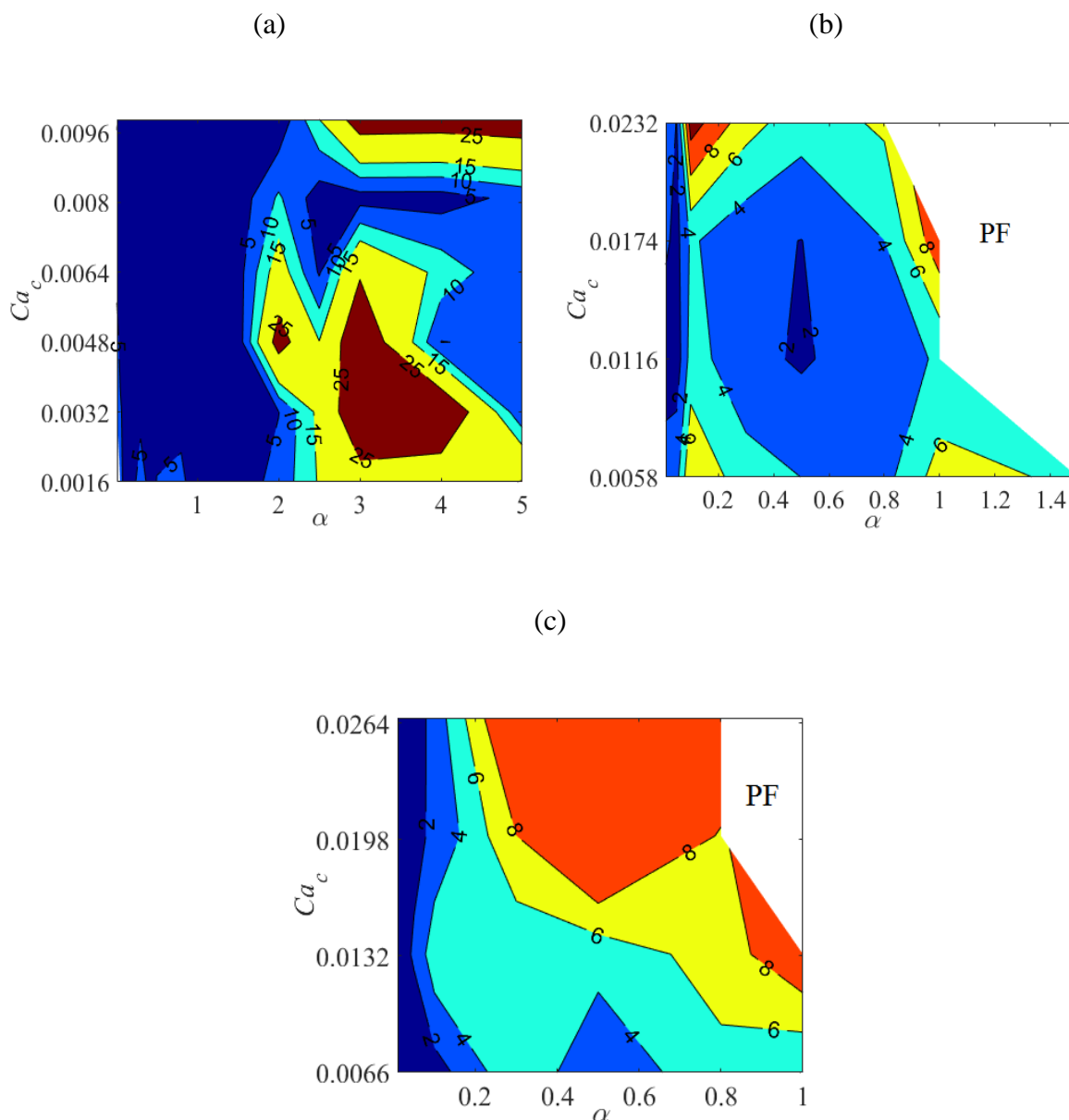


Figure 3.8. Polydispersity Pl of droplet as a function of Ca_c and flow rate ratio α for different dispersed phases: (a) W, (b) 0.3 XG+T and (c) 0.5 XG+T in silicone oil.

In order to give more detailed information about the value of polydispersity associated to the droplets generated during the experimental runs, Table 3.3 and for 0.3 XG+T and 0.5 XG+T, respectively gives the values of polydispersity obtained by changing the values of volumetric flow rates imposed at the inlets of the cross-junction.

Table 3.3. Polydispersity of D^* as a function of the imposed values of α and Q_c for 0.3 XG+T droplets in silicone oil.

α	Q_c (ml/h)			
	0.5	1	1.5	2
0.01	-	0.60	2.35	3.03
0.05	3.39	0.89	1.40	1.91
10.1	7.91	4.81	4.29	11.01
0.3	4.79	2.68	2.50	6.84
0.5	3.99	1.71	1.96	4.82
0.8	3.32	3.40	3.99	6.37
1.0	6.90	4.15	9.43	-
1.5	5.55	0.60	-	-

It is evident that, for all the combinations of imposed flow rates at the inlets, polydispersity values lower than 15% are obtained. This result confirms that the cross-junction can be efficiently used as droplet generator also in presence of shear thinning non-Newtonian dispersed phases even if an increase of the variation of the droplet sizes is observed by increasing both Q_c and α .

Table 3.4. Polydispersity of D^* as a function of the imposed values of α and Q_c for 0.5 XG+T droplets in silicone oil.

α	Q_c (ml/h)			
	0.5	1	1.5	2
0.01	-	1.31	1.09	1.40
0.05	0.91	2.16	1.65	0.89
0.1	1.08	5.41	2.24	2.78
0.3	5.56	4.39	7.97	11.32
0.5	2.44	4.73	12.33	12.80
0.8	5.40	6.87	7.77	10.76
1.0	3.94	9.97	-	-

3.2 Newtonian and non-Newtonian emulsions at large Ca_c values

The second step of this experimental investigation was to enlarge the analysis of the droplet regimes to large values of the imposed volumetric flow rate linked to the continuous phase, by considering $Ca_c > 0.02$.

A wide range of volumetric flow rates has been tested in order to be able to detect different droplet patterns including squeezing (SR), dripping (DR) and jetting regime (JR).

In these tests the continuous phase flow rate covers a thorough range ($0.3 \leq Q_c \leq 20$ ml/h) and the dispersed phase flow rate varies between 0.01 to 3 ml/h for non-Newtonian solutions. It's worth mentioning that the range of Q_d for emulsion of water with Tween 20 has been extended to 8 ml/h while continuous and dispersed flow rates for the droplets of water without surfactant vary between $0.8 \leq Q_c \leq 49.9$ and $0.016 \leq Q_d \leq 59.25$ ml/h, respectively to repeat the experimental runs in the same range of Capillary number. These data are also reported in Table 3.1.

By varying the inlet flow rate of both dispersed and continuous phase three different droplet regimes can be generally observed as reported in Figure 3.9.

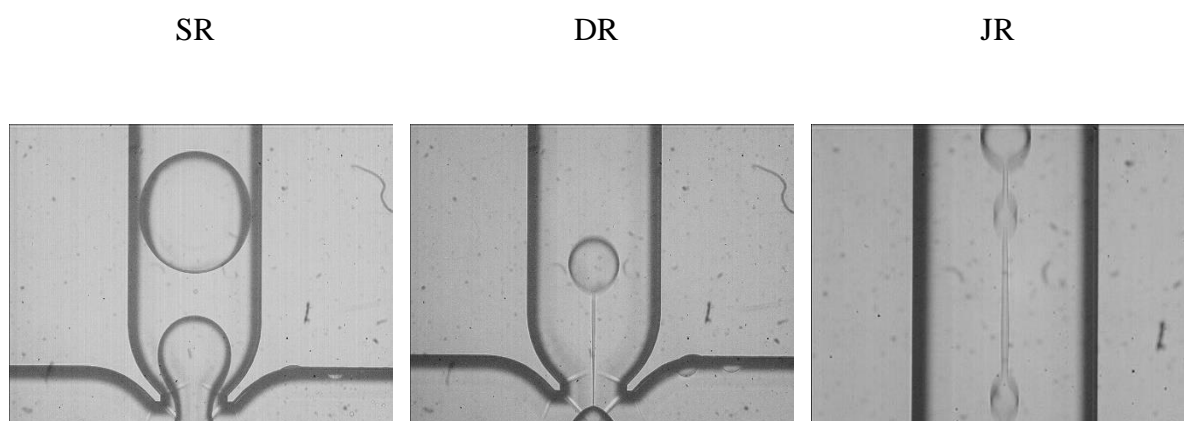


Figure 3.9. Droplet regimes obtained by fixing the volumetric flow rate of the Xanthan gum aqueous solution (0.2 XG+T) equal to $Q_d = 0.1$ ml/h and $Q_c =$ (a) 0.3 ml/h (squeezing regime), (b) 3 ml/h (dripping regime) and (c) 10 ml/h (jetting regime).

On the basis of the droplet breakup mechanism, it is possible to distinguish squeezing regime (SR), observed at low velocity of both continuous and dispersed phase (low Capillary

numbers and low flow rate ratios), from dripping regime (DR), which takes place at higher velocity of the continuous phase (moderate Capillary number) and jetting regime (JR), occurring when the Capillary number exceeds critical value. This last droplet regime was not activated at low values of Ca_c (see the previous Section 3.1).

In Figure 3.9 typical droplet patterns linked to these three regimes are obtained by fixing the volumetric flow rate Q_d of a Xanthan gum aqueous solution (0.2 XG+T) equal to 0.1 ml/h and by increasing the volumetric flow rate of the silicone oil (continuous phase, Q_c) from 0.3 ml/h (Figure 3.9a) to 3 ml/h (Figure 3.9b) up to 8 ml/h (Figure 3.9c).

By observing Figure 3.9a it is evident that the thin layers close to the solid walls in which the continuous phase is forced to flow is responsible of the squeezing of the dispersed phase and the formation of a droplet having dimensions equal or larger than the width of the outlet microchannel.

By increasing the volumetric flow rate of the continuous phase (Figure 3.9b) the viscous drag due to the co-flow of the continuous and dispersed phases along the outlet microchannel is responsible of the formation of the filament originated between the nozzle and the droplet. In this case the breakup is located downstream of the junction by dripping and the dimensions of the droplets are generally lower than those of the outlet channel. The presence of the long filament is a characteristic of the shear thinning liquid used as dispersed phase and the presence of Tween 20 inside the aqueous solution tends to increase the length of the thread due to the reduction of the interfacial forces which oppose the viscous drag.

When the velocity of the continuous phase is increased over a critical value, the external surface of the thread starts to show an unstable behavior (Figure 3.9c); in this case the droplet detachment point gradually moves downstream until a stable jet is formed (jetting regime). In this regime the droplet dimensions are only marginally decreased in correspondence of an increase of Q_c . The length of the slender thread between the nozzle and the droplet detachment point can be very long, especially in presence of shear thinning liquids, and, after the breakup, the thread can originate small satellite droplets.

3.2.1 Squeezing regime

In the squeezing regime, the interfacial tension and pressure drop force along the main

channel govern the dynamics of the droplet formation process and breakup mechanism. Due to the action of the transversal introduction of the continuous phase, the interface penetrates the main channel and grows until to block completely the channel (see Figure 3.10) which leads to an increase of the pressure drop, as observed by Kashid *et al.* [107] through a numerical simulation.

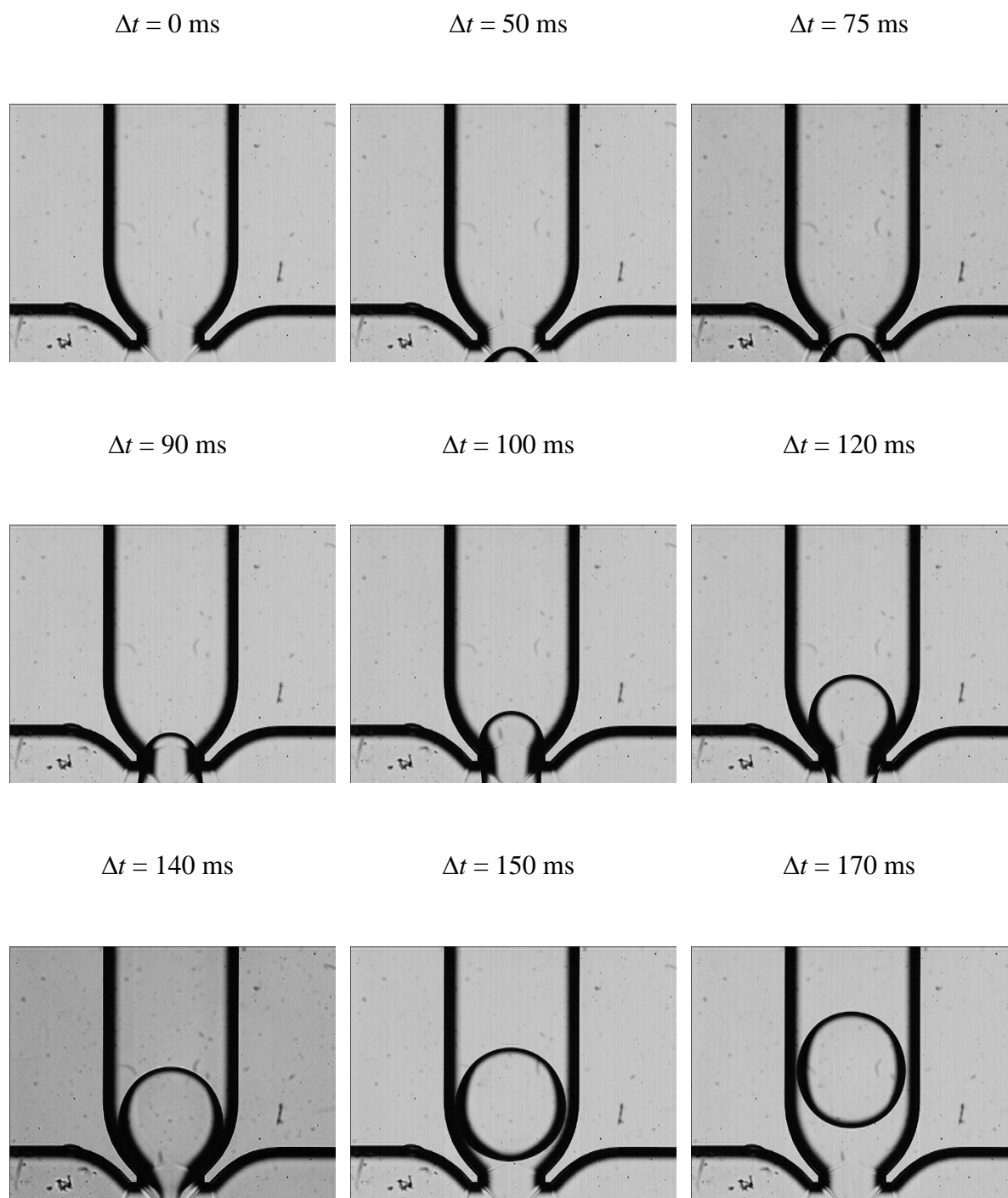


Figure 3.10. Squeezing regime when $Q_c = 0.8$ ml/h and $Q_d = 0.08$ ml/h for pure water (W) emulsions.

They showed that the back pressure is larger than that in the dispersed phase channel. The carrier fluid displaces the droplet downstream of the junction when the back pressure rises above the pressure in the dispersed phase channel. It stretches the droplet and squeezes the neck connecting the droplet to the source of the dispersed phase. In this regime the continuous phase is not able to deform the tip of the droplet. As a result, the continuous phase is confined in a thin layer close to the walls of the junction in which the flow is subjected to an increased viscous resistance which is responsible of the pressure build-up in the continuous phase upstream of the droplet tip. Since this pressure is larger than the pressure in the immiscible dispersed phase, the continuous phase squeezes the neck of the inner fluid determining the breakup and detachment of the droplet. In this droplet regime the interfacial stress is able to play an active role only during the very last stage before the droplet detachment; for this reason, the dependence of the droplet characteristics on the interfacial tension or on the viscosity ratio λ is usually weak.

3.2.2 Dripping regime

In the dripping regime (DR), the dynamics of the droplet formation process is governed by a balance between the shear force and the interfacial tension. The dispersed phase as the propulsion exerted on the dispersed phase to pinch-off the droplet is countered by the interfacial tension which opposes the elongation of the neck of the droplet. The droplet size in dripping regime is smaller than that of squeezing regime as the shear force increases. By increasing the continuous phase flow rate Q_c (Ca_c) the droplet is sheared off earlier. Therefore Ca_c is expected to play a more important role in the dripping regime and impact of the pressure drop force diminishes although in some cases the droplet partially blocks the channel.

In other words, in the dripping regime the droplet breakup is due to the opposite action of the viscous drag exerted by the continuous fluid on the emerging droplet, which is responsible of the formation of a thread between the nozzle and the droplet, and the interfacial tension that opposes the elongation of the thread. In this regime the droplet diameter is inversely proportional to the capillary number associated to the continuous phase (Ca_c). Cramer *et al.* [19] observed experimentally that for Newtonian immiscible fluids in dripping regime the viscosity of the droplet does not influence the size of the droplet appreciably because the drag force depends only very weakly on this parameter.

Figure 3.11 shows the evolution of the interface during the droplet generation of 0.3

XG+T in silicone oil flow. It can be observed that, generally, by increasing Ca_c the size of the droplets is reduced; this means that in dripping regime the droplets are generally smaller than that obtained by squeezing.

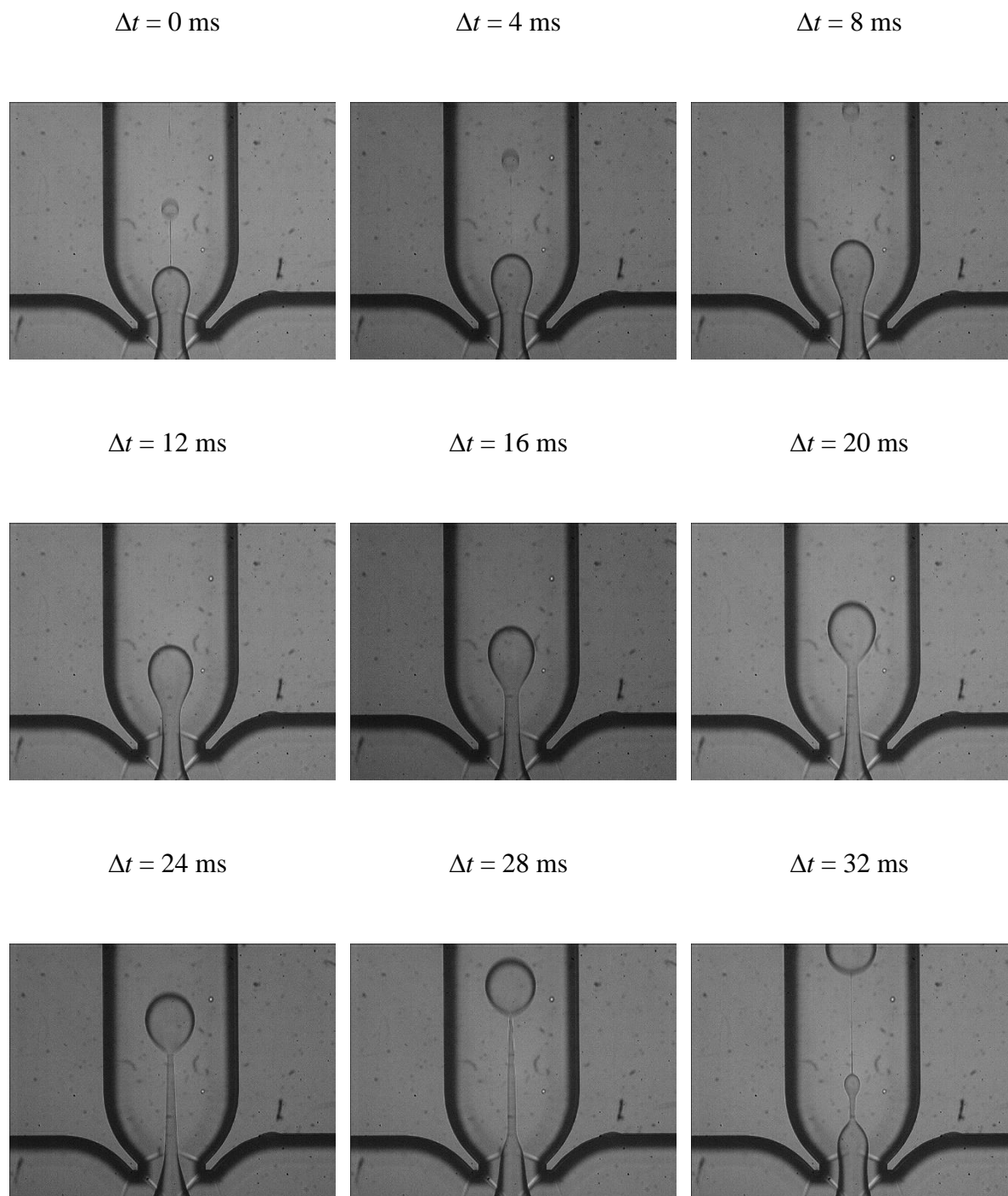


Figure 3.11. Dripping regime when $Q_c = 4$ ml/h and $Q_d = 0.2$ ml/h for 0.3 XG+T emulsions.

3.2.3 Jetting regime

In jetting regime (JR), the shear force dominates over the interfacial tension and the droplets are generated by the instability of the flat interface of the parallel co-flow which can be triggered when the Capillary number is very high.

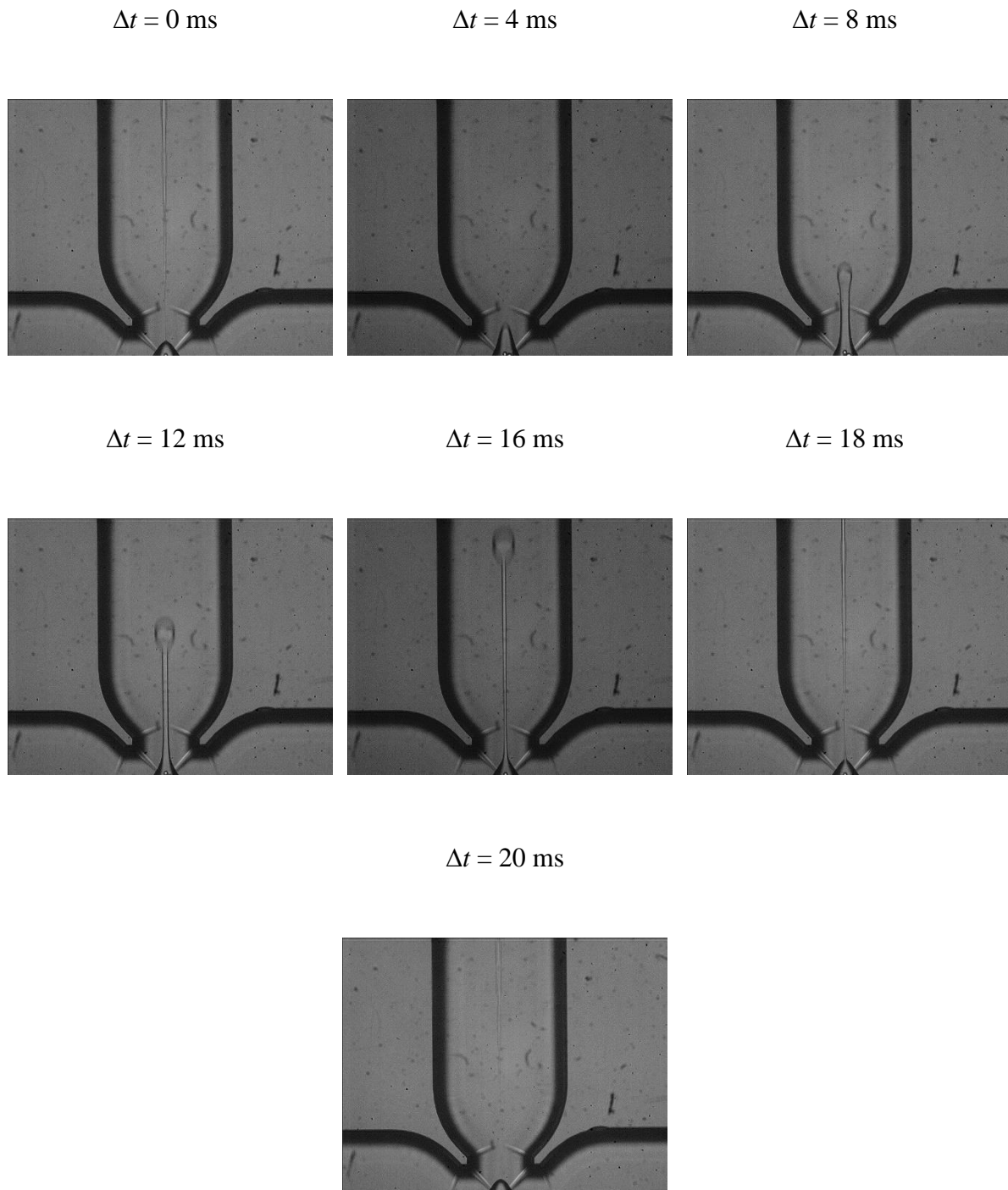


Figure 3.12. Jetting regime when $Q_c = 10$ ml/h and $Q_d = 0.1$ ml/h for 0.4 XG+T emulsions.

In this case, the droplets are characterized by a strongly variable diameter due to the random detachment of the droplets from the unstable thread focused in the centre of the outlet microchannel. The shear force becomes predominant and the droplets are produced by a shear-driven mechanism. As the shear force is large in magnitude, dispersed phase properties are less important in controlling the droplet size. Figure 3.12 also shows that the breakup point moves downstream of the junction as the dispersed phase viscosity increases, as evidenced by Cramer *et al.* [19]. It is interesting to note that with non-Newtonian fluids like Xanthan gum solutions a very long and slender thread may be seen before the breakup due to the higher viscosity of the dispersed phase. The dispersed phase material contained in the thread follows the main droplet after the breakup by creating a series (one or more) satellite droplets.

In Figure 3.13 zoomed views of the threads existing between the nozzle and the droplet are shown for pure water in presence of large α values (Figure 3.13a) and for 0.3 XG+T for large values of Ca_c (Figure 3.13b). It is possible to observe on the thread surface the formation and propagation of waves which are responsible of the jetting of droplets from the end of the filament. Figure 3.13 highlights the difference in terms of thickness of the thread when the instability of the surface is obtained by imposing large values of α (Figure 3.13a) or large values of Ca_c (Figure 3.13b). At large Ca_c values, thanks to the shear-thinning properties of the tested non-Newtonian solutions, it is possible to obtain very thin and long threads which are not observable when water is used as dispersed phase.

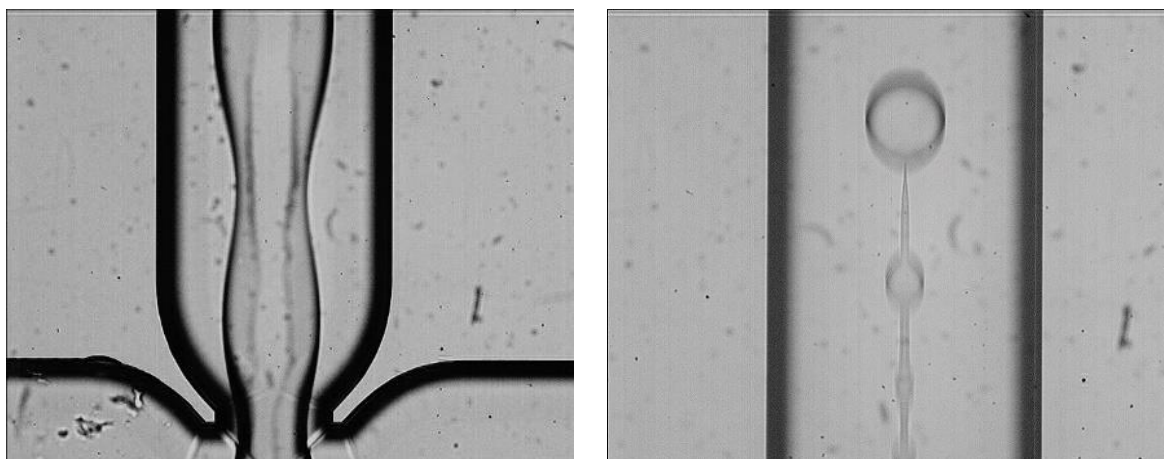


Figure 3.13. Thread instability during jetting: (a) pure water W ($Q_c = 4$ ml/h and $Q_d = 20$ ml/h); (b) 0.3 XG+T ($Q_c = 8$ ml/h and $Q_d = 0.1$ ml/h).

3.2.4 Effect of Ca_c

The effect of continuous Capillary number on the droplet sizes has been studied in Figure 3.14 for different combinations of immiscible liquids. It is clear that with an increase of Capillary number the non-dimensional droplet diameter decreases. At low Capillary numbers $Ca_c \leq 0.01$ squeezing regime is recognizable. In squeezing regime the shear force is negligible and the pressure drop force is the only force able to overcome the interfacial tension by making possible to generate the droplet. The channel is nearly blocked and, due to the surge in pressure drop and consequently high back-pressure as compared to the dispersed phase pressure, the interface of the fluid is displaced by the continuous phase. The filament gets stretched and the neck is squeezed at the rupturing moment [107]. In dripping regime the droplet does not fully block the channel, so the pressure drop force is not as important as it is in squeezing regime. In this case shear force as the positive force, a force which helps to generate the droplet by shearing the interface off, and interfacial tension as the negative force, which opposes the generation of the droplet, constitute the main physical governing forces. With more increase of Capillary number (dripping regime) variation in the diameter becomes less evident than before. In this regime the shear force overcomes the interfacial tension and a shear-driven mechanism governs.

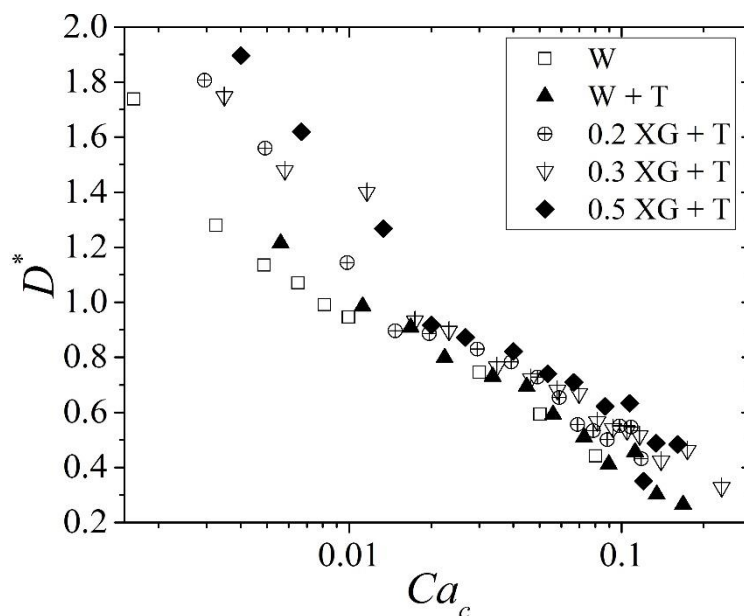


Figure 3.14. Effect of continuous Capillary number where $0.3 \leq Q_c \leq 20$ and $Q_d = 0.1$ ml/h for W, W+T and three concentrations of Xanthan gum solution, 0.2 XG+T, 0.3 XG+T and 0.5 XG+T.

In the squeezing regime the droplet diameter is a function of both flow rates. Due to the high values of continuous flow rate and consequently high value of shear force, the influence of Ca_c on D^* is significant in dripping regime. In dripping regime the shear force is already predominant and an increase of the volumetric flow rate ratio has a secondary impact on the droplet size and results in only a slight decrease.

It is evident that droplet diameter decreases with increasing Ca_c through the investigated range (Figure 3.14). Two zones are present in Figure 3.14; the dependency of the non-dimensional diameter D^* on Ca_c varies for $Ca_c > 0.01$ as compared to the region of $Ca_c < 0.01$.

By focusing the attention on the trend for large Capillary numbers ($Ca_c > 0.01$) the experimental results highlight that in dripping and jetting regime the droplet dimensions scale with ($\sim 1/Ca_c^{0.4}$), in agreement with the numerical observations of De Menech *et al.* [46]. In dripping regime, D^* depends weakly on the dispersed phase properties, as confirmed by Figure 3.15a and b. In fact, the trend of D^* as a function of Ca_c tends to be independent of the liquid used as dispersed phase, especially for Newtonian liquids (pure water and water with Tween 20). This result confirms that in shear-driven breakup, typical of large Ca_c values, the viscosity of the dispersed phase does not influence the size of the droplets appreciably, as confirmed experimentally by Cramer *et al.* [19].

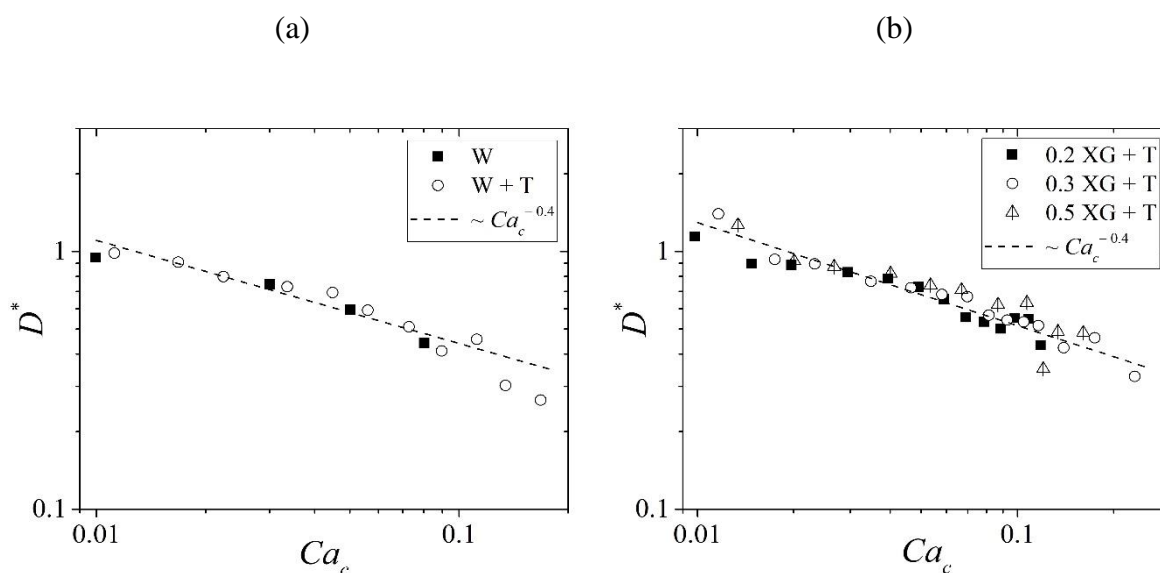


Figure 3.15. Droplet dimensionless diameter of the (a) Newtonian and (b) non-Newtonian emulsions as a function of the continuous Capillary number obtained when $Ca_c \geq 0.01$ and $Q_d = 0.1$ ml/h.

3.2.5 Effect of Q_d

Figure 3.16 shows the influence of the imposed dispersed phase flow rate on the droplet size when the Capillary number (Ca_c) is kept constant while Q_d varies. It shows non-dimensional droplet diameter as a function of flow rate ratio for a wide range of flow rates. Regardless of the flow regime or flow rates, D^* enhances with the flow rate ratio α . It is evident that an increase of Q_d (larger α values) while the continuous flow rate is fixed makes larger droplets in presence of both Newtonian (Figure 3.16a) and non-Newtonian (Figure 3.16b) dispersed phases. In fact, an increase of Q_d causes a larger injection of the dispersed phase into the junction and larger droplets are generated especially at low values of Q_c (Ca_c). When the continuous phase flow rate is increased (larger Ca_c and lower α), the role of the shear forces becomes more important and the influence of Q_d on the droplet size decreases. At high values of α (> 1 in Figure 3.16a, and > 0.1 in Figure 3.16b), the dimensionless diameter D^* is a strong function of the flow rate ratio α .

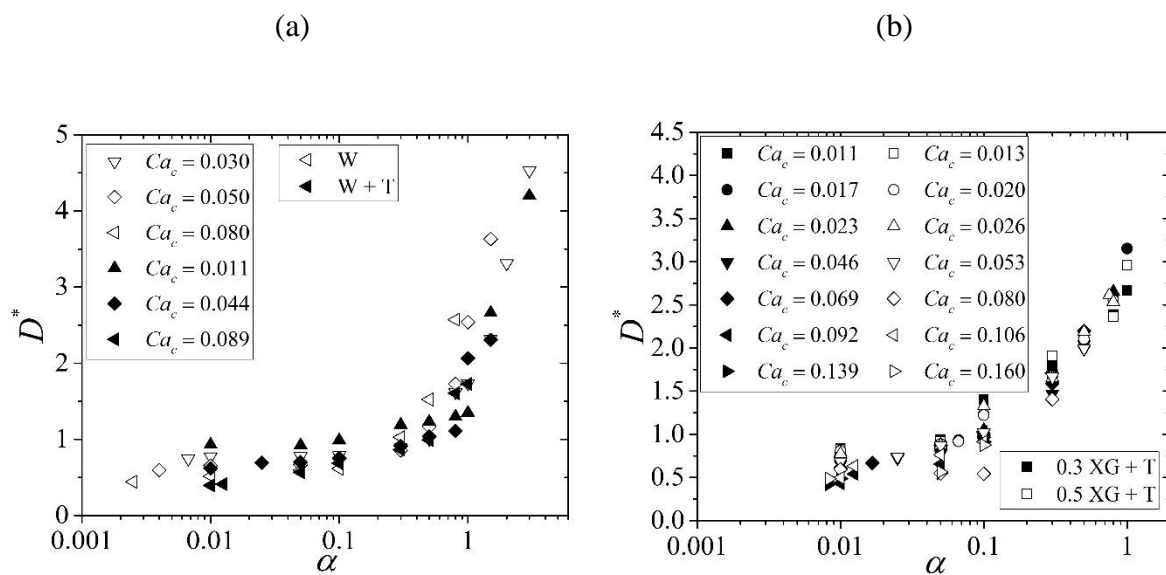


Figure 3.16. Non-dimensional diameter of the droplet as a function of the flow rate ratio α when $Ca_c > 0.01$: (a) Newtonian dispersed phases (W and W+T) and (b) non-Newtonian dispersed phases (0.3 XG+T and 0.5 XG+T).

The droplet size is highly dependent on flow rate ratio in cases with low values of continuous flow rate and/or in squeezing regimes because of relatively high droplet formation time. The more increase of Q_c , the less formation time is needed for the drop to be generated and the less dependence of the drop size on Q_d is observed. In high values of α (> 1), the

dimensionless diameter of the droplet is a strong function of flow rate ratio in spite of the case of $\alpha < 1$ in which D^* is not changing with α drastically.

3.2.6 The droplet regime maps

In Figure 3.17 the flow maps with the droplet regimes observed by varying the Capillary number linked to the continuous phase (Ca_c) and the flow rate ratio (α) are shown for different liquids used as the dispersed phase: W (Figure 3.17a); W+T (Figure 3.17b); 0.3 XG+T (Figure 3.17c) and 0.5 XG+T (Figure 3.17d).

By comparing the maps of Figure 3.17 it is possible to observe that a series of common factors are present. As a rule of thumb, for low velocity of the continuous phase the transition among the regimes can be obtained by increasing α . This result has been deeply commented by many researcher by using not only experimental results [41, 44] but also theoretical models [46] and numerical simulations [39].

It is interesting to observe that, for very low values of Ca_c (< 0.01), the jetting regime (JR) can be activated by increasing α in presence of Newtonian dispersed liquids (see Figure 3.13a) but this is not possible when Xanthan gum solutions are used; and, after the dripping regime, parallel flow is obtained without production of droplets; in this last case, by increasing the flow rate of the dispersed phase only squeezing and dripping regimes can be observed at $Ca_c < 0.03$. In dripping regime (DR), further increase of the dispersed flow rate is not able to generate instability of the thread interface and a parallel flow (PF) without droplet formation is generally observed. On the contrary, for high velocity of the continuous phase (low α and high Ca_c) the transition between squeezing and dripping is obtained when Ca_c becomes larger than a critical value which depend on the geometry of the cross-junction and on the properties of the immiscible liquids used. At very high velocity of the continuous phase jetting is generally observed especially at low α values.

More in detail, in Figure 3.17a it is possible to observe the domains in the α - Ca_c plane of squeezing, dripping and jetting regimes obtained by using pure water as dispersed phase and silicone oil as continuous phase ($\lambda = 0.049$). It is evident that the squeezing regime is the most important regime when the micro cross-junction is used at low Capillary numbers ($Ca_c < 0.01$).

As underlined numerically by Liu and Zhang [39], for $Ca_c < 0.01$ the transition between

squeezing and dripping regime is influenced by both α and Ca_c . Dripping is activated only for large values of the flow rate ratio ($\alpha > 1$); by increasing the velocity of the dispersed phase. On the contrary, at low values of α (< 1) dripping can be activated only by increasing the velocity of the continuous phase; by increasing Ca_c , the droplet regime goes from squeezing to dripping when Ca_c is larger than a critical value which increases when α decreases. The transition from dripping to jetting is possible only for $\alpha > 0.1$. These findings are coherent with those obtained by other researchers for similar cross-flow configurations [50].

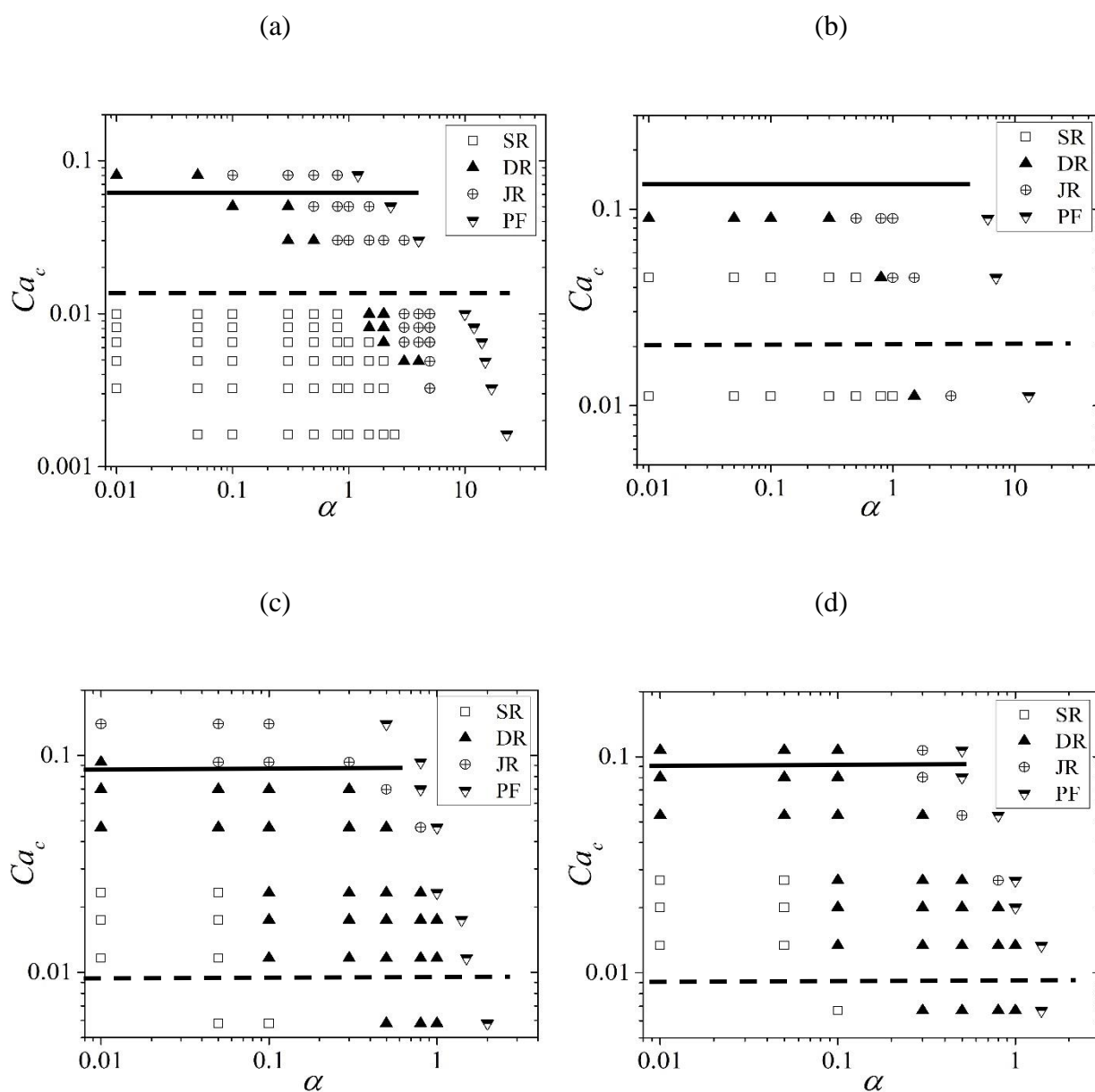


Figure 3.17. Droplet regimes as a function of the continuous Capillary number (Ca_c) and the flow rate ratio (α) by considering as dispersed phase: (a) W, (b) W+T, (c) 0.3 XG+T and (d) 0.5 XG+T.

In Figure 3.17b the effect of the addition of surfactant in the dispersed phase can be highlighted. A concentration of 2% in weight of Tween 20 in pure water is able to reduce of six times the interfacial tension (see Table 2.4). By observing Figure 3.17b it is possible to highlight that, at low values of Ca_c (< 0.01), the transition between squeezing and dripping occurs at the same values of α with respect to pure water. The same seems to occur if the velocity of the continuous phase is increased, for a fixed velocity of the dispersed phase; also in this case the transition from squeezing to dripping occurs at the same critical values of Ca_c ($Ca_c \cong 0.01-0.1$) observed for pure water. Since a concentration of 2% in weight of Tween 20 in pure water is able to reduce of six times the interfacial tension (see Table 2.4) this means that in presence of Tween 20 it is possible to obtain the transition between squeezing and dripping at low α values by using a continuous flow rate and velocity six times lower than the value needed if pure water is used as dispersed phase.

Even when Xanthan gum aqueous solutions are used as dispersed phase (Figure 3.17c and d), the transition between squeezing and dripping regime is influenced not only by Ca_c but also by α . At low values of α (low dispersed volumetric flow rate) dripping occurs at larger Capillary numbers. At low values of α (< 0.2), jetting regime is generally reached only for very large velocity values of the continuous phase ($Ca_c > 0.09$). On the contrary, for large values of α jetting can be obtained also for lower values of Ca_c (down to 0.03).

The effect of the Xanthan gum concentration on the droplet regimes can be deduced by comparing Figure 3.17c and d; it is evident that the differences in terms of droplet regimes are very limited if the Xanthan gum concentration is increased from 0.3 wt% to 0.5 wt%.

On the contrary, by comparing Newtonian (Figure 3.17a and b) with non-Newtonian (Figure 3.17c and d) emulsions, it is possible to observe that when the viscosity ratio λ increases, the droplet breakup point moves downstream of the junction and dripping regime is enhanced. This result was confirmed numerically by De Menech *et al.* [46] for T-junctions observing that large values of λ dampen the pressure fluctuation upstream the junction. In addition, for large values of λ the thread between the nozzle and the droplet becomes longer and thicker because the dispersed phase is able to accept greater deformations. The non-negligible effect of λ on the transition between the droplet regimes underlines that in presence of non-Newtonian liquids having an apparent viscosity influenced by the shear rate the description of the droplet breakup by using only the Capillary number linked to the continuous

phase can be not sufficient because the Capillary numbers for both phases have to be considered as governing parameters.

It is also possible to individuate the flow patterns based upon the previously explained regimes, DJ, DC and PF (Figure 3.18). As a rule of thumb the range of Ca_c and α in which the droplet generation occurs is much wider in Newtonian fluids compared to non-Newtonian emulsions.

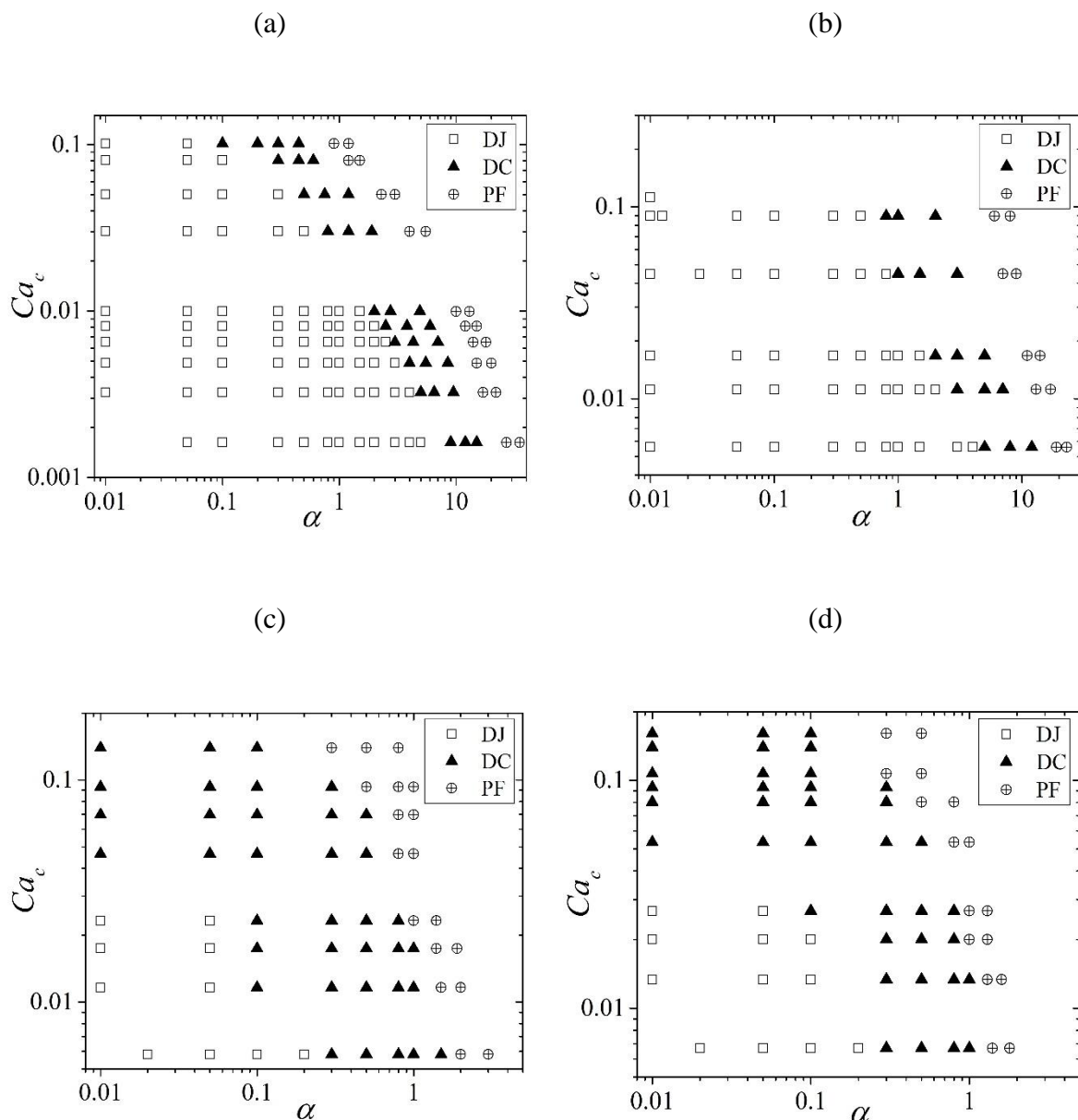


Figure 3.18. Droplet regimes, DJ, DC and PF, of the emulsions by considering in silicone oil: (a) W, (b) W+T, (c) 0.3 XG+T and (d) 0.5 XG+T as dispersed phase.

With the increase of viscosity the interface of the dispersed phase is pinched-off far from the junction and a long filament takes form through the channel (DC regime). On the contrary in Newtonian droplets most of the flow map is dedicated to the droplets generated at the junction (DJ regime). In other words, for non-Newtonian solutions, DJ to DC happens at lower values of α due to the higher values of viscosity. The use of 0.3 or 0.5 wt% Xanthan gum solution makes an elongated filament to generate before the breakup and fills the channel. It is more likely to see DC in non-Newtonian solutions while for Newtonian ones in most cases the droplets are generated at the junction.

3.2.7 Prediction of droplet regimes

Four different identification methods have been employed to predict the transition between the droplet regimes [22] in a micro junction:

- (i) By means of a detailed analysis of the controlling forces and droplet formation dynamics thanks to numerical simulations coupled to experimental tests (Fu *et al.* [108] and Kashid *et al.* [107]); this technique helps to understand the meaning of experimental data but it needs a calibration of the numerical results obtained by using experimental results.
- (ii) By means of the analysis of the droplet formation images; relatively large droplets stand for the squeezing regime, moderate-sized droplets in the microchannel are generated in dripping regime and the jetting regime is delineated by small droplets along with long filament [51, 64] as shown in Figure 3.9. This method provides only limited information on the mechanisms and dynamics involved.
- (iii) By means of a droplet regime map, like those presented in this thesis, [17, 40, 46, 109, 110]; this method is very accurate because based on pure observations by it needs a tremendous amount of experimental data in order to scan all the possible combinations of operative conditions.
- (iv) By using the experimental link between the droplet size and Ca_c , as shown in Figure 3.14; in fact, the variation of the droplet diameter with Ca_c can be easily used in order to identify the droplet regimes as discussed in [41, 45, 51, 65].

As observed by Gu [22], a general and widely accepted criterion in order to individuate the boundary among the different droplet regimes was not individuated until now in the literature. A qualitative method proposed by Gu [22], able to individuate the transition between

a droplet regime and another one, can be obtained by considering the trend of the droplet diameter (D^*) as a function of the Capillary number linked to the continuous phase (Ca_c), for all the values of the flow rate ratio like the trends reported in Figure 3.14. As an example, in Figure 3.19a. the trend of D^* as a function of Ca_c for 0.3 XG+T is shown for values of α ranging from 0.0066 to 0.333.

By observing Figure 3.19a it is evident that for 0.3 XG+T each transition between two droplet regimes can be linked to a variation of the slope of the function $D^*(Ca_c)$. Similar results can be evidenced with other Newtonian and non-Newtonian dispersed phases. If a fitting of the experimental data in which D^* is plotted as a function of Ca_c is made, it becomes possible to calculate the derivative of D^* with respect to Ca_c ($\chi = dD^*/dCa_c$) as a function of Ca_c . In Figure 3.19b the derivative of D^* with respect to Ca_c (χ) is shown as a function of Ca_c for the dispersed phases considered in the tests, in the range of Capillary numbers from 0.002 up to 0.2 and for all the values of α tested. It is possible to observe that all of the working fluids considered in this work evidence a similar trend: at low Ca_c values, χ tends to increase when Ca_c is increased until a maximum is reached. After the maximum, χ decreases when Ca_c increases.

From the trend of χ as a function of Ca_c it becomes possible to individuate the critical values of Ca_c in correspondence of which the transition from one droplet regime to another one takes place. More in detail, the boundary between the squeezing and the dripping regime can be individuated by the position of the inflection point (point *a* in Figure 3.19) occurring before the maximum of χ is reached. In fact, in correspondence of the point of inflection (point *a*), the sensitivity of the droplet diameter on the Capillary number linked to the continuous phase changes. At the end of the dripping regime, χ changes slowly and reverses (point *b*) towards larger negative values which remarks the onset of the jetting regime.

In Figure 3.19b the position of points *a* and *b* are evidenced for the dispersed phases considered in this work. For Xanthan gum aqueous solutions the transition between squeezing and dripping regime occurs at the same Capillary number for all the concentrations considered here.

The critical values of the Capillary number linked to the transitions among the droplet regimes obtained by Figure 3.19b are independent from the value assumed by α and this aspect

is a limitation of the method because, as evident by observing Figure 3.17, the boundaries of the droplet regimes are a combined function of Ca_c , α and λ .

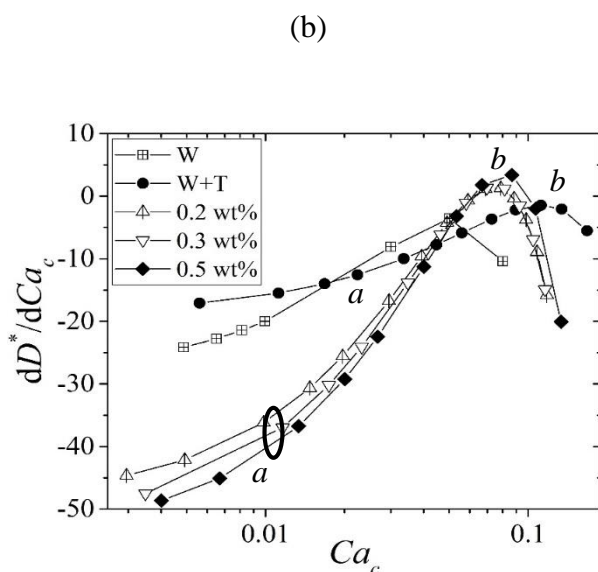
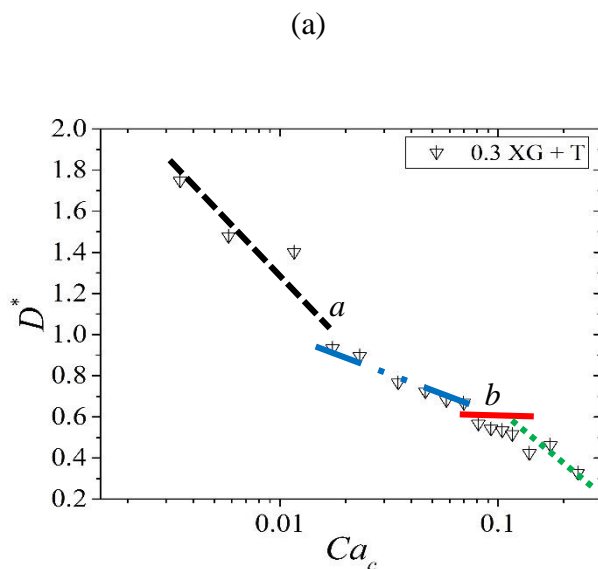


Figure 3.19. (a) Trend of the droplet diameter D^* as a function of Ca_c ; (b) derivative of D^* with respect to Ca_c as a function of Ca_c .

The critical Capillary number which corresponds to the position of the points a and b of Figure 3.19b are indicated in Figure 3.17 by means of a solid line (transition between dripping and jetting) and a dashed line (transition between squeezing and dripping). By observing the droplet maps of Figure 3.17 and the critical values of Ca_c obtained by the procedure proposed by Gu [22] it is evident that this method is only in qualitative agreement with the experimental

observations, especially in terms of prediction of the transition between dripping and jetting at large Ca_c and/or large values of α , both for Newtonian and non-Newtonian dispersed phases.

3.2.8 Polydispersity

The level of uniformity of the droplet size is investigated by means of the values assumed by the polydispersity Pl defined by Equation (2-10).

The higher values of Q_c , relatively higher dispersed droplets are generated especially in fluids with surfactant; it can be observed that the typical values of polydispersity are very low. On the contrary, polydispersity decreases when higher concentrated non-Newtonian fluids are employed. Generally, by increasing Q_c and/or decreasing wt%, the polydispersity increases.

By varying the operative condition (Ca_c and α) different values of Pl can be observed. In order to show that the level of uniformity of the droplets produced by using the cross-junction at high Ca_c values ($Ca_c > 0.01$) depends on both Capillary number and flow rate ratio, in Figure 3.20 the droplet polydispersity Pl is plotted as a function of Ca_c and α for W (Figure 3.20a), W+T (Figure 3.20b), 0.3 XG+T (Figure 3.20c) and 0.5 XG+T (Figure 3.20d).

For pure water (Figure 3.20a), droplets are generated at high Ca_c (> 0.01) with a low polydispersity ($Pl < 8\%$) only if the flow rate ratio α is lower than 0.5. In this region the cross-junction is able to guarantee the generation of droplets having very uniform sizes. On the contrary, when the value of α is increased ($\alpha > 0.5$), the polydispersity increases as well. For $Ca_c > 0.05$ and $\alpha > 1$ no droplets are obtained and a parallel co-flow downstream of the junction is observed (PF).

By adding Tween 20 to water (Figure 3.20b) a significant extension of the region characterized by lower Pl values ($< 8\%$) is obtained; in this case uniform droplets are generated if $\alpha < 1.5$ for $Ca_c > 0.01$. This fact confirms that the reduction of the interfacial tension between the immiscible liquids is beneficial for the generation of monodispersed emulsions using cross-junctions. In presence of non-Newtonian Xanthan gum solutions (Figure 3.20c and d) droplets with uniform sizes ($Pl < 8\%$) can be obtained only for low flow rate ratio ($\alpha < 0.2$) when Ca_c is larger than 0.05. This region is smaller when the Xanthan gum concentration is increased (Figure 3.20d); this result highlights that an increase of the viscosity of the dispersed phase tends to reduce the range of the operative conditions in correspondence of which

monodispersed droplets can be generated.

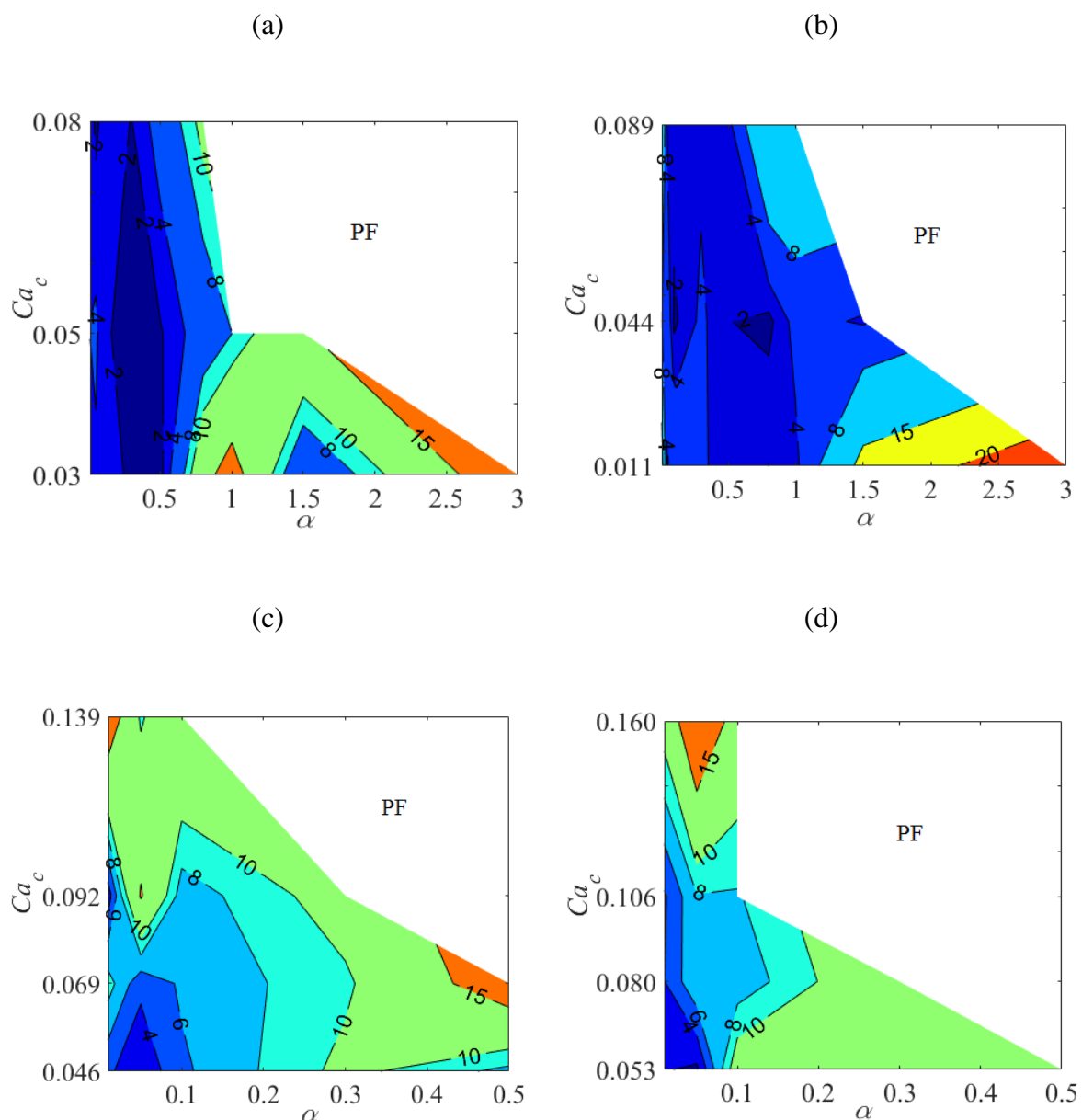


Figure 3.20. Polydispersity PI of droplet as a function of Ca_c and α for different dispersed phases in silicone oil; (a) W, (b) W+T, (c) 0.3 XG+T and (d) 0.5 XG+T.

The polydispersity increases, for all the dispersed phases considered, if α and Ca_c are increased. By comparing the plots of Figure 3.20 it is evident that in presence of non-Newtonian dispersed phases characterized by larger values of apparent viscosity, larger values of PI are generally obtained.

The large values of the viscosity ratio λ associated to the combination of SO/(XG+T) (see

Table 2.2) are responsible of the presence of a long thread before the droplet breakup; on the contrary, the thread is usually very short when pure water (W) or water with Tween 20 (W+T) are used as dispersed phase. The thread becomes more and more evident when the Capillary number Ca_c increases. After the droplet breakup, part of the thread generates satellite droplets which follow the main droplet. In many cases, the satellite droplets and the main droplet coalesce downstream of the junction.

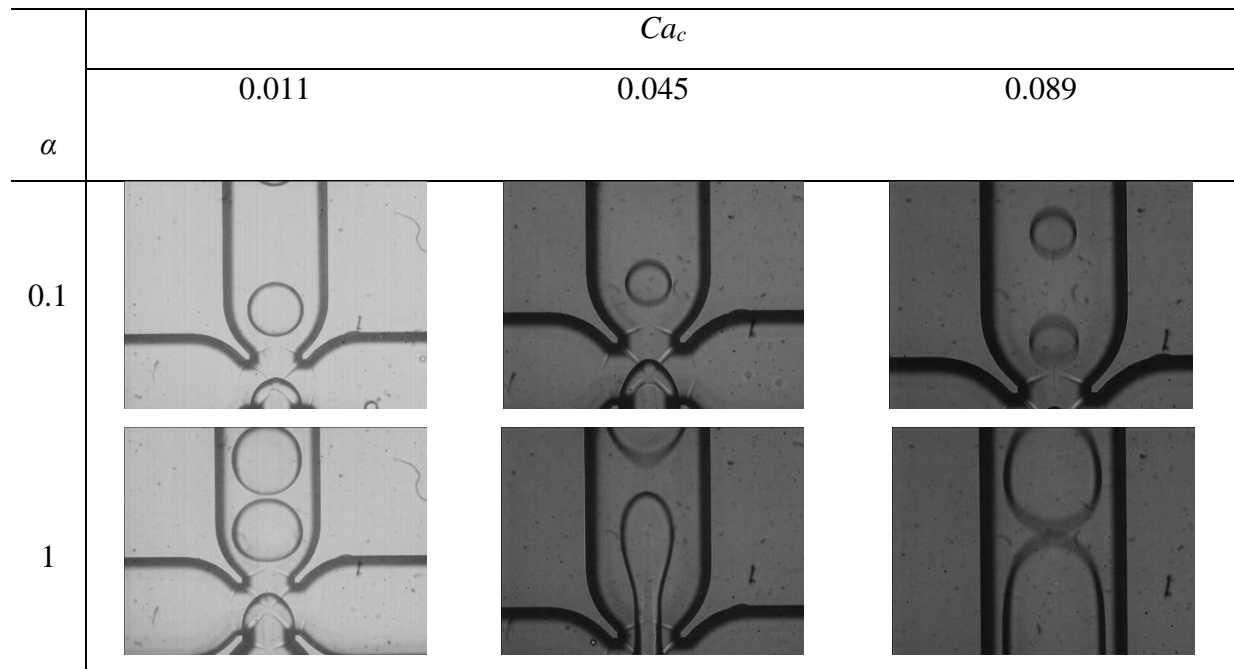


Figure 3.21. Droplets of water and Tween 20 (W+T) in silicone oil (SO) obtained by fixing the value of the flow rate ratio (α) and the Capillary number linked to the continuous phase (Ca_c).

In Figure 3.21 the images of the droplets of water with Tween 20 (W+T) in silicone oil generated for two values of flow rate ratio (0.1 and 1) by increasing the Capillary number from 0.011 to 0.089 are shown. By using water with Tween 20, for $\alpha = 0.1$, it is possible to see the presence of a short tail after the main droplet only at large values of Ca_c ; the tail is part of the thread broken during the droplet breakup. The liquid contained in the tail is merged to the main droplet downstream of the junction but this mass addition is not significant and the droplet size is not influenced by the incorporation of the tail. This is the reason for which at low values of α polydispersity assumes low values for water with Tween 20. No evident satellite droplets are originated after the droplet breakup even if α is increased. At $\alpha = 1$ the droplet size increases with respect to $\alpha = 0.1$ and if the flow rate of the continuous phase is increased, the droplets assume an elongated shape due to the lateral confinement of the channel walls. The coalescence between two consecutive droplets is promoted, especially when the Capillary number is large

and this coalescence is responsible of the large values of polydispersity of the generated droplets at large α .

Large values of flow rate ratio combined with the absence of surfactant determine for pure water large values of Q_d (for $\alpha = 3$ and $Ca_c = 0.03$, $Q_c = 14.8$ ml/h and $Q_d = 44.4$ ml/h). These large dispersed flow rates increase the probability to have the coalescence among the consecutive droplets and higher values of polydispersity can be observed as evidenced by Figure 3.20a. With the addition of surfactant (W+T) the coalescence starts earlier and droplets can be observed at large flow rate ratio ($\alpha > 2$) only for low values of Ca_c , as evidenced by Figure 3.20b. However in this region the polydispersity is larger than 15%. As a rule of thumb, polydispersity increases when the junction is operated close to the region of the parallel flow (PF).

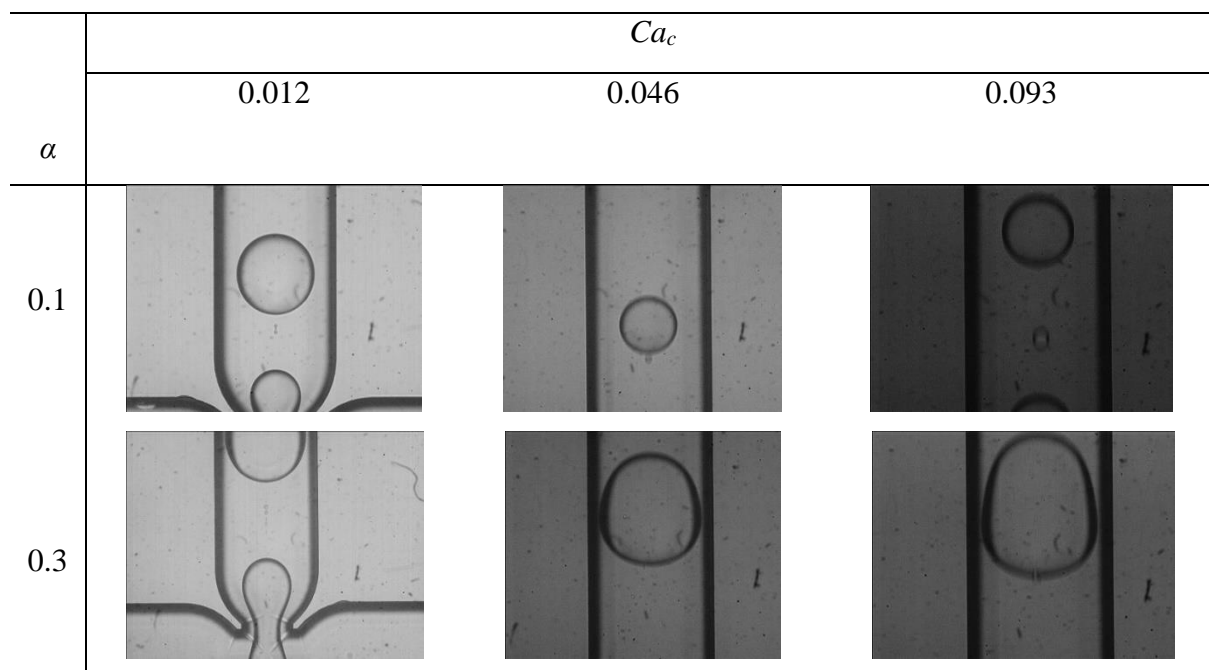


Figure 3.22. Droplets of Xanthan gum aqueous solution (0.3 XG+T) in silicone oil obtained by fixing the value of the flow rate ratio (α) and the continuous Capillary number (Ca_c).

Figure 3.22 shows the droplet of Xanthan gum aqueous solution (0.3 XG+T) in silicone oil obtained by fixing the value of the flow rate ratio α and the continuous Capillary number Ca_c . In this case, even at low values of α and Ca_c , the presence of satellite droplets is confirmed by the experimental observation. At $Ca_c = 0.012$ the main droplet is followed by multiple satellite droplets having small dimensions both for $\alpha = 0.1$ and $\alpha = 0.3$. When the Capillary number is increased, the dimensions of the satellite droplets increase as well; this is evident by

the images of Figure 3.22 obtained at $\alpha = 0.1$. The presence of large satellite droplets at large Capillary numbers (Ca_c) and low α is responsible of the large polydispersity values indicated in Figure 3.20c; in fact, in these conditions the emulsion becomes a combination of droplets having different sizes due to the presence of the satellite droplets among the main droplets and due to the coalescence between satellites and main droplets. By increasing α , satellite droplets are still present but the elongation of the droplets along the flow direction enhances the coalescence between satellites and main droplets leading to increasing the polydispersity of the emulsion.

In Figure 3.23 the images of three consecutive droplets obtained by imposing a flow rate ratio α equal to 0.1 and a Capillary number $Ca_c = 0.106$ in presence of a Xanthan gum aqueous solution (0.5 XG+T) as dispersed phase are shown. By comparing the dimensions of the satellite droplets with those shown in Figure 3.22, it is evident that the dimensions of the satellite droplets increase with the viscosity ratio of the immiscible liquids.

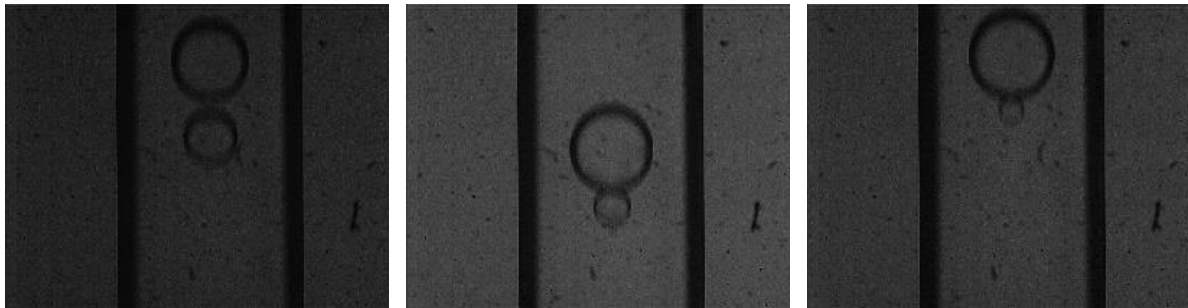


Figure 3.23. Main droplet and satellite droplet observed for three consecutive droplets obtained for $Ca_c = 0.160$ and $\alpha = 0.1$ using 0.5 XG+T as dispersed phase.

The images of Figure 3.23 highlight that the size of the satellite droplets can be very different each time that the droplet detachment is completed. For this reason, the dimensions of the droplet after the coalescence with the satellite can be very different in size and this explains the increase of the droplet polydispersity evidenced by the observation of the droplets far from the junction.

By comparing Figure 3.20a and b it is evident that the addition of surfactant is able to extend the region in which the junction is able to produce monodispersed emulsions at low values of Capillary numbers. On the contrary, the values of Pl shown in Figure 3.20 suggest

that in presence of a combination of immiscible liquids having a large viscosity ratio λ and a dispersed phase with a shear-thinning behaviour, the range of α and Ca_c in correspondence of which the cross-junction can be used in order to generate monodispersed emulsions is limited because the presence of significant satellite droplets tends to increase the polydispersity of the emulsion both at large values of α and low Ca_c as well as at large Ca_c and low α .

3.2.9 Effect of Xanthan gum concentration

A series of experimental runs are carried out to investigate the effect of Xanthan gum concentration on the size of the droplets (Figure 3.24). Low flow rates for both continuous and dispersed phase flows have been employed to avoid long microthreads due to the high viscosity of the solutions. Although the phases have different properties, the variation in droplet diameters is not remarkable. In most cases the larger droplets are produced in fluids with higher concentration of Xanthan gum solution. In other words, the higher viscosity, the larger droplet is produced which is different from findings of Newtonian solutions and it can be due to the non-Newtonian properties of the solutions.

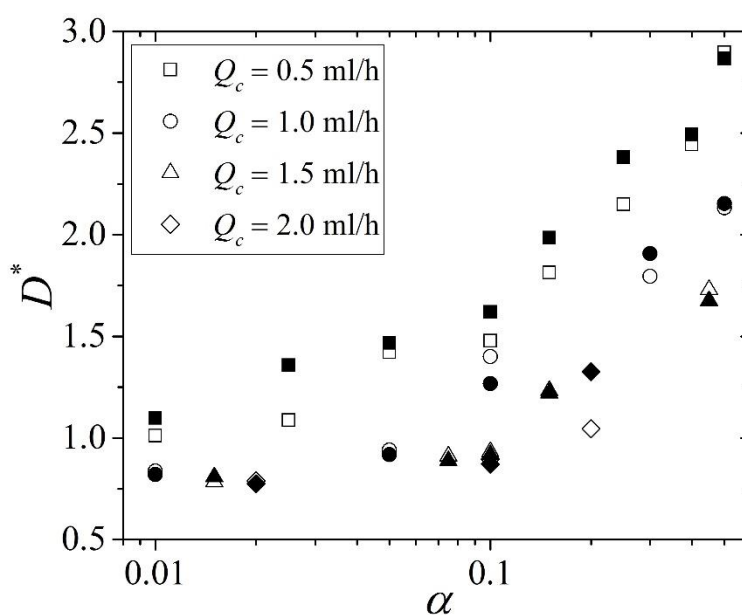


Figure 3.24. Effect of Xanthan gum concentration on droplet non-dimensional diameter for various flow rates while open symbols stand for 0.3 XG+T and close symbol represent 0.5 XG+T.

In Newtonian fluids larger drops with less viscous solutions are generated due to the higher viscous pressure in the thread which results in longer filaments with less material being formed [111, 112]. On the other hand increase of dispersed phase viscosity will cause the shear

force to increase, due to the direct relationship of viscosity ratio λ ($=\mu_d/\mu_c$) and shear force, and resulting in smaller droplets [111]. An increasing drop formation frequency takes place with increasing μ_d and smaller droplets are produced

In order to have a better understanding about the effects of Xanthan gum concentration on the droplet size, Figure 3.25 presents the variation of droplet diameter as a function of the Xanthan gum concentration in comparison with water with 2 wt% of Tween 20 (W+T).

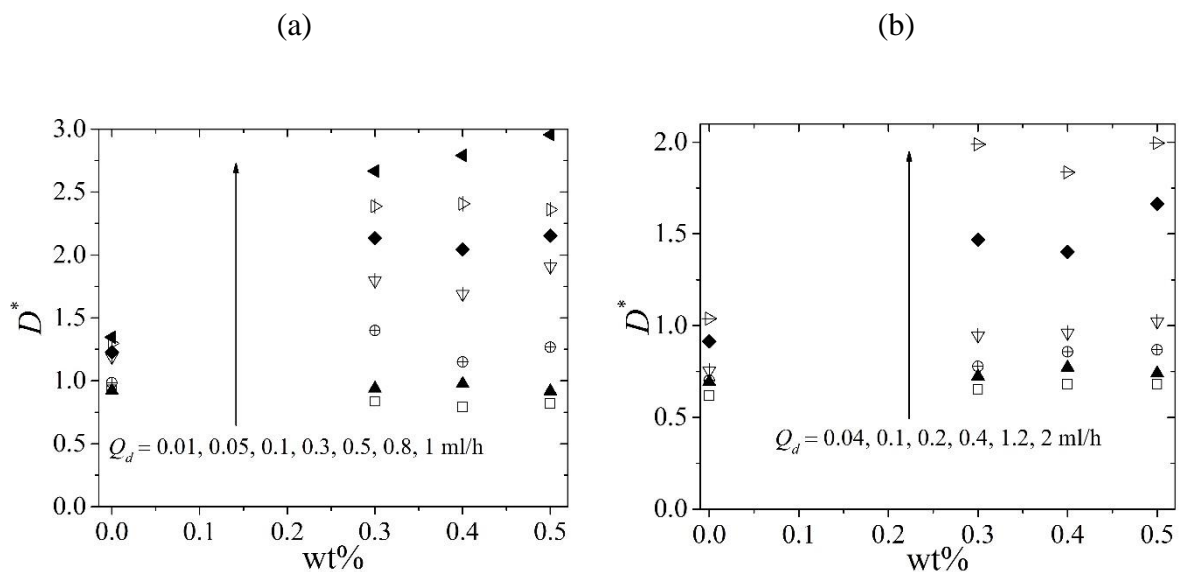


Figure 3.25. Effect of Xanthan gum concentration on droplet non-dimensional diameter as a function of Xanthan gum concentration (wt%) when $Q_c =$ (a) 1 and (b) 4 ml/h.

Although the droplet size variation is not very large with the concentration of Xanthan gum used in the aqueous solutions, within each regime larger droplets are generally produced by using non-Newtonian solutions with higher concentrations of Xanthan gum. It seems that the viscosity is not responsible of the droplet variation. However, further work is needed in order to better understand the physics of the process. In fact, interactions between polymer molecules can play an important role in droplet formation mechanism, as observed by Southwick *et al.* [113].

3.2.10 Effect of Ca_d

The different working fluids used in these tests allow exploiting information about the role played by the viscosity ratio λ on the droplet formation.

In the literature most studies are dedicated to the role played by the continuous Capillary number Ca_c on the droplet characteristics. For Newtonian fluids, it is easy to demonstrate that the droplet regimes depends only on Ca_c , α and λ (see the data reduction section of this thesis). In fact, starting from the definition of Ca_d ($Ca_d = u_d \mu_d / \sigma$) it is easy to demonstrate that this parameter is univocally linked to the volumetric flow rate ratio and to the Capillary number linked to the continuous phase as follows:

$$Ca_d = 2\lambda\alpha Ca_c \quad (3-1)$$

where λ is the viscosity ratio of the immiscible liquids ($= \mu_d / \mu_c$). Since for Newtonian fluids λ is constant, if the values of α and Ca_c are fixed the value of Ca_d is fixed too.

For non-Newtonian liquids, during the droplet formation the shear rate varies and the viscosity of the dispersed phase varies too. It is not easy to take into account the variation of the rheological properties during the droplet formation. However, an order of magnitude of the values assumed by the viscosity ratio during the experimental runs can be obtained by calculating the viscosity of the continuous and of the dispersed phase at the inlet of the cross-junction in correspondence with the maximum and minimum values of the imposed flow rates at the inlets. In Table 3.5 the typical values of λ , obtained by considering the values of the shear rate of the dispersed phase at the inlet of the cross-junction, are shown as a function of the droplet regime.

Table 3.5. Characteristic values of viscosity ratio λ for the working fluids considered in this work.

Dispersed/Continuous	W/SO	(W+T)/SO	(XG+T)/SO
λ @ 23°C	0.049	0.056	0.2 XG+T
			0.3 XG+T
			0.5 XG+T
			$1.1 < \lambda < 48.5$
			$1.7 < \lambda < 109.2$
			$5.6 < \lambda < 472.5$

The data quoted in Table 3.5 highlight that for the Xanthan gum aqueous solutions (XG+T), the viscosity ratio is strongly variable with the applied shear rate ($\dot{\gamma}$). It is evident that a large variation of the viscosity ratio is expected going from low flow rate values at the inlet (low shear rates at the entrance) to large flow rate values.

In Table 3.6 the values assumed by the viscosity ratio (λ) in presence of Xanthan gum solutions as dispersed phase for each droplet regime are shown. These values have been obtained by considering the range of values of Q_c and Q_d obtained by Figure 3.17 for each droplet regime. The regimes obtained by imposing, at the inlet of the cross-junction, lower flow rate values (i.e. SR) are characterized by larger values of λ . Lower values of λ are coupled to the regimes which need larger flow rates at the inlets.

It is important to highlight that, since the position of the liquid/liquid interface varies during the droplet formation, the local value of the viscosity of the non-Newtonian dispersed phase changes and the value assumed by λ varies locally. The local variation of λ during the droplet formation is not accounted for by the values reported in Table 3.6; in fact these values have been obtained by estimating the viscosity of the continuous and dispersed phase at the inlet of the cross-junction.

Table 3.6. Typical viscosity ratio range for each observed droplet regime.

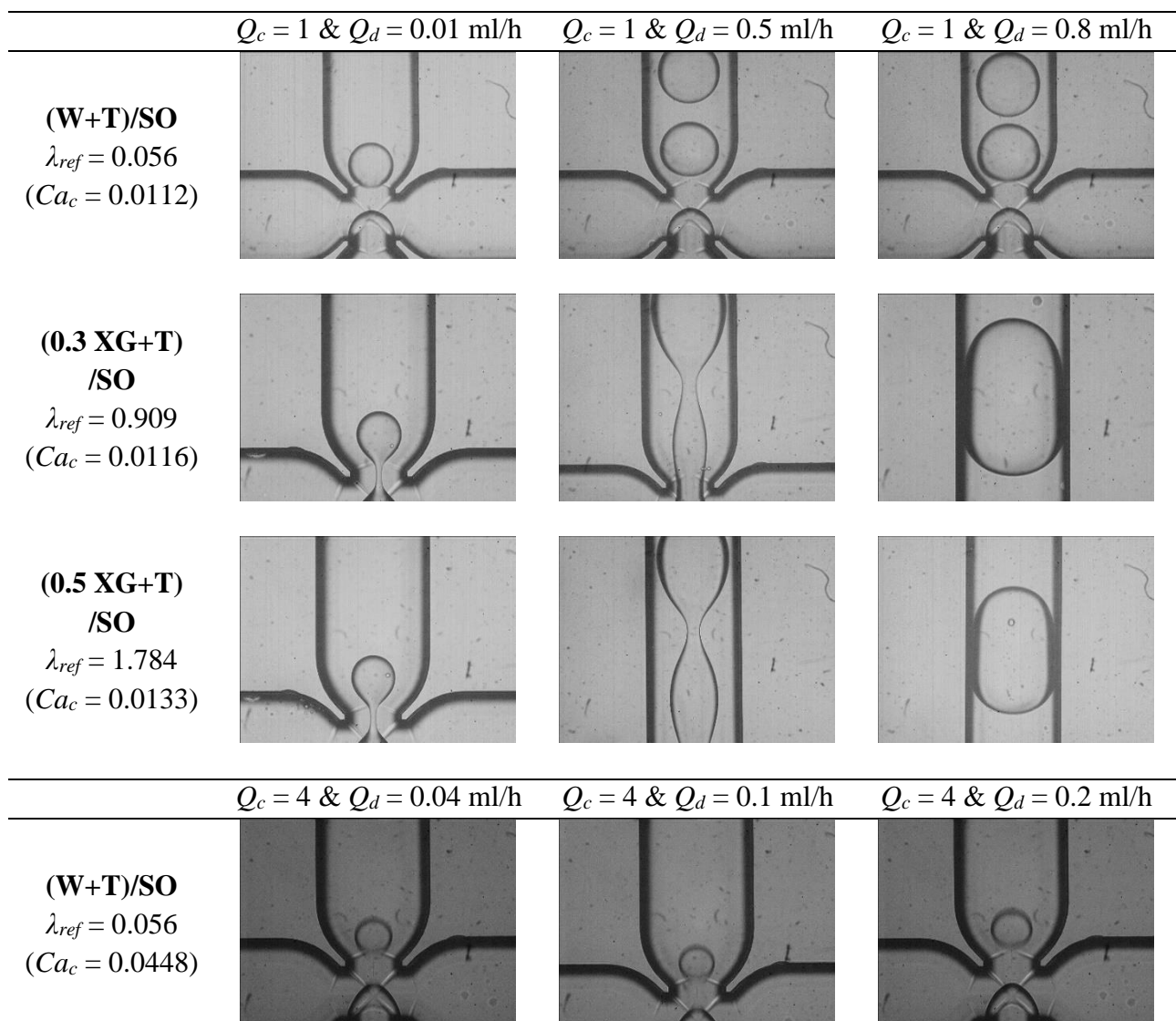
Droplet regime	Dispersed/Continuous phase	
	(0.3 XG+T)/SO	(0.5 XG+T)/SO
Squeezing (SR)	$9.08 < \lambda < 109.2$	$48.8 < \lambda < 472.5$
Dripping (DR)	$2.4 < \lambda < 29.4$	$8.5 < \lambda < 82.7$
Jetting (JR)	$1.7 < \lambda < 7.36$	$5.6 < \lambda < 15.3$

The values of λ shown in Table 3.6 underline that Xanthan gum solutions coupled to silicone oil are characterized by very large values of the viscosity ratio if compared with the values of W/SO and W+T/SO. For large values of λ the thread between the nozzle and the droplet becomes longer and thicker because the dispersed phase is able to accept greater deformations. The non-negligible effect of λ on the transition between the droplet regimes underlines that in presence of non-Newtonian liquids having an apparent viscosity influenced by the shear rate the description of the droplet breakup by using only the Capillary number linked to the continuous phase can be not sufficient because the Capillary numbers for both phases have to be considered as governing parameters.

Figure 3.26 depicts the droplet formation process of different dispersed phase emulsions

including Newtonian (W+T) and non-Newtonian (0.3 XG+T and 0.5 XG+T) droplets.

By observing Figure 3.26, an increase of the flow rate ratio α in each row is responsible for the increase of the dispersed phase flow rate Q_d at the same continuous Capillary number Ca_c ($Q_c = Const.$). The droplet regime observed varies with different values of Q_d imposed at the entrance of the junction. The transition among the controlling regimes may be easier understood by considering the images for emulsions of 0.3 XG+T. It is evident that the droplets generated in microchannels are controlled by the properties of both phases.



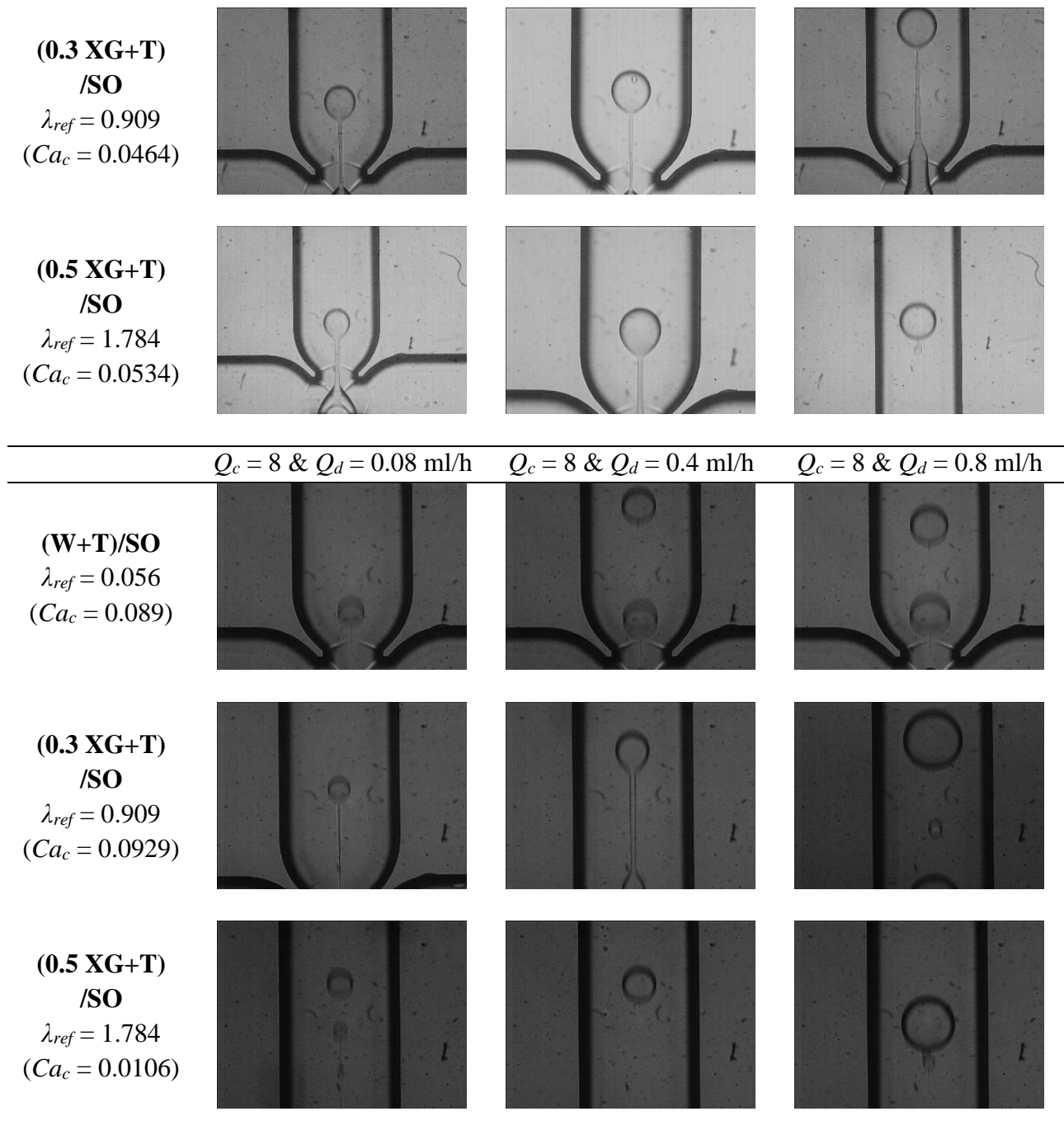


Figure 3.26. Images of the droplet formation process for different controlling regimes.

Husny and Cooper-White [63] modified the Capillary number by applying a force balance between the shear force and interfacial tension on the droplet and included the effect of viscosity ratio as follows:

$$Ca_c = \left(\frac{3 + 2\lambda}{1 + \lambda} \right) \frac{\mu_c u_c}{\sigma} \quad (3-2)$$

where λ ($= \mu_d/\mu_c$) is the viscosity ratio and $((3+2\lambda)/(1+\lambda))$ used also in shear force is obtained from the modified drag coefficient for creeping flow outside a fluid sphere as first defined by Hadamard [89] and Rybczinski [90].

$$C_{Def} = \frac{8}{Re_D} \left(\frac{3+2\lambda}{1+\lambda} \right) \quad (3-3)$$

However, the Capillary number presented in Equation (3-2) is only useful for the description of the droplet behavior in dripping and jetting regimes where shear force plays a more important role.

The droplet flow regimes for Water (W), Water with Tween 20 (W+T) and 0.3 and 0.5 wt% Xanthan gum solutions with Tween 20 (0.3 XG+T, 0.5 XG+T) are presented in Figure 3.27 at different Ca_c and Ca_d values.

The distribution of the different droplet regimes in the plane (Ca_d, Ca_c) indicates that, for a fixed Ca_c , the droplet regime can be changed by increasing Ca_d .

The value of Ca_d is obtained by using Equation (3-1); it is evident that the use of Ca_d enables to take into account, at the same time, the effect of the flow rate ratio (α) and of the viscosity ratio (λ) on the droplet regimes. It is possible to observe that the plot of the droplet regimes on the (Ca_d, Ca_c) plane enables to distinguish better the boundaries of each droplet regime.

Figure 3.27 underlines that the transition from squeezing to dripping to jetting is generally obtained by increasing both Ca_c and Ca_d . An increase of λ produces an increase of Ca_d and hence is beneficial in order to obtain a transition from a droplet regime to another one for a fixed value of Ca_c and α .

These results are qualitatively in agreement with a series of previous studies [29, 60, 66, 114] and with the results shown by Nunes *et al.* [50].

It is evident that three regions can be evidenced; at low values of both Ca_d and Ca_c the squeezing regime is generally observed. On the contrary for large values of both Ca_d and Ca_c jetting is activated. Dripping regime is obtained as intermediate regime by modulating Ca_d and

Ca_c . However, the boundaries between the three regimes are not so clear, as indicated by the data reported between dripping and jetting regimes.

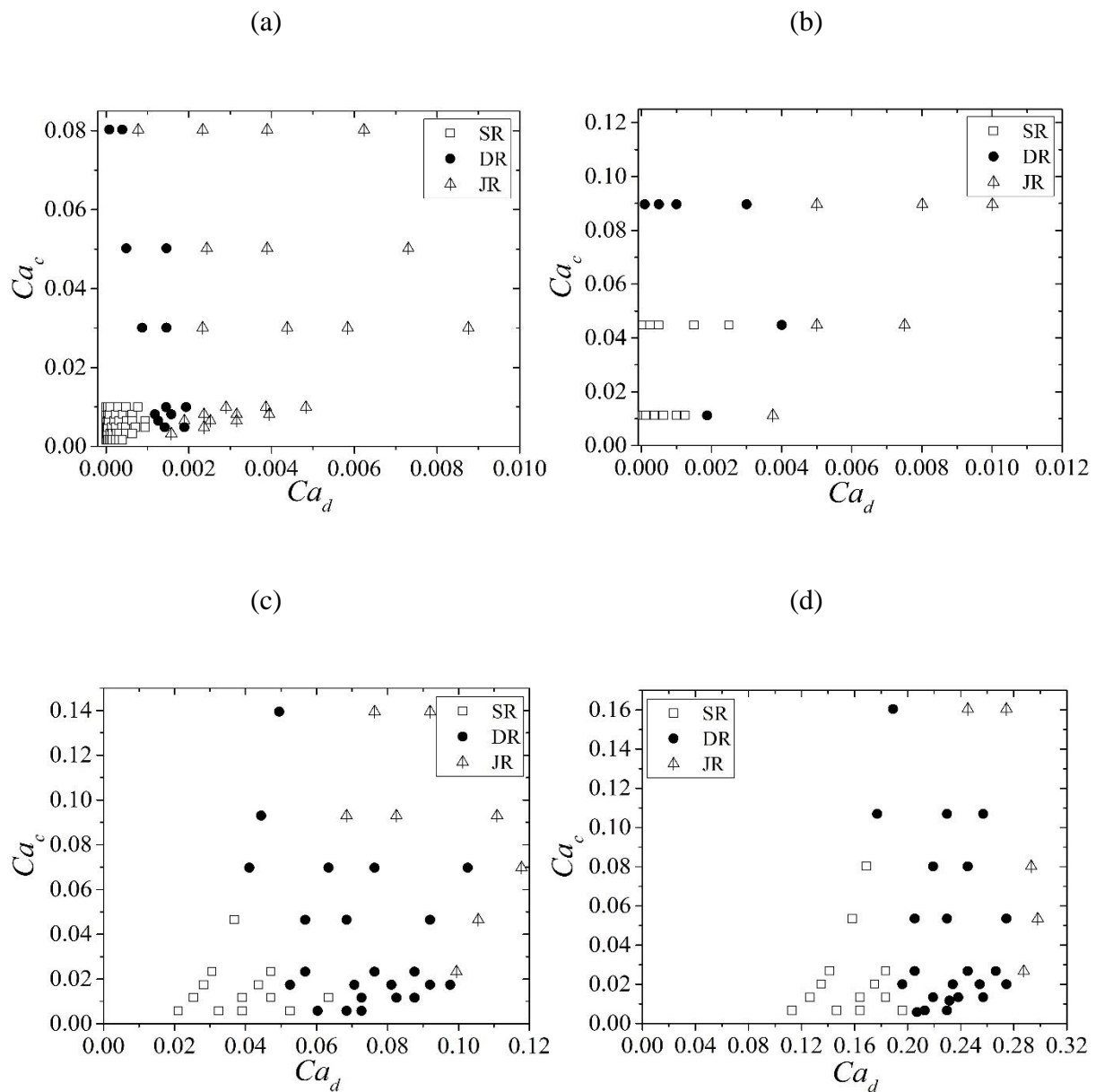


Figure 3.27. Droplet regime map at different Ca_c and Ca_d ; (a) W, (b) W+T, (c) 0.3 XG+T and (d) 0.5 XG+T.

3.3 Droplet formation dynamics

Until now a characterization of the droplet generation in terms of droplet regimes has been described without to give specific indications about the evolution of the droplet interface

during the droplet formation. However, this kind of information is very useful for the calibration of the numerical models and in this section the analysis of the droplet formation, restricted to low values of the Capillary number Ca_c , will be given.

3.3.1 Droplet formation time

The droplet formation time t_f , as an important parameter that must be taken into account if a droplet generator must be characterized. This parameter is important because it is linked to the droplet size and to the frequency of the droplet at the exit of the generator.

The droplet formation time is defined as the time interval between the breakups of two consecutive droplets; this time can be obtained as the sum of the duration of three stages:

- (i) Induction stage t_i ,
- (ii) Growth stage t_g and
- (iii) Breakup stage t_b

The order of magnitude of these intervals depends on the imposed flow rates of the fluids at the inlets of the generator, as well as on the properties of the fluids. At low values of the dispersed volumetric flow rate the time interval linked to the induction stage is generally negligible. By increasing the continuous phase flow rate Q_c and keeping fixed the flow rate ratio α , the droplet generation becomes more difficult because the interface is not able to penetrate within the main channel and the time interval linked to the induction stage becomes very large. For instance, in water emulsions when the continuous phase flow rate Q_c is equal to 39.5 ml/h and α is less than 0.1, the duration of the induction stage can be very long.

3.3.1.1 Effect of Q_c

The influence of the continuous phase flow rate Q_c on the droplet formation time t_f has been studied both for Newtonian (W+T) as well as non-Newtonian (0.3 XG+T and 0.5 XG+T) emulsions by varying Q_c from 0.3 to 12 ml/h for a fixed value of $Q_d = 0.1$ ml/h. The results are shown in Figure 3.28 in a log-log plot.

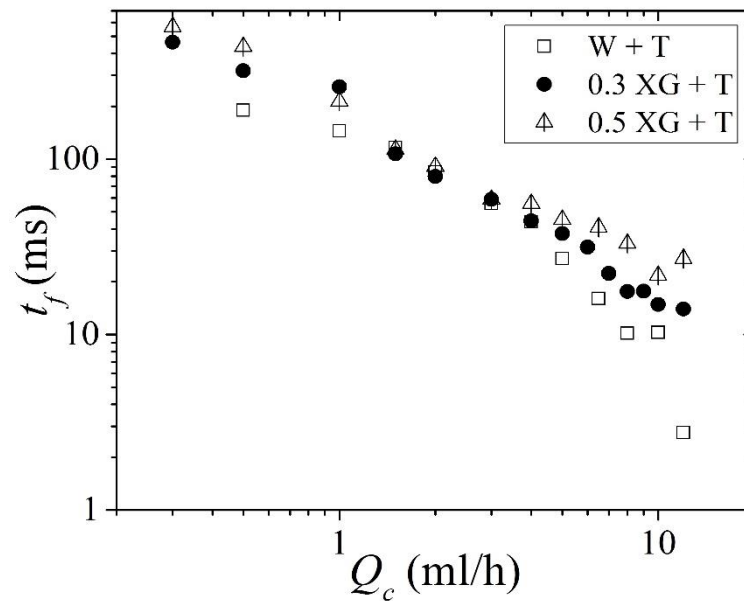
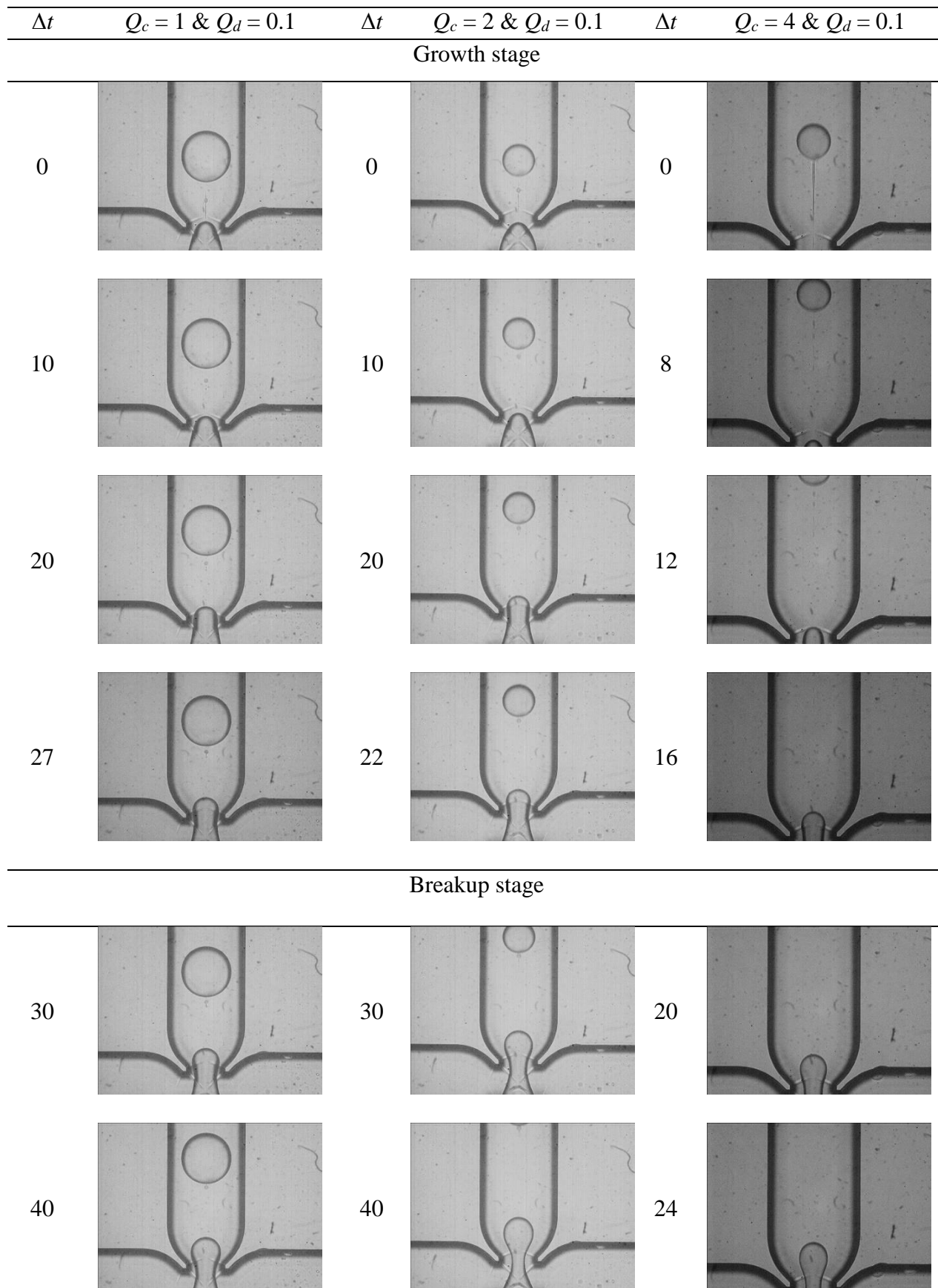


Figure 3.28. Droplet formation time against Q_c .

The drop formation time shows an exponential decrease with the increase of Q_c when Q_d is fixed. This fact can be explained by considering that an increase of the continuous flow rate pinches-off the interface earlier and propels it downstream of the junction. On the other hand, at low values of Q_c the droplet grow lasts more and t_f increases. A similar same trend has been reported recently by Hunsny and Cooper-White [63].

In presence of a non-Newtonian dispersed liquid the droplet formation time is longer due to the formation, before the droplet breakup, of a long filament which delay the detachment of the droplet due to the higher dispersed phase viscosity μ_d of the non-Newtonian solution. In fact, the viscous pressure increases with viscosity and opposes the capillary pressure, dampening surface oscillations and, hence, increasing the lifetime (and length) of the primary thread [69, 115].

The droplet formation time of 0.2 XG+T by varying Q_c is illustrated in Figure 3.29 by means of a series of images which put in evidence the typical evolution of the droplet interface during the droplet formation.



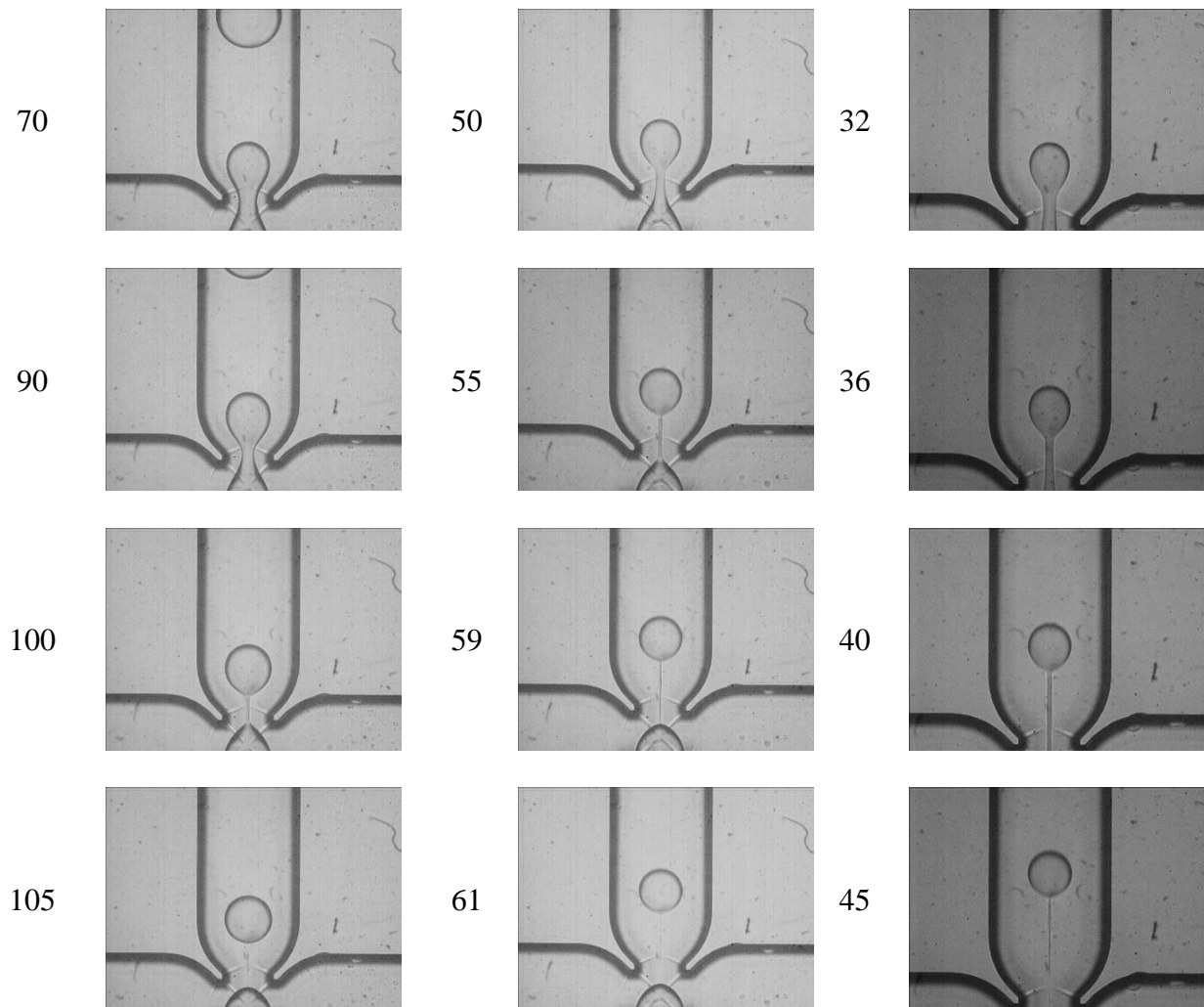


Figure 3.29. Droplet formation time t_f (ms) as a function of Q_c (ml/h) for 0.2 XG+T.

When Q_c is increased, the formation time linked both to growth and droplet stage is strongly reduced thanks to the enhancement of the shear force responsible of the droplet detachment.

3.3.1.2 Effect of Q_d

The droplet formation time depends on dispersed phase flow rate as well. The role of Q_d has been studied by fixing $Q_c = 4$ ml/h and changing Q_d from 0.04 to 4 ml/h. The droplet formation time decreases with increasing Q_d with an approximately exponential trend regardless of variation in viscosity for both Newtonian and non-Newtonian properties as verified by Arratia *et al.* [72] as a function of flow rate ratio. Increase of Q_d causes a decrease of all stages of the droplet formation time as shown in Figure 3.30.

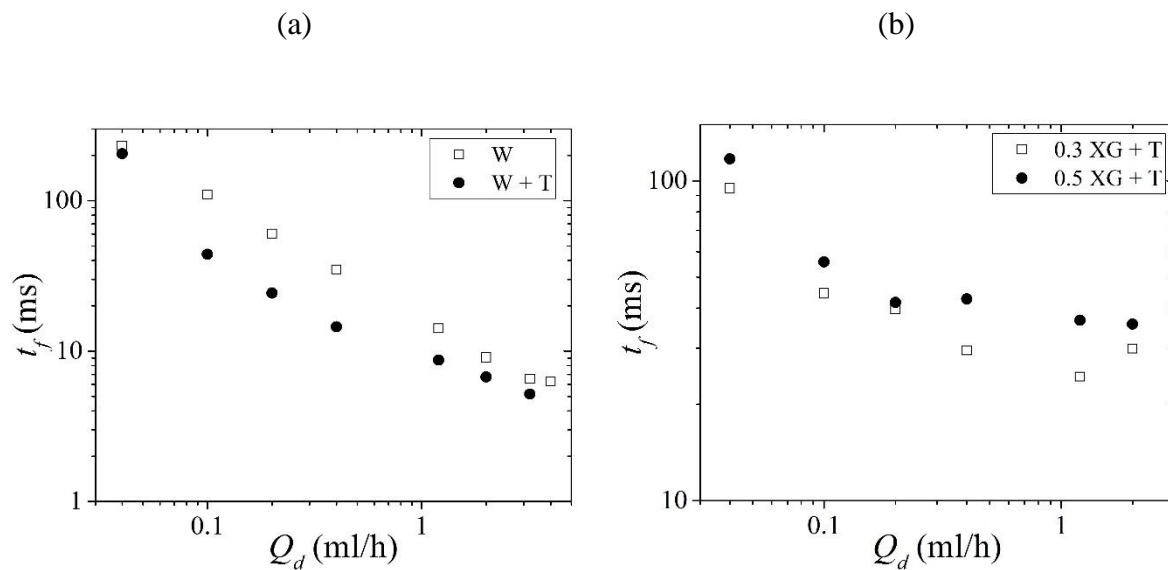
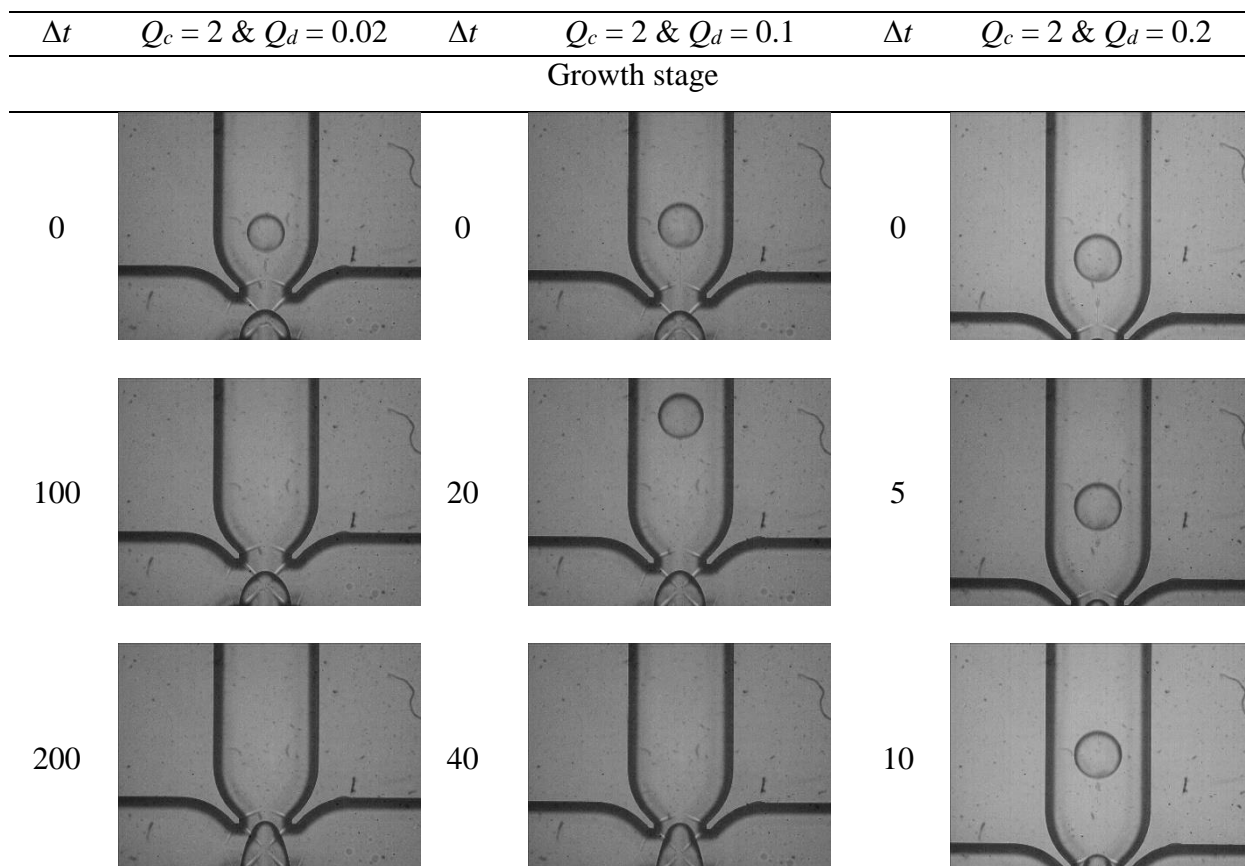


Figure 3.30. Droplet formation time against Q_d for (a) Newtonian and (b) non-Newtonian emulsions.

The interface evolution during the droplet formation is shown for different combinations of Q_c and Q_d in Figure 3.31.



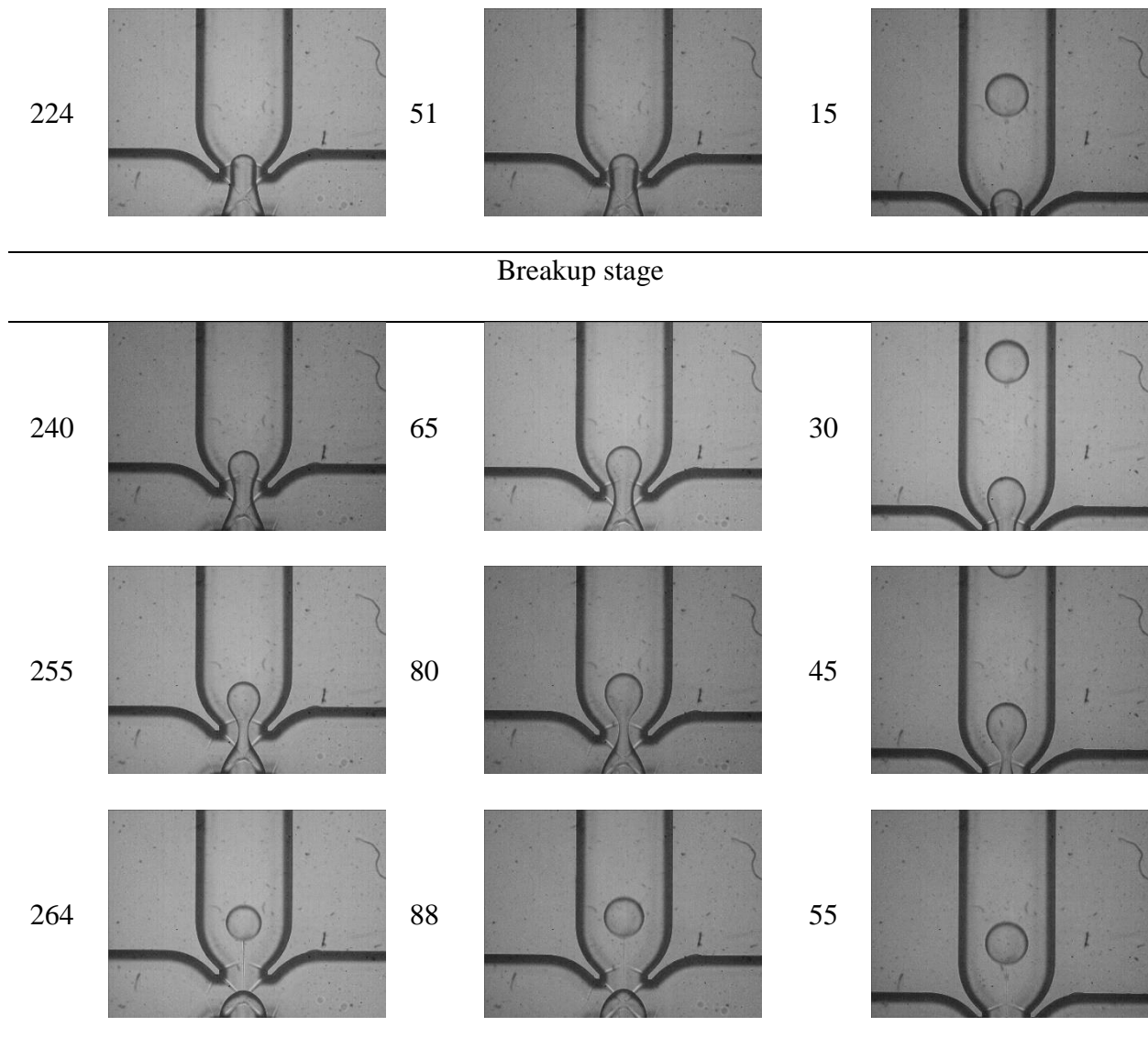


Figure 3.31. Droplet formation time t_f (ms) as a function of Q_d (ml/h) for 0.3 XG+T.

When the volumetric flow rate of the dispersed phase is increased, more material is injected into the junction and the droplet formation time diminishes. At low values of dispersed flow rate the duration of the induction stage becomes long because a long time is needed to the droplet to penetrate the main channel. As the detachment of the droplet depends in the conditions shown in Figure 3.31 on the continuous flow rate, the breakup stage is more or less constant.

In Figure 3.32 the droplet generation frequency obtained by using pure water as dispersed phase, linked to the inverse of the droplet generation time, is shown as a function of the dispersed volumetric flow rate. Each point has an error bar which shows the variation of the droplet frequency observed experimentally. This variation is essentially due to the duration of

the induction time interval which can vary from a droplet to another one under the same operative conditions. It is well evident that the induction time becomes extremely variable when low values of Q_d are introduced into the junction.

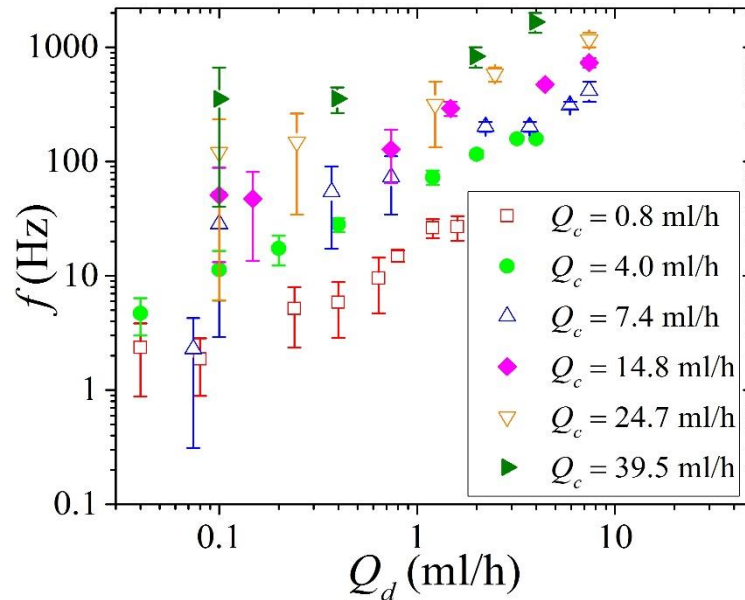


Figure 3.32. Frequency of the droplet f for various values of Q_c and Q_d for pure water (W) emulsions.

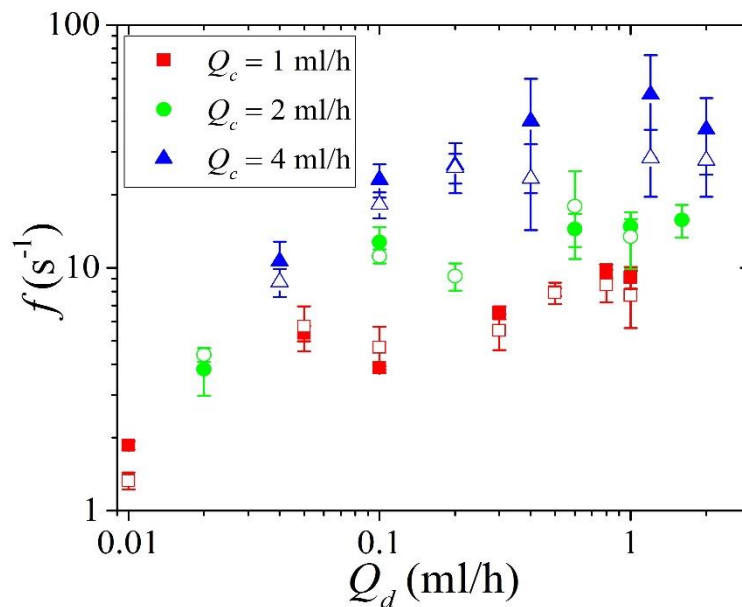


Figure 3.33. Frequency of the droplet f for various values of Q_d when $Q_c = 1, 2$ and 4 ml/h; closed symbols represent 0.3 XG+T while open symbols stand for 0.5 XG+T.

Figure 3.33 shows the droplet frequency as a function of Q_c and Q_d . obtained for two

Xanthan gum solutions (0.3 XG+T and 0.5 XG+T). It is evident that the frequency becomes more stable at low values of Q_d ; on the contrary, the frequency becomes variable at large values of Q_c and Q_d . due to the random breakup of the long thread between the nozzle and the droplet. It is interesting to observe that the droplet frequency obtained with Xanthan gum solutions is one order of magnitude lower than that obtained for water.

3.3.1.3 Effect of Xanthan gum concentration

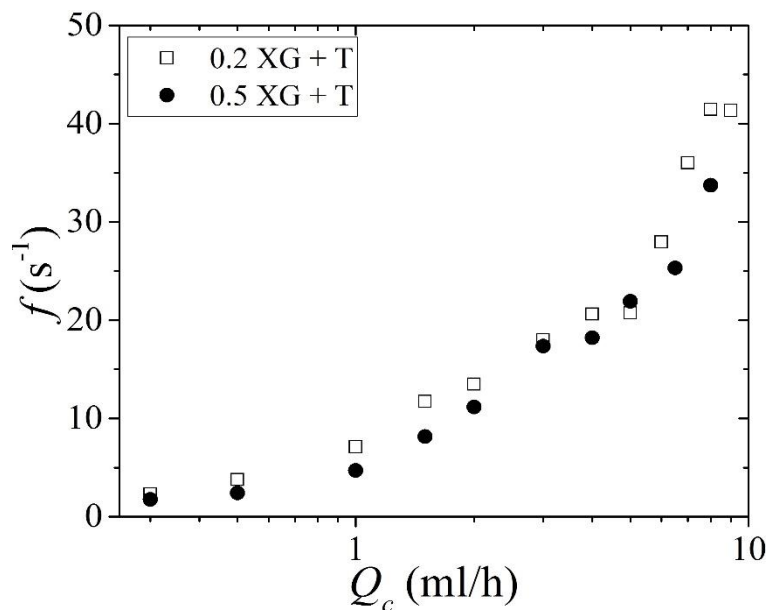


Figure 3.34. Frequency of the droplet f as a function of Q_c for 0.2 XG+T and 0.5 XG+T when $Q_d = 0.1$ ml/h.

Figure 3.34 shows the frequency f of the droplet generation observed for 0.2 XG+T and 0.5 XG+T as a function of Q_c . The data of Figure 3.34 highlight that the difference in terms of frequency obtained by varying the Xanthan gum concentration from 0.2 wt% to 0.5wt% is limited.

In summary, an increase of Q_d generates more droplets and decreases the droplet formation time. On the other hand, it is found that an increase of Q_c increases shear force and causes an earlier detachment of the droplet. As consequence, an increase of Q_d or Q_c will enhance the number of droplets generated per second (f). The effect of the use of surfactant on the droplet frequency has been studied by comparing the data obtained for pure water droplets with those obtained by adding Tween 20 to water. The introduction of surfactant in water increases the droplet generation. By increasing the concentration of Xanthan gum, which is

equivalent to increase the viscosity of the dispersed phase, the number of droplets generated tends to decrease. Higher viscosity values contribute to obtain larger pressure values inside the thread, which opposes the thread breakup and is responsible of longer droplet time formation with respect to water Figure 3.28).

3.3.1.4 Length of microthread

In Figure 3.35 the dimensionless length of the microthread ($\bar{L} = L_{micro}/H$) is plotted as a function of the flow rate ratio α for different concentrations of Xanthan gum. The thread is defined as the liquid connecting the droplet to the source of the dispersed fluid at the entrance of the junction and its length is reduced by increasing α ; longer threads are obtained by introducing a large flow rate of the continuous phase and/or a lower flow rate of the dispersed phase. The microthread is transformed in satellite droplets after the breakup in non-Newtonian emulsions. If the dispersed flow rate introduced into the junction is low, the size of the secondary droplets is small.

The error bars shown in Figure 3.35 highlight the variability of the thread length observed.

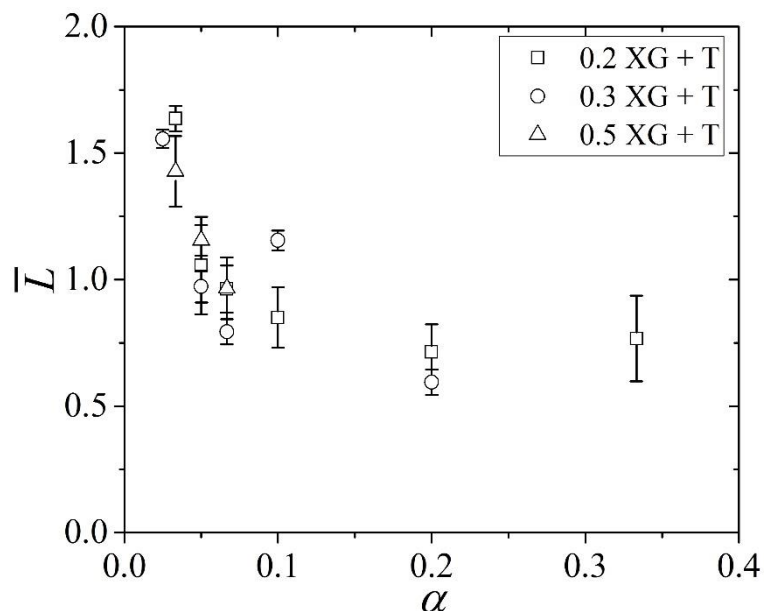


Figure 3.35. Non-dimensional microthread length \bar{L} for three different concentrations of Xanthan gum solution as a function of the flow rate ratio α when $Q_d = 0.1$ ml/h.

Both Q_c and Q_d increase the length of the microthread before the breakup. An increase

of the dispersed flow rate moves the detachment point downstream of the junction. On the other hand, an increase of the continuous flow rate pushes the interface into the junction. In Table 3.7 the values of microthread length as a function Q_c when α increases are shown.

A slight increase of the length of the microthread with an increase of the concentration of Xanthan gum can be observed due to the increase of the viscosity of the dispersed phase.

Table 3.7. Length of microthread L_{micro} (μm) as a function of flow rates of 0.3 XG+T and 0.5 XG+T.

α	$Q_c = 1 \text{ ml/h}$		$Q_c = 2 \text{ ml/h}$	
	0.3 XG+T	0.5 XG+T	0.3 XG+T	0.5 XG+T
0.01	146.85	151.19	182.57	213.41
0.05	149.66	154.33	185.82	221.56

3.3.2 Breakup mechanism

In this section a detailed analysis of the breakup mechanism observed at low Capillary numbers (low Q_c and low Q_d values) is reported. In this subsection the experiments have been carried out for the range of Capillary number ($0.0032 \leq Ca_c \leq 0.0081$) and flow rate ratio ($0.1 \leq \alpha \leq 0.5$) in which squeezing mechanism is dominant. The analysis of the droplet breakup has been limited to low Capillary numbers in order to obtain the complete droplet detachment within the field of view of the microscope.

The analysis of the dynamic evolution of the droplet interface during the breakup is important in order to better understand the physical mechanisms of the detachment. Despite some early work [17, 102, 103], the experimental investigation of the droplet breakup mechanism in cross-junctions has received a little attention. On the contrary, detailed information about this aspect can be very useful for the calibration of the numerical methods proposed for the analysis of droplet generation in micro junctions.

Figure 3.36 shows the evolution of the interface between the immiscible liquids as a function of time for water and Tween 20 (W+T) as dispersed phase in a flow of silicone oil (continuous phase). Time is here indicated by considering as initial time the breakup ($t = 0 \text{ ms}$). Negative times mean that the droplet is in formation process. In Figure 3.36a ($t = -46.4 \text{ ms}$)

the generation of a new droplet after the breakup of the previous one is started; when $t = -26.4$ ms the water droplet starts to penetrate into the exit arm of the junction (Figure 3.36b). Figure 3.36c represents the situation when the necking of the interface starts (at $t = -17.2$ ms before the breakup). From this moment the neck connecting the droplet to the source of the dispersed phase gets thinner (Figure 3.36d).

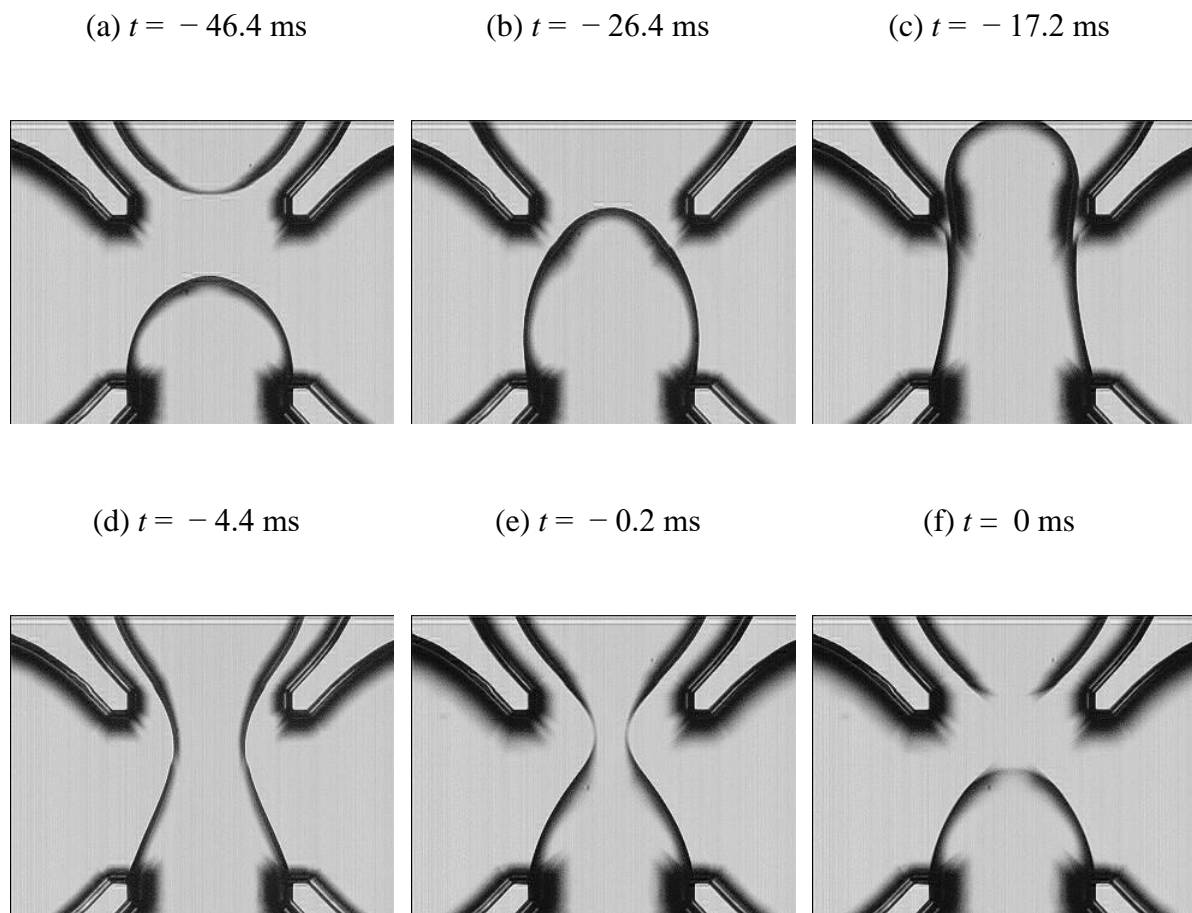


Figure 3.36. The necking in different moments when $Ca_c = 0.0032$ and $\alpha = 0.3$.

The minimum width reached by the water flow during the necking process is $w_{min} = 40.97$ μm , and it occurs when $t = -0.2$ ms (Figure 3.36e). w_{min} indicates the minimum neck of the water flow into the junction before the breakup. Figure 3.36f shows the rupturing moment of the droplet; the generated droplet goes downstream of the junction and the process is repeated to form a new droplet.

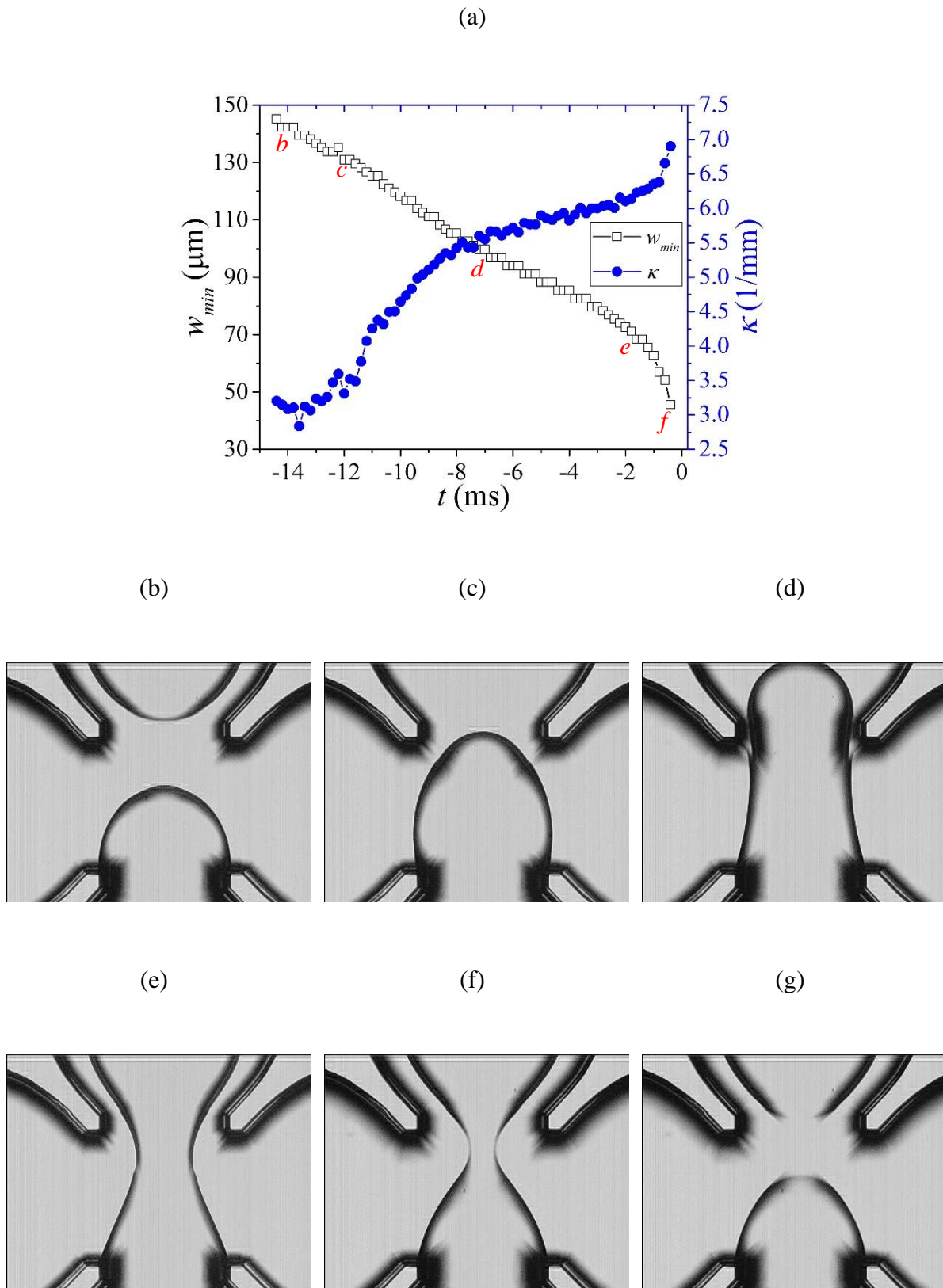


Figure 3.37. (a) Evolution of minimum width w_{min} and the radius of curvature κ of water-oil interface and (b) – (g) necking to rupturing of a water droplet in oil flow when $Ca_c = 0.0032$ and $\alpha = 0.5$.

Thanks to the MATLAB code described in Section 2.6.4, the minimum width of the thread before the breakup has been calculated. The breakup mechanism can be divided in different stages as indicated in Figure 3.37 where the dynamic evolution of the thread thickness (w) and of the radius of curvature of the interface (κ) during the squeezing is shown as a function of time. After the penetration of the interface inside the outlet channel (Figure 3.37b), a very slow movement of the dispersed phase with a little change in minimum width of the thread is observed (Figure 3.37b-c). In the second stage a visible neck develops and the thread width is reduced approximately with a constant rate (Figure 3.37c-d). Now, the aqueous thread is entered inside the channel, the trend of the necking faces a slow variation (Figure 3.37d-e). There is a critical moment (in this case on $t = -2$ ms, Figure 3.37e), in which the penetration of the interface accelerates and the thread reaches its minimum width in a very short period of time (Figure 3.37f). After the breakup (Figure 3.37g), the whole process starts again. On the contrary, the radius of the curvature shows an increasing behavior with time (Figure 3.37a) with a strong acceleration close to breakup.

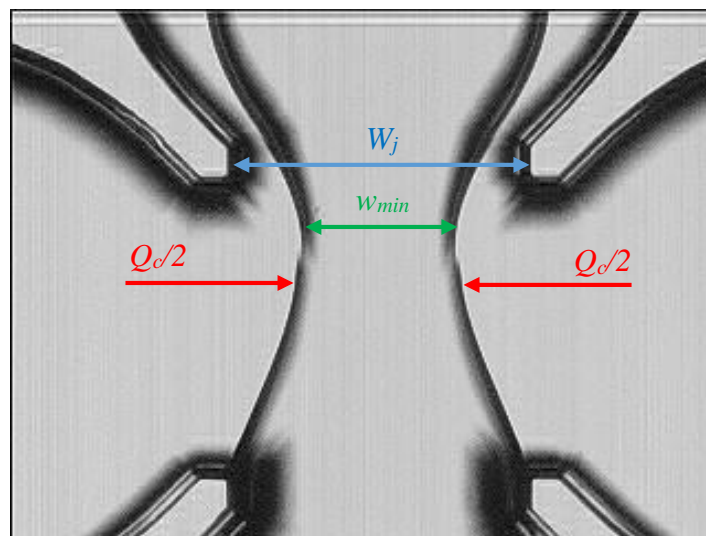


Figure 3.38. The characteristics of the channel and water-oil interface.

By introducing t_{com} as the theoretical time required to the continuous phase to reach the center of the junction under a constant velocity equal to the velocity of the continuous phase at the inlets (Figure 3.38), one can easily find a relationship between the continuous volumetric flow rate and the width of the channel as follows:

$$t_{com} = \frac{W_j}{u_c} = \frac{W_j S}{Q_c} \tag{3-4}$$

where S represents the area of the cross-section of the lateral arms of the junction.

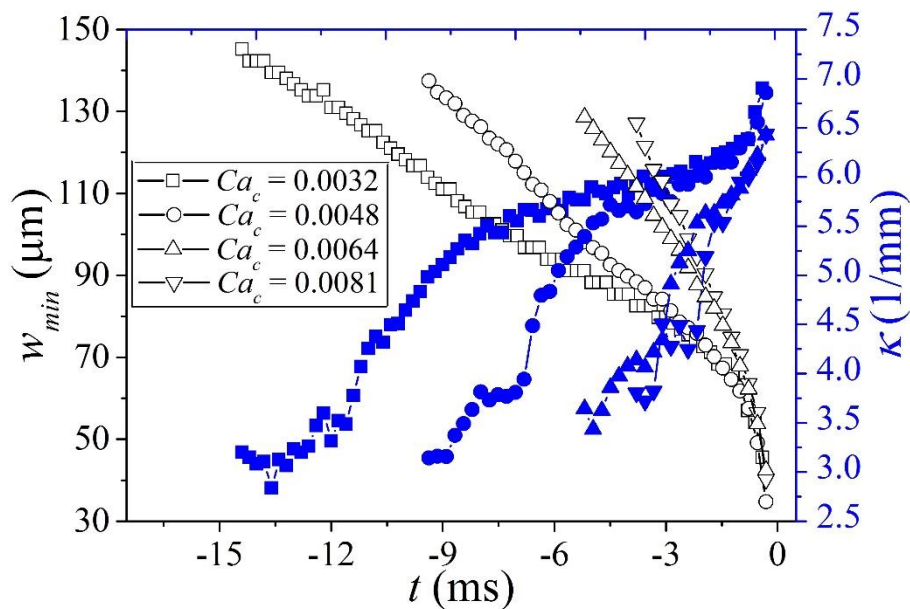


Figure 3.39. The trend of the variation in minimum width w_{min} and radius of curvature κ versus t when $\alpha = 0.5$; open symbols correspond to w_{min} while closed symbols denote κ .

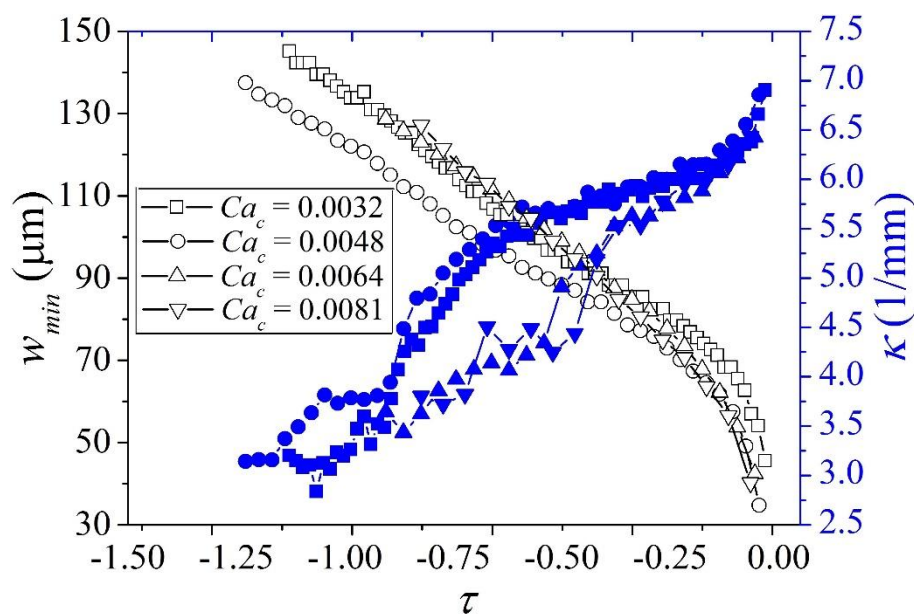


Figure 3.40. The trend of the variation in minimum width w_{min} and radius of curvature κ versus τ when $\alpha = 0.5$; open symbols correspond to w_{min} while closed symbols denote κ .

Figure 3.39 presents the evolution of the width and of the radius of curvature when Capillary number varies from 0.0032 to 0.0081. As anticipated, when w and κ are plotted versus time, with an increase of Ca_c the breakup time decreases but, despite the reasonable trend observed in Figure 3.39, the data are dispersed. In order to obtain a more general trend, it is possible to scale the time by using as characteristic time for this system t_{com} defined previously thanks to Equation (3-4); by using the non-dimensional time τ ($\tau = \frac{t}{t_{com}}$) it is possible to obtain a reduction of the dispersion of the data (Figure 3.40).

3.3.3 Geometry effects

In order to highlight the effect of the junction geometry on the droplet characteristics a comparative study of pure water droplet generation in silicone oil flow has been made by using two commercial micro cross-junctions having a different junction geometry. In Figure 3.41 the geometry of the two junctions are shown; junction #1 is characterized by a gradual reduction of the width of the channels at the junction. On the contrary, junction #2 presents a smaller central region with a constant reduced width of the crossed channels at the junction.

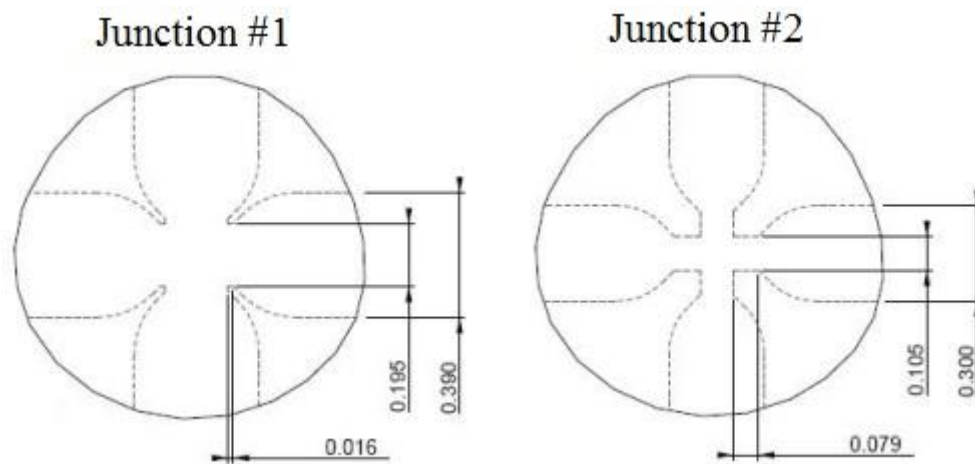


Figure 3.41. Junction geometry and channel dimensions.

Table 3.8 summarizes the main geometrical characteristics of these two micro cross-junctions.

Table 3.8. Characteristic values of the cross-junctions.

Characteristic	Junction #1	Junction #2
W_j (μm)	195	105
W_w (μm)	390	300
H (μm)	190	100
$R = W_j/W_w$	0.5	0.35
$A_j = H/W_j$	0.97	0.95
$A_w = H/W_w$	0.49	0.33

3.3.3.1 Flow maps

A series of experimental runs has been made in order to obtain a droplet regime map by using the two junctions with silicone oil used as continuous phase and pure water as dispersed phase. The map has been obtained by varying the volumetric flow rates of water (Q_d) in the range $0.04 \leq Q_d \leq 49$ ml/h and the silicone oil flow rate (Q_c) in the range $0.8 \leq Q_c \leq 4.9$ ml/h.

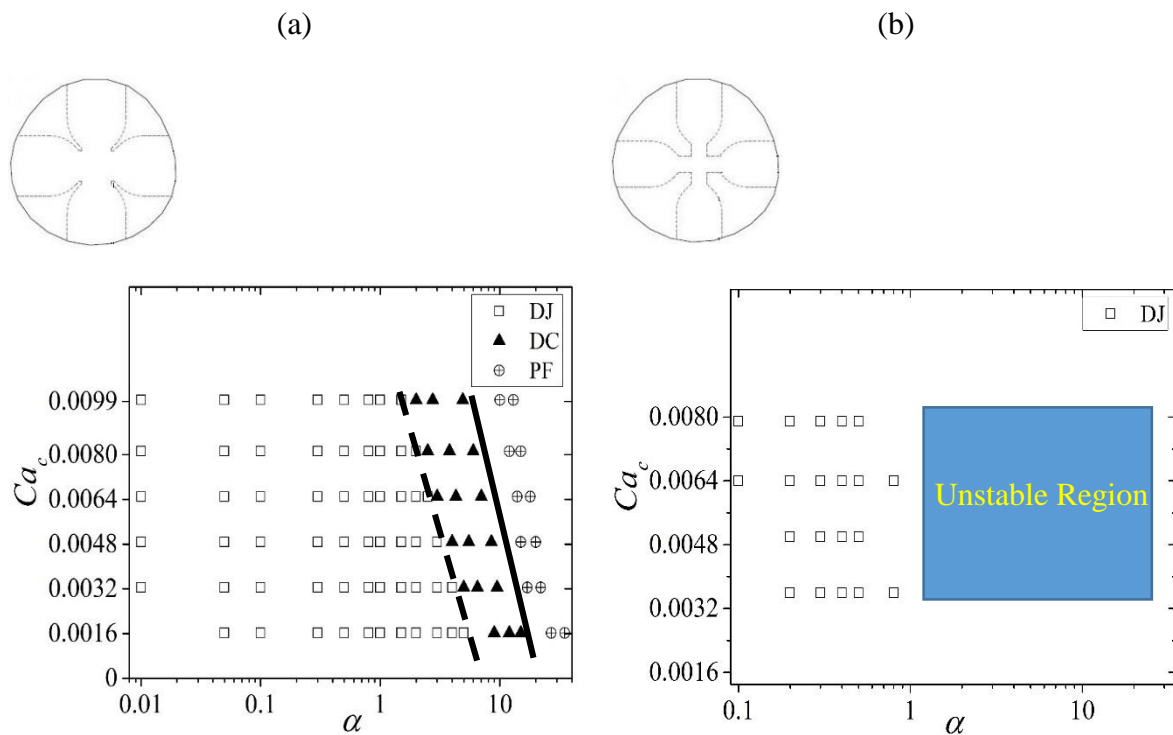


Figure 3.42. Droplet flow regimes as a function of α ; (a) channel #1 and (b) channel #2.

Figure 3.42a puts in evidence that, by changing α and Ca_c , it is possible to obtain with junction #1 all the three droplet regimes (Droplet formed at the Cross-Junction (DJ)), Droplet formed Downstream of the Channel (DC) and Parallel Flow (PF)) observed at low values of Ca_c . On the contrary, by using junction #2 the droplet is generally formed at the cross-junction for low values of Q_d and Q_c but for $\alpha > 1$ an unstable region is observed (Figure 3.42b) where the repeatability of the experimental tests is weak. In that region, characterized by large values of α ; it becomes impossible to generate droplets in a repeatable manner. The low value of R (see Equation (1-11)), characteristic of junction #2, helps to stabilize the squeezing region (which coincides with the DJ regime) by reducing the possibility to obtain droplets thanks to dripping. Junction #2 seems to be very efficient only at low values of Q_d and Q_c .

3.3.3.2 Droplet size at low flow rate ratio

Figure 3.43 shows another evident difference between the two junctions; junction #2, characterized by low values of the restriction ratio R , is able to generate smaller droplets thanks to the reduced dimensions of the central region of junction #2. In junction #2 the distance between the droplets and the channel walls is large; in this case the confinement effect of the channel walls on the droplet is lower than that obtained by using junction #1.

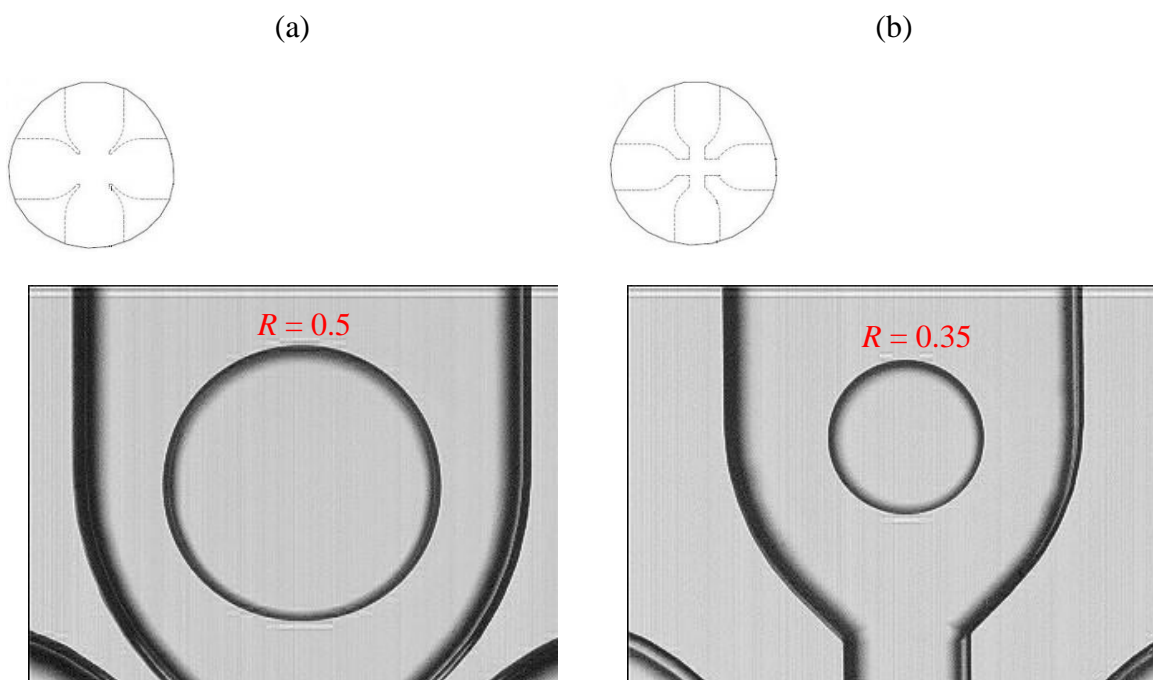


Figure 3.43. Typical droplets generated by using: (a) junction #1 and (b) junction #2.

These results show that the restriction ratio R of the junction is a parameter that can be used to promote the generation of smaller droplets thanks to squeezing at low values of both Q_d and Q_c .

This conclusion is confirmed by the experimental data shown in Figure 3.44 where the non-dimensional diameter D^* of the droplet is plotted as a function of the flow rate ratio (α) for both junction #1 (Figure 3.44a) and junction #2 (Figure 3.44b). For junction #2 the experimental data are obtained only for low values of flow rate ratio since the droplet generation is not stable and repeatable for $\alpha > 1$. In junction #1 D^* can be reduced only by increasing the Capillary number (Ca_c).

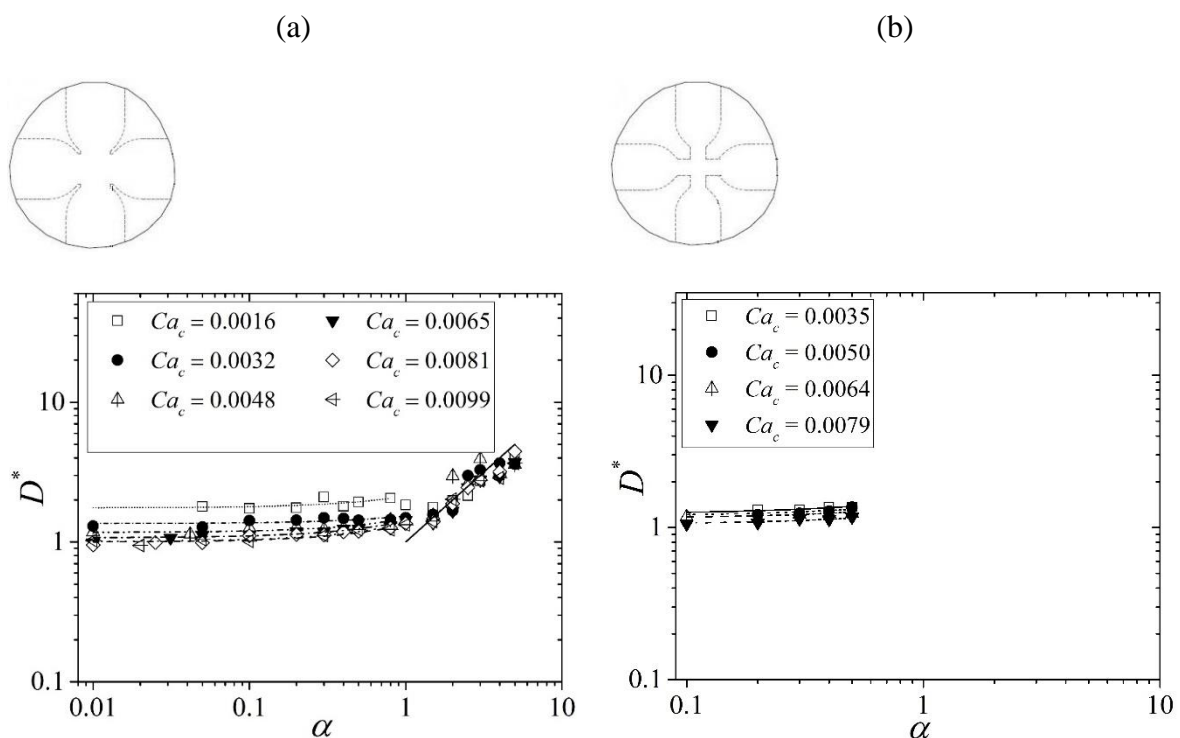


Figure 3.44. D^* as a function of the flow rate ratio (α) for different values of the Capillary numbers Ca_c ; (a) junction #1 and (b) junction #2.

The minimum width of the thread which connects the droplet to the source of the fluid (w_{min}) has been calculated by post-processing the images of the evolution of the interface between the immiscible liquids during the droplet formation. The value of w_{min} is obtained by measuring the minimum width of the thread before the droplet breakup. This value has been scaled on the total width of the junction in the central region (W_j).

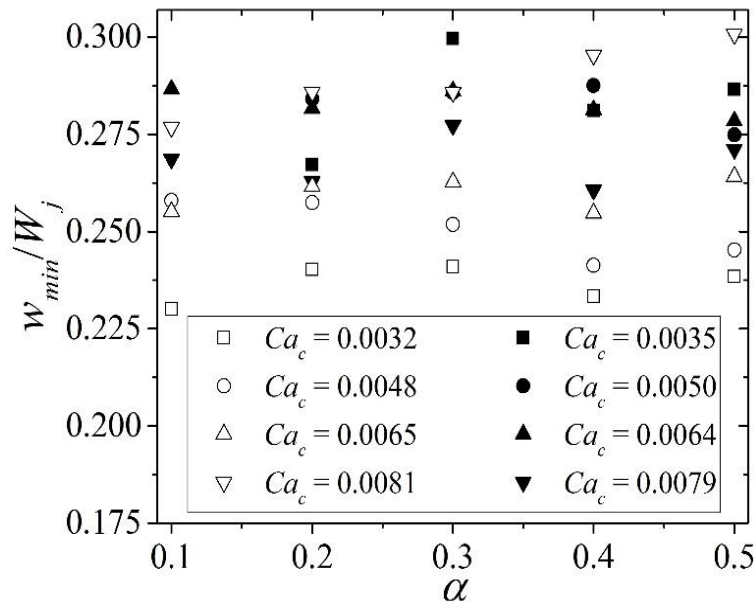


Figure 3.45. The dimensionless minimum width as a function of α ; open symbols correspond to the data for channel #1 while closed symbols denote of channel #2.

Figure 3.45 presents the minimum width as a function of flow rate ratio (α) and of the Capillary number (Ca_c). It is evident that for $\alpha < 0.5$ the minimum width is independent by α ; on the contrary, w_{min} increases with Ca_c . In addition, w_{min} is larger for junction #2.

In Figure 3.46 the dimensionless droplet diameter D^* at low Capillary numbers ($Ca_c < 0.01$) is shown as a function of the volumetric flow rate ratio. Since Q_d affects the droplet volume through the formation time, especially at low flow rates, it can be concluded that both Q_d and Q_c influence the droplet size. A linear correlation in the form of $(\varepsilon + \omega\alpha)$, where ε and ω are two fitting constants, is able to fit the experimental data. Although a general correlation could not be observed for all the experiments, as suggested by Garstecki *et al.* [41], there is a good agreement between data and the correlation if ε and ω are considered as a function of Ca_c .

The correlations presented for junction #1 (Figure 3.46a) fit in a good way the results of channel #2 when $Ca_c > 0.0035$ (Figure 3.46b). It is clear that, by increasing the Capillary number, the agreement between the experimental data obtained by using junction #2 and the correlations enhances. Figure 3.46 highlights that, although the Capillary number is not the dominant parameter in squeezing regime, it still influences the final droplet volume especially at low α values.

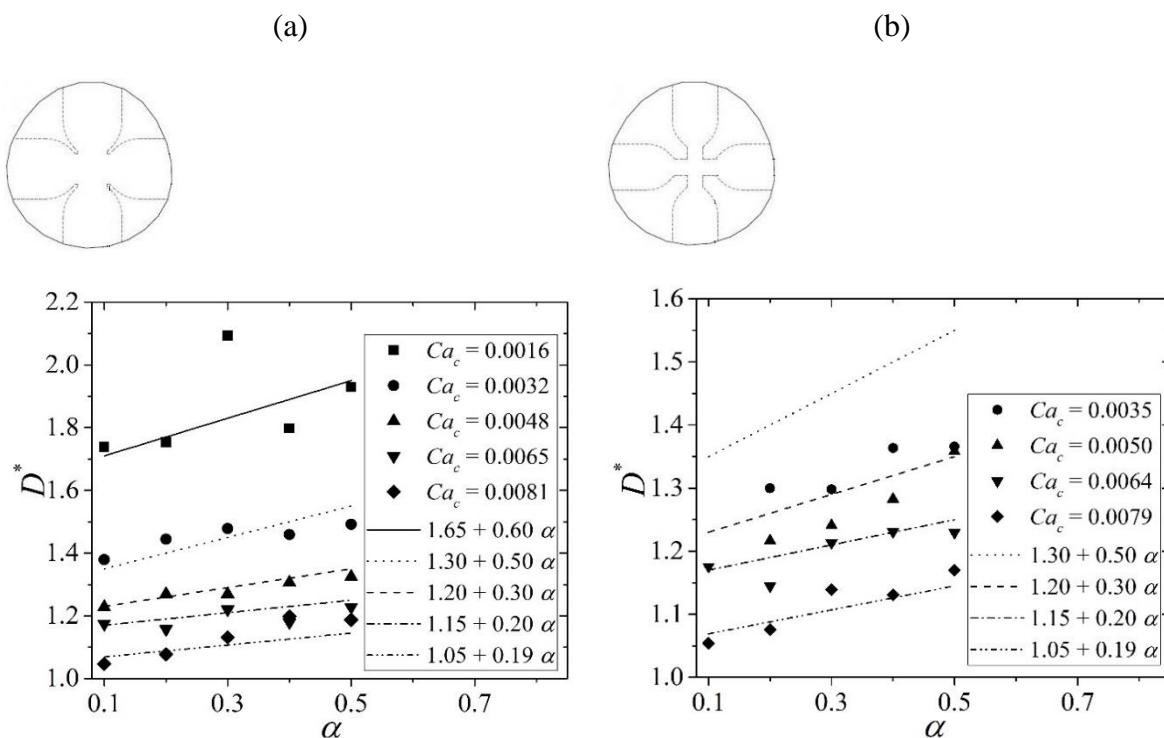


Figure 3.46. D^* as a function of α for different Ca_c values; (a) junction #1 and (b) junction #2.

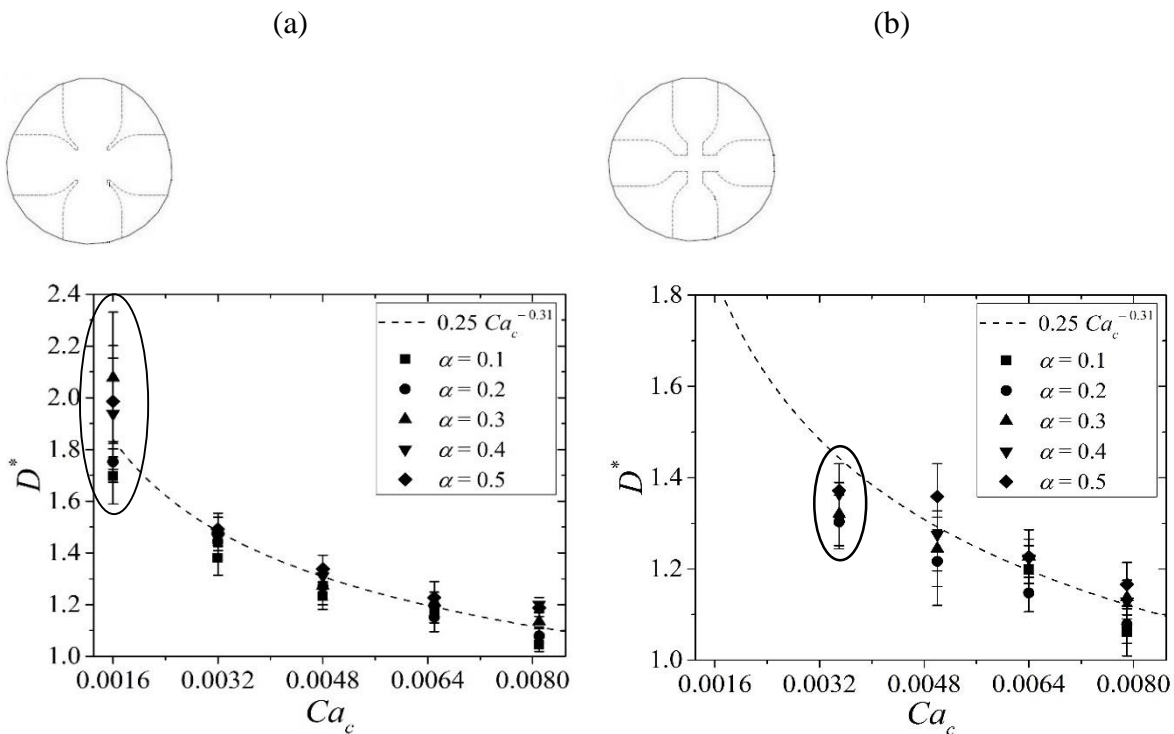


Figure 3.47. Comparison between the power-law correlation ($q Ca_c^x$) and experimental data obtained for (a) junction #1 and (b) junction #2.

In Figure 3.47 a power-law correlation in the form of $q Ca_c^x$, proposed for T-junctions by many authors [39, 42, 57, 105, 106], has been used in order to fit the experimental data obtained with the two junctions. In agreement with the results presented by [39, 57] the power-law exponent x is here taken equal to -0.31 .

It is evident that the correlation able to fit in a good way the experimental data obtained with junction #1 tends to overestimate D^* for junction #2. This result confirms that a junction having a low restriction ratio R tends to produce smaller droplets. R must be inserted in the correlation in order to take into account the effect of the junction geometry.

In order to improve the agreement with the experimental data a new correlation is proposed in which both linear dependence on α and power-law dependence on Ca_c have been considered in Figure 3.48.

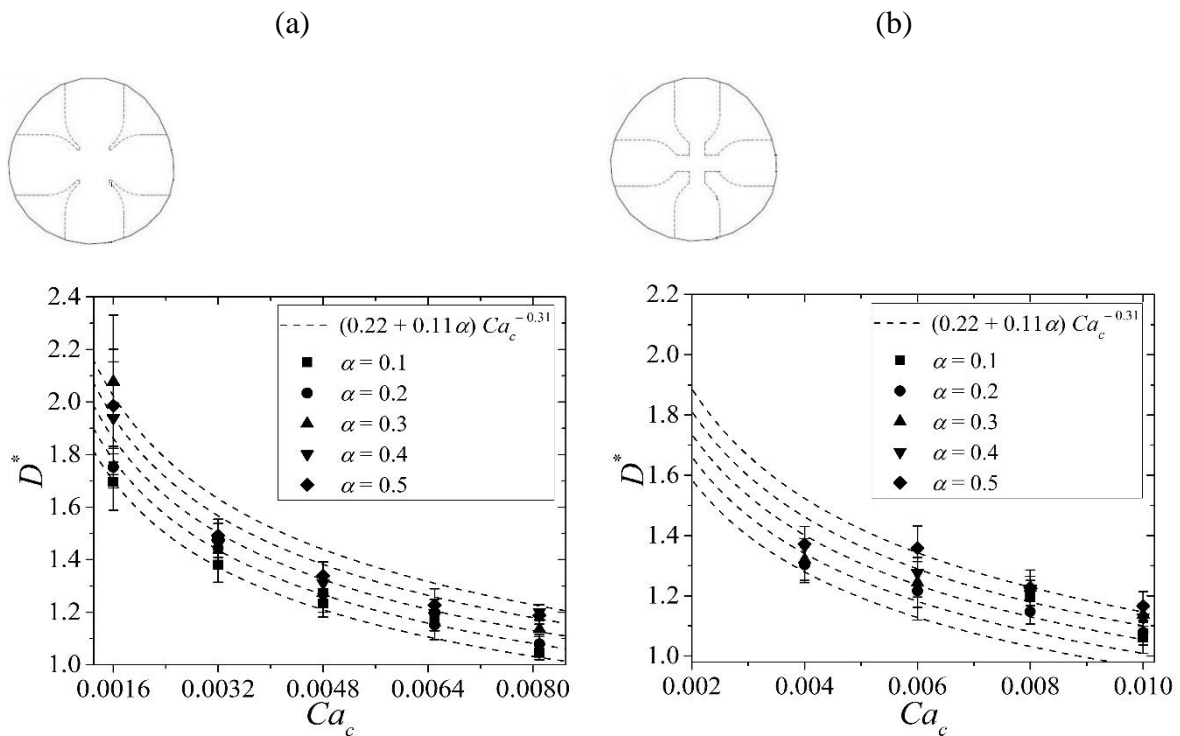


Figure 3.48. Comparison between the new correlation $(\varepsilon + \omega\alpha) Ca_c^x$ and experimental data obtained for (a) junction #1 and (b) junction #2.

The new form of the correlation is the following:

$$D^* = (\varepsilon + \omega\alpha)Ca_c^x \quad (3-5)$$

By tuning the correlation with the experimental data obtained by using junction #1 ε , ω and x can be calculated in order to minimize the difference between the correlation and the data. The coefficients ε , ω and x are taken equal to 0.22, 0.11 and -0.31 , respectively.

The proposed correlation seems to be able to predict qualitatively the trend of the experimental data but the agreement with the experimental data is different for junction #1 and junction #2.

In order to take into account the effect of the different geometry of the junctions, a new definition of the Capillary number can be introduced (modified Capillary number Ca_m). By calculating the shear rate as $G = \Delta u/\Delta z$, the modified Capillary number is defined as:

$$Ca_m = \frac{\mu Ga}{\sigma} \quad (3-6)$$

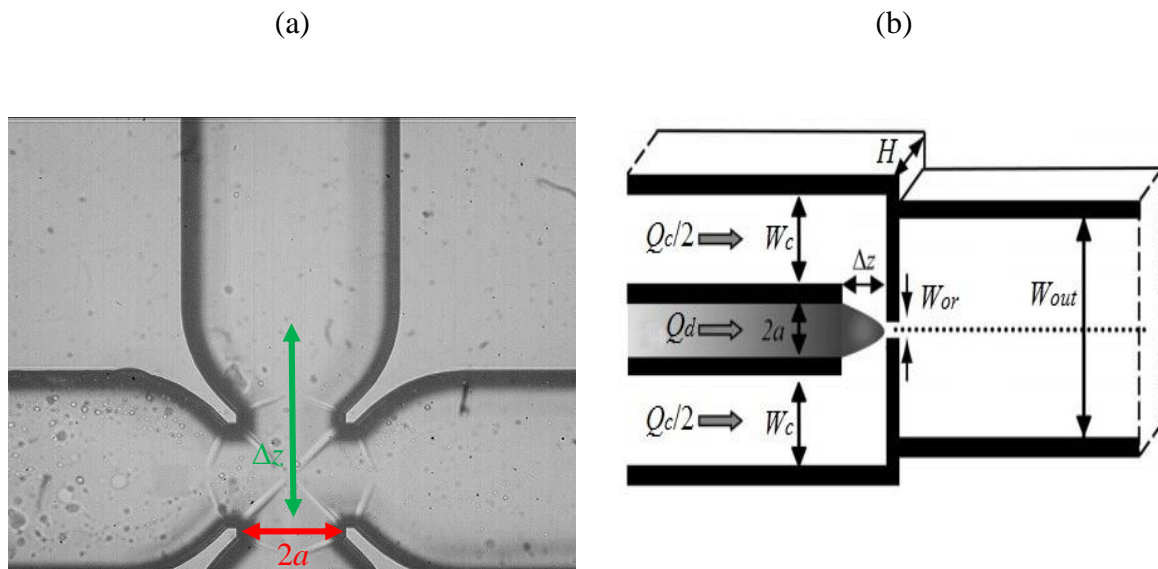


Figure 3.49. Δz and a for (a) the junction used in this thesis and (b) a planar flow-focusing device [28].

This definition has been introduced for planar flow focusing devices in [116]. Here Δz is the distance between the end of the dispersed phase inlet channel and the exit channel (see Figure 3.49a); a denotes the half-width of the microchannel in which the dispersed phase is

introduced into the junction ($W_d = 2a$). In order to create a parallel between the planar flow focusing device geometry and the geometry of the junctions used in this thesis, in Figure 3.49 Δz and a are shown for both the geometries.

The modified Capillary number has been introduced in the correlation described by Equation (3-6). The results obtained with the correlation are compared to the experimental results obtained by testing junction #1 and #2 in Figure 3.50. It is possible to appreciate that the agreement between the correlation and the experimental data is slightly improved.

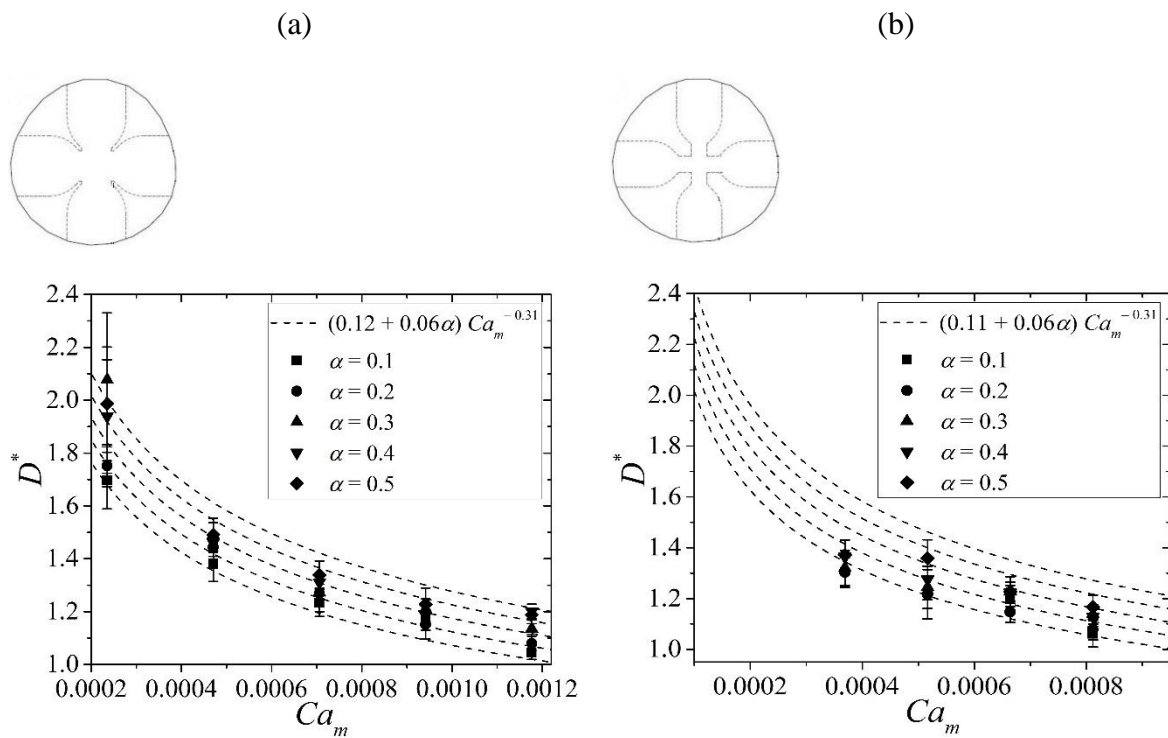


Figure 3.50. Comparison between the new correlation $(\varepsilon + \omega\alpha) Ca_m^x$ and experimental data obtained for (a) junction #1 and (b) junction #2.

Another possible improvement of the correlation could be obtained by introducing the restriction ratio R in the correlation. However, the available experimental results obtained for two geometries are not enough in order to test a correlation in which R is introduced. A larger number of junction geometries is needed in order to test a correlation in which R is introduced.

Chapter 4

Experimental Investigation of Droplet Formation at a

Micro T-Junction

In this section the experimental investigation of the oil-in-water (O/W) droplet production by means of a micro T-junction is described. The experimental data are presented in absence and presence of the Tween 20 to highlight the influence of the surfactant on the flow regimes by varying the flow rates of the continuous and dispersed phase flows in a very wide range.

It has been selected the face-to-face configuration of the T-junction (see Figure 1.2c) because this configuration is less studied than the others for droplet generation. The range of the flow rates imposed at the inlets of the junction is reported in Table 4.1. In this chapter the silicone oil (SO) droplets are being investigated within water (W) and water with surfactant (W+T) along with 0.2 wt% Xanthan gum aqueous solution with (0.2 XG+T) and without surfactant (0.2 XG) as the carrier medium through a glass microchannel, produced by *Translume Co.* described in Chapter 2 (Figure 2.7). All the properties of the liquids have been accurately measured and a detailed discussion about their characterization is reported in Chapter 2 (see Section 2.4).

The glass surfaces of the chip are pure fused silica glass. Nonetheless the surface wettability is a strong function of both the channel material and the manufacturing procedure. As described in Chapter 2 (Section 2.3.2) the width (W) and height of the channel (H) are equal to 300 μm ; therefore, the aspect ratio $A (= H/W)$ and the width ratio $\Lambda (= W_d/W_c)$ are equal to 1.

Table 4.1. Range of volumetric flow rates α and Ca_c tested in T-junction.

DP	CP			
	W	W+T	0.2 XG	0.2 XG+T
SO	$0.05 < Q_d < 100$	$0.1 < Q_d < 13$	$0.01 < Q_d < 16$	$0.01 < Q_d < 8$
	$2 < Q_c < 120$	$1 < Q_c < 25$	$1 < Q_c < 30$	$0.5 < Q_c < 20$
	$3E-4 < Ca_c < 7E-3$	$4E-4 < Ca_c < 1E-2$	$9E-3 < Ca_c < 34E-3$	$37E-3 < Ca_c < 13E-2$
	$0.01 < \alpha < 2$	$0.1 < \alpha < 3.5$	$0.01 < \alpha < 5$	$0.01 < \alpha < 4$

The kind of coating is not the best one in order to obtain O/W droplets because it is problematic to obtain a stable layer of continuous phase (water) close to the microchannel walls. In addition, face-to-face configuration tends to enhance the formation of a parallel co-flow at the outlet of the junction and not droplets as needed. These conditions highlight that we are testing a configuration which is not optimized for the production of O/W droplets. The aim of the investigation is to study in which way it is possible to force to obtain droplets this configuration.

4.1 Water without surfactant

When pure water is introduced into the junction as the continuous phase, it is possible to observe that the generation of the microdroplets is not possible. This is due to the combination of the T-junction configuration (face-to-face) and of the coating of the walls. A co-flow in which two parallel flows (PF regime) fill the microchannel is generally observed at the outlet of the junction for a large range of volumetric flow rates of the continuous and dispersed phases.

Figure 4.1 shows the parallel flow (PF regime) for two values of the continuous volumetric flow rate equal to 3 and 126.2 ml/h. It's worth mentioning that $Q_c = 126.2$ ml/h is the maximum volumetric flow rate reachable by the *Cole-Parmer Version Hills* syringe pump. Therefore, it clearly illustrates the main flow regime of the T-junction in a very wide range of volumetric flow rates.

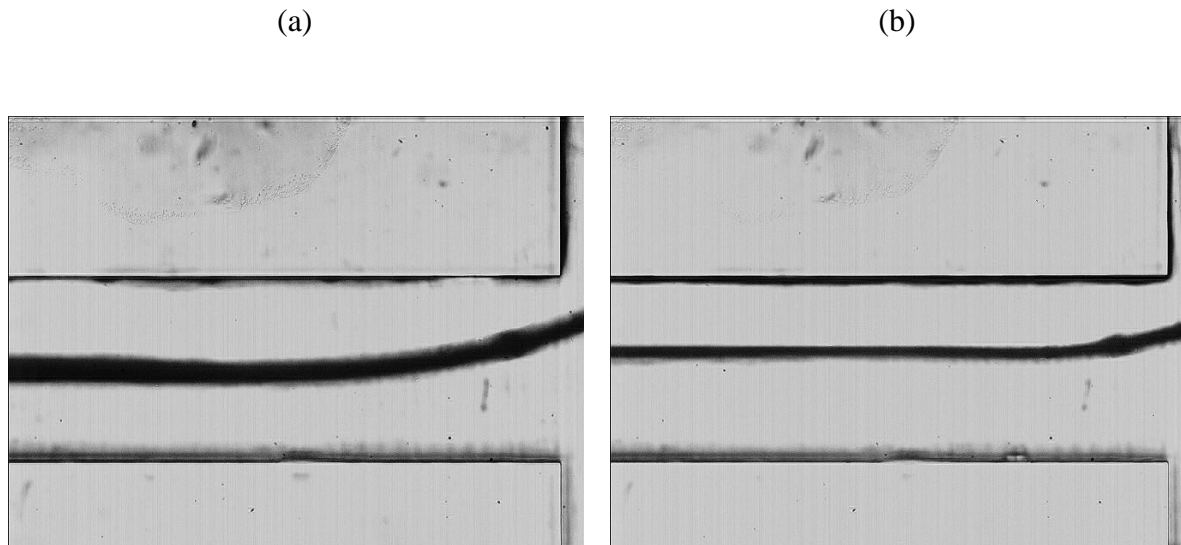


Figure 4.1. Parallel flow obtained by introducing pure water and silicone oil in the micro T-junction when (a) $Q_c = 3$ ml/h and $Q_d = 0.9$ ml/h and (b) $Q_c = 126.2$ ml/h, $Q_d = 15$ ml/h.

It is possible to measure the height of the two co-flow phases during parallel flow regime. By means of the acquired images of the parallel flow obtained at the outlet of the junction when Q_c and Q_d are fixed, it is possible to individuate the thickness of the two immiscible liquids (h_c , h_d) and of the interface, as indicated by Figure 4.2. It is important to observe that the thickness of the interface is not negligible; this is due to the curvature of the interface which assumes a non-planar configuration.

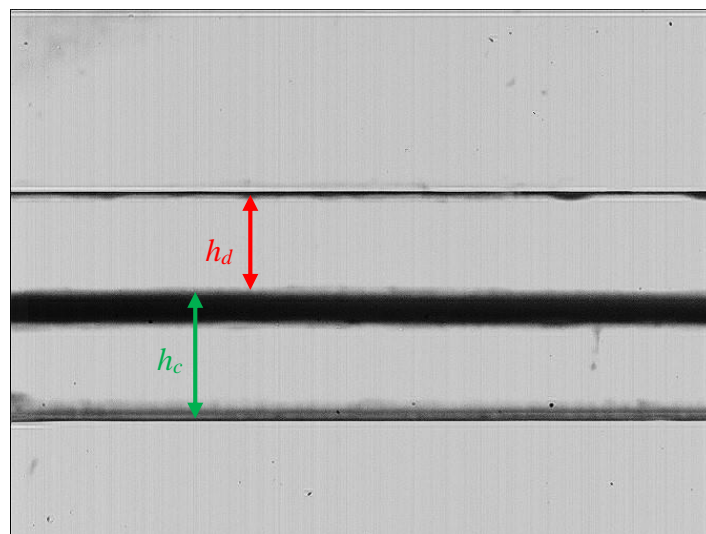


Figure 4.2. A sketch with the indication of the height of the continuous (h_c) and dispersed (h_d) phase in a parallel flow. The interface thickness is highlighted.

In the current experimental runs the typical thickness of the interface is of the order of 24 pixel which corresponds to a value of about 33 μm . In a channel having a height of 300 mm the thickness of the interface represents 10% of the total channel height.

In the current dissertation the whole thickness of the interface is considered into the continuous height (h_c). In order to obtain a theoretical prediction of the dependence of h_c and h_d by the main governing parameters of the system which are:

- The volumetric flow rate ratio ($\alpha = Q_d/Q_c$)
- The viscosity ratio ($\lambda = \mu_d/\mu_c$)

In this case the viscosity ratio $\lambda^{-1} (= \mu_c/\mu_d)$ is fixed by the choice of the immiscible liquids and it is equal to 0.0467 and the depth ratio ($\beta^{-1} = h_c/h_d$) associated to the parallel flow is a function of $\alpha (= Q_d/Q_c)$ only. The theoretical relationship between λ , β and α can be calculated by solving the balance of momentum equation for a parallel-plate channel in which two immiscible liquids flow in parallel. Under the action of a pressure gradient, the velocity profile within the layers can be obtained by using the momentum balance equation written as follows [117].

$$\frac{d\tau}{dx} = \frac{\Delta P}{l} \quad (4-1)$$

where x is the distance from the channel walls and τ is the tangential shear rate, $\Delta P/l$ is the pressure gradient which pushes the fluids

By integrating Equation (4-1) considering $\Delta P/l$ as a constant, it is possible to obtain a linear relationship between τ and the wall distance x :

$$\tau = -\mu \frac{du}{dx} = \left(\frac{\Delta P}{l} \right) x + C_1 \quad (4-2)$$

The constant C_1 can be obtained by applying the no-slip boundary condition at the channel walls; in this way the dependence of τ by x and by the height of the continuous and dispersed layers can be obtained:

$$\tau = \left(\frac{\Delta P}{l} \right) \left[x - \frac{1}{2} \left(\frac{h_d^2 \mu_c - h_c^2 \mu_d}{h_c \mu_d + h_d \mu_c} \right) \right] \quad (4-3)$$

By considering the Newton law which correlates τ with the local velocity gradient it becomes possible to obtain the velocity profile within the two layers by integrating once more Equation (4-3) and by imposing the continuity of the velocity at the interface:

$$v_c = \left(\frac{\Delta P}{2\mu_c l} \right) \left[-x^2 + \left(\frac{h_d^2 \mu_c - h_c^2 \mu_d}{h_c \mu_d + h_d \mu_c} \right) x + \frac{h_c h_d \mu_c (h_c + h_d)}{h_c \mu_d + h_d \mu_c} \right] \quad (4-4)$$

$$v_d = \left(\frac{\Delta P}{2\mu_d l} \right) \left[-x^2 + \left(\frac{h_d^2 \mu_c - h_c^2 \mu_d}{h_c \mu_d + h_d \mu_c} \right) x + \frac{h_c h_d \mu_d (h_c + h_d)}{h_c \mu_d + h_d \mu_c} \right] \quad (4-5)$$

If the dispersed and the continuous phases have the same viscosity, the slit is half filled by each liquid and the velocity profile assumes the classic parabolic trend.

For two fluids having a different viscosity the velocity profile is the combination of two parabolic profiles which have an angular point in correspondence of the interface. It is now possible to calculate the average velocity of the immiscible fluids as follows

$$u_c = \frac{1}{h_c} \int_{-h_c}^0 v_c dx, \quad u_d = \frac{1}{h_c} \int_{-h_c}^0 v_d dx \quad (4-6)$$

From the average velocity it is possible to obtain the continuous and dispersed flow rate per unit of length of the parallel plate channel as:

$$Q_c = u_c W h_c, \quad Q_d = u_d W h_d \quad (4-7)$$

By introducing Equation (4-4) and (4-5) in Equation (4-7) the volumetric flow rates can be expressed as follows:

$$Q_c = \left(\frac{\Delta P W h_c^2}{12 \mu_c l} \right) \left[\frac{(4h_c h_d + 3h_d^2) \mu_c + (h_c^2) \mu_d}{h_c \mu_d + h_d \mu_c} \right] \quad (4-8)$$

$$Q_d = \left(\frac{\Delta P W h_d^2}{12 \mu_d l} \right) \left[\frac{(4h_c h_d + 3h_c^2) \mu_d + (h_d^2) \mu_c}{h_c \mu_d + h_d \mu_c} \right] \quad (4-9)$$

In this way, the volumetric flow rates are univocally linked to the thickness of the dispersed and continuous phase as well as to the viscosity of the immiscible liquids.

By dividing Equation (4-8) with Equation (4-9) and recalling the definition of volumetric flow rate (α) and viscosity ratio (λ), as well as the depth ratio (β) the following relationship is obtained:

$$\alpha^{-1} = \frac{(\beta^{-1})^2}{\lambda^{-1}} \left[\frac{(\beta^{-1})^2 + 4\lambda^{-1}\beta^{-1} + 3\lambda^{-1}}{3(\beta^{-1})^2 + 4\beta^{-1} + \lambda^{-1}} \right] \quad (4-10)$$

It is important to observe that Equation (4-10) is valid for parallel plate channels which can be considered as a limit case obtainable with rectangular channels having a very large aspect ratio (H/W). In this case, since the channel cross-section is squared, Equation (4-10) can be considered as an approximation of the real link existing between β , α and λ .

However, Equation (4-10) is important in order to know which relationship is theoretically foreseen among the governing parameters (α , λ) and the depth ratio β . Equation (4-10) can be used in order to obtain, by fixing α and λ , the value assumed by β .

Now it is possible to compare the experimental results in terms of depth ratio β^{-1} obtained by varying α^{-1} with the theoretical predictions of Equation (4-10). In Figure 4.3 the comparison between the theoretical predictions of Equation (4-10) (dashed line) and the experimental values of β observed by varying the flow rates from $5 < Q_c < 120$ ml/h ($0.00032 < Ca_c < 0.0076$) and $5 < Q_d < 100$ ml/h ($0.0065 < Ca_d < 0.131$) is shown.

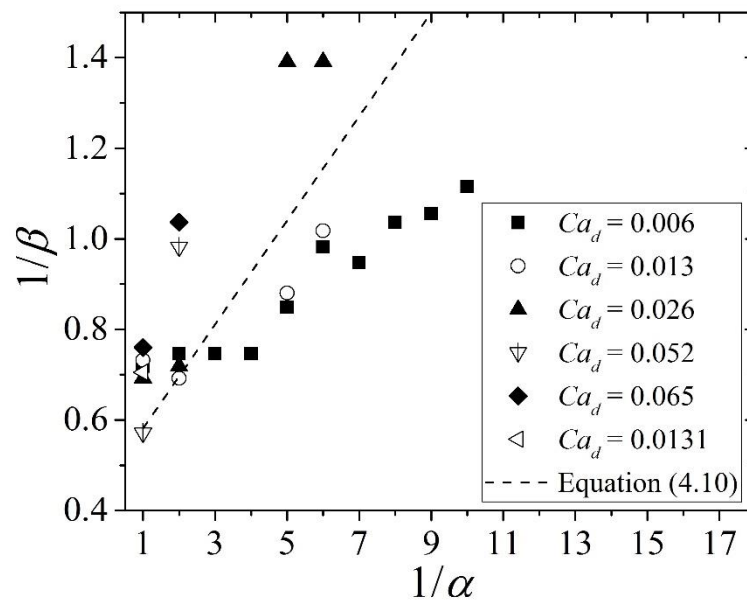


Figure 4.3. Comparison between the prediction of Equation (4-10) and the experimental results in terms of depth ratio β^{-1} as a function of α^{-1} .

The deviation between experimental and theoretical results increases at higher values of α^{-1} but when $\alpha^{-1} \leq 2$ and/or $Ca_d = 0.026$, a good agreement between experimental results and theoretical predictions may be seen, especially if one consider the uncertainty on experimental evaluation of β . The same comparison has been made in Figure 4.4 in terms of h_c and h_d .

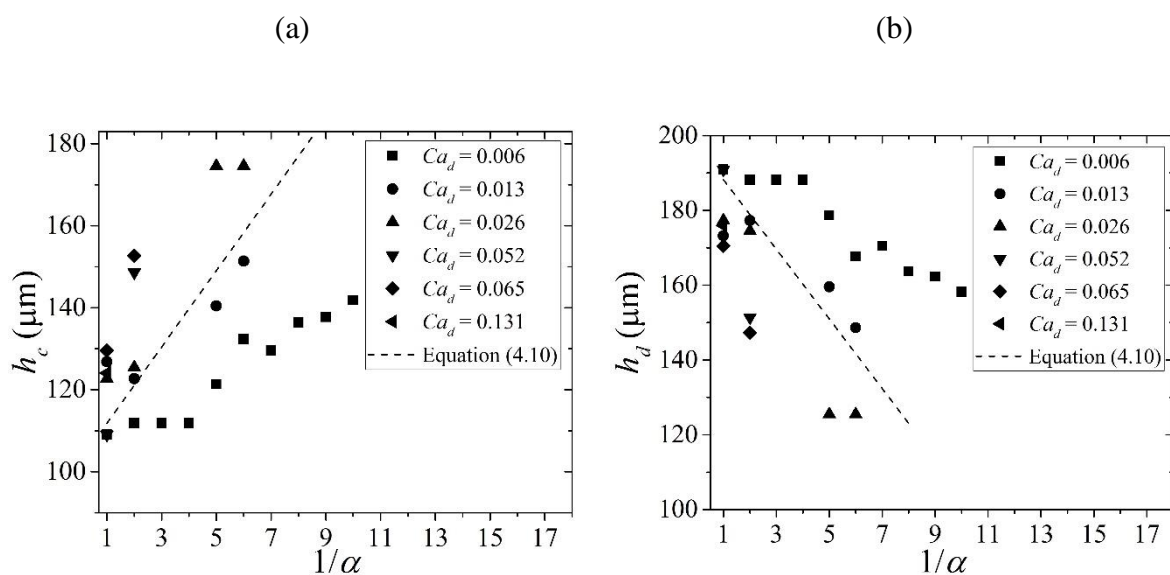


Figure 4.4. (a) Depth of the continuous phase h_c and (b) of the dispersed phase h_d compared with the theoretical predictions of Equation (4-10).

In order to obtain for the T-junction the dependence of the activated flow patterns on the value of the volumetric flow rate (α) and of the Capillary number linked to the continuous phase (Ca_c), a series of experimental tests have been made by varying the values of the imposed volumetric flow rates of the continuous and of the dispersed phase introduced in the T-junction. For each combination (α , Ca_c) the droplet regime (if any) has been observed (DJ, DC or PF) and indicated in the flow pattern map shown in Figure 4.5.

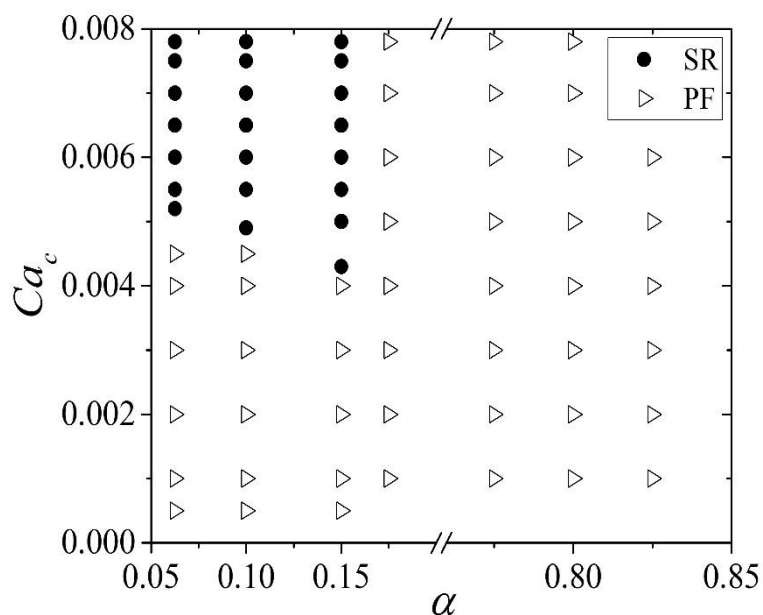


Figure 4.5. Droplet regimes as a function of flow rate ratio α and of Ca_c for silicone oil droplets in pure water.

It is interesting to note that the generation of the droplets takes place for this T-junction configuration (face-to-face) only at very high values of the continuous flow rates (large Ca_c) and low flow rate ratio ($\alpha < 0.15$). An increase of the continuous flow rate while the dispersed phase flow rate is fixed causes droplet formation at the junction (DJ regime).

For low values of α (< 0.15) and large continuous flow rates a critical value of the water flow rate exists above which the droplet generation begins. With the increase of water flow rate, in some cases, the generation of the oil droplets could be observed due to the high difference between the flow rates. As depicted in Figure 4.5 droplet generation starts only when $Q_c > 80$ ml/h ($Ca_c > 0.0051$) but for $Q_d = 10$ ml/h ($Ca_d = 0.0131$), the droplet appears when $Q_c > 60$ ml/h ($Ca_c > 0.0038$). With the increase of Q_d , the transition between droplet-based flow and parallel flow cannot be observed due to the increase of oil flow which cannot be pinched-

off by the continuous phase.

In Figure 4.6 it is shown the droplet formation obtained by imposing a large values of the water flow rate at the inlet ($Q_c = 85$ ml/h) for a low value of α ($= 11$). In these conditions the droplets are very fast and their observation becomes problematic also with a speed camera. Droplets are obtained thanks to the large continuous flow rate which squeezes the dispersed phase against the corner of the T-junction.

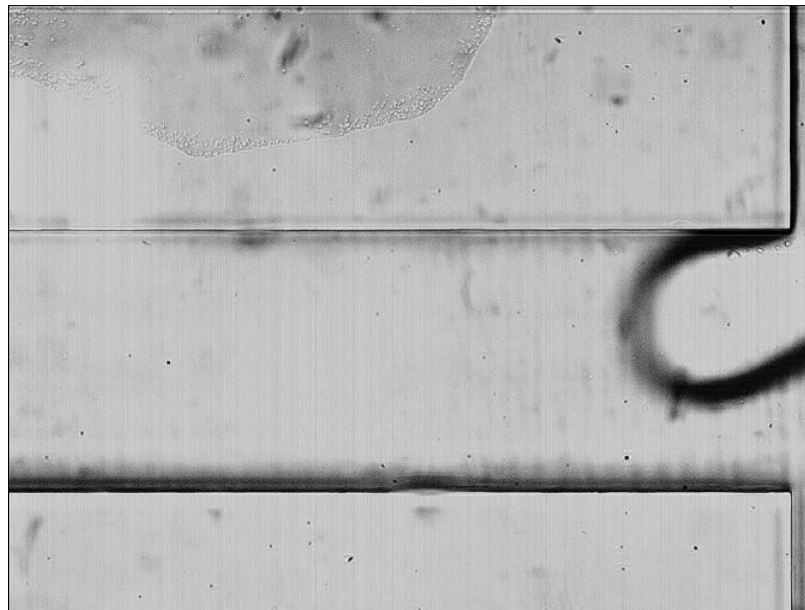


Figure 4.6. The generation of a silicone oil droplet at large values of Q_c obtained by squeezing by using pure water as continuous phase.

It is possible to conclude that the face-to-face T-junction configuration, combined with a hydrophobic coating of the channel walls, can be recommended only if the goal is to obtain parallel co-flows at the exit of the junction and not droplets. As an example, a controlled parallel flow is desired in a series of applications like micro fuel cells in order to avoid the use of membranes between the two phases.

In this case a controllable co-flow can be easily produced by changing the volumetric flow rate ratio (α) of the immiscible liquids introduced in the junction as well as their viscosity ratio (λ). The cross-section geometry of the channels plays a role on the depth ratio because the length of the wetted perimeter can change the thickness of the co-flow layers.

4.2 Water with surfactant

In order to obtain droplet with the configuration of the T-junction used in these experimental tests, the value of the interfacial tension σ_i ($= \sigma_{il}$) between the immiscible liquids must be strongly reduced. This can be obtained by adding Tween 20 to water.

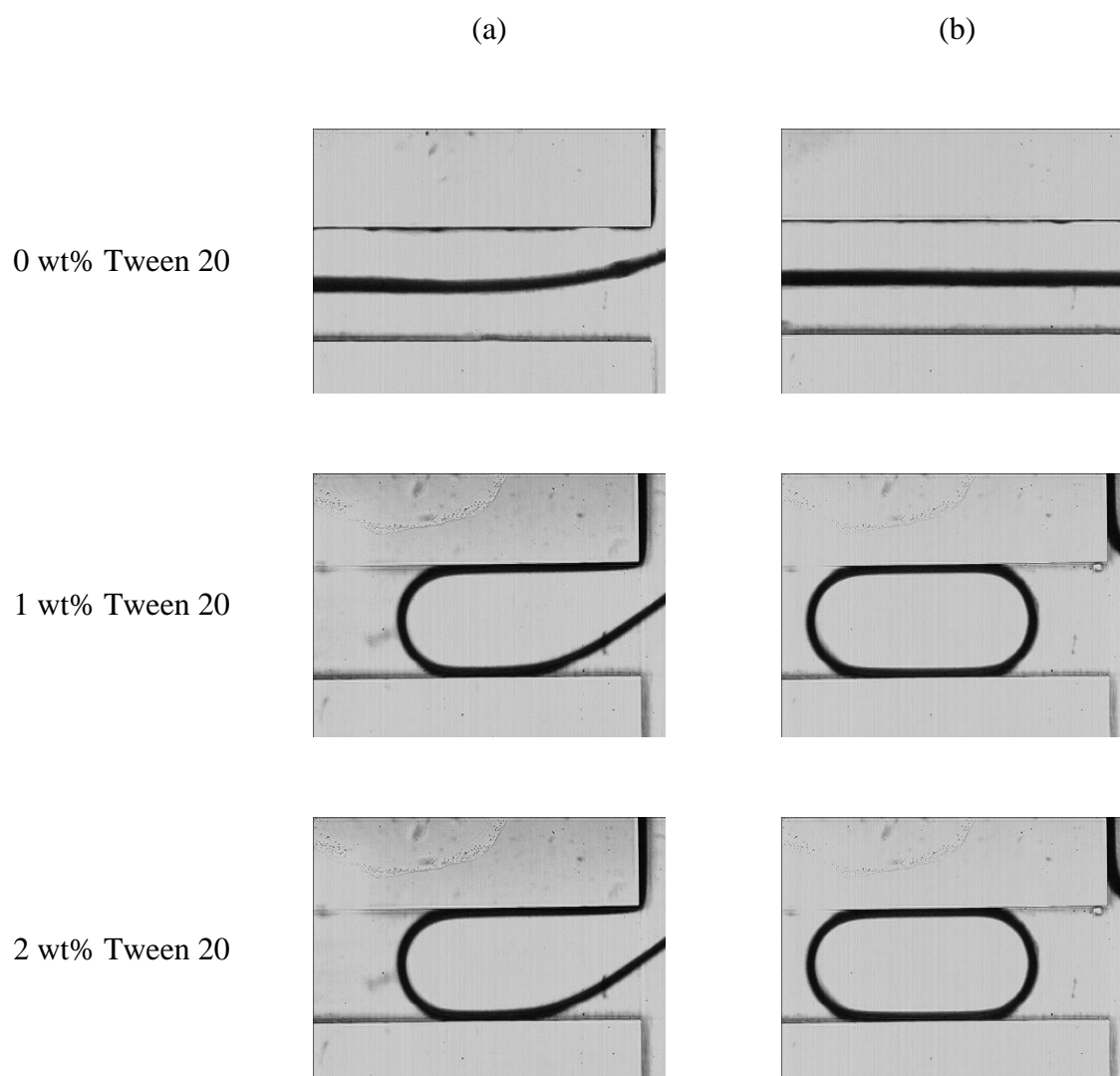


Figure 4.7. Effect of Tween 20 on the flow pattern (a) at the junction and (b) downstream of the junction in the absence as well as two different concentrations of Tween 20

Figure 4.7 clarifies the effect of Tween 20 on the emulsion of silicone oil in water. The images of Figure 4.7 highlight that, by tuning σ , it is possible to change the flow pattern of the two-phase flow from parallel flow (PF) to droplet-based flow. In fact a reduction of the interfacial tension enhances the droplet formation by reducing the interfacial forces between

the immiscible liquids. In Figure 4.7 the flow pattern obtained in correspondence of two different positions along the outlet arm of the T-junction (close to the junction (Figure 4.7a) and far from the junction (Figure 4.7b)). The images have been obtained by imposing at the inlets a value of $Q_c = 25$ ml/h and $Q_d = 5$ ml/h.

It is evident that, for the same value of the viscosity ratio (λ) and volumetric flow rate ratio (α) different flow patterns can be obtained at the outlet of the T-junction by introducing Tween 20 in the continuous phase (water). A concentration of 2% in weight of Tween 20 in water is able to reduce the interfacial tension between the continuous and the dispersed phase from 42.44 mN/m down to 8 mN/m (see Table 2.4 in Section 2.4.3). This strong reduction of the interfacial tension increases the value of the Capillary number associated to both continuous and dispersed phase and triggers the droplet-based flow. From the images of Figure 4.7 it is evident that the effect of a variation of the Tween 20 concentration from 1 wt% to 2 wt% on the droplet size can be considered negligible.

This fact can be explained by observing that the Tween 20 concentrations used in these tests ($> 1\%$) are larger than the critical micelle concentration (CMC) value of Tween 20 in water, which is equal to 0.0074 wt% [99]. When a surfactant concentration larger than the CMC value is used the interfacial tension reaches a stable minimum value which is no more influenced by the surfactant concentration. For this reason the droplet-based flow is independent on the surfactant concentration in water.

4.2.1 Flow map

Droplet formation can be obtained, at low flow rates, in two distinct way: the droplet is obtained by squeezing the dispersed flow against the corner of the T-junction (DJ regime) or by inducing the droplet breakup far from the junction (DC regime).

In Figure 4.8 these two modes are clearly illustrated by the sequence of images acquired by fixing the continuous flow rate ($Q_c = 3$ ml/h) and by increasing the dispersed flow rate from 0.3 ml/h up to 5.1 ml/h.

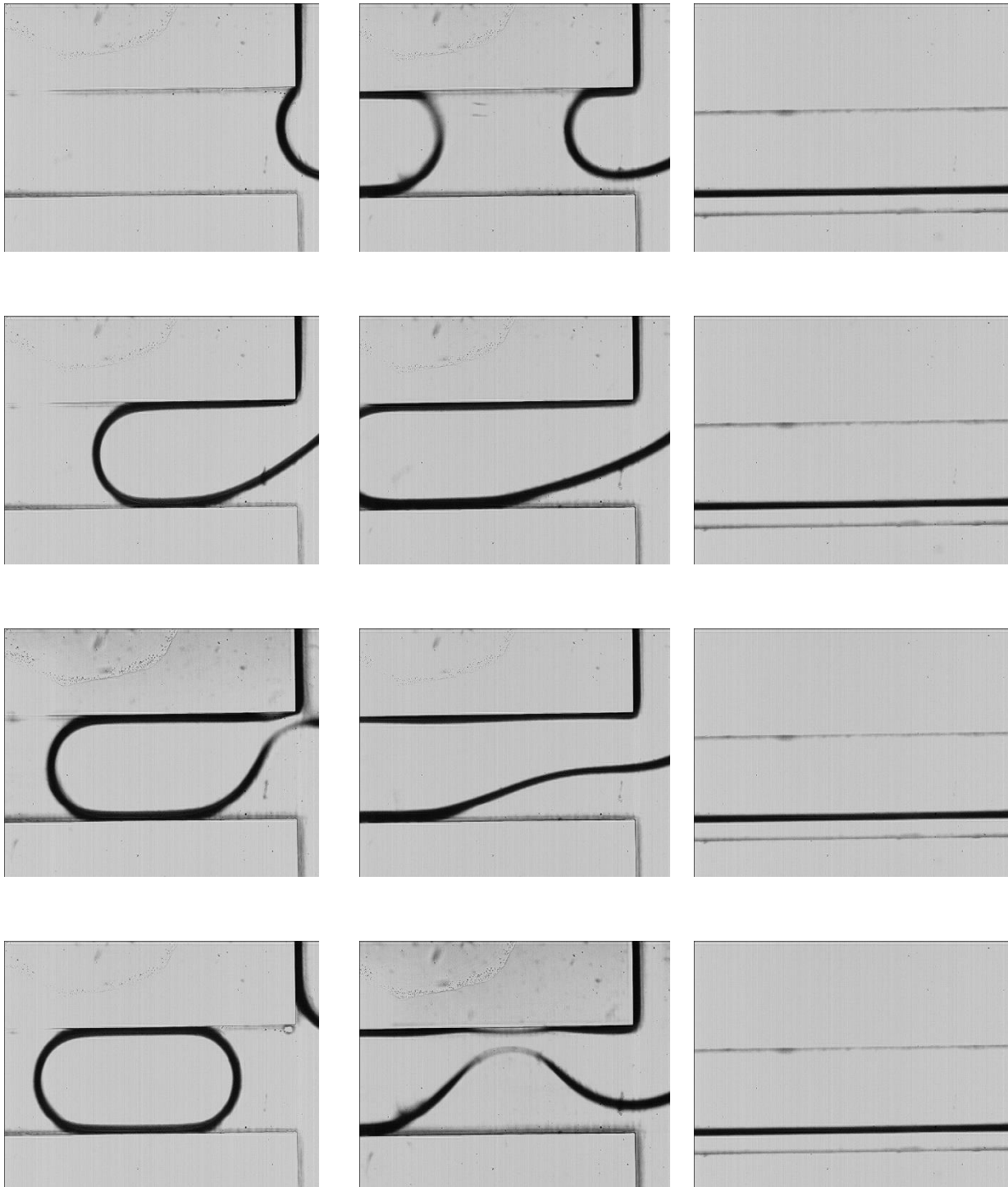
DJ ($Q_c = 3$ & $Q_d = 0.3$ ml/h)DC ($Q_c = 3$ & $Q_d = 3$ ml/h)PF ($Q_c = 3$ & $Q_d = 5.1$ ml/h)

Figure 4.8. Images sequence obtained by fixing $Q_c = 3$ ml/h and by varying Q_d from 0.3 ml/h (a) to 3 ml/h (b) to 5.1 ml/h (c).

For low values of Q_d ($\alpha = 0.1$), the detachment of the droplet occurs at the junction (see

Figure 4.8a) thanks to the action of the continuous phase which squeezes the dispersed phase against the corner of the T-junction (DJ regime). The droplet formation and breakup mechanism is dictated by the pressure drop force and the interfacial tension between the immiscible liquids. Since the shear force is negligible, the interface enters the main channel and blocks the whole channel; when the increased upstream pressure overcomes the pressure of the dispersed phase, the continuous phase displaces the droplet downstream, stretches the interface and finally squeezes the neck which leads to the generation of the droplet.

When the dispersed phase introduced in the junction increases ($\alpha = 1$ in Figure 4.8b), the continuous phase is not able to squeeze the dispersed phase at the junction; the dispersed phase fills a large part of the junction and the continuous phase is forced to go through a restricted portion of the exit cross-section. This fact increases the pressure which is responsible of the droplet breakup which occurs far from the junction (DC regime). If the flow rate of the dispersed phase introduced in the junction is further increased ($\alpha = 17$ in Figure 4.8c) the continuous flow is so low that it is no more able to create the droplet breakup. In these conditions a stratified parallel flow (PF regime) is observed at the outlet of the junction.

The images of Figure 4.8 highlight that droplet formation regime is strongly influenced by the flow rate ratio α .

In order to obtain for the T-junction the dependence of the activated flow patterns on the value of the volumetric flow rate (α) and of the Capillary number linked to the continuous phase (Ca_c) a series of experimental tests have been made by varying the values of the imposed volumetric flow rates of the continuous and of the dispersed phase introduced in the T-junction. For each combination (α , Ca_c) the droplet regime has been observed (DJ, DC or PF) and indicated in the flow pattern map shown in Figure 4.9.

In this way it becomes possible to know which kind of droplet regime is activated for fixed operative conditions of the T-junction.

By observing Figure 4.9 it is clear that squeezing mechanism, which causes the droplets breakup at the junction (DJ regime), is met only by using the T-junction at low values of α (< 0.5). For a fixed Capillary number, by increasing α ; the droplet is found to pinch-off downstream along the exit channel (DC regime) forming an unstable thread. The breakup point further moves downstream with a further increase of α . Droplet generation ceases when the

flow rate ratio overcomes a critical value (α_{cr}) which depends on the Capillary number.

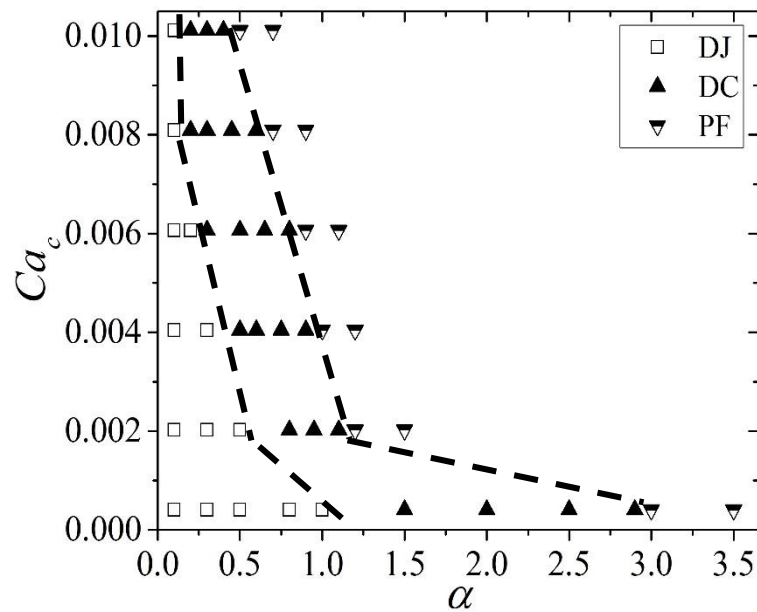


Figure 4.9. Droplet regimes as a function of flow rate ratio α and of Ca_c for silicone oil droplets in water with the addition of Tween 20 (2 wt%).

Larger values of Ca_c means lower values of α_{cr} ; this fact underlines that it is more difficult to obtain a droplet-based flow at the exit of the junction if large values of Ca_c are considered.

Also the transition from DJ to DC regime is influenced by Ca_c ; larger Ca_c values anticipate the transition between DJ and DC regime.

In addition, it's worth mentioning that the distance between two neighboring droplets decreases with higher α values.

In fact, when the continuous phase flow rate increases the continuous flow rate is strong enough to detach the droplets, due to the effect of the shear force. The results shown in Figure 4.9 are similar to those reported by Guillot and Colin [118]. Similar results have been obtained by Tan *et al.* [105] and Liu and Zhang [39] numerically.

4.2.2 Effect of Ca_c and Q_d

In this section, the non-dimensional lengths of the droplets, defined as the ratio of the droplet length to the height of the channel $\bar{L} = L/H$, for droplets generated under DJ or DC

regimes are presented. Figure 4.10 shows the trend of \bar{L} with α for fixed values of Ca_c .

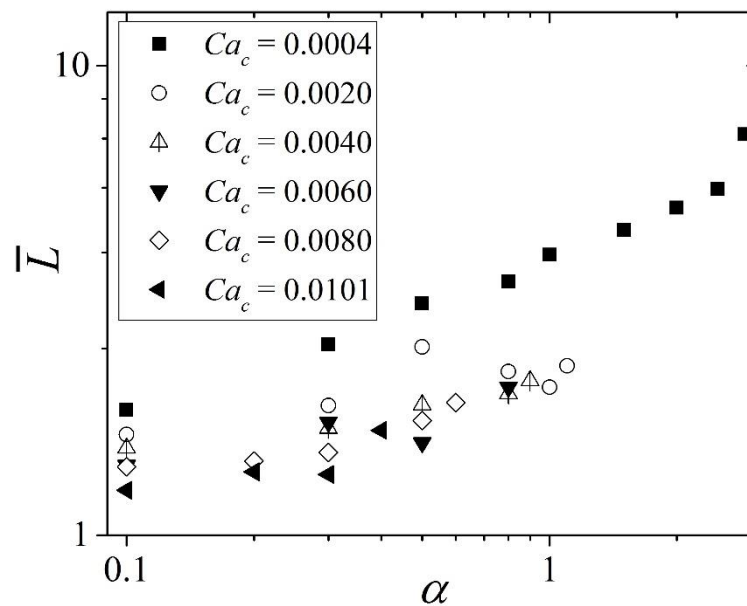


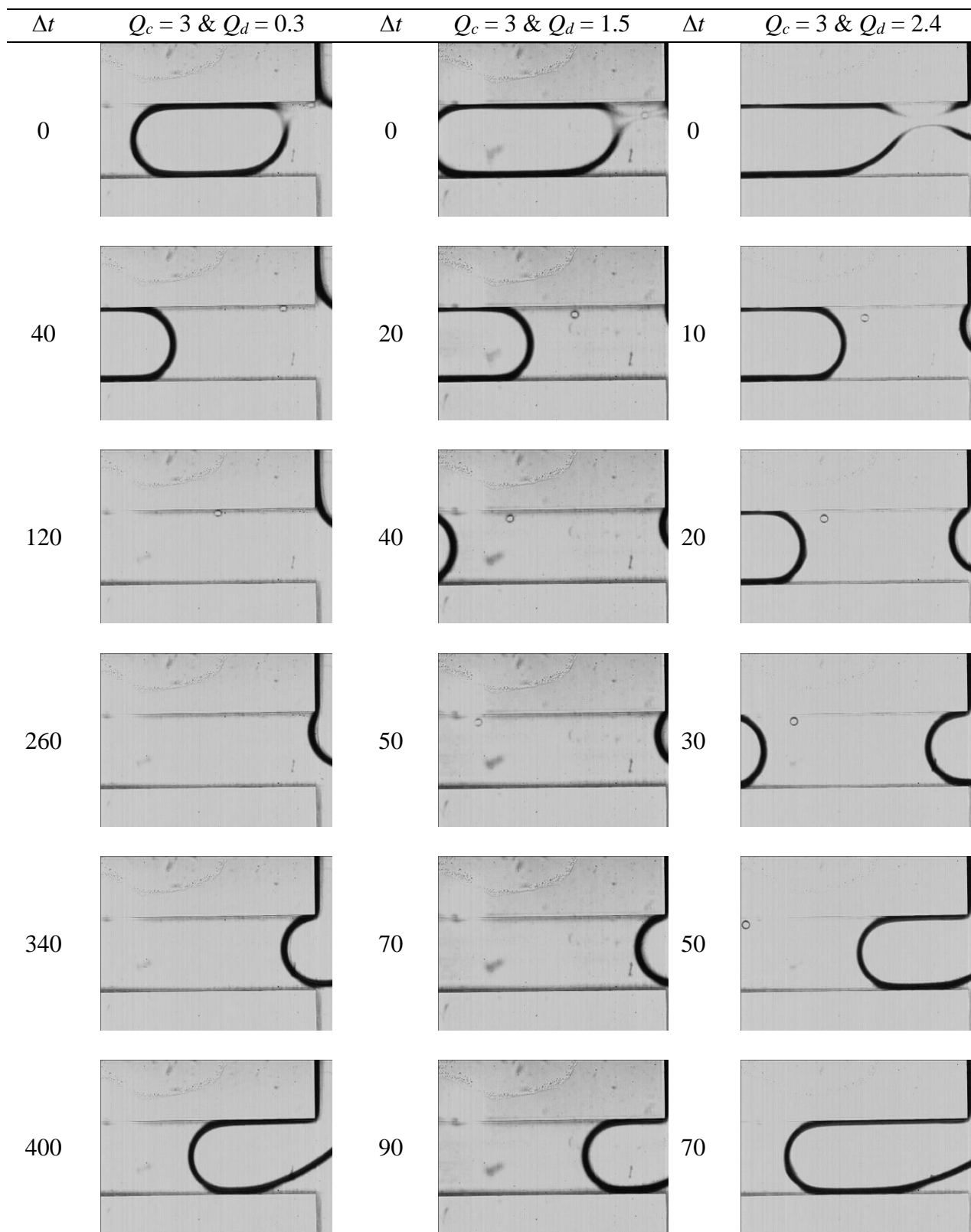
Figure 4.10. Non-dimensional length of the droplets as a function of flow rate ratio α for different continuous Capillary numbers Ca_c

An increase of the flow rate ratio α while Q_c is kept constant means a larger introduction of dispersed phase into the junction. In this case larger droplets are produced (Figure 4.10).

The evolution of the interface between the immiscible liquids is shown by imposing a fixed value of the continuous flow rate at the inlet ($Q_c = 3$ ml/h) and three different values of Q_d equal to 0.3 ml/h (Figure 4.11a), 1.5 ml/h (Figure 4.11b) and 2.4 ml/h (Figure 4.11c).

Higher values of Q_d are responsible of longer filaments between the droplet and the source of dispersed material before the breakup (DC regime). It is possible to observe that distance from the junction in correspondence of which the droplet breakup occurs, moves downstream of the junction if Q_d increases. The larger Q_d , the longer filament may be observed and this trend continues till the critical value of α is reached for which no droplet-based flow is observed (PF regime).

In addition, an increase of Q_d is responsible of longer droplets because the droplet formation time becomes longer in DJ regime because of the blockage of the channel that occurs at low flow rates. For this reason, the droplet volume is strongly affected by Q_d in the squeezing regime and low continuous flow rates.



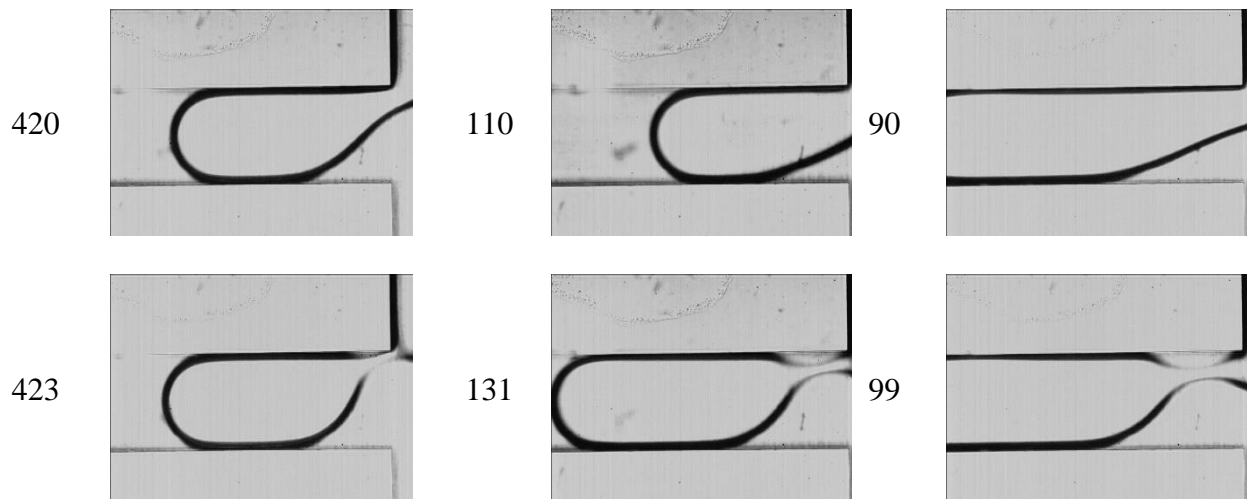


Figure 4.11. Effect of Q_d (ml/h) on the transition between DJ and DC regime.

On the contrary, in DC regime with the increase of Q_c the droplet formation time (filling stage) decreases significantly. Therefore, it is clear that an increase of Q_c has a reduced influence on the droplet formation time and hence on the droplet volume.

It is interesting to note that at high continuous flow rates, the increase of α (Q_d) does not influence the droplet volume significantly and it confirms the idea that the dispersed flow rate affects the droplet volume through the formation time, so it is able to influence the droplet volume especially at low continuous flow rates.

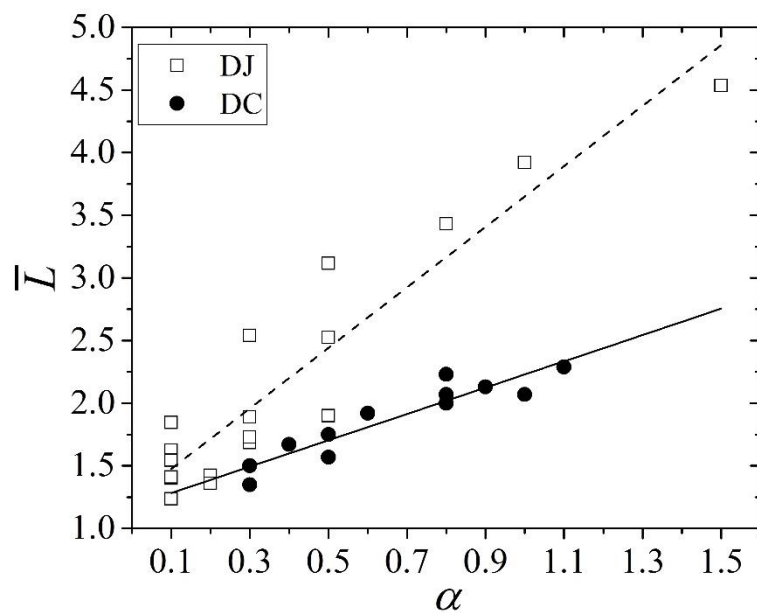


Figure 4.12. Non-dimensional droplet length as a function of α for both DJ and DC regimes.

The increase of the droplet volume in DC regime, for a fixed value of Q_c , is mainly due to the increase of the length of the thread between the droplet and the source of the dispersed phase. With the increase of α , the increase of the droplet length is larger in DJ regime than in DC regime; this is confirmed by the experimental data shown in Figure 4.12.

In Figure 4.13 a linear correlation between the droplet length and the volumetric flow rate ratio is used in order to fit the experimental data obtained for DJ regime ($\bar{L} = \varepsilon + \omega\alpha$); this correlation is based on the squeezing model proposed by Gartseki *et al.* [39]. ε and ω are two fitting constants which depend on the channel geometry [44] and flow configuration.

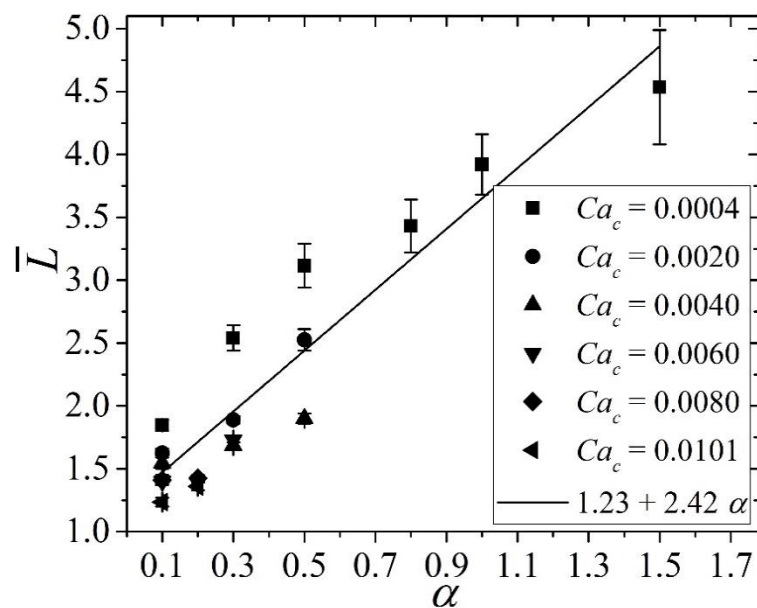


Figure 4.13. Dimensionless plug length as a function of α for DJ regime.

In Figure 4.13 each experimental point is coupled to a Y-bar with shows the typical variability of the droplet lengths observed experimentally. Y-bar increases with the increase of the flow rate ratio.

In Figure 4.14 the non-dimensional length of the droplets is given as a function of the continuous Capillary number (Ca_c) for fixed values of α . These results confirm, as highlighted by other researchers for different flow configurations [39, 42, 44], that \bar{L} is also influenced by the Capillary number and for this reason a power-law dependence of the droplet length on Ca_c , can be useful in order to obtain a more precise characterization of the droplets generated.

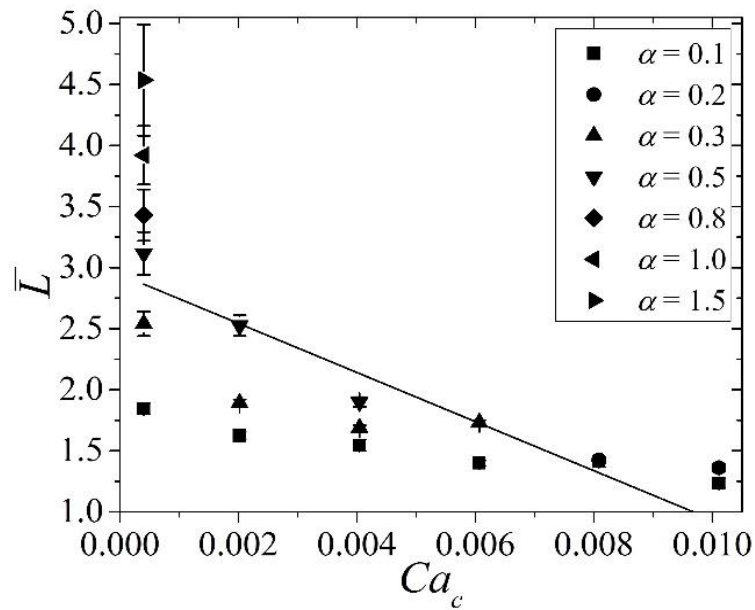


Figure 4.14. Non-dimensional length of the droplets as a function of Ca_c for different values of α for DJ regime.

With the aim to improve the correlation for the prediction of the dimensionless droplet length, the dependence of the dimensionless droplet length on the continuous Capillary number Ca_c is used in order to fit the experimental results.

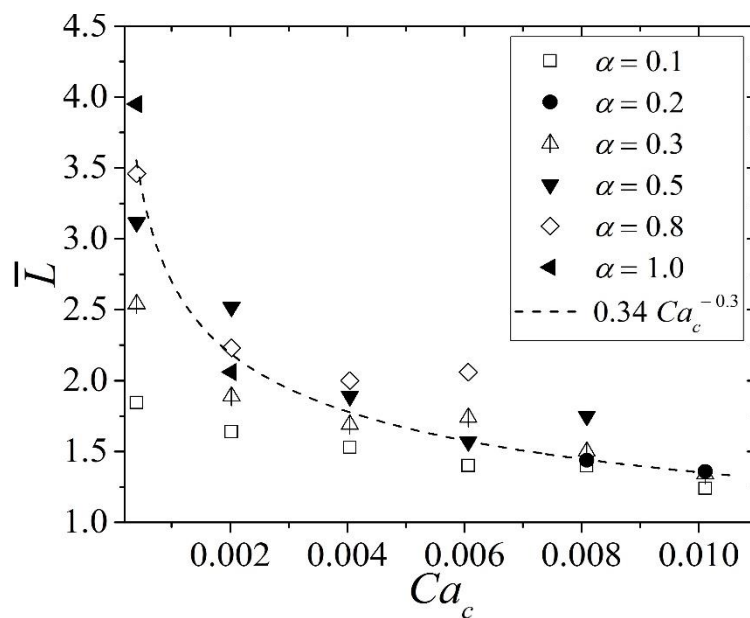


Figure 4.15. Comparison between the power-law correlation of Equation (4-11) and the experimental data obtained.

The proposed correlation adopts the same expression originally presented by Christopher *et al.* [57] in the form of:

$$\bar{L} = qCa_c^x \quad (4-11)$$

The experimental results obtained in this work by using T-junction under opposed-flow configuration suggest to use $x = -0.3$, in agreement with Christopher *et al.* [57]. Figure 4.15 confirms that this correlation is able to better predict the trend of droplet length as a function of Ca_c evidenced by the experimental data.

4.2.3 Breakup distance

Thanks to the detailed images obtained during the droplet formation with the speed camera, especially for low values of the continuous and dispersed flow rates, an investigation about the dependence on the main operative parameters (α , Ca_c) of the length of the thread which connects the droplet to the source of the dispersed phase in DC regime has been conducted. This kind of information, very useful for the tuning of the numerical models devoted to the analysis of droplet-based flows in microdevices, has received until now a scarce attention in the open literature.

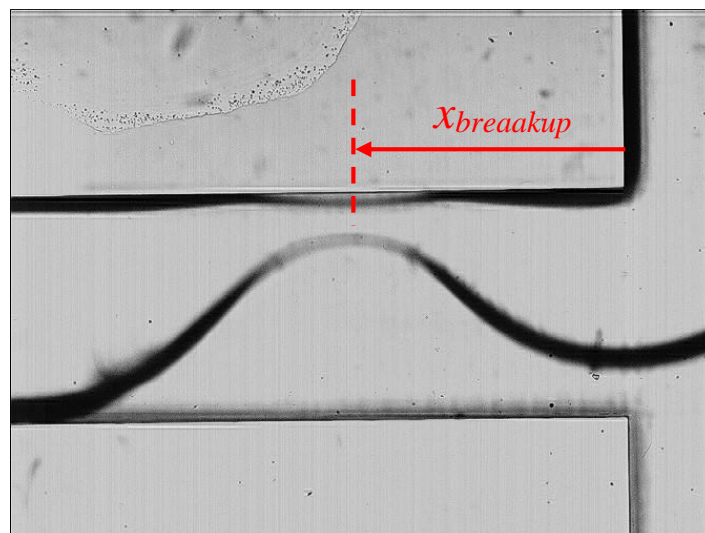


Figure 4.16. Typical shape assumed by the interface in DC regime before the droplet breakup and definition of $x_{breakup}$.

In Figure 4.16 the typical shape assumed by the interface before the droplet breakup in

DC regime is show. By post-processing the images acquired with the speed camera, it is possible to obtain the distance ($x_{breakup}$) from the corner of the junction in correspondence of which the droplet breakup occurs with the crash of the filament which link the droplet to the source of dispersed phase. In Figure 4.16 the image of the interface before the droplet breakup is shown; $x_{breakup}$ is extracted by the image by considering the distance between the corner of the junction and the position in which the thread assumes its minimum width (Figure 4.16). The position of the minimum width of the thread is obtained by MATLAB thanks to the reconstruction of the interface by using the procedure described in Section 2.6.4.

In Figure 4.17 the values of $x_{breakup}$ are shown as a function of the flow rate aspect ratio (α) for a fixed value of the Capillary number (Ca_c). It is evident that the breakup distance increases with α . This fact can be explained by considering that, for a fixed Ca_c , a larger value of α means more dispersed fluid introduced in the junction; if the dispersed phase flow rate increases, for the continuous phase becomes more difficult to induce the droplet breakup and the length of the filament produced before the droplet detachment increases. Of course, a longer filament means a longer droplet formation time. In addition, it seems that, for $\alpha > 1$ the increase of the breakup distance when α is increased becomes more significant, especially at low Ca_c .

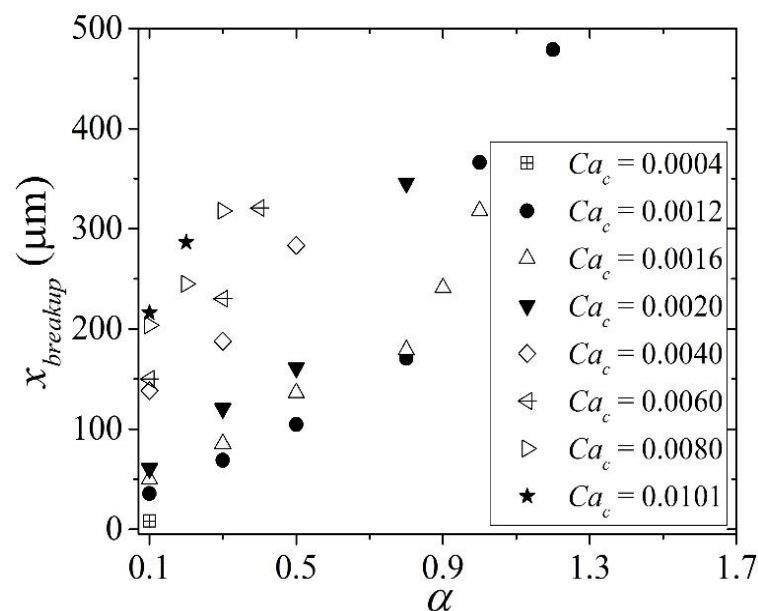


Figure 4.17. Breakup distance $x_{breakup}$ as a function of the flow rate ratio α for fixed values of the Capillary number Ca_c .

From Figure 4.17 is also evident that an increase of the breakup distance can be obtained

by increasing the Capillary number linked to the continuous phase. This fact can be explained by considering that an increase of the continuous flow rate introduced in the junction is responsible of an increase of the shear force effects which contribute to elongate the filament before the droplet detachment.

4.2.4 Polydispersity

With the aim to individuate in which operative conditions, in terms of α and Ca_c , for a fixed value of viscosity ratio (in this case, λ^{-1} ($= \mu_c/\mu_d$) equal to 0.047), the T-junction in opposed-flows configuration can be used in order to obtain at the outlet of the junction a monodispersed emulsion, the droplets have been analysed in order to obtain the value of polydispersity Pl which characterize the droplet set observed at the exit of the junction for each set of (α, Ca_c) values. The definition of polydispersity Pl is given by Equation (2-10).

The results have been organized in a 2D plot in which the value of Pl is shown as a function of α and Ca_c . The results refer to an O/W emulsion in which silicone oil droplets are obtained in a carrier medium of water with the addition of a concentration of 2% in weight of Tween 20 (W+T).

By observing the polydispersity values associated to the droplets generated with the T-junction in opposite flow configuration it is evident that droplets can be generated at low Ca_c (≤ 0.01) with a low value of polydispersity Pl ($< 4\%$) when the volumetric flow rate ratio α ranges between 0.1 and 0.5. This result highlights that in this region the T-junction is able to guarantee the generation of a monodispersed emulsion.

On the contrary, for values of α larger than 0.5 ($0.5 < \alpha < 1.1$), only for low values of Ca_c ($Ca_c \leq 0.004$) the polydispersity can be maintained lower than 4 %.

Another general observation which confirms the results already presented for a micro cross-junction (see Figure 3.8) is that polydispersity tends to increase significantly in correspondence of the transition region between droplet-based regime and parallel flow regime. This fact becomes clear by comparing Figure 4.18 with the flow map of Figure 4.9. It is evident that the droplet formation becomes unstable in correspondence of the region in which the droplet-based regime is changing in parallel flow; as consequence, the emulsion is formed by droplets with a variable length and with a non-uniform frequency since the droplet formation

time becomes unstable

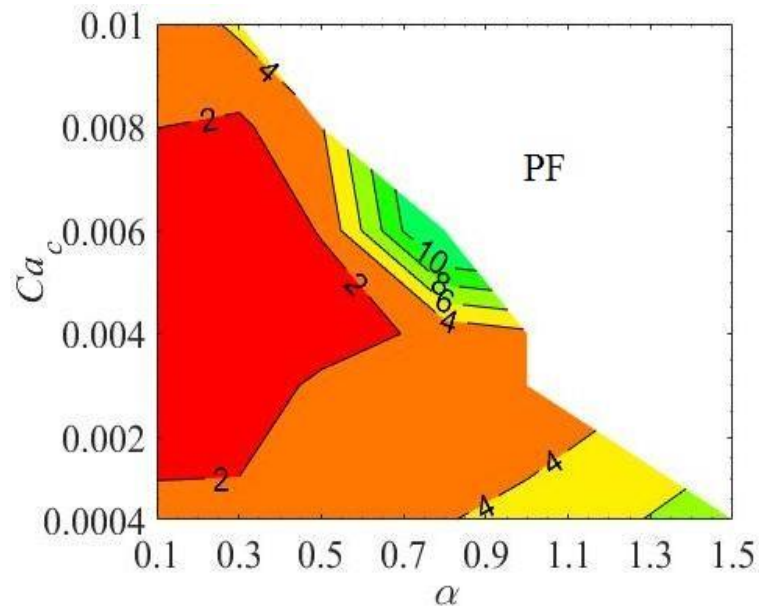


Figure 4.18. Polydispersity Pl of silicone oil droplets in water with 2 wt% of Tween 20 as a function of α and Ca_c .

It is possible to conclude the analysis of the behavior of a T-junction in opposite-flow configuration by observing that:

- This configuration allows to obtain a droplet-based flow at the exit of the junction only if the interfacial tension between the immiscible liquids is low; this is the reason for which this configuration is generally used for bubble formation.
- For O/W emulsions, hydrophilic coatings have to be preferred in order to obtain more stable emulsions.
- With the introduction of surfactants which reduce the value of the interfacial tension between the immiscible liquids introduced in the junction, the T-junction in opposite-flow configuration can generate a droplet-based flow by squeezing (DJ regime) and by dripping or jetting (DC regime).
- The T-junction in opposite-flow configuration can be used in order to generate monodispersed emulsions but in this case it is better to work with low values of the Capillary number linked to the continuous phase ($Ca_c < 0.01$) and low flow rate ratio ($\alpha < 0.5$).

4.3 Droplets in Newtonian and non-Newtonian carrier medium by a new microchannel

In the rest of this chapter a new micro T-junction having the same geometrical characteristics of the T-junction tested in the previous sections, purchased from the same manufacturer (*Translume Co.*), has been used both with non-Newtonian and Newtonian dispersed phases.

4.3.1 Droplet-based flow regime

The second T-junction has been tested by varying Q_c and Q_d at the inlets for four different continuous phases (pure water (W), water with Tween 20 (W+T), aqueous Xanthan gum solution without (0.2 XG) and with Tween 20 (0.2 XG+T)). The range of volumetric flow rate of the continuous phase tested is reported in Table 4.2 with the corresponding range of the continuous Capillary number (Ca_c). In general, for a fixed value of the volumetric flow rate of the dispersed phase, by increasing the value of the continuous flow rate Q_c a transition from DJ regime to DC regime occurs at lower values of α for non-Newtonian fluids with respect to Newtonian carrier medium.

Table 4.2. Range of volumetric continuous flow rate Q_c with the corresponding Ca_c .

Continuous Phase			
W	W+T	0.2 XG	0.2 XG+T
$2 < Q_c < 30$ ml/h	$2 < Q_c < 20$ ml/h	$1 < Q_c < 30$ ml/h	$0.5 < Q_c < 20$ ml/h
$0.00012 < Ca_c < 0.0019$	$0.0008 < Ca_c < 0.008$	$0.009 < Ca_c < 0.034$	$0.037 < Ca_c < 0.129$

In Figure 4.19 the observed droplet regimes are depicted as a function of flow rate ratio α and of the continuous Capillary number Ca_c . It is evident that an increase of the continuous Capillary number Ca_c reduces the critical value of the flow rate ratio α_{cr} in correspondence of which the transition from DJ to DC regime occurs. For non-Newtonian continuous fluids, the continuous Capillary number increases significantly due to the higher values of the fluid viscosity.

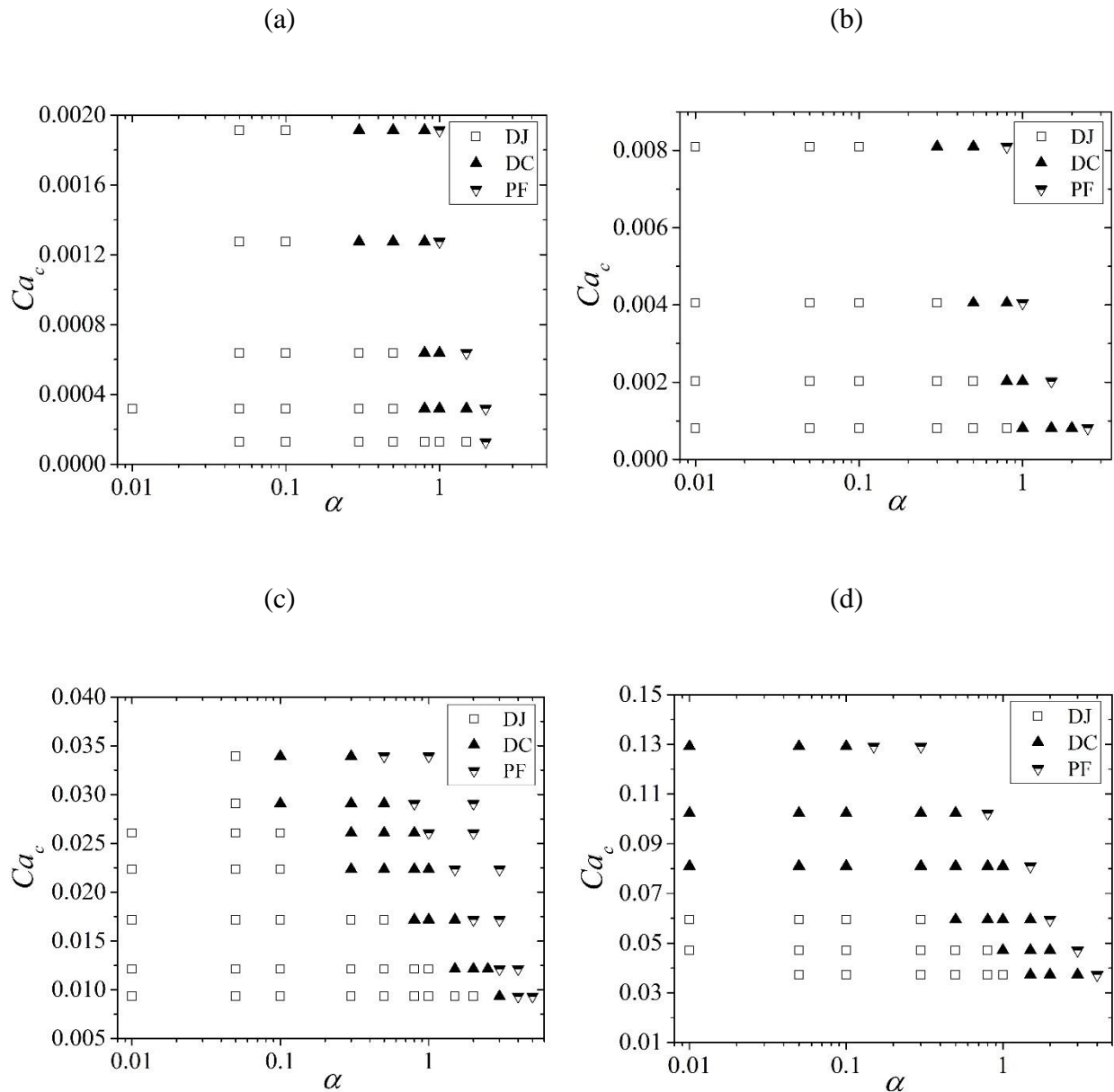


Figure 4.19. Droplet flow maps for silicone oil (SO) droplets as a function of flow rate ratio α and Capillary number Ca_c in hydrophilic T-junction with (a) W, (b) W+T, (c) 0.2 XG and (d) 0.2 XG+T as the continuous phase.

Unlike the first T-junction in which only a parallel flow regime was observed without the use of Tween 20 in the continuous phase (see Figure 4.5), by using the second micro T-junction silicone oil droplets are generated in presence of both pure water (W) and 0.2 wt% aqueous Xanthan gum solution without surfactant (0.2 XG) as carrier medium.

This result puts in evidence that the walls of the second T-junction justify a different value of the solid-liquid interfacial tension with respect to the first T-junction. In fact, as

highlighted by Shui *et al.* [32], unlike macroscopic systems, solid-liquid interfacial tension σ_{sl} plays a predominant role in droplet generation in microjunctions; on the contrary, liquid-liquid interfacial tension σ_{ll} , which can be modified by addition of surfactant, plays a secondary role. The experimental observations about the droplet regimes obtained in these two micro T-junctions can be explained by assuming that the walls of the first micro T-junction are hydrophobic while the walls of the second one are hydrophilic.

In presence of surfactant, comparing Figure 4.9 with Figure 4.19b, one can observe that the same trend of the droplet regimes are observed for the two micro T-junctions tested with Water with 2 wt% Tween 20 (W+T).

By recalling the definition of squeezing, dripping and jetting regimes, as explained in the previous sections, the droplet-based flows can be divided on the basis of the observation of the droplet breakup mechanism.

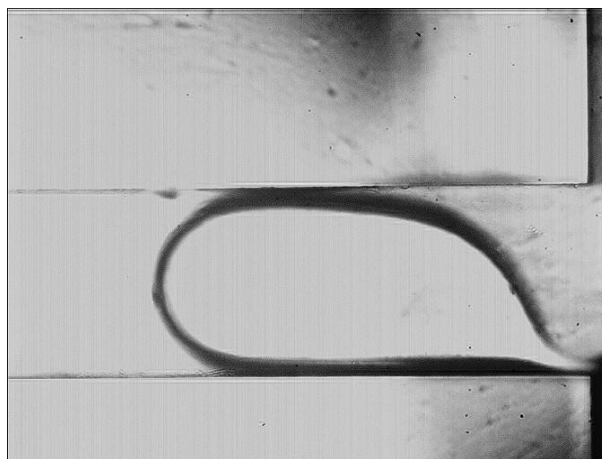


Figure 4.20. Squeezing regime for silicone oil (SO) droplet in 0.2 wt% Xanthan gum solution with 2 wt% Tween 20 (0.2 XG+T) when $Q_c = 0.5$ and $Q_d = 0.05$ ml/h.

The breakup mechanism changes by varying the continuous (Q_c) and/or the dispersed flow rate (Q_d); at low flow rates the droplet almost blocks the whole channel in squeezing regime (see Figure 4.20) whilst with the increase of the continuous flow rate the size of the microdroplet is reduced (Figure 4.21a). On the other hand, an increase of the dispersed flow rate moves the droplet generation downstream the T-junction (Figure 4.21b).

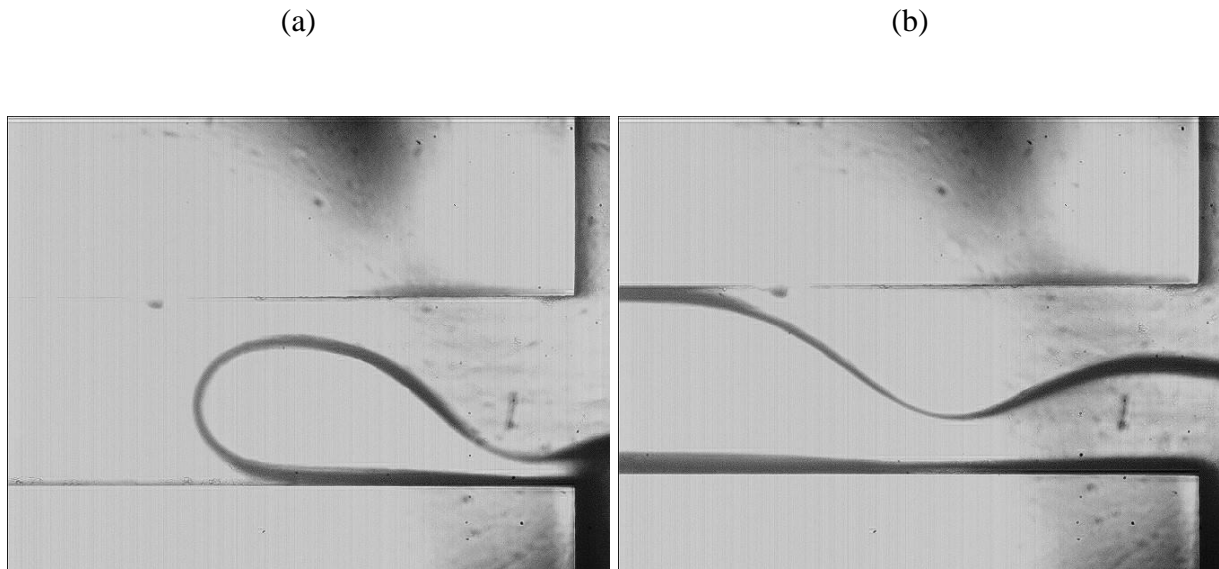


Figure 4.21. Dripping regime for silicone oil (SO) droplet in 0.2 wt% Xanthan gum solution with 2 wt% Tween 20 (0.2 XG+T) when (a) $Q_c = 5$ and $Q_d = 0.05$ ml/h and (b) $Q_c = 2$ and $Q_d = 2$ ml/h.

A further increase of the flow rates can generate the jetting regime (JR). In jetting regime a stable jet close to the junction is observed (Figure 4.22a) while the unstable region of the jet is placed downstream the T-junction (Figure 4.22b).

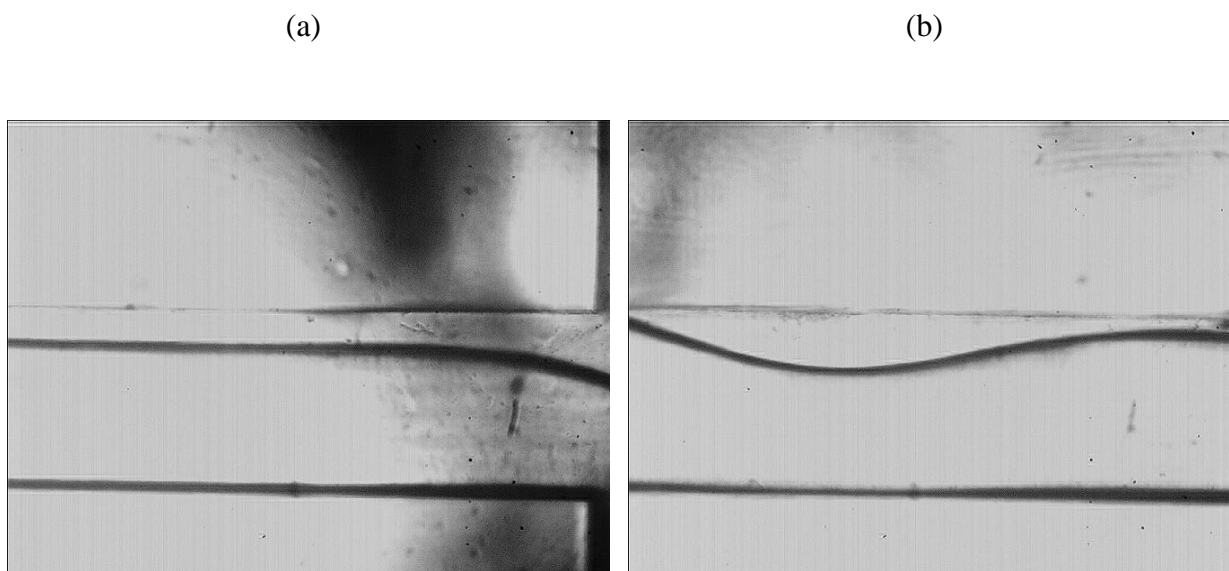


Figure 4.22. Jetting regime for silicone oil (SO) droplet in water with 2 wt% Tween 20 (W+T) when $Q_c = 2$ and $Q_d = 4$ ml/h; (a) at the junction and (b) downstream of it.

When the dispersed flow rate is very large jetting regime cannot be obtained and a stable

co-flow (parallel flow regime) is observed without droplet formation.

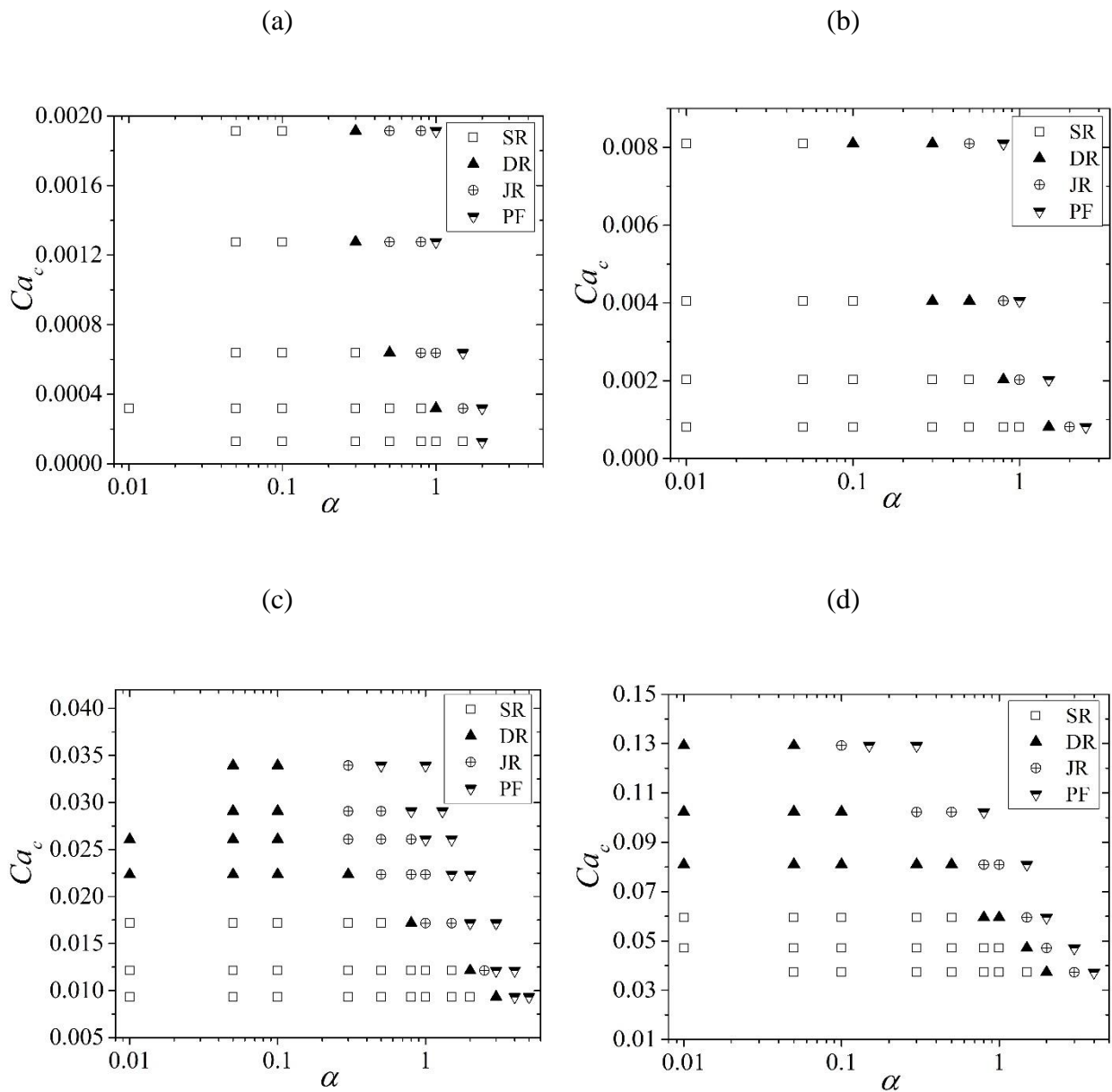


Figure 4.23. Droplet breakup mechanism for silicone oil (SO) droplets as a function of flow rate ratio α and Capillary number Ca_c in hydrophilic T-junction with (a) W, (b) W+T, (c) 0.2 XG and (d) 0.2 XG+T as the continuous phase.

Figure 4.23 illustrates the dependence of the droplet breakup on the combination of volumetric flow rates. Keeping the continuous flow rate constant ($Ca_c = Const.$), one can see the transition of the flow regimes starting from squeezing (SR) to dripping (DR) and jetting (JR) by increasing the dispersed flow rate and hence α ($= Q_d/Q_c$). As described in the previous sections, transition from a droplet regime to another one can be also obtained by increasing the

continuous Capillary number for a fixed value of the flow rate ratio α . In presence of a non-Newtonian carrier medium the transition from SR to DR is also observed at low values of α when Q_c is increased (see Figure 4.23c and d).

In order to take into account the effects of both continuous and dispersed phase Capillary number (Ca_c, Ca_d), the flow regimes for the silicone oil droplets within non-Newtonian carrier fluids (0.2 XG and 0.2 XG+T) have been re-plotted in a plane as a function of continuous (Ca_c) and dispersed Capillary number (Ca_d).

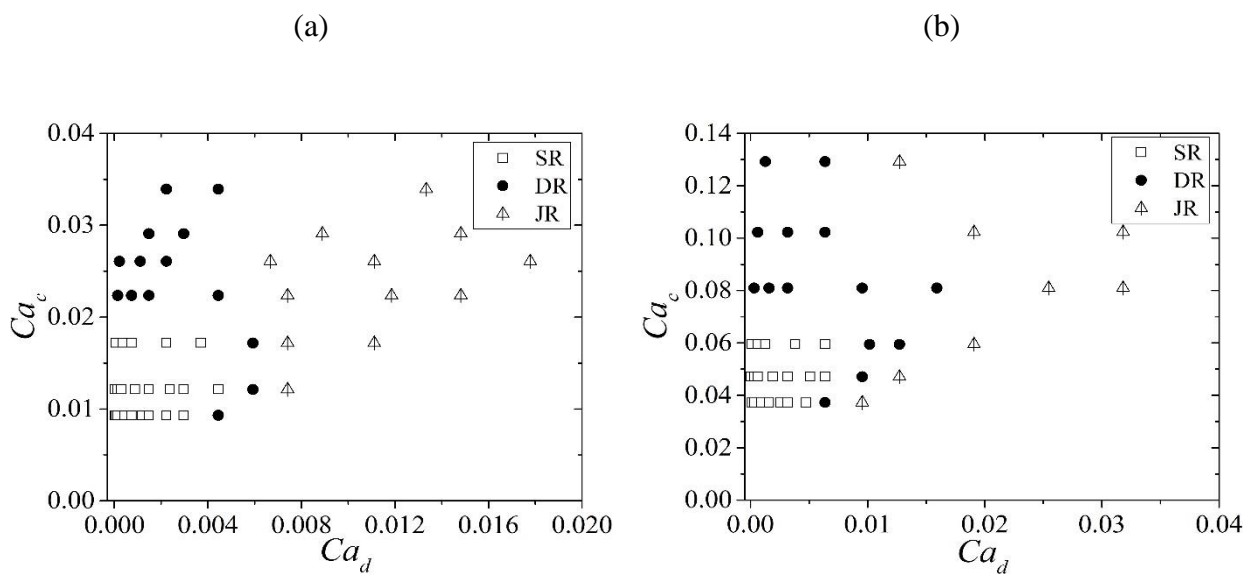


Figure 4.24. Droplet breakup mechanism for silicone oil (SO) droplets as a function of dispersed Ca_d and continuous Capillary number Ca_c in hydrophilic T-junction with (a) 0.2 XG and (b) 0.2 XG+T as the continuous phase.

Figure 4.24 shows that the variation of the flow regimes can be easily recognized by using a (Ca_d, Ca_c) plot. The results obtained with the T-junction are similar to those observed for a cross-junction (see Chapter 3) and reported in literature [50]. As expected, an increase of Ca_d or Ca_c causes the flow regime transition from SR to DR and JR. It's worth mentioning that in presence of a Newtonian continuous phase, an increase of volumetric flow rate (Q_c) is responsible of the increase of the Capillary number with a constant viscosity ratio λ . On the contrary, in presence of non-Newtonian continuous phase an increase of volumetric flow rate (Q_c) is responsible of an increase of the continuous Capillary number as well as of the viscosity ratio λ due to the viscosity μ change. The use of a (Ca_d, Ca_c) plot is able to take into account the combined effects on the droplet regimes of the variation of Ca_c , α and λ .

4.3.1.1 Effect of α and Ca_c

In Figure 4.25 the non-dimensional length \bar{L} of the silicone oil droplets within the micro T-junction filled with water without and with Tween 20 (W, W+T) as well as in presence of 0.2 wt% aqueous Xanthan gum solution with and without Tween 20 (0.2 XG+T, 0.2 XG) is plotted as a function of flow rate ratio α .

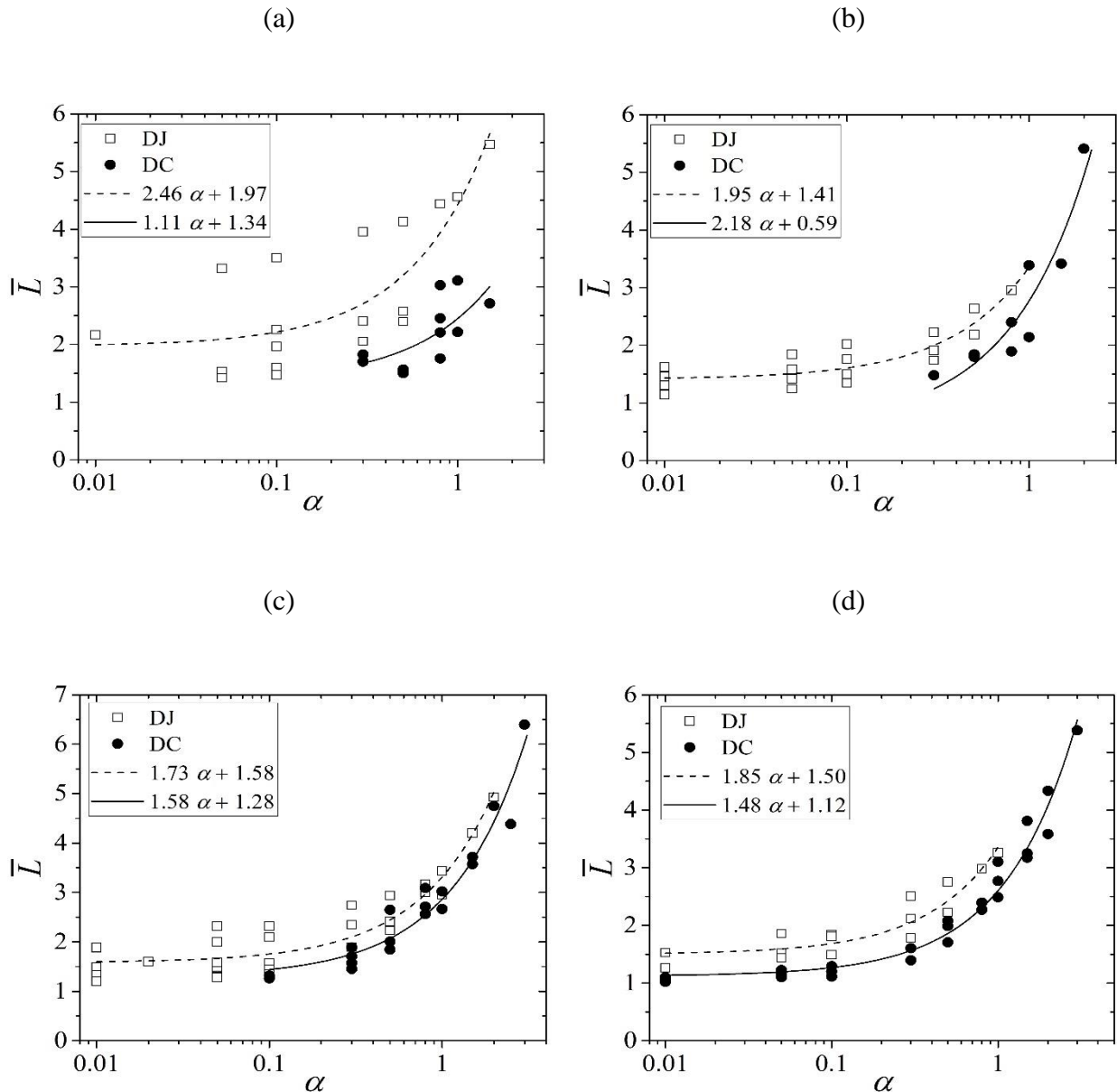


Figure 4.25. Non-dimensional length \bar{L} of the silicone oil (SO) droplets as a function of flow rate ratio α in hydrophilic T-junction with (a) W, (b) W+T, (c) 0.2 XG and (d) 0.2 XG+T as continuous phase.

Figure 4.25a shows that, in presence of pure water (W) as continuous phase, scattered

values of the non-dimensional length \bar{L} of the silicone oil droplets are obtained in comparison with the other results (Figure 4.25b, c and d).

As one knows, longer droplets are produced by increasing α ($= Q_d/Q_c$). As evidenced by Garstecki *et al.* [41], although the droplet length tends to increase with α , the slope of the variation of the droplet length varies with α . In Figure 4.25 two linear correlations having the conventional expression suggested by Garstecki *et al.* [41] ($\bar{L} = \varepsilon + \omega\alpha$) for the droplet length \bar{L} and the flow rate ratio are used to correlate the experimental data for DJ and DC regimes. As explained in Section 4.2.2, ε and ω are two fitting constant. The increase of the droplet volume in DC regime is originated by the absorption of the longer thread before the droplet detachment.

The dimensionless length of the droplet as a function of Ca_c is plotted in Figure 4.26. A power-law correlation in the form of $\bar{L} = qCa_c^x$ has been used in order to fit the experimental data. Figure 4.26 confirms that this correlation is able to predict the droplet size as a function of Capillary number in the range of the values of α imposed during these tests with a good accuracy when $x = -0.3$ for Newtonian carrier medium (in agreement with Figure 4.15) or $x = -0.5$ for non-Newtonian continuous phase. The data confirm that the non-Newtonian nature of the continuous phase affects the dependence of the droplet length on the continuous Capillary number Ca_c .

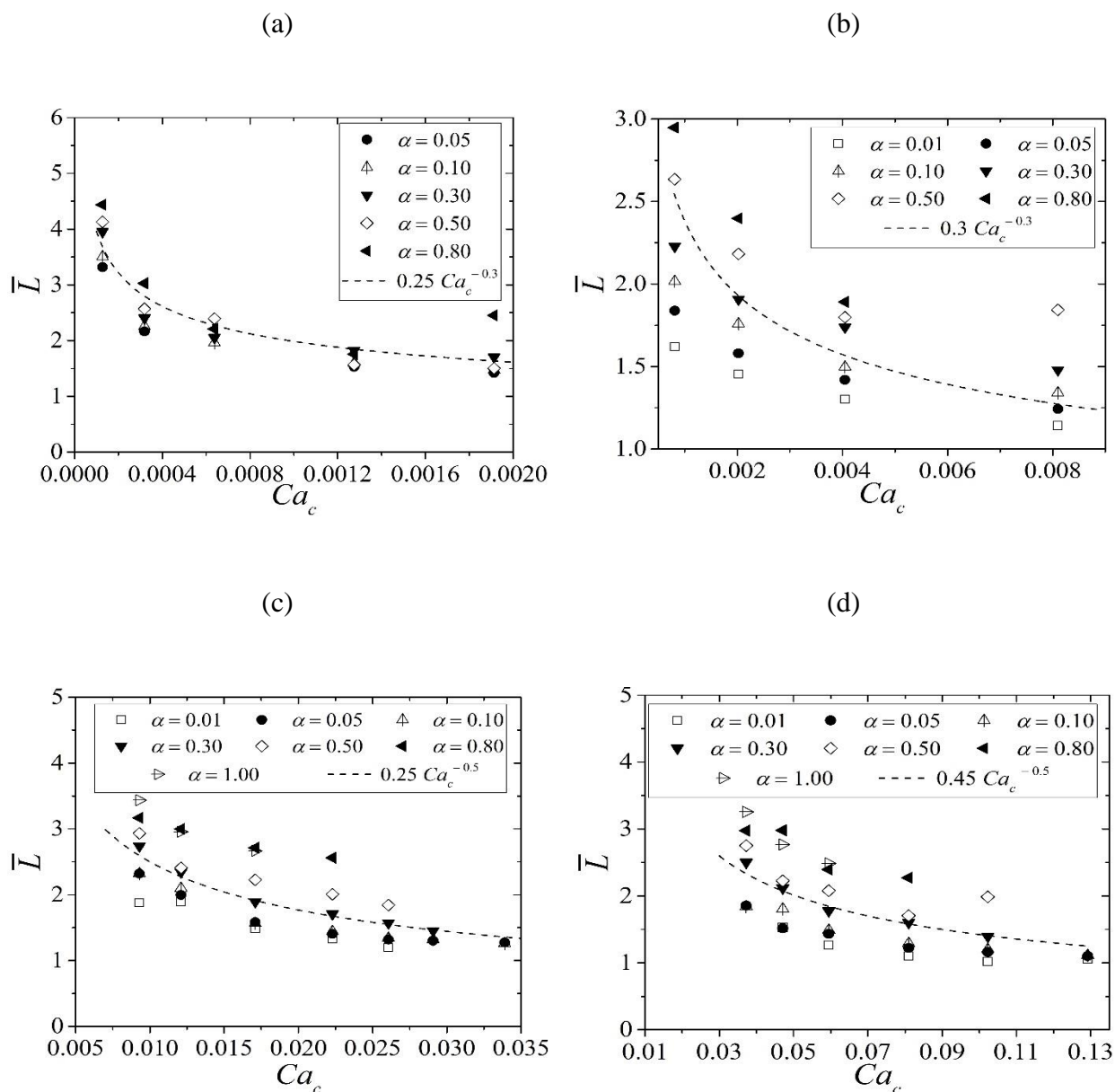


Figure 4.26. The power-law correlation fitted to the experimental data for different values of α as a function of Ca_c in hydrophilic T-junction with (a) W, (b) W+T, (c) 0.2 XG and (d) 0.2 XG+T as the continuous phase.

Figure 4.27 shows how the non-dimensional length of the silicone oil droplet varies with continuous Capillary number Ca_c and flow rate ratio α when water with 2 wt% Tween 20 (W+T) is considered as continuous phase.

At low values of the flow rate ratio α (< 0.5), almost identical values for dimensionless droplet length may be observed for the two T-junctions tested in this work. On the contrary, the data scattering increases in correspondence of larger values of α due to the coalescence of

the droplets when larger values of the dispersed flow rate are introduced into the junction.

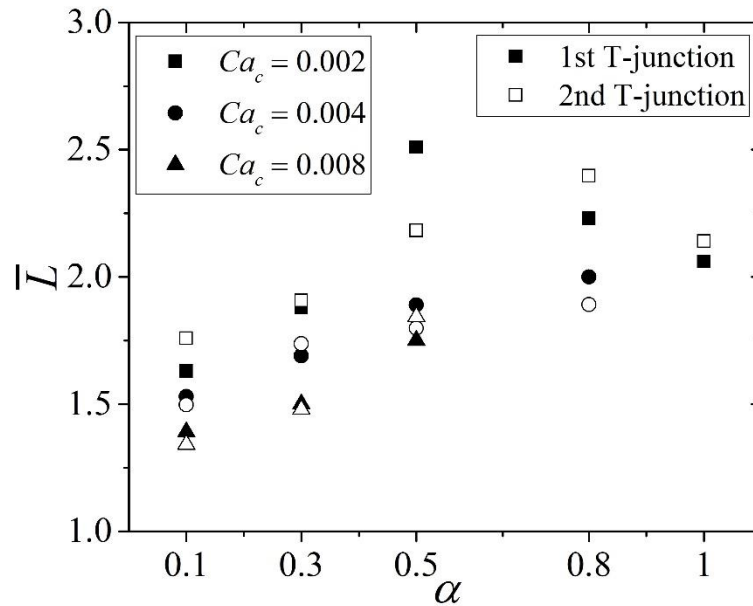


Figure 4.27. The non-dimensional length of the silicone oil microdroplets in water with Tween 20 (W+T) as carrier medium; closed symbols represent the first T-junction (hydrophobic) while open symbols stand for the second T-junction (hydrophilic).

4.3.1.2 Breakup distance

As explained in previous section (see Figure 4.17) the breakup position of the immiscible thread ($x_{breakup}$) increases with the increase of the flow rate ratio (α) for a fixed value of the Capillary number (Ca_c). The same trend may be observed by increasing the values of continuous Capillary number. In fact, an increase of Ca_c causes an increase of the shear force which acts on the dispersed phase by elongating the thread between the droplet and the nozzle before the breakup.

The breakup distance of the thread from the junction has been presented in Figure 4.28 for the silicone oil (SO) droplets in pure water (W), water with 2 wt% Tween 20 (W+T) and 0.2 wt% aqueous Xanthan gum solution in the absence and presence of 2 wt% Tween 20, 0.2 XG and 0.2 XG+T, as the continuous phase.

At low values of the continuous Capillary number Ca_c and/or low flow rate ratio α , the droplet pinch-off occurs close to the center of the T-junction while by increasing α or Ca_c the breakup position tends to move downstream of the junction.

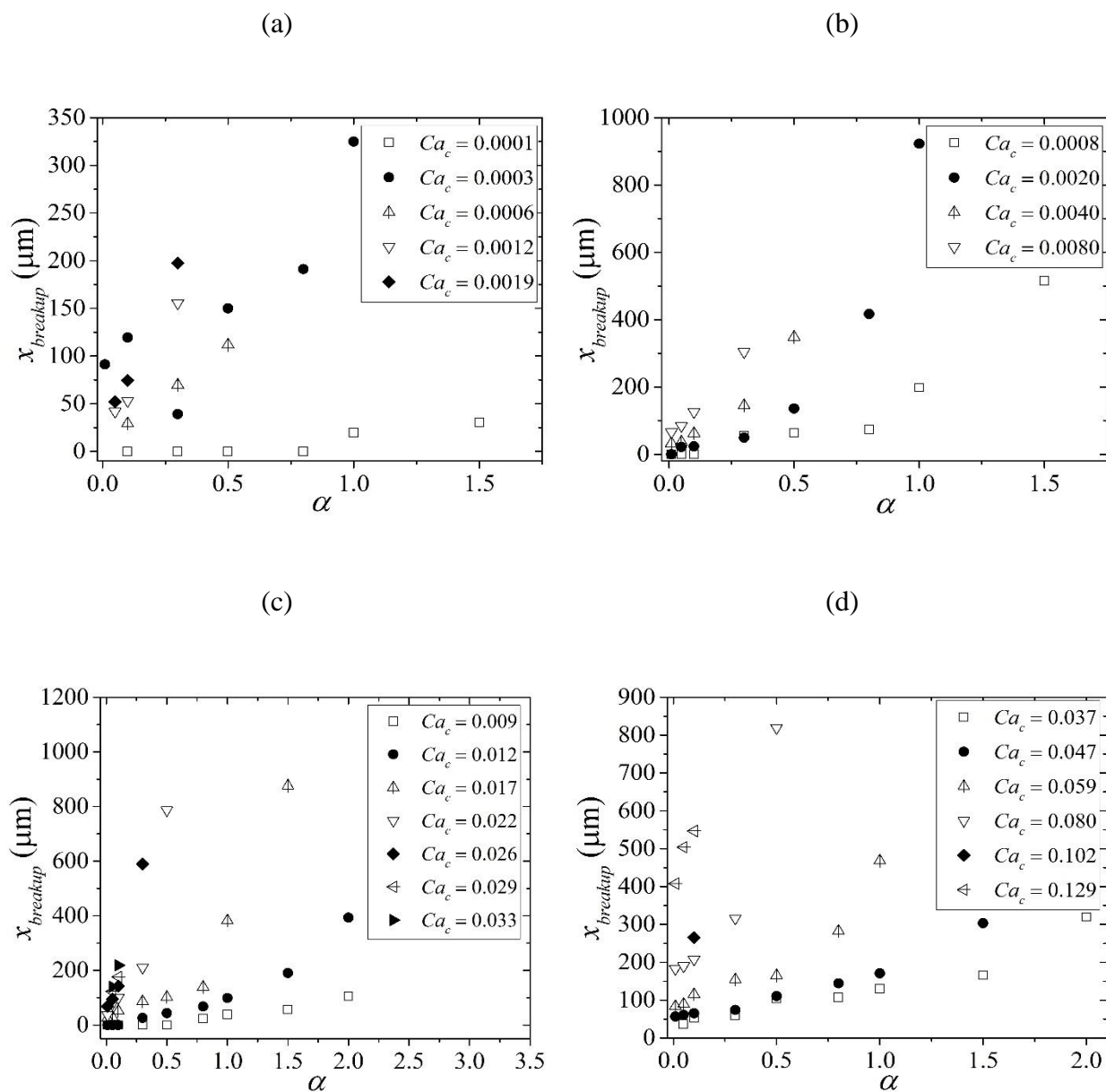


Figure 4.28. The breakup distance from the junction for different values of α as a function of Ca_c in hydrophilic T-junction with (a) W, (b) W+T, (c) 0.2 XG and (d) 0.2 XG+T as the continuous phase.

4.3.1.3 Polydispersity

The variation of the diameter of the silicone oil droplets generated in the T-junction have been analysed in order to obtain the value of polydispersity Pl . The definition of polydispersity Pl is given by Equation (2-10).

The polydispersity values obtained for silicone oil emulsions generated in both Newtonian (W, W+T) and non-Newtonian (0.2 XG, 0.2 XG+T) carrier fluids have been shown

as a function of α and Ca_c in Figure 4.29.

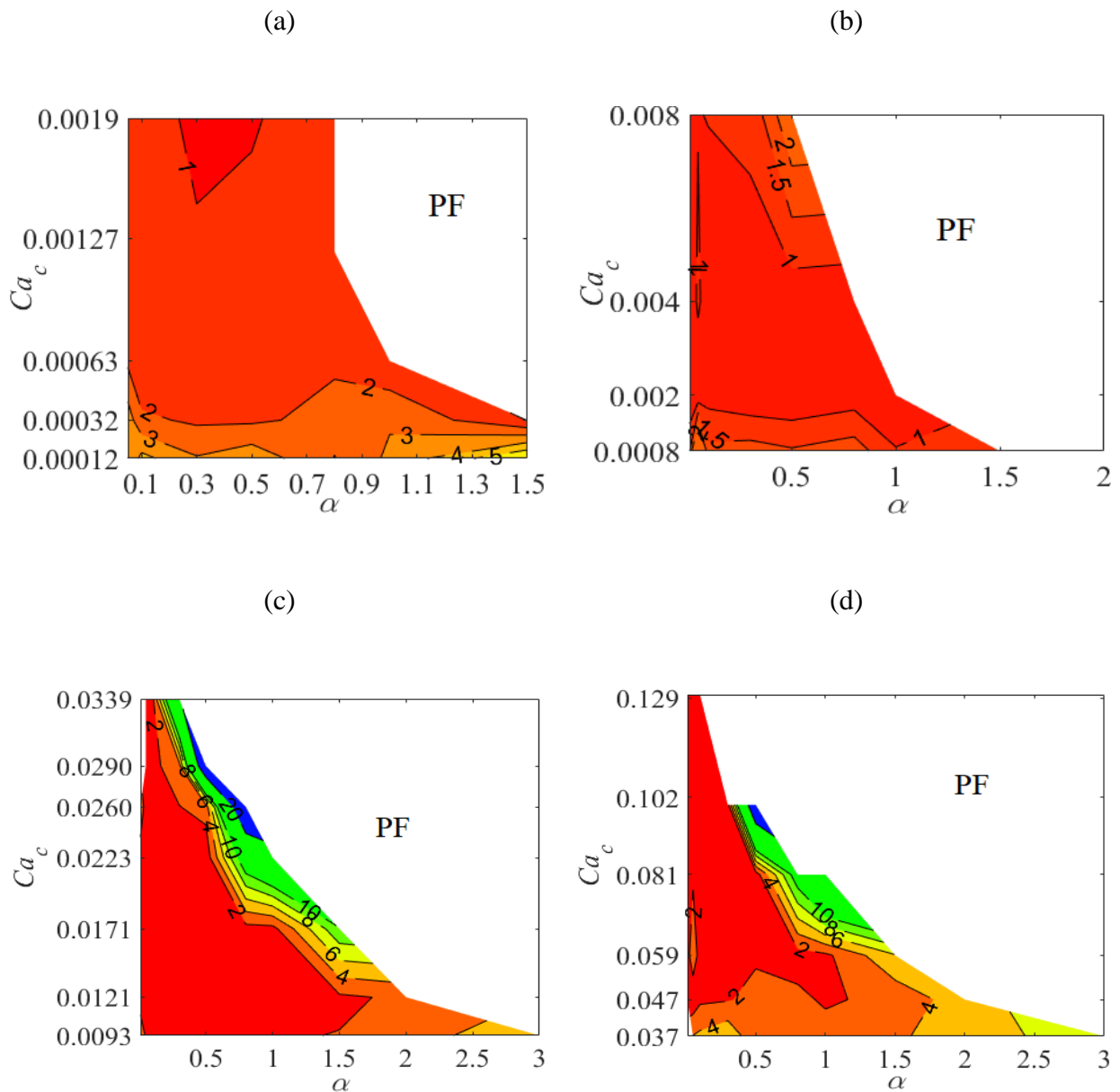


Figure 4.29. The polydispersity Pl values for different values of α as a function of Ca_c in hydrophilic T-junction with (a) W, (b) W+T, (c) 0.2 XG and (d) 0.2 XG+T as the continuous phase.

It is evident that droplets generated in Newtonian continuous phase of pure water (W) and water with 2 wt% Tween 20 (W+T) are characterized by low values of polydispersity Pl ($< 5\%$) when the continuous Capillary number Ca_c is lower than 0.008. This result highlights that in this region the T-junction can be used in order to generate monodispersed emulsion. On the contrary, for non-Newtonian fluids the values of polydispersity Pl show a larger scattering and the generation of monodispersed droplets can be obtained for larger values of either

Capillary number Ca_c or volumetric flow rate ratio α .

Comparing Figure 4.18 and Figure 4.29b it is possible to conclude that in presence of hydrophilic walls the region in correspondence of which the generation of monodispersed droplets is obtained is enlarged with respect the same T-junction geometry with hydrophobic walls. Figure 4.29 confirms that in non-Newtonian carrier fluids the polydispersity Pl is within the range of ($Pl < 2\%$) in correspondence of all the Capillary numbers tested in this work in presence of hydrophilic walls. At high values of the Capillary number, polydispersity tends to increase if α is increased.

Chapter 5

Conclusions and Recommendations for Future Work

In this dissertation an experimental analysis of the use of microjunctions for droplet generation is described. The analysis has been focused on two types of micro cross-junctions and a T-junction under opposite-flow configuration by using different liquids (Newtonian and non-Newtonian) as dispersed and continuous phase. The main goal of this thesis is the systematic analysis of the influence of the main control parameters (i.e. flow rates, viscosity ratio, geometry of the junction, continuous and dispersed Capillary numbers) on the characteristics of the droplet-based flow generated at the outlet of the microdevice. Since the topic has been extensively investigated in the past and many results are available in the open literature, the attention of this thesis has been focused on a series of aspects disregarded until now, like, among others, the following:

- The role of the viscosity ratio on the droplet formation in presence of non-Newtonian fluid;
- The use of T-junctions in opposite-flow configuration for generation of monodispersed emulsions in presence of Newtonian and non-Newtonian continuous phases;
- The detailed experimental analysis of the breakup mechanism in terms of breakup distance, velocity of the reduction of the thread width, droplet frequency and formation time.

This kind of information is very important for the development of accurate numerical models able to predict the droplet-based flow generation in complex microfluidic devices and hence for an optimal design of droplet generators based on microjunctions.

5.1 Key findings of the thesis

The results summarized in this thesis give a contribution to the understanding of the droplet-based flow generation, using both Newtonian and non-Newtonian solutions, in microdevices. The major outcomes of this study are here summarized.

Large part of the thesis has been devoted to the analysis of the behavior of micro cross-junctions for the production of a droplet-based flow (Chapter 3). Two micro cross-junctions having a different geometry have been employed during the experimental tests. Different combinations of dispersed and continuous phases have been used as working fluids by considering both Newtonian (i.e. Water, Water with the addition of Tween 20, Silicone oil) and non-Newtonian (i.e. Xanthan gum aqueous solutions) liquids.

In all the experimental tests silicone oil has been used as the continuous phase in which droplets of water, water with Tween 20, Xanthan gum solutions are generated.

A large amount of experimental runs have been made with the aim to characterize the capability of the micro cross-junctions to generate monodispersed emulsions in which Newtonian or non-Newtonian droplets are created in a Newtonian flow of silicone oil.

With a speed camera connected to an inverse microscope, up to 1500 frames per second have been acquired with the aim to reconstruct the evolution of the interface shape between the immiscible liquids. For the post-processing of the acquired images a home-made numerical code based on the functions of MATLAB Image Toolbox for image treatment and analysis has been developed. In this way the main droplet regimes responsible of droplet formation have been individuated. Three droplet-based regimes have been identified: squeezing, dripping and jetting regimes. In squeezing regime large droplets that block the main channel are generally obtained; in dripping regime the size of the generated droplets is reduced and they partially fill the outlet channel. In jetting regime smaller droplets are sheared-off far from the junction thanks to an unstable core of dispersed liquid which is present along the exit channel.

In order to check in which way the three regimes are affected by the properties of the dispersed phase four flow maps have been obtained in which the droplet regimes are correlated to the values assumed by the volumetric flow rate ratio (α) and by the Capillary number of the continuous (Ca_c) and dispersed phase (Ca_d).

A similar aspect of the flow maps obtained by using pure water, water with Tween 20 (2 wt%) and aqueous Xanthan gum solutions as dispersed phases has been obtained.

In Figure 5.1 the typical flow map observed for cross-flow junctions is represented.

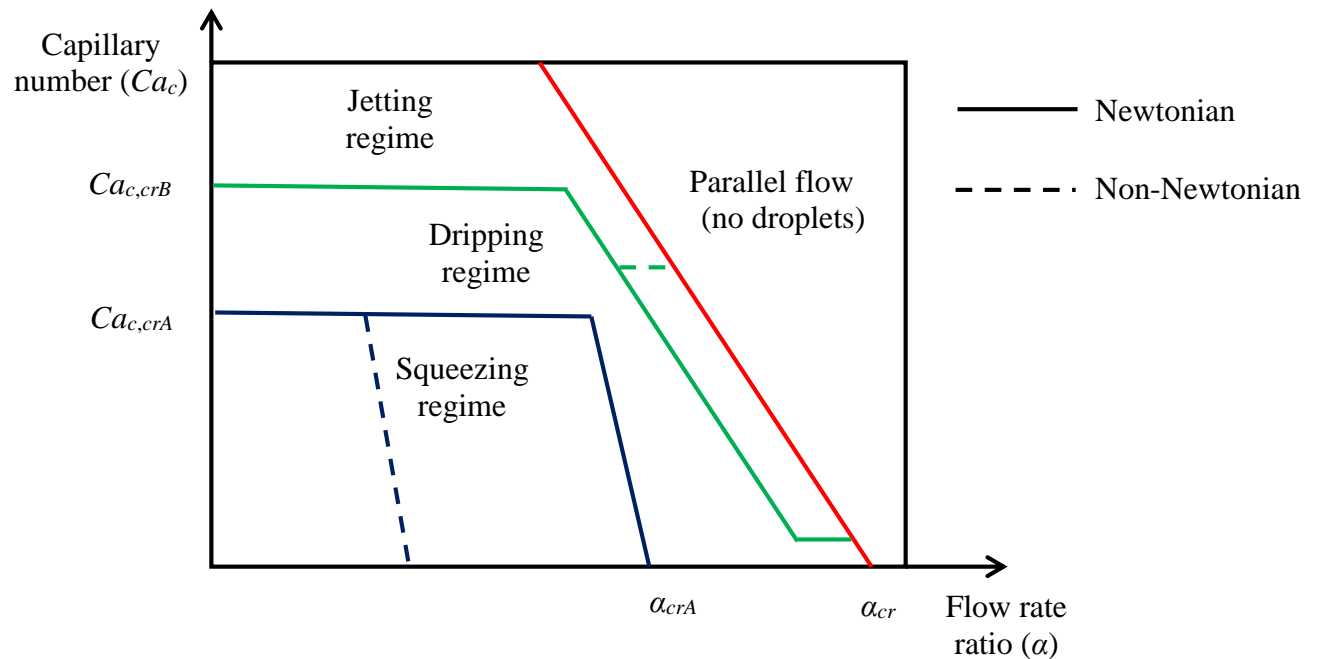


Figure 5.1. Typical droplet-based flow map obtained for a micro cross-junction.

From Figure 5.1 can be observed that:

- At low Capillary numbers droplets are generally obtained by squeezing, especially for low values of the flow rate ratio. By Figure 5.1 it is evident that this occurs if $Ca_c < Ca_{c,crA}$. The value of $Ca_{c,crA}$ is the value of the Capillary number in correspondence of which at low values of α the transition from squeezing regime to dripping regime occurs. The experimental data obtained in this thesis demonstrate that $Ca_{c,crA}$ is weakly influenced by the properties of the dispersed phase and by the viscosity ratio of the immiscible liquids. $Ca_{c,crA}$ ranges from 0.01 to 0.03. This value is in agreement with the values observed by many other researchers for junctions having a different geometry (i.e. T-junctions).
- At low Capillary numbers ($Ca_c < Ca_{c,crA}$), the transition between squeezing and dripping (blue line in Figure 5.1) is a function of both α and Ca_c even if α is more important than Ca_c .

- In the case of non-Newtonian droplets, the range of the flow rates in which squeezing regime is observed decreases and dripping regime becomes the dominant droplet breakup mechanism.
- Jetting regime is observed at low Ca_c values only in the case of Newtonian droplets for large values of flow rate ratio before than the droplet generation is stopped and a parallel co-flow is obtained at the exit of the cross-junction. On the contrary, in presence of non-Newtonian emulsions jetting is activated only for large values of the continuous Capillary number (i.e. $Ca_c > 0.03$).
- The addition of Tween 20 within the dispersed phase is not able to modify the boundary between squeezing and dripping regime; this means that the transition between these two regimes occurs at the same values of α and Ca_c with and without surfactant. However, since the interfacial tension is strongly reduced by the surfactant, for a fixed value of the dispersed flow rate the transition between squeezing and dripping is obtained in correspondence of lower values of the continuous flow rate.
- At low Capillary numbers ($Ca_c < Ca_{c,crA}$), droplet-based flow can be obtained only for values of α less than a critical value (α_{cr}). This critical value is strongly influenced by the properties of the dispersed phase as well as by the viscosity ratio. In the thesis it has been demonstrated that α_{cr} depends on Ca_c (see the red line in Figure 5.1) and the values of α_{cr} goes from values larger than 10 for pure water and water with Tween 20 down to 1 for aqueous Xanthan gum solutions.
- At low flow rate ratio ($\alpha < \alpha_{crA}$), jetting can be obtained only for Capillary numbers larger than a critical value ($Ca_{c,crB}$). The flow rate ratio value is able to influence the transition from dripping to jetting for α larger than α_{crA} (see the green line in Figure 5.1). The values of the critical Capillary number $Ca_{c,crB}$ are weakly dependent on the properties of the immiscible liquids. In this thesis values of $Ca_{c,crB}$ of the order of 0.1 are observed for all the combinations of working liquids examined.

In the thesis the experimental data about the droplet size (D^*) as a function of the Capillary number has been used in order to obtain the values of $Ca_{c,crA}$ and $Ca_{c,crB}$ by following the method recently proposed by Gu [22]. The values of $Ca_{c,crA}$ and $Ca_{c,crB}$ obtained with this method are found to be in qualitative agreement with the experimental flow maps obtained for both Newtonian and non-Newtonian dispersed fluids.

About the characteristics of the droplets, it has been observed that:

- Larger droplets are produced by decreasing the volumetric flow rate of the continuous phase (Q_c) and the viscosity of the dispersed phase (μ_d) and/or increasing Q_d . Generally, the effect of Q_c (Ca_c) is more important in dripping regime and less important in squeezing and jetting regimes. On the contrary, Q_d plays an important role in order to influence the droplet size in squeezing regime and it is less important in dripping and jetting regimes.
- Xanthan gum concentration influences the viscosity of the solution; an increase of the concentration is able to produce a significant increase of the liquid viscosity. Larger droplets are produced by using Xanthan gum solutions as dispersed phase with higher Xanthan gum concentration in each droplet regime.
- The combined effect on the droplet regimes due to the flow rate ratio α and the viscosity ratio λ can be taken into account by using a (Ca_d, Ca_c) plot. The transition from squeezing to dripping and jetting is generally obtained by increasing both Ca_c and Ca_d . An increase of λ produces an increase of Ca_d which can be responsible of a transition from a droplet regime to another one for a fixed value of Ca_c and α .
- The droplet characteristics are influenced by the geometry characteristics of the junction; in particular it has been demonstrated that the restricted ratio R of the junction can play an important role on the droplet size when the junction operates in squeezing regime.

In addition, a series of detailed information about the droplet formation dynamics obtained by varying in a wide range the main controlling parameters (α and Ca_c) including the measure of the droplet formation time, of the length of the microthread existing in dripping regime between droplet and the source of dispersed phase, of droplet frequency have been discussed.

About the analysis of the use of T-junctions in opposite-flow configuration (Chapter 4) for the generation of droplet-based flows two micro T-junctions with the same characteristics have been tested. The behavior of these identical T-junctions from a geometrical point of view in terms of droplet formation was quite different due to a different status of the wall surfaces (hydrophilic and hydrophobic). The experimental data have shown that, in presence of hydrophobic walls:

- A T-junction in opposite-flow configuration allows to obtain a droplet-based flow at the exit of the junction only if either the interfacial tension between the immiscible liquids is low by the addition of surfactant or the continuous phase flow rate is very high in the absence of surfactant.
- Without surfactant in the continuous phase (W) the droplet formation may be observed only at very high values of the continuous flow rate (large Ca_c) and low flow rate ratio ($\alpha \leq 0.15$). For $\alpha = 0.05$ the droplet is generated when $Q_c \geq 80$ ml/h ($Ca_c \geq 0.0051$) but with the increase of the flow rate ratio ($\alpha = 0.15$) Q_c needs to be higher than 60 ml/h ($Ca_c \geq 0.0038$) in order to obtain droplets.
- The use of Tween 20 in the continuous phase with concentrations larger than CMC value (= 0.0074 wt%) is able to modify the flow regime from parallel flow to droplet-based flow within a limited range of continuous Capillary numbers.

In Figure 5.2 the typical flow map observed for the T-junctions in opposed-flow configuration with hydrophobic walls is depicted when a Newtonian continuous phase is introduced in the T-junction.

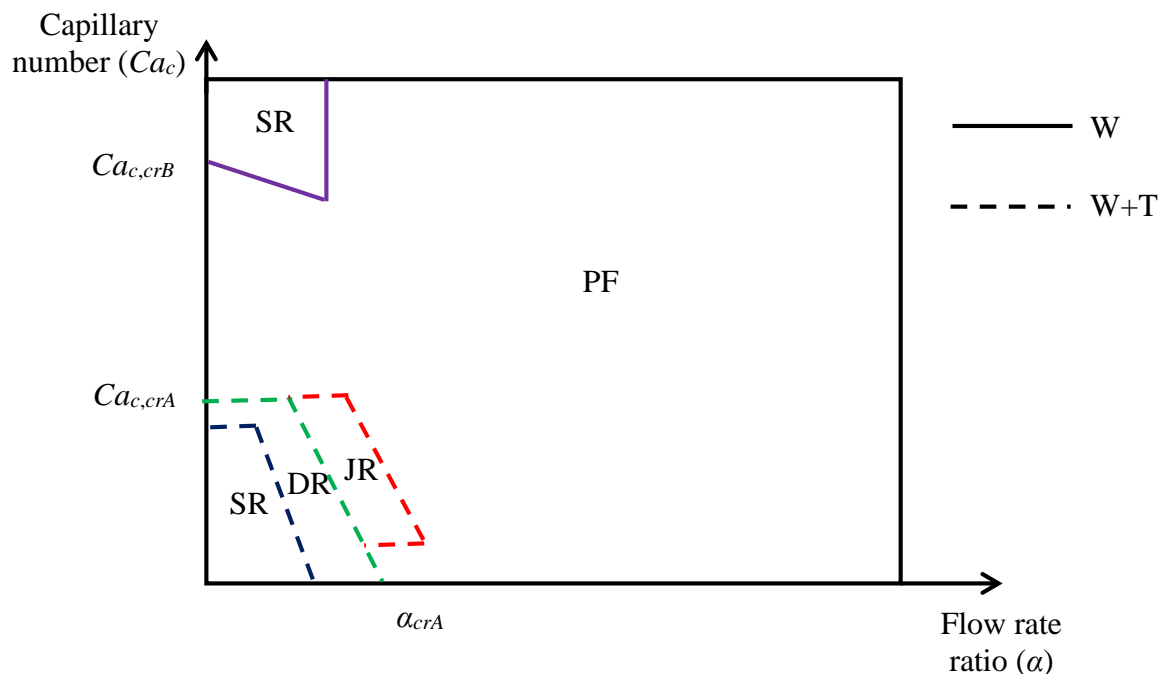


Figure 5.2. Typical flow map obtained for the first micro T-junction in opposed flow configuration (hydrophobic walls).

- By reducing the interfacial tension between the immiscible liquids introduced in the junction (i.e. thanks to the introduction of a surfactant), the T-junction in opposite-flow configuration can generate a droplet-based flow by squeezing, dripping or jetting mechanism.
- The T-junction in opposite-flow configuration can be used in order to generate monodispersed emulsions but in this case the junction must work with low values of the Capillary number linked to the continuous phase ($Ca_c < 0.01$) and low flow rate ratio ($\alpha < 0.5$).
- When a droplet-based flow is generated by squeezing (DJ regime) at the exit of the junction, the droplet length \bar{L} is influenced both by the volumetric flow rate ratio (α) and by the Capillary number (Ca_c).
- The non-dimensional length of the microthread is found to be a power-law function of continuous Capillary number in the form of $\bar{L} \sim Ca_c^{-0.3}$ in agreement with the literature.
- For large values of the interfacial tension between the immiscible liquids the most common flow pattern obtained at the exit of the junction is the stratified parallel flow in which dispersed and continuous flows are separated by a curved interface. It has been demonstrated that by changing α and Ca_c a good control of the depth of the two parallel layers can be obtained. This flow pattern can be useful when it is important to guarantee the separation of the liquids by avoiding to insert a membrane in between (i.e. microreactors for micro fuel cells).
- The breakup position of the droplets tends to move downstream if the continuous Capillary number Ca_c and/or the flow rate ratio α is increased.

For the micro T-junction having hydrophilic walls it has been observed that

- In presence of hydrophilic walls the T-junction allows to obtain a droplet-based flow even without the use of surfactant within the continuous phase for a large range of values of Ca_c and α . In this case the droplet regime map of Figure 5.2 changes as indicated by Figure 5.3.
- By increasing the continuous phase flow rate Q_c , transition from a droplet regime to another one occurs at lower values of α for non-Newtonian fluids with respect to Newtonian carrier medium. Also the introduction of surfactant into the carrier medium anticipates the transitions among the droplet regimes.

- With a Newtonian carrier fluid (W), silicone oil droplets are generated in squeezing regime for low values of α (≤ 0.1). No dripping is observed at low α values.
- On the contrary, for non-Newtonian fluids, even at very low values of α , a critical value of the Capillary number there exists beyond which the transition from squeezing to dripping can be observed.
- At low values of the volumetric flow rate, squeezing is the predominant droplet regime while with an increase in either α or Ca_c the transition from squeezing to dripping generally is observed.
- Jetting regime can be observed only for large values of α and/or Ca_c .

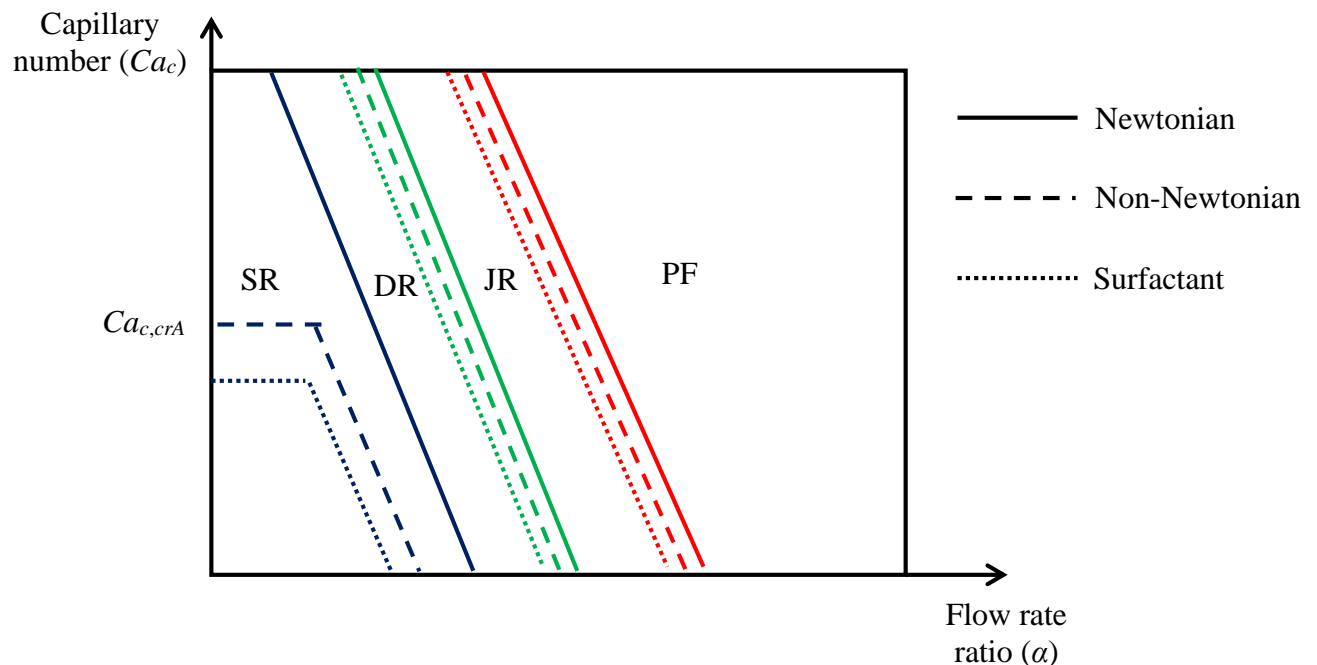


Figure 5.3. Typical flow map obtained for the micro T-junction in opposed flow configuration with hydrophilic walls.

The dimensionless length of the droplets can be expressed as a function of the continuous Capillary number thanks to a power law; for Newtonian continuous phase (W, W+T) \bar{L} depends on $Ca_c^{-0.3}$ in agreement with the literature. On the contrary, \bar{L} varies with $Ca_c^{-0.5}$ for a non-Newtonian continuous phase.

Finally, by observing the polydispersity values associated to the droplets generated with T-junctions in opposite flow configuration it has been evidenced in which conditions droplet-

based flows can be generated with a low value of polydispersity Pl ($< 6-8\%$). In this way it has been possible to individuate, for each tested microjunction, the range of values of α and Ca_c able to guarantee the generation of a monodispersed emulsion.

The analysis of the variation of the diameter of the droplets observed at the exit of the T-junction in presence of hydrophobic or hydrophilic walls highlights that mono-dispersed silicone oil droplets with $Pl < 2\%$ can be obtained easily in presence of hydrophilic channel walls. For non-Newtonian continuous phase the polydispersity increases with the flow rate ratio but at low values of α (< 0.5) highly monodispersed droplets ($Pl < 2\%$) can be generated in presence of hydrophilic walls.

5.2 Recommendations for future work

Three years of Ph.D. is a long period but not enough to fill all the gaps that one can meet during its research path. A series of aspects, originally individuated as key aspects, remains not fully investigated. To obtain a further understanding of droplet formation in microjunctions by using Newtonian and non-Newtonian solutions, several aspects need to be addressed in future studies.

A large amount of solutions used in biological and medical applications exhibit elastic and viscoelastic behavior. The analysis of non-Newtonian droplet generation, started with this thesis, needs to be completed by enlarging the number (and the kind) of non-Newtonian working fluids used as dispersed phase. As an example, shear thickening fluids are not studied in this thesis but they can be interesting working fluids for some specific application. The data presented in this dissertation for shear thinning fluids can be compared in the next future with the results obtained by using shear thickening non-Newtonian fluids.

An experimental investigation of the local velocity distribution within the continuous and dispersed phases during the droplet formation could be very useful in order to clarify the role played by the main controlling forces on the liquid-liquid interface during the droplet formation. Further studies are needed in order to investigate the velocity distributions in the two phases into the junction by using in a combined way both numerical simulations and experimental measurements (i.e. micro-PIV measurements, pressure drop measurements). This combined analysis could greatly advance the understanding of the controlling mechanisms of the droplet breakup in microdevices, especially in presence of non-Newtonian liquids.

Finally, more complex geometries of the micro devices could be proposed and investigated both numerically and experimentally with the aim to stabilize the monodispersed droplet generation by increasing in the same time their droplet productivity (i.e. the rate of droplet generation). This could be very beneficial in order to improve the introduction of these microdevices in large-scale applications in biological and medical areas.

Future is going; and future in this field is Microfluidics!

References

- [1] C. N. Baroud, F. Gallaire, R. Dangla, Dynamics of microfluidic droplets, *Lab on a Chip*, 10 (16); 2032-2045, (2010).
- [2] A. S. Utada, E. L. Lorenceau, D. R. Link, P. D. Kaplan, H. A. Stone, D. A. Weitz, Monodisperse double emulsions generated from a microcapillary device, *Science*, 308 (5721); 537-541, (2005).
- [3] P. B. Umbanhowar, V. Prasad, D. A. Weitz, Monodisperse emulsion generation via drop break off in a coflowing stream, *Langmuir*, 16 (2); 347-351, (2000).
- [4] P. S. Dittrich, A. Manz, Lab-on-a-chip: microfluidics in drug discovery, *Nature Reviews Drug Discovery*, 5 (3); 210-218, (2006).
- [5] N. Shembekar, C. Chaipan, R. Utharala, C. A. Merten, Droplet-based microfluidics in drug discovery, transcriptomics and high-throughput molecular genetics, *Lab on a Chip*, 16 (8); 1314-1331, (2016).
- [6] B. Rotman, Measurement of activity of single molecules of β -D-galactosidase, *Proceedings of the National Academy of Sciences*, 47 (12); 1981-1991, (1961).
- [7] D. S. Tawfik, A. D. Griffiths, Man-made cell-like compartments for molecular evolution, *Nature Biotechnology*, 16 (7); 652-656, (1998).
- [8] P. Kuhn, K. Wilson, M. G. Patch, R. C. Stevens, The genesis of high-throughput structure-based drug discovery using protein crystallography, *Current Opinion in Chemical Biology*, 6 (5); 704-710, (2002).
- [9] Y. Yu, X. Wang, D. Oberthür, A. Meyer, M. Perbandt, L. Duan, Q. Kang, Design and application of a microfluidic device for protein crystallization using an evaporation-based crystallization technique, *Journal of Applied Crystallography*, 45 (1); 53-60, (2012).
- [10] M. Maeki, S. Yoshizuka, H. Yamaguchi, M. Kawamoto, K. Yamashita, H. Nakamura, M.

Miyazaki, H. Maeda, X-ray Diffraction of Protein Crystal Grown in a Nano-liter Scale Droplet in a Microchannel and Evaluation of Its Applicability, *Analytical Sciences*, 28 (1); 65-65, (2012).

[11] H. Song, D. L. Chen, R. F. Ismagilov, Reactions in droplets in microfluidic channels, *Angewandte Chemie-International Edition*, 45 (44); 7336-7356, (2006).

[12] X. Xiang, L. Chen, Q. Zhuang, X. Ji, Z. He, Real-time luminescence-based colorimetric determination of double-strand DNA in droplet on demand, *Biosensors and Bioelectronics*, 32 (1); 43-49, (2012).

[13] A. Giapos, C. Pachatouridis, M. Stamatoudis, Effect of the number of impeller blades on the drop sizes in agitated dispersions, *Chemical Engineering Research and Design*, 83 (12); 1425-1430, (2005).

[14] P. B. O'Donnell, J. W. McGinity, Preparation of microspheres by the solvent evaporation technique, *Advanced Drug Delivery Reviews*, 28 (1); 25-42, (1997).

[15] D. Poncelet, Production of alginate beads by emulsification/internal gelation, *Annals of the New York Academy of Sciences*, 944 (1); 74-82, (2001).

[16] T. Thorsen, R. W. Roberts, F. H. Arnold, S. R. Quake, Dynamic pattern formation in a vesicle-generating microfluidic device, *Physical Review Letters*, 86 (18); 4163, (2001).

[17] S. L. Anna, N. Bontoux, H. A. Stone, Formation of dispersions using "flow focusing" in microchannels, *Applied Physics Letters*, 82 (3); 364-366, (2003).

[18] L. Yobas, S. Martens, W.-L. Ong, N. Ranganathan, High-performance flow-focusing geometry for spontaneous generation of monodispersed droplets, *Lab on a Chip*, 6 (8); 1073-1079, (2006).

[19] C. Cramer, P. Fischer, E. J. Windhab, Drop formation in a co-flowing ambient fluid, *Chemical Engineering Science*, 59 (15); 3045-3058, (2004).

[20] J. D. Tice, H. Song, A. D. Lyon, R. F. Ismagilov, Formation of droplets and mixing in multiphase microfluidics at low values of the Reynolds and the capillary numbers, *Langmuir*, 19 (22); 9127-9133, (2003).

[21] A. Günther, S. A. Khan, M. Thalmann, F. Trachsel, K. F. Jensen, Transport and reaction in microscale segmented gas-liquid flow, *Lab on a Chip*, 4 (4); 278-286, (2004).

[22] Z. Gu, Experimental and Theoretical Study of Droplet Formation at a T-junction with

Xanthan Gum Solutions, School of Engineering and Information Technology, University of New South Wales, Ph.D. Thesis, Sydney, Australia, (2013).

[23] I. Kobayashi, S. Mukataka, M. Nakajima, Novel asymmetric through-hole array microfabricated on a silicon plate for formulating monodisperse emulsions, *Langmuir*, 21 (17); 7629-7632, (2005).

[24] A. Gupta, R. Kumar, Effect of geometry on droplet formation in the squeezing regime in a microfluidic T-junction, *Microfluidics and Nanofluidics*, 8 (6); 799-812, (2010).

[25] I. Kobayashi, G. T. Vladisavljević, K. Uemura, M. Nakajima, CFD analysis of microchannel emulsification: Droplet generation process and size effect of asymmetric straight flow-through microchannels, *Chemical Engineering Science*, 66 (22); 5556-5565, (2011).

[26] A. Gupta, R. Kumar, Flow regime transition at high capillary numbers in a microfluidic T-junction: Viscosity contrast and geometry effect, *Physics of Fluids*, 22 (12); 122001, (2010).

[27] Z. Nie, M. Seo, S. Xu, P. C. Lewis, M. Mok, E. Kumacheva, G. M. Whitesides, P. Garstecki, H. A. Stone, Emulsification in a microfluidic flow-focusing device: effect of the viscosities of the liquids, *Microfluidics and Nanofluidics*, 5 (5); 585-594, (2008).

[28] W. Lee, L. M. Walker, S. L. Anna, Role of geometry and fluid properties in droplet and thread formation processes in planar flow focusing, *Physics of Fluids*, 21 (3); 032103, (2009).

[29] M. Seo, C. Paquet, Z. Nie, S. Xu, E. Kumacheva, Microfluidic consecutive flow-focusing droplet generators, *Soft Matter*, 3 (8); 986-992, (2007).

[30] J. M. Zook, W. N. Vreeland, Effects of temperature, acyl chain length, and flow-rate ratio on liposome formation and size in a microfluidic hydrodynamic focusing device, *Soft Matter*, 6 (6); 1352-1360, (2010).

[31] P. M. Korczyk, O. Cybulski, S. Makulska, P. Garstecki, Effects of unsteadiness of the rates of flow on the dynamics of formation of droplets in microfluidic systems, *Lab on a Chip*, 11 (1); 173-175, (2011).

[32] L. Shui, A. van den Berg, J. C. T. Eijkel, Interfacial tension controlled W/O and O/W 2-phase flows in microchannel, *Lab on a Chip*, 9 (6); 795-801, (2009).

[33] R. Pichot, F. Spyropoulos, I. T. Norton, O/W emulsions stabilised by both low molecular weight surfactants and colloidal particles: The effect of surfactant type and concentration, *Journal of Colloid and Interface Science*, 352 (1); 128-135, (2010).

-
- [34] R. Pichot, F. Spyropoulos, I. T. Norton, Competitive adsorption of surfactants and hydrophilic silica particles at the oil–water interface: interfacial tension and contact angle studies, *Journal of Colloid and Interface Science*, 377 (1); 396-405, (2012).
- [35] J. H. Xu, G. S. Luo, S. W. Li, G. G. Chen, Shear force induced monodisperse droplet formation in a microfluidic device by controlling wetting properties, *Lab on a Chip*, 6 (1); 131-136, (2006).
- [36] D. Qian, A. Lawal, Numerical study on gas and liquid slugs for Taylor flow in a T-junction microchannel, *Chemical Engineering Science*, 61 (23); 7609-7625, (2006).
- [37] T. Fu, Y. Wu, Y. Ma, H. Z. Li, Droplet formation and breakup dynamics in microfluidic flow-focusing devices: from dripping to jetting, *Chemical Engineering Science*, 84; 207-217, (2012).
- [38] T. Glawdel, C. Elbuken, C. L. Ren, Droplet formation in microfluidic T-junction generators operating in the transitional regime. I. Experimental observations, *Physical Review E*, 85; 016322, (2012).
- [39] H. Liu, Y. Zhang, Droplet formation in microfluidic cross-junctions, *Physics of Fluids*, 23 (8); 082101, (2011).
- [40] P. Guillot, A. Colin, Stability of parallel flows in a microchannel after a T junction, *Physical Review E*, 72 (6); 066301, (2005).
- [41] P. Garstecki, M. J. Fuerstman, H. A. Stone, G. M. Whitesides, Formation of droplets and bubbles in a microfluidic T-junction-scaling and mechanism of break-up, *Lab on a Chip*, 6 (3); 437-446, (2006).
- [42] E. Chiarello, L. Derzsi, M. Pierno, G. Mistura, E. Piccin, Generation of oil droplets in a non-Newtonian liquid using a microfluidic T-junction, *Micromachines*, 6 (12); 1825-1835, (2015).
- [43] E. Piccin, D. Ferraro, P. Sartori, E. Chiarello, M. Pierno, G. Mistura, Generation of water-in-oil and oil-in-water microdroplets in polyester-toner microfluidic devices, *Sensors and Actuators B: Chemical*, 196; 525-531, (2014).
- [44] J. H. Xu, S. W. Li, J. Tan, G. S. Luo, Correlations of droplet formation in T-junction microfluidic devices: from squeezing to dripping, *Microfluidics and Nanofluidics*, 5 (6); 711-717, (2008).

- [45] H. Liu, Y. Zhang, Droplet formation in a T-shaped microfluidic junction, *Journal of Applied Physics*, 106 (3); 034906, (2009).
- [46] M. De Menech, P. Garstecki, F. Jousse, H. A. Stone, Transition from squeezing to dripping in a microfluidic T-shaped junction, *Journal of Fluid Mechanics*, 595; 141-161, (2008).
- [47] J. H. Xu, S. W. Li, J. Tan, Y. J. Wang, G. S. Luo, Preparation of highly monodisperse droplet in a T-junction microfluidic device, *AIChE Journal*, 52 (9); 3005-3010, (2006).
- [48] H. Liu, Y. Zhang, Lattice Boltzmann simulation of droplet generation in a microfluidic cross-junction, *Communications in Computational Physics*, 9 (5); 1235-1256, (2011).
- [49] G. F. Christopher, S. L. Anna, Microfluidic methods for generating continuous droplet streams, *Journal of Physics D: Applied Physics*, 40; R319-R336, (2007).
- [50] J. K. Nunes, S. S. H. Tsai, J. Wan, H. A. Stone, Dripping and jetting in microfluidic multiphase flows applied to particle and fibre synthesis, *Journal of Physics D: Applied Physics*, 46 (11); 114002, (2013).
- [51] R. Raj, N. Mathur, V. V. Buwa, Numerical simulations of liquid-liquid flows in microchannels, *Industrial & Engineering Chemistry Research*, 49 (21); 10606–10614, (2010).
- [52] S. Yeom, S. Y. Lee, Dependence of micro-drop generation performance on dispenser geometry, *Experimental Thermal and Fluid Science*, 35 (8); 1565-1574, (2011).
- [53] M. L. J. Steegmans, K. G. P. H. Schroën, R. M. Boom, Microfluidic Y-junctions: A robust emulsification system with regard to junction design, *AIChE Journal*, 56 (7); 1946–1949, (2010).
- [54] A. K. Das, P. K. Das, Simulation of drop movement over an inclined surface using smoothed particle hydrodynamics, *Langmuir*, 25 (19); 11459–11466, (2009).
- [55] K. Wang, Y. C. Lu, J. H. Xu, J. Tan, G. S. Luo, Generation of micromonodispersed droplets and bubbles in the capillary embedded T-junction microfluidic devices, *AIChE Journal*, 57 (2); 299-306, (2011).
- [56] W. Wang, Z. Liu, Y. Jin, Y. Cheng, LBM simulation of droplet formation in microchannels, *Chemical Engineering Journal*, 173 (3); 828-836, (2011).
- [57] G. F. Christopher, N. N. Noharuddin, J. A. Taylor, S. L. Anna, Experimental observations of the squeezing-to-dripping transition in T-shaped microfluidic junctions, *Physical Review E*, 78 (3); 036317, (2008).

- [58] T.-D. Dang, Y. H. Kim, H. G. Kim, G. M. Kim, Preparation of monodisperse PEG hydrogel microparticles using a microfluidic flow-focusing device, *Journal of Industrial and Engineering Chemistry*, 18; 1308-1313, (2012).
- [59] Y. Li, D. G. Yamane, S. Li, S. Biswas, R. K. Reddy, J. S. Goettert, K. Nandakumar, C. S. S. R. Kumar, Geometric optimization of liquid–liquid slug flow in a flow-focusing millifluidic device for synthesis of nanomaterials, *Chemical Engineering Journal*, 217; 447-459, (2013).
- [60] A. R. Abate, A. Poitzsch, Y. Hwang, J. Lee, J. Czerwinska, D. A. Weitz, Impact of inlet channel geometry on microfluidic drop formation, *Physical Review E*, 80 (2); 026310, (2009).
- [61] S. Gulati, K. Vijayakumar, W. W. Good, W. L. Tamayo, A. R. Patel, X. Niu, Microdroplet formation in rounded flow-focusing junctions, *Microfluidics and Nanofluidics*, 20 (2); doi:10.1007/s10404-10015-11680-10403, (2016).
- [62] E. Castro-Hernández, M. P. Kok, M. Versluis, D. F. Rivas, Study of the geometry in a 3D flow-focusing device, *Microfluidics and Nanofluidics*, 20 (40); doi:10.1007/s10404-10016-11708-10403, (2016).
- [63] J. Husny, J. J. Cooper-White, The effect of elasticity on drop creation in T-shaped microchannels, *Journal of Non-Newtonian Fluid Mechanics*, 137 (1); 121-136, (2006).
- [64] S. Yeom, S. Y. Lee, Size prediction of drops formed by dripping at a micro T-junction in liquid-liquid mixing, *Experimental Thermal and Fluid Science*, 35 (2); 387-394, (2011).
- [65] S. Bashir, J. M. Rees, W. B. Zimmerman, Simulations of microfluidic droplet formation using the two-phase level set method, *Chemical Engineering Science*, 66 (20); 4733-4741, (2011).
- [66] T. Cubaud, T. G. Mason, Capillary threads and viscous droplets in square microchannels, *Physics of Fluids*, 20 (5); 053302, (2008).
- [67] K. Wang, Y. C. Lu, J. H. Xu, G. S. Luo, Determination of dynamic interfacial tension and its effect on droplet formation in the T-shaped microdispersion process, *Langmuir*, 25 (4); 2153-2158, (2009).
- [68] B. Steinhaus, A. Q. Shen, R. Sureshkumar, Dynamics of viscoelastic fluid filaments in microfluidic devices, *Physics of Fluids*, 19 (7); 073103, (2007).
- [69] J. S. Hong, J. Cooper-White, Drop formation of Carbopol dispersions displaying yield stress, shear thinning and elastic properties in a flow-focusing microfluidic channel, Korea-

Australia Rheology Journal, 21 (4); 269-280, (2009).

[70] W. Lee, L. M. Walker, S. L. Anna, Competition Between Viscoelasticity and Surfactant Dynamics in Flow Focusing Microfluidics, *Macromolecular Materials and Engineering*, 296 (3-4); 203-213, (2011).

[71] P. E. Arratia, J. P. Gollub, D. J. Durian, Polymeric filament thinning and breakup in microchannels, *Physical Review E*, 77 (3); 036309, (2008).

[72] P. E. Arratia, L. A. Cramer, J. P. Gollub, D. J. Durian, The effects of polymer molecular weight on filament thinning and drop breakup in microchannels, *New Journal of Physics*, 11 (11); 115006, (2009).

[73] V. Tirtaatmadja, G. H. McKinley, J. J. Cooper-White, Drop formation and breakup of low viscosity elastic fluids: Effects of molecular weight and concentration, *Physics of Fluids*, 18 (4); 043101, (2006).

[74] S. J. Peng, R. A. Williams, Controlled production of emulsions using a crossflow membrane: Part I: Droplet formation from a single pore, *Chemical Engineering Research and Design*, 76 (8); 894-901, (1998).

[75] X. Zhang, Dynamics of growth and breakup of viscous pendant drops into air, *Journal of Colloid and Interface Science*, 212 (1); 107-122, (1999).

[76] T. A. Kowalewski, On the separation of droplets from a liquid jet, *Fluid Dynamics Research*, 17 (3); 121-145, (1996).

[77] K. Loubière, V. Castaignède, G. Hébrard, M. Roustan, Bubble formation at a flexible orifice with liquid cross-flow, *Chemical Engineering and Processing: Process Intensification*, 43 (6); 717-725, (2004).

[78] C.-J. Liu, B. Liang, S.-W. Tang, H.-G. Zhang, E.-Z. Min, A theoretical model for the size prediction of single bubbles formed under liquid cross-flow, *Chinese Journal of Chemical Engineering*, 18 (5); 770-776, (2010).

[79] J. H. Xu, G. S. Luo, G. G. Chen, J. D. Wang, Experimental and theoretical approaches on droplet formation from a micrometer screen hole, *Journal of Membrane Science*, 266 (1); 121-131, (2005).

[80] K. Loubière, G. Hébrard, Bubble formation from a flexible hole submerged in an inviscid liquid, *Chemical Engineering Science*, 58 (1); 135-148, (2003).

- [81] M. L. J. Steegmans, C. G. P. H. Schroën, R. M. Boom, Generalised insights in droplet formation at T-junctions through statistical analysis, *Chemical Engineering Science*, 64 (13); 3042-3050, (2009).
- [82] S. Van der Graaf, T. Nisisako, C. G. P. H. Schroen, R. G. M. Van Der Sman, R. M. Boom, Lattice Boltzmann simulations of droplet formation in a T-shaped microchannel, *Langmuir*, 22 (9); 4144-4152, (2006).
- [83] Y. Zhang, J. Fan, L. Wang, Formation of nanoliter droplets in a confined microfluidic T-shaped junction: Formation time and droplet volume, *Current Nanoscience*, 5 (4); 519-526, (2009).
- [84] L. Sang, Y. Hong, F. Wang, Investigation of viscosity effect on droplet formation in T-shaped microchannels by numerical and analytical methods, *Microfluidics and Nanofluidics*, 6 (5); 621-635, (2009).
- [85] T. Glawdel, C. Elbuken, C. L. Ren, Droplet formation in microfluidic T-junction generators operating in the transitional regime. II. Modeling, *Physical Review E*, 85 (1); 016323, (2012).
- [86] M. L. J. Steegmans, J. De Ruiter, K. G. P. H. Schroën, R. M. Boom, A descriptive force-balance model for droplet formation at microfluidic Y-junctions, *AIChE Journal*, 56 (10); 2641-2649, (2010).
- [87] X.-B. Li, F.-C. Li, J.-C. Yang, H. Kinoshita, M. Oishi, M. Oshima, Study on the mechanism of droplet formation in T-junction microchannel, *Chemical Engineering Science*, 69 (1); 340-351, (2012).
- [88] V. van Steijn, M. T. Kreutzer, C. R. Kleijn, μ -PIV study of the formation of segmented flow in microfluidic T-junctions, *Chemical Engineering Science*, 62 (24); 7505-7514, (2007).
- [89] J. S. Hadamard, Mouvement permanent lent d'une sphère liquide et visqueuse dans un liquide visqueux, *Comptes Rendus de l'Académie des Sciences*, 152; 1735-1752, (1911).
- [90] W. Rybczynski, On the translatory motion of a fluid sphere in a viscous medium, *Bulletin International de l'Académie des Sciences de Cracovie, Series A*, 40 (1911).
- [91] CPKelco, Xanthan Book, A Huber Company, 8th edition, (2007).
- [92] P. J. Carreau, Rheological equations from molecular network theories, *Transactions of the Society of Rheology*, 16 (1); 99-127, (1972).

- [93] C. Huh, S. G. Mason, A rigorous theory of ring tensiometry, *Colloid & Polymer Science*, 253 (7); 566-580, (1975).
- [94] O. Kuksenok, D. Jasnow, A. C. Balazs, Local control of periodic pattern formation in binary fluids within microchannels, *Physical Review Letters*, 95 (24); 240603, (2005).
- [95] O. Kuksenok, D. Jasnow, J. Yeomans, A. C. Balazs, Periodic droplet formation in chemically patterned microchannels, *Physical Review Letters*, 91 (10); 108303, (2003).
- [96] O. Kuksenok, D. Jasnow, A. C. Balazs, Diffusive intertwining of two fluid phases in chemically patterned microchannels, *Physical Review E*, 68 (5); 051505, (2003).
- [97] M. J. Geerken, R. G. H. Lammertink, M. Wessling, Tailoring surface properties for controlling droplet formation at microsieve membranes, *Colloids and Surfaces A: Physicochemical and Engineering Aspects*, 292 (2-3); 224-235, (2007).
- [98] R. Dreyfus, P. Tabeling, H. Willaime, Ordered and disordered patterns in two-phase flows in microchannels, *Physical Review Letters*, 90 (14); 144505, (2003).
- [99] M. Evans, L. Han, I. Ratcliffe, P. A. Williams, *Synthesis, Characterisation and Properties of Novel Biosurfactants Based on Hydrophobically-Modified Inulins, Gums and Stabilisers for the Food Industry 18: Hydrocolloid Functionality for Affordable and Sustainable Global Food Solutions*; The Royal Society of Chemistry, 123-134, (2016).
- [100] N. Otsu, A threshold selection method from gray-level histograms, *IEEE Transactions on Systems, Man, and Cybernetics*, 9 (1); 62-66, (1979).
- [101] J. Canny, A computational approach to edge detection, *IEEE Transactions on Pattern Analysis and Machine Intelligence*, 8 (6); 679-698, (1986).
- [102] P. Garstecki, I. Gitlin, W. DiLuzio, G. M. Whitesides, Formation of monodisperse bubbles in a microfluidic flow-focusing device, *Applied Physics Letters*, 85 (13); 2649-2651, (2004).
- [103] P. Garstecki, H. A. Stone, G. M. Whitesides, Mechanism for flow-rate controlled breakup in confined geometries: A route to monodisperse emulsions, *Physical Review Letters*, 94 (16); 164501, (2005).
- [104] R. J. Moffat, Describing the uncertainties in experimental results, *Experimental Thermal and Fluid Science*, 1 (1); 3-17, (1988).
- [105] J. Tan, J. H. Xu, S. W. Li, G. S. Luo, Drop dispenser in a cross-junction microfluidic

device: Scaling and mechanism of break-up, *Chemical Engineering Journal*, 136 (2–3); 306-311, (2008).

[106] J. Tan, S. W. Li, K. Wang, G. S. Luo, Gas–liquid flow in T-junction microfluidic devices with a new perpendicular rupturing flow route, *Chemical Engineering Journal*, 146 (3); 428-433, (2009).

[107] M. N. Kashid, A. Renken, L. Kiwi-Minsker, CFD modelling of liquid–liquid multiphase microstructured reactor: Slug flow generation, *Chemical Engineering Research and Design*, 88 (3); 362-368, (2010).

[108] T. Fu, Y. Ma, D. Funfschilling, C. Zhu, H. Z. Li, Squeezing-to-dripping transition for bubble formation in a microfluidic T-junction, *Chemical Engineering Science*, 65 (12); 3739-3748, (2010).

[109] T. Cubaud, C.-M. Ho, Transport of bubbles in square microchannels, *Physics of Fluids*, 16 (12); 4575-4585, (2004).

[110] M. Zagnoni, J. Anderson, J. M. Cooper, Hysteresis in multiphase microfluidics at a T-junction, *Langmuir*, 26 (12); 9416-9422, (2010).

[111] A. Timgren, G. Trägårdh, C. Trägårdh, Effects of cross-flow velocity, capillary pressure and oil viscosity on oil-in-water drop formation from a capillary, *Chemical Engineering Science*, 64 (6); 1111-1118, (2009).

[112] X. Zhang, O. A. Basaran, An experimental study of dynamics of drop formation, *Physics of Fluids*, 7 (6); 1184-1203, (1995).

[113] J. G. Southwick, A. M. Jamieson, J. Blackwell, Quasi-elastic light scattering studies of semidilute xanthan solutions, *Macromolecules*, 14 (6); 1728-1732, (1981).

[114] T. Ward, M. Faivre, M. Abkarian, H. A. Stone, Microfluidic flow focusing: Drop size and scaling in pressure versus flow-rate-driven pumping, *Electrophoresis*, 26 (19); 3716-3724, (2005).

[115] J. J. Cooper-White, J. E. Fagan, V. Tirtaatmadja, D. R. Lester, D. V. Boger, Drop formation dynamics of constant low-viscosity, elastic fluids, *Journal of Non-Newtonian Fluid Mechanics*, 106 (1); 29-59, (2002).

[116] H. A. Stone, B. J. Bentley, L. G. Leal, An experimental study of transient effects in the breakup of viscous drops, *Journal of Fluid Mechanics*, 173; 131-158, (1986).

-
- [117] R. B. Bird, W. E. Stewart, E. N. Lightfoot, *Transport Phenomena*, Wiley, Second Edition, 56-58, (2007).
- [118] P. Guillot, A. Colin, Stability of parallel flows in a microchannel after a T-junction, *Physical Review E*, 72 (6); 066301, (2005).